PTNSS

193(2), 2023

COMBUSTION ENGINES

Politechnika Poznańska

Wydział Inżynierii Lądowej i Transportu
Instytut Silników Spalinowych i Napędów

- Emisyjność napędów spalinowych i hybrydowych
- Energochłonność napędów HEV, FCHEV, EV
- Wodorowe i wielopaliwowe silniki spalinowe
- Eksploatacja napędów lotniczych
- Symulatory pojazdu i samolotu
- Bezzałogowe statki powietrzne
- Systemy spalania
- Ogniwa paliwowe

Instytut Silników Spalinowych i Napędów
Zakład Silników Spalinowych | Zakład Napędów Alternatywnych | Zakład Lotnictwa
ul. Piotrowo 3, 60-965 Poznań,
tel. 61-665-2207; office_ice@put.poznan.pl

Due to the dynamic development of machine and vehicle powertrains, the "Combustion Engines" scientific journal, while retaining its historical title, currently publishes works related not only to internal combustion engines, but also other powertrains, including hybrid drives, electric drives and fuel cells.

PTNSS Supporting Members
Członkowie wspierający PTNSS

BOSMAL Automotive Research and Development Institute Ltd
Instytut Badań i Rozwoju Motoryzacji BOSMAL Sp. z o.o

Motor Transport Institute
Instytut Transportu Samochodowego

Institute of Aviation
Sieć Badawcza Łukasiewicz – Instytut Lotnictwa

Automotive Industry Institute
Sieć Badawcza Łukasiewicz – Przemysłowy Instytut Motoryzacji

Sieć Badawcza Łukasiewicz – Poznański Instytut Technologiczny

AVL List GmbH

Solaris Bus & Coach S.A.

Air Force Institute of Technology
Instytut Techniczny Wojsk Lotniczych

Military Institute of Armoured & Automotive Technology
Wojskowy Instytut Techniki Pancernej i Samochodowej

Toyota Motor Poland Ltd. Sp. z o.o.

RADWAG Balances and Scales
RADWAG Wagi Elektroniczne

MS Mechatronic Solutions Group

FOGO Sp. z o.o.

COMBUSTION ENGINES
A Scientific Magazine

2023, 193(2)

Year LXII

PL ISSN 2300-9896
PL eISSN 2658-1442

Publisher:
Polish Scientific Society of Combustion Engines
60-965 Poznan, pl. M. Skłodowskiej-Curie 5, Poland
tel.: +48 61 6475966, fax: +48 61 6652204
E-mail: sekretariat@ptnss.pl
WebSite: http://www.ptnss.pl
Papers available on-line: http://combustion-engines.eu

Contents

Publisher:
Polish Scientific Society of Combustion Engines
60-965 Poznan, pl. M. Sklodowskiej-Curie 5, Poland
tel.: +48 61 6475966, fax: +48 61 6652204
E-mail: sekretariat@ptnss.pl
WebSite: http://www.ptnss.pl

Subscriptions
Send subscription requests to the Publisher's address.
Cost of a single issue PLN 65.

Preparation for print
ARS NOVA Publishing House
60-782 Poznan, ul. Grunwaldzka 17/10A

Circulation: 260 copies

Printing and binding

Zakład Poligraficzny Moś i Łuczak, sp. j.,
Poznań, ul. Piwna 1

The journal is under the patronage of the Transport Committee of the Polish Academy of Sciences

The journal is registered and listed in the Polish and international database

Papers published in the
Combustion Engines
quarterly receive 70 points as stated by the Notification of the Minister of Science and Education dated 1 December 2021.

Declaration of the original version
The original version of the Combustion Engines journal is the printed version.

Cover
I – Liebherr H964, 4-cylinder hydrogen combustion engines *(www.liebherr.com)*;
background *(night horizon – www.peakpx.com)*
IV – Hyundai Mobis – fuel cell powerpack for non-road vehicles *(www.hyundaimotorgroup.com)*

Article citation info:
Zhou L, Li K, Sun T. Studies on the flame structure and drag of a combusting droplet group. Combustion Engines. 2023;193(2):3-8. https://doi.org/10.19206/CE-160506

Lixing ZHOU
Ke LI
Ting SUN

Combustion Engines
Polish Scientific Society of Combustion Engines

Studies on the flame structure and drag of a combusting droplet group

ARTICLE INFO

Received: 16 December 2022
Revised: 26 January 2023
Accepted: 3 February 2023
Available online: 13 February 2023

Droplet combustion has been studied by experiments and numerical simulation for many years, and most of studies were done about single droplets. As for droplet groups, some theoretical and experimental studies were reported, but less of numerical studies. One of the important characteristics is the drag of combusting droplets, which is closely related to flame structure, and is a sub-model in numerical simulation of spray combustion. There are contradictory research results for the drag of combusting droplets. In the present paper, large-eddy simulation (LES) is used to study the flame structure and drag of a combusting ethanol-droplet group. The results show that there are three combustion modes: fully-enveloped flame, partially-enveloped flame and wake flame in a droplet group, leading to the change of the drag with inlet velocities. It is found that the drag of droplets in the group is much smaller than that of a non-combusting particle in isothermal flows.

Key words: *droplet-group combustion; large-eddy-simulation; flame structure; drag force*

1. Introduction

Spray combustion is widely encountered in various engines [1–3]. It was studied by large-eddy simulation [4, 5], where droplets were taken as volume-less point-source particles. Droplet combustion is an important part of spray combustion. The droplet combustion has been studied both experimentally and analytically for many decades since the middle's years of the last century [6–9]. The experiments were done for suspended droplets, falling droplets and flying droplets of different fuels. The so-called d^2-law was examined and the "evaporation constant" $K = d(d_p^2/dt)$ under different gas relative velocities, gas temperatures and pressures were studied. In analytical studies, most of them are based on simplified 1-D "spherical stagnant-film" models. Even now, the sub-models for spray combustion in modern CFD software are still based on these models. These simplified studies cannot give the detailed structures of droplet flames. In recent years, more detailed theoretical, experimental and numerical studies of droplet combustion were reported. Awasthi et al. [10] simulated the effect of ambient temperature and initial droplet size on the combustion of a heptane droplet. The focus was paid on the heptane-droplet ignition delay and the comparison between the heptane and methanol droplets in flame location and evaporation rates. Kitano et al. [11] simulated single and multiple-droplet combustion, but used a given evaporation model to study the effect of ambient pressure and gas temperature on droplet evaporation. No information on the detailed gas flow, species concentration and gas temperature distributions surrounding the droplets were reported. Zhao et al. [12] simulated the effect of gas temperature on droplet combustion, only the effect of gas temperature on the droplet evaporation rate was reported and the comparison was given with the numerical results of other investigators. Chiu et al. [13, 14] reported an analytical model of droplet-group combustion. Segawa et al. [15] studied experimentally the ignition and early combustion behavior of 49 droplets under microgravity condition. Mikami et al. [16, 17] reported the droplet interactions in flame spreading characteristics of 100 n-decane droplets under micro-gravity conditions. Manish and Sahu [18] used PIV (particle imaging velocimetry) to measure the group combustion of droplet clusters in spray flames.

Regarding to droplet combustion characteristics, the drag force of evaporating/combusting droplets is an important sub-model in spray combustion modeling. Different research results were reported. The measurement results reported by Eisenklam et al. [19] are that evaporation reduces the droplet drag. Yuen et al. [20] did experimental studies, and Renksizbulut and Yuen [21] did analytical studies of different evaporating droplets; the conclusion is that evaporation does not affect the droplet drag. Makino and Fukada [22] measured the velocity of a falling combusting sodium droplet. The results show that combustion increases the droplet drag. Sugimoto [23] measured the velocity of a combusting methanol droplet; the results are that combustion reduces the droplet drag.

In general, the flow and flame structures surrounding a combusting droplet-group are unclear and the drag of combusting droplet group has not been reported. In this paper, large-eddy simulation (LES) is used to study a combusting ethanol-droplet group. The obtained flame structures and drag force are reported. The results will help to improve the drag model in numerical simulation of spray combustion in engines

2. Controlling equations and closure models for LES of a droplet-group combustion

To study the detailed flow and flame structures surrounding ethanol droplet group, the filtered governing equations for 3-D LES are given as

$$\frac{\partial \rho}{\partial t} + \frac{\partial \rho}{\partial t}(\rho \bar{u}_i) = 0 \tag{1}$$

$$\frac{\partial}{\partial t}(\rho \bar{u}_i) + \frac{\partial}{\partial x_j}(\rho \bar{u}_i \bar{u}_j) = \frac{\partial}{\partial x_j}\left(\mu \frac{\partial \bar{u}_i}{\partial x_j}\right) - \frac{\partial \bar{p}}{\partial x_i} - \frac{\partial \tau^{sgs}{}_{ij}}{\partial x_j} \tag{2}$$

$$\frac{\partial \rho \bar{Y}_s}{\partial t} + \frac{\partial}{\partial x_j}(\rho \bar{u}_j \bar{Y}_s) = \frac{\partial}{\partial x_j}\left(\frac{\mu}{S_c}\frac{\partial \bar{Y}_s}{\partial x_j}\right) - \overline{w_s} - w_{sgs} - \frac{\partial g_{jsgs}}{\partial x_j} \tag{3}$$

$$\frac{\partial \rho \bar{h}}{\partial t} + \frac{\partial}{\partial x_j}\left(\rho \bar{h} \bar{u}_j\right) = \frac{\partial}{\partial x_j}\left(\frac{\mu}{Pr}\frac{\partial \bar{h}}{\partial x_j}\right) - \frac{\partial q_{jsgs}}{\partial x_j} \quad (4)$$

The sub-grid-scale (SGS) stress was closed by the dynamic eddy-viscosity model [24]

$$\tau_{ij}^{sgs} = 2\rho C_s \bar{\Delta}^2 |\bar{S}| \overline{S_{ij}}$$

$$C_s = -\frac{1}{2}\frac{\langle L_{ij}\bar{S}_{ij}\rangle}{\hat{\Delta}^2\langle|\hat{\bar{S}}|\hat{\bar{S}}_{ij}\bar{S}_{ij}\rangle - \bar{\Delta}^2\langle|\hat{\bar{S}}|\hat{\bar{S}}_{ij}\bar{S}_{ij}\rangle} \quad (5)$$

where $L_{ij} = \bar{u}_i\bar{u}_j - \tilde{\bar{u}}_i\tilde{\bar{u}}_{ij}$, $\tilde{\Delta} = 2\bar{\Delta}$, $\bar{\Delta}$ is the filter size/grid size, and

$$A = \frac{1}{2}\left(\frac{\partial \tilde{\bar{u}}_i}{\partial x_j} + \frac{\partial \tilde{\bar{u}}_j}{\partial x_i}\right);\ \left|\hat{\bar{S}}\right| = \sqrt{2\hat{\bar{S}}_{ij}\hat{\bar{S}}_{ij}}$$

The SGS mass and heat fluxes are closed by gradient modeling

$$g_{jsgs} = \rho\left(u_j Y_s - \bar{u}_j \bar{Y}_s\right) = \frac{\mu_t}{\sigma_Y}\frac{\partial \bar{Y}_s}{\partial x_j} \quad (6)$$

$$q_j{}^{sgs} = \rho\left(u_j T - \bar{u}_j \bar{T}\right) = \frac{\mu_t}{\sigma_T}\frac{\partial \bar{T}}{\partial x_j} \quad (7)$$

The sub-grid scale reaction rate is closed by the second-order moment combustion model [25]

$$w_{sgs} = \bar{w}_s\left(\frac{\overline{Y_1'Y_2'}}{\bar{Y}_1\bar{Y}_2} + \frac{\overline{K'Y_1'}}{\bar{K}\bar{Y}_1} + \frac{\overline{K'Y_2'}}{\bar{K}\bar{Y}_2}\right)$$

$$\overline{\phi\varphi} = \frac{c\mu_t\left(\frac{\partial \Phi}{\partial x_j}\right)\left(\frac{\partial \Psi}{\partial x_j}\right)}{\rho} \Big/ \left(\frac{a}{\tau_T} + \frac{1-a}{\tau_c}\right) \quad (8)$$

where Φ, Ψ, ϕ and φ denote the filtered and sub-grid-scale fluctuation values of Y_1, Y_2 and K respectively.

$$\tau_T = 1/|\bar{S}|;\ \tau_c = \left[B\rho\left(\bar{Y}_{O_2} + \beta\bar{Y}_{CH_4}\right)\exp\left(-\frac{E}{R\bar{T}}\right)\right]^{-1}$$

For ethanol-oxygen reaction mechanism, a global single-step reaction is used

$$2C_2H_5OH + 6O_2 \rightarrow 4CO_2 + 6H_2O \quad (9)$$

The Arrhenius expression of the single-step global reaction kinetics for the reaction rate is

$$w_s = 8.345 \times 10^9 \rho^2 Y_{fu} Y_{ox} \exp[-1.26 \times 10^8/(RT)] \quad (10)$$

with boundary conditions at the droplet surface, accounting for the Stefan flux

$$\lambda_w\left(\frac{dT}{dr}\right)_w = \rho_w \nu_w q_e =$$

$$= \frac{G}{4\pi r_w^2} q_e - D_w \rho_w \left(\frac{dY}{dr}\right)_w + Y_s \rho_w \nu_w = \alpha \rho_w \nu_w$$

$$\Sigma Y_s = \Sigma Y_F + \Sigma Y_{ox} + \Sigma Y_{pr} + \Sigma Y_{in} = 1$$

where, s = F(fuel), $\alpha = 1$, $s \neq F$, $\alpha = 0$. α is a notation for different species. For obtaining the fuel vapor concentration, the fuel vapor partial pressure should be obtained by using the Antoine equation.

3. Computation domain and solution procedure

The computation domain is shown in Fig. 1. The sizes and position of simulated droplets are shown in Fig. 2 and Table 1. The grid sizes in x, y, and z directions are 10–300 μm; the time step was taken as 0.000001 s; and the grid number is about 1400000.

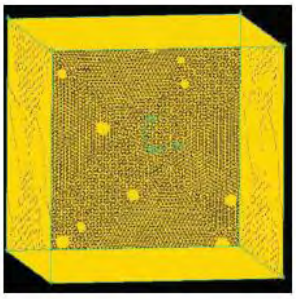

Fig. 1. Computation domain

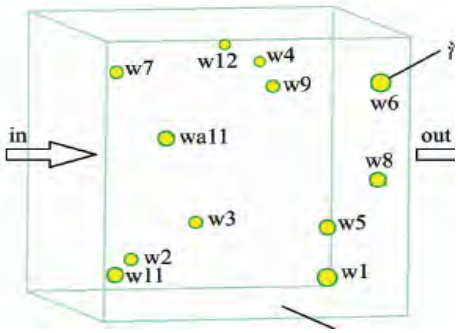

Fig. 2. Droplet sizes and position

The PISO algorithm was used for p–v corrections; the second-order implicit difference scheme was taken for the time-dependent term, the second-order upwind difference scheme was taken for the convection term, and the central difference scheme was taken for the diffusion term. For the gas boundary conditions, a uniform gas inlet velocity was taken. The boundary condition at the exit was based on a fully developed flow assumption, where the gradients for all flow variables in the axial direction were set to be zero.

Table1. Droplet sizes and position

Group No./ Droplet size [μm]		Droplet position x [μm]	y [μm]	z [μm]
w1	34.3	301.5	–433.7	515.1
w2	21.5	–293.9	–420.8	–180.0
w3	27.3	7.1	–291.0	–364.1
w4	17.1	238.9	408.9	–298.7
w5	29.2	469.1	–294.9	–139.3
w6	36.4	551.1	377.1	334.1
w7	23	–507.9	451.4	394.6
w8	27.9	496.1	–17.5	520.8
w9	20.3	158.8	360.3	214.5
w10	32.8	–483.0	–429.7	309.3
w11	19.4	56.3	498.9	–129.3
w12	30.6	–257.0	137.0	195.5

4. Simulation results

4.1. Instantaneous flame structures

Figure 3 shows three combustion modes of the droplet group. There are fully-enveloped flame, partially-enveloped flame and wake flame under different gas relative velocity, similar to the numerical results of a single droplet [26], and the PLIF measurement results obtained by Mercier et al.

[27]. However, in case of the droplet group, different combustion modes may exist in the same region, since there are different droplet sizes in a computation domain. Since the Stefan flow surrounding the droplets in the azimuthal direction is non-uniform, which will cause the change of drag with the inlet velocity.

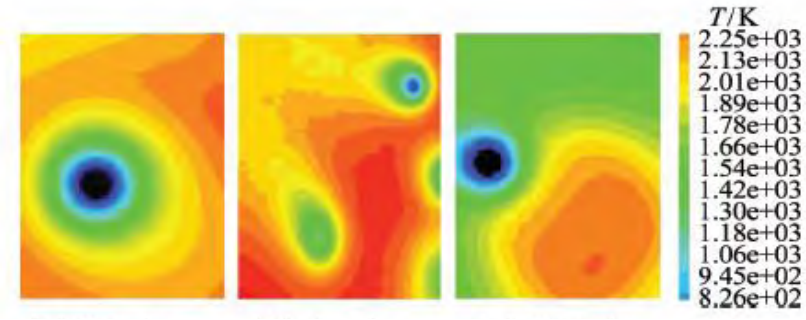

(a) 1 m/s (b) 4 m/s (c) 10 m/s

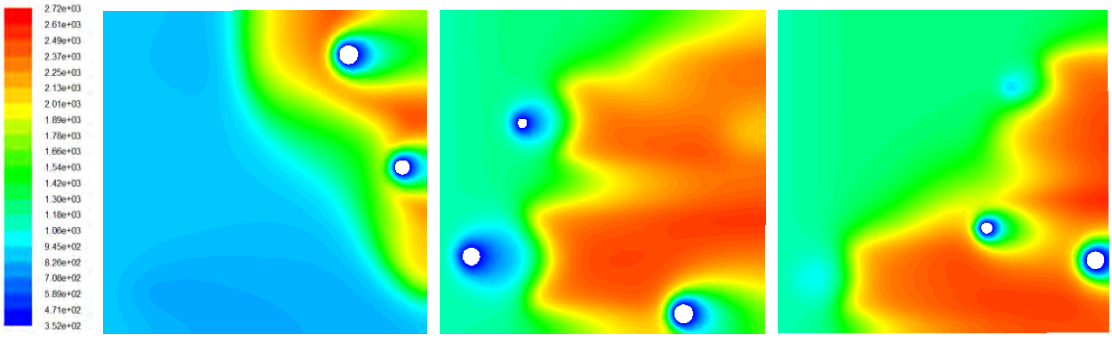

(d) (gas velocity 4m/s, gas temperature 1200 K)

Fig. 3. Three combustion modes of multiple droplets

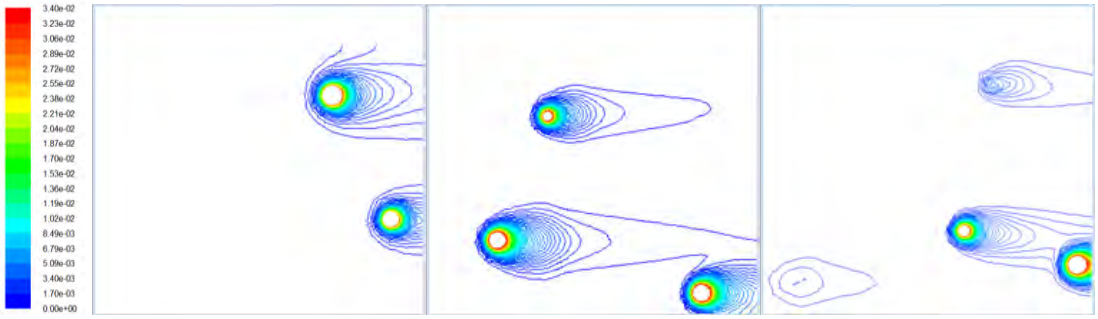

Fig. 4. Molar fraction of ethanol-vapor concentration

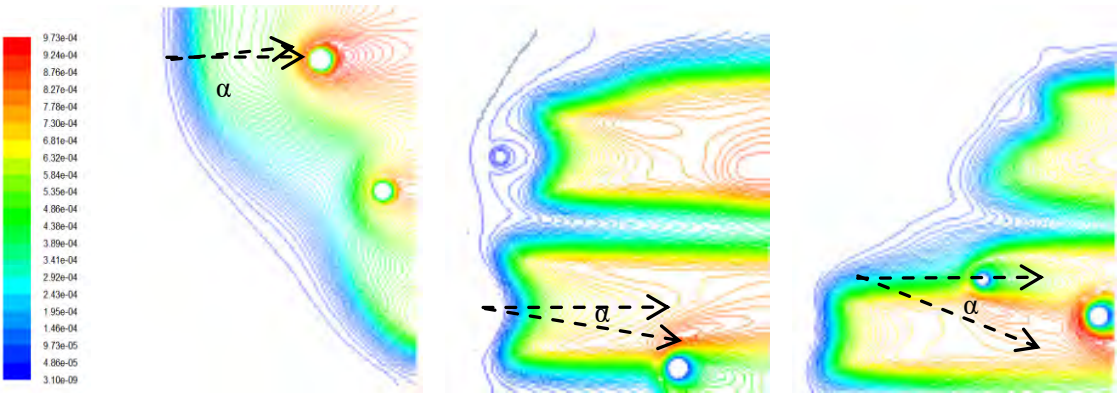

Fig. 5. Molar fraction of H_2O concentration

Figures 4 and 5 show the predicted molar fractions of ethanol-vapor and H_2O surrounding the droplet group respectively. The distribution of ethanol-vapor concentration is axis-symmetrical, but the reaction zones are somewhat declined with an angle of α due the interaction between droplets. Figures 6 and 7 are velocity vectors and streamlines surrounding the combusting droplet group respectively. Obviously, velocities ahead of droplets are larger than those behind droplets due to the Stefan flow, leading to the change of drag. The similar phenomenon was observed in the velocity vectors surrounding a single droplet [26]. The streamlines are distorted due to the interaction between droplets.

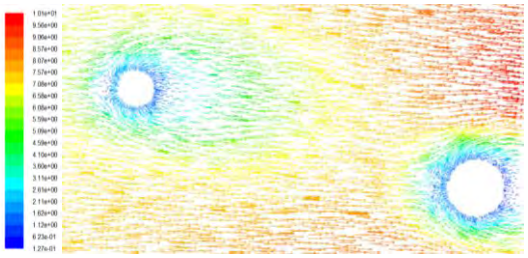

Fig. 6. Velocity vectors surrounding combusting droplets

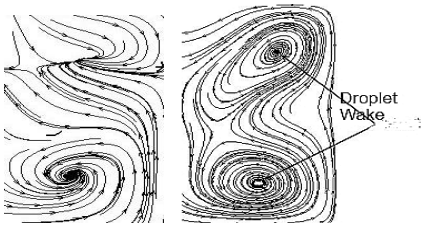

Fig. 7. Streamlines surrounding combusting droplets

Figure 8 gives the vorticity maps surrounding a droplet group and a single droplet. The vortex shedding in a droplet inside the group is weaker than that in a single droplet owing to droplet-droplet interactions.

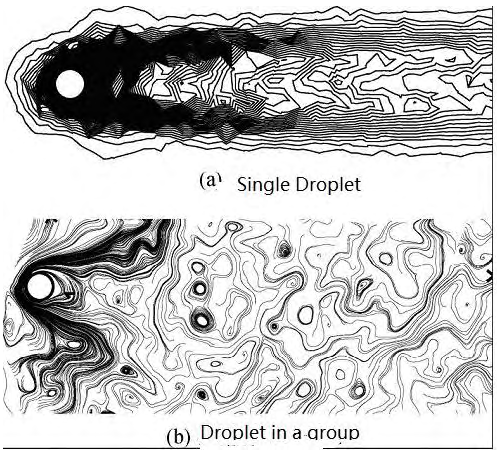

Fig. 8. Vorticity maps surrounding a droplet group

4.2. Statistics of the combusting droplet drag

The statistics gives the comparison between the widely-used Wallis-Kliachko formula of the drag for non-combusting particles in isothermal flows, modified droplet drag accounting the effect of the Stefan Flow given by the 1-D model [28] and the LES results for a single combusting droplet, as shown in Table 2. The Wallis-Kliachko formula [28] gives

$$C_{D0} = \begin{cases} \dfrac{24}{Re_p}\left(1 + Re_p^{2/3}/6\right) & Re_p < 1000 \\ 0.44 & Re_p \geq 1000 \end{cases}$$

$$Re_p = \frac{\rho_f d_p \left|\vec{U}_f - \vec{U}_p\right|}{\mu_f}$$

The modified formula in the 1-D stagnant-film theory [28] gives

$$C_D = C_{D0}\ln(1+b)/B;\ B = c_p(T_g - T_b)/L$$

where B is the transfer number, related to the boiling point and latent heat of the liquid.

Obviously, the drag coefficient of combusting droplet is much smaller than that of non-combusting particles in isothermal flows. The physical explanations may be the injection effect of non-uniform Stefan flow surrounding the combusting droplet and the effect of cold droplet-surface temperature on the reduction of friction force due to the reduction of gas viscosity.

Table 2. Drag coefficients for a single combusting droplet (T_g = 1200 K)

V_{rel} [m/s]	C_{D0} (Wallis-Kliachko Formula)	C_D (LES)	C_{D0} × × ln (1+B)/B
0.2	3.950	1.100	2.370
1.0	1.960	0.344	1.176
4.0	0.963	0.235	0.576

The drag coefficient of a droplet in its group is still smaller than that of a single droplet, as shown in Table 3.

Table 3. Drag coefficients for a droplet in its group

V_{rel} [m/s]	C_D (Wallis-Kliachko)	C_D (Single droplet)	C_D (Droplet in a group)
1	1.960	0.344	0.297
4	0.963	0.235	0.144

Figure 9 gives the drag coefficient of the single combusting droplet vs droplet Reynolds number, reported in [26]. It is seen that as the droplet Reynolds number increases to be greater than 280, the reduction effect of drag gradually diminishes.

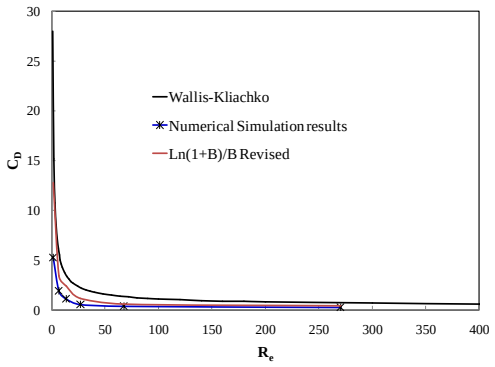

Fig. 9. Drag coefficient vs droplet Reynolds number

Figure 10 shows drag coefficients of droplets of different sizes in their group under various gas relative velocities and temperatures, indicating that the effect of gas temperature is more sensitive to drag reduction.

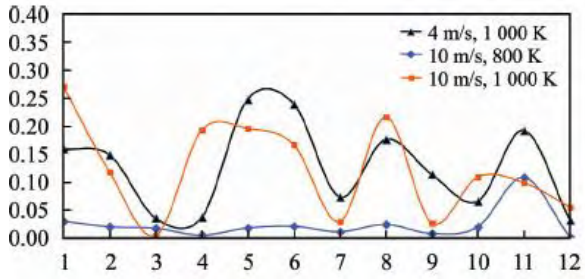

Fig. 10. Drag coefficients of different droplets in their group

Conclusions

Three modes of flame structures were observed in a droplet group: fully-enveloped, partially-enveloped and wake flames, and Stefan-flow structure was observed for the droplet-group combustion, leading to the change of drag force with the increasing inlet velocity. The drag force of combusting multiple droplets is much smaller than that of non-combusting particles in isothermal flows. Future work should be done for finding a new drag-force model of combusting droplets in numerical simulation of spray-combustion engines.

Acknowledgements

This study was sponsored by the Key Project of National Natural Science Foundation of China under the Grant 51390493.

Bibliography

[1] Stelmasiak Z, Matyjasik M. Simulation of the combustion in a dual fuel engine with a divided pilot dose. Combustion Engines, 2012;151(4):43-54. https://doi.org/10.19206/CE-117020

[2] Kniaziewicz T, Zacharewicz M. A physical model of energetic processes in a diesel marine generator set. Combustion Engines. 2018;175(4):10-17. https://doi.org/10.19206/CE-2018-402

[3] Kowalski J. The theoretical investigation on influence the fuel spray geometry on the combustion and emission characteristic of the marine diesel engine. Combustion Engines. 2017;169(2):101-107. https://doi.org/10.19206/CE-2017-218

[4] Li K, Zhou LX, Chan CK, Wang HG. Large-eddy simulation of ethanol spray combustion using a SOM combustion model and its experimental validation. Applied Mathematical Modeling. 2015;39(1):36-49. https://doi.org/10.1016/j.apm.2014.04.011

[5] Li K, Zhou LX. Studies of the effect of spray inlet conditions on the flow and flame structures of ethanol-spray combustion by large-eddy simulation. Numer Heat Transfer, 2012;62(1):44-59. https://doi.org/10.1080/10407782.2012.672865

[6] Godsave GAE. Studies of the combustion of drops in a fuel spray: The burning of single drops of fuel. Symposium (International) on Combustion. 1953;4(1):818-830. https://doi.org/10.1016/S0082-0784(53)80107-4

[7] Spalding DB. The combustion of liquid fuels. Symposium (International) on Combustion. 1953;4(1):847-864. https://doi.org/10.1016/S0082-0784(53)80110-4

[8] Zhou LX. Evaporation and combustion of individual droplets and liquid spray of hydrocarbons in air (in Russian), Ph.D. Thesis, Department of Physics and Mechanics, Leningrad Polytechnic University, USSR, 1961.

[9] Law CK. Recent advances in droplet vaporization and combustion. Prog Energ Combust. 1982;8(3):171-201. https://doi.org/10.1016/0360-1285(82)90011-9

[10] Awasthi I, Pope DN, Gogos G. Effects of the ambient temperature and initial diameter in droplet combustion. Combust Flame. 2014;161(7):1883-1899. https://doi.org/10.1016/j.combustflame.2014.01.001

[11] Kitano T, Nishio J, Kurose R, Komori S. Effects of ambient pressure, gas temperature and combustion reaction on droplet evaporation, Combust Flame. 2014;161(2):551-564. https://doi.org/10.1016/j.combustflame.2013.09.009

[12] Zhao Y, Yang LB, et al. Numerical simulation of impacts of gas flow temperature on combustion characteristics of single droplet. Journal of Combustion Science and Technology (in Chinese). 2014;20:77-83.

[13] Tsai HL, Chiu HH. Anomalous group combustion phenomena in DI diesel engines. Atomization Sprays. 2005;15:377-400. https://doi.org/10.1615/AtomizSpr.v15.i4.20

[14] Tsai HL, Chiu HH. Cluster statistical theory based on group combustion, 4th Asia-Pacific Conference on Combustion. 2003:491-494.

[15] Segawa D, Yoshida M, Nakaya S, Katoda T. Auto-ignition and early flame behavior of a spherical cluster of 49 monodispersed droplets. P Combust Inst. 2007;31(2):2149-2156. https://doi.org/10.1016/j.proci.2006.07.124

[16] Mikami M, Matsumoto K, Yoshida Y, Kikuchi M, Dietrich DL. Space-based microgravity experiments on flame spread over randomly distributed n-decane droplet clouds: anomalous behavior in flame spread. P Combust Inst. 2021;38(2):3167-3174. https://doi.org/10.1016/j.proci.2020.07.139

[17] Mikami M, Yoshida Y, Seo T, Sakashita T, Kikuchi M, Suzuki T et al. Space-based microgravity experiments on flame spread over randomly distributed n-decane droplet clouds: overall flame spread characteristics. Microgravity Sci Tech. 2018;30:535-542. https://doi.org/10.1007/s12217-018-9637-2

[18] Manish M, Sahu S. Optical characterization of droplet clusters and group combustion in spray diffusion flames. P Combust Inst. 2021;38(2):3409-3416. https://doi.org/10.1016/j.proci.2020.08.016

[19] Eisenklam P, Arunachalam SA. The drag resistance of burning drops. Combust Flame. 1966;10(2):171-176. https://doi.org/10.1016/0010-2180(66)90065-4

[20] Yuen MC, Chen LW. On drag of evaporating liquid droplets. Combust Sci Technol. 1976;14(4-6):147-154. https://doi.org/10.1080/00102207608547524

[21] Renksizbulut M, Yuen MC. Numerical study of droplet evaporation in a high-temperature stream. J Heat Transf. 1983;105(2):389-397. https://doi.org/10.1115/1.3245591

[22] Makino A, Fukada H. Combustion behavior of a falling sodium droplet: burning rate and drag coefficient. Heat Transfer-Asian Research. 2005;34(7):481-495. https://doi.org/10.1002/htj.20084

[23] Sugimoto A. Investigation of combustion of liquid sprays II: drag coefficient of a droplet. Bulletin of University of Osaka Prefecture, Series A. 1970;19:35-44.

[24] Germano M, Piomelli U, Moin P, Cabot WH. A dynamic subgrid-scale eddy viscosity model. Phys Fluids A-Fluid. 1991;3:1760-1765. https://doi.org/10.1063/1.857955
[25] Zhou L. Development of SOM combustion model for Reynolds-averaged and large-eddy simulation of turbulent combustion and its validation by DNS. Sci China Ser E-Technol Sci. 2008;51:1073-1086. https://doi.org/10.1007/s11431-008-0157-y
[26] Zhou L, Li K. Analytical and numerical studies on a single-droplet evaporation and combustion under forced convection. Acta Mech Sin. 2015;31:523-530. https://doi.org/10.1007/s10409-015-0424-7
[27] Mercier X, Orain M, Grisch F. Investigation of droplet combustion in strained counterflow diffusion flames using planar laser-induced fluorescence. Appl. Phys B. 2007;88: 151-160. https://doi.org/10.1007/s00340-007-2605-y
[28] Zhou L. Combustion Theory and Dynamics of Reacting Fluids. Beijing: Science Press; 1986.

Prof. Lixing Zhou, DSc., DEng. – Engineering Mechanics, Tsinghua University, China.
e-mail: *zhoulx@mail.tsinghua.edu.cn*

Prof. Ke Li, DSc., DEng. – School of Energy and Environmental Engineering, Inner Mongolia University of Science and Technology, China.
e-mail: *kelitsinghua@hotmail.com*

Ting Sun, DEng. – Engineering Mechanics, Tsinghua University, China.
e-mail: *sunting@imust.edu.cn*

Article citation info:
Puzdrowska P. Evaluation of the influence of the opening pressure of a marine Diesel engine injector on the results of numerical simulation of the working cycle and their comparison with the results of the laboratory experiment. Combustion Engines. 2023;193(2):9-14. https://doi.org/10.19206/CE-155873

Patrycja PUZDROWSKA

Combustion Engines
Polish Scientific Society of Combustion Engines

Evaluation of the influence of the opening pressure of a marine diesel engine injector on the results of numerical simulation of the working cycle and their comparison with the results of the laboratory experiment

ARTICLE INFO

Received: 27 September 2022
Revised: 18 October 2022
Accepted: 18 October 2022
Available online: 4 December 2022

The article presents the results of a numerical simulation of the working process carried out in a diesel engine. In the applied utility program DIESEL-RK, the laboratory engine Farymann Diesel type D10 was implemented. A selected inoperability of its functional fuel supply system – reduced opening pressure of the injector p_{inj} – was introduced. The values of adequate diagnostic parameters were determined: working gas temperature in the cylinder T_{cyl}, exhaust gas temperature T_{exh}, combustion (flame) temperature T_{comb} and concentration of nitrogen oxides in the exhaust gas NO_x. Experimental tests were carried out on the experimental engine with the inoperative condition actually introduced, analogous to the numerical simulation, and the diagnostic parameters T_{exh} and NO_x were recorded. The results obtained by numerical simulation of the processes and during the active experiment on the experimental engine were compared.

Key words: *marine diesel engine, numerical simulation, diagnostic parameters, injector opening pressure*

1. Introduction

Parametric diagnostics of marine diesel engines is essential for the long-term and safe operation of a ship's engine room and power plant. It is a rapidly developing area in terms of the measurement sensors (e.g., temperature or pressure) used in diagnostic systems [3, 6, 13, 14]. An important support for these systems and the operators themselves are usable computer programs that allow numerical simulation of the processes occurring in the engine during the realized operating cycle. It is also important to determine, by means of further calculations, the values of diagnostic parameters, authoritative in the case of the occurrence of impurities or inefficiency of structural elements surrounding the combustion chamber, but also of the fuel supply system or intake air. Carrying out numerical simulations of the working process allows the selection of adequate diagnostic parameters, which, recorded during experimental tests or normal operation of a marine engine, can give the most diagnostic information about the analyzed inefficiency. This article proposes a method of determining the effect of a selected inefficiency in the functional fuel supply system of a marine diesel engine on its diagnostic parameters, according to the following steps:

1. Selection of one of the most common inefficiencies in the functional systems of marine diesel engines, based on literature data.
2. Introduction of design changes in the DIESEL-RK computer program and determination of adequate diagnostic parameters by numerical simulation of the working process occurring in a 4-stroke marine diesel engine, for the Farymann Diesel type D10 experimental engine implemented in the program.
3. Conduct an active experiment on the experimental engine's laboratory stand and determine the diagnostic parameters for the actual change in the structural design, analogous to the numerical simulation.
4. Comparison of the effect of changing the structural design parameter of a selected component of the engine's fuel supply functional system on the diagnostic parameters obtained by numerical simulation of the working process and as a result of an active experiment on an laboratory engine.

2. Results of numerical simulation of diesel engine working cycle in DIESEL-RK program

A numerical simulation of the operating process of a Farymann Diesel type D10 laboratory engine was carried out. The DIESEL-RK program for numerical simulation of thermodynamic processes occurring in a piston engine was used [7, 8, 17, 19]. The DIESEL-RK computer program in the public version is designed to simulate and optimize the thermodynamic processes of two-stroke and four-stroke engines, for all types of supercharging and for the various fuels used. The possibilities of the software allowed to implement into the program the structural (e.g. piston diameter, combustion chamber volume) and operational data (such as rotational speed of the crankshaft or type of fuel) of the laboratory engine Farymann Diesel type D10 – Fig. 1. The elementary composition of the marine gas oil (MGO) feed fuel used during the laboratory tests was entered. Calculations of the working process were carried out for two engine states: reference and for reduced opening pressure of the injector p_{inj} ($2 \cdot 10^6$ Pa less).

The choice of injector opening pressure was based on the fact that the fuel supply system is one of the functional systems of a marine diesel engine that most often malfunctions [14–16]. Analyzing the damage to marine diesel engines, the most critical functional systems are the fuel system (nearly 50% of all damage) and the working gas exchange (24.7%). In the case of the fuel supply system, injectors (41%) and injection pumps (38%) are the components most frequently damaged [15].

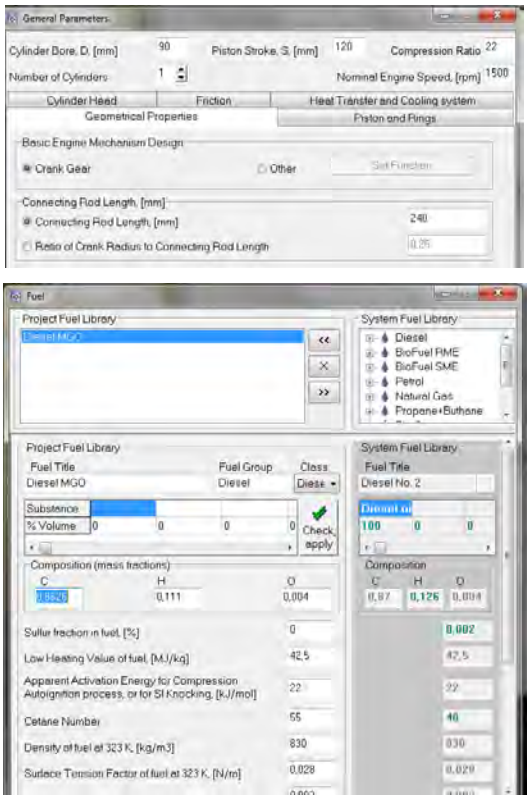

Fig. 1. View of the window of the DIESEL-RK computer program, in options: "General parameters" and "Fuel"

In his dissertation, Dr. Eng. S. Bruski presented the results of a statistical study for medium-speed engines operated on the Navy's ships [1]. The author shows that the most frequent failures happened in the fuel supply (72%), the valve train (19%) and the air supply (9%) systems. With 54% of injector failures in the fuel supply system, they accounted for 38.9% of all engine failures in operation. A research team from Vietnam, on the basis of their reliability analysis of the structural components included in the functional systems of a marine diesel engine, identified the injection system as one of all the functional systems of a marine engine that wears out at the fastest rate – each additional 500 hours of engine operation doubles the probability of damage to the components of this system [11].

Due to the subject matter of the author's research, this article presents simulation results on the following output parameters, calculated in the DIESEL-RK program [9, 10]:

- temperature of working gas in the cylinder (T_{cyl}),
- temperature of the exhaust gas in the outlet channel (T_{exh}),
- combustion (flame) temperature in the cylinder (T_{comb}),
- concentration of nitrogen oxide particles NO_x in the exhaust gas (ppm).

The results of calculations of the working process carried out in the engine implemented in the program, for the two analyzed states of the design structure are presented in graphical form in Fig. 2–5. In the case of the introduced changes in the design structure of the fuel injection system of the experimental engine, their effect on the working gas temperature in the T_{cyl} cylinder was most evident in the work stroke, in the area of the maximum value of this parameter of engine operation – Fig. 2a. The introduced change in injector opening pressure resulted in a decrease in the temperature of the working gas in the cylinder. The largest difference occurred at the maximum value of T_{cyl} and was about 25 K – Fig. 2b. The difference between the waveforms of the working gas temperature in the cylinder for the rest of the working cycle realized in the modeled engine was much smaller or did not occur at all. Also in the case of the waveforms of changes in the temperature of the exhaust gas T_{exh}, the greatest differences in the values of this parameter occur in the region of the maximum – Fig. 3a. Reduced injector opening pressure p_{inj} resulted in an increase in exhaust gas temperature by about 10 K at the maximum value of T_{exh} – Fig. 3b. The difference in the value of exhaust gas temperature T_{exh} for the two analyzed states is also visible for the rest of the engine cycle, however it is smaller – Fig. 3a. The course of changes in the temperature of combustion (flame) of gas in the cylinder T_{comb} in the case of lowering the opening pressure of the injector p_{inj} showed a slight decrease – about 6 K. This difference remained at a similar level during the whole duration of combustion of the fuel-air mixture – Fig. 4a and b. Thus, all considered parameters of the design structure of the modeled engine and changes in their values influenced variations in the values of temperatures T_{cyl}, T_{exh} and T_{comb}.

a)

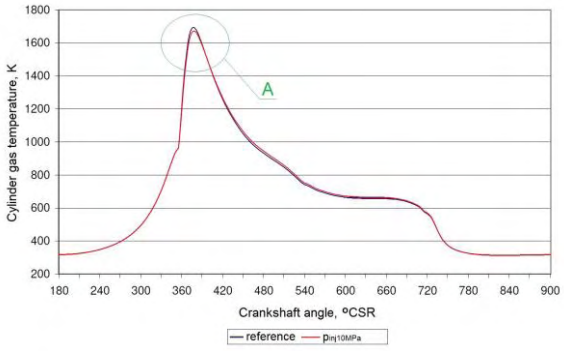

b)

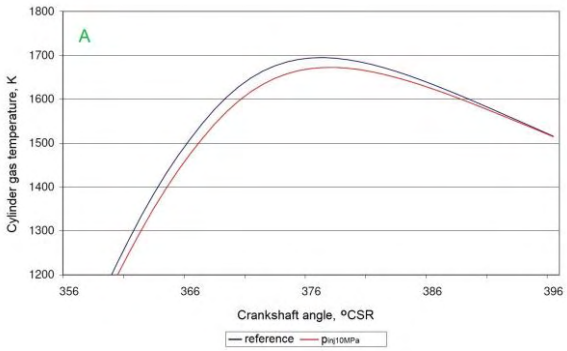

Fig. 2. Courses of changes in the temperature of the working gas in the cylinder T_{cyl} as a function of the angle of rotation of the crankshaft, for the whole working cycle of the engine (a) and for the range of occurrence of the maximum value of the temperature in the cylinder (b), achieved as a result of numerical simulation of the working process of the engine in the program DIESEL-RK under the conditions of introduced changes in the opening pressure of the injector p_{inj}

a) b)

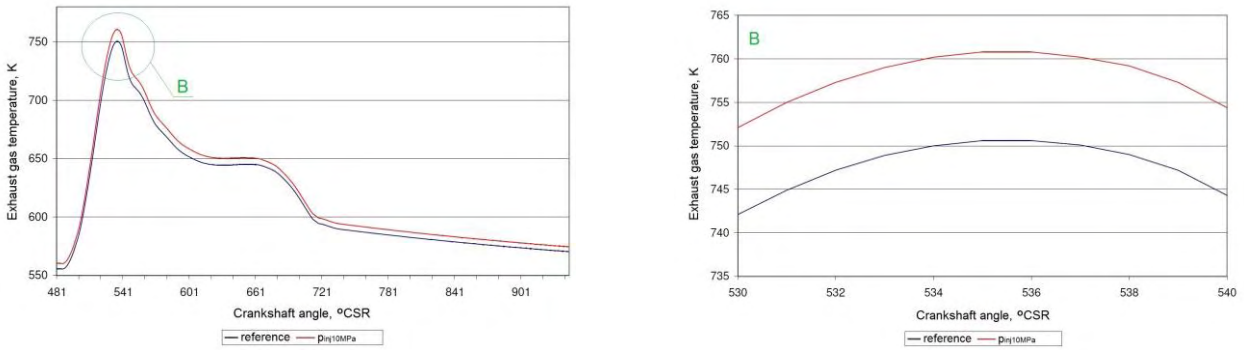

Fig. 3. Courses of changes in the temperature of the exhaust gas T_{exh} as a function of the angle of rotation of the crankshaft, for the part of the working cycle of the engine (a) and for the range of occurrence of the maximum value of the temperature of exhaust gas (b), achieved as a result of numerical simulation of the working process of the engine in the program DIESEL-RK under the conditions of introduced changes in the opening pressure of the injector p_{inj}

a) b)

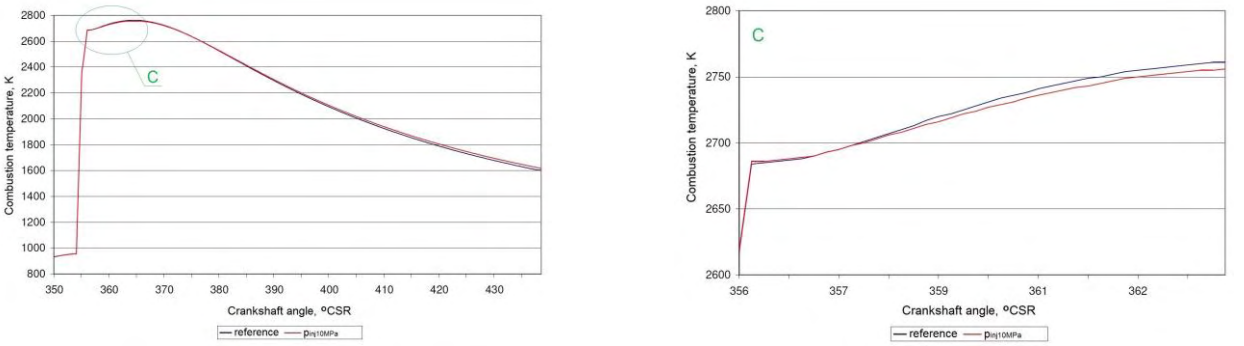

Fig. 4. Courses of changes in the combustion temperature (flame) in the cylinder T_{comb} as a function of the angle of rotation of the crankshaft, for the engine working stroke (a) and for the range of occurrence of the largest differences in combustion temperature for the considered states (b), achieved as a result of numerical simulation of the working process of the engine in the program DIESEL-RK under the conditions of introduced changes in the opening pressure of the injector p_{inj}

a) b)

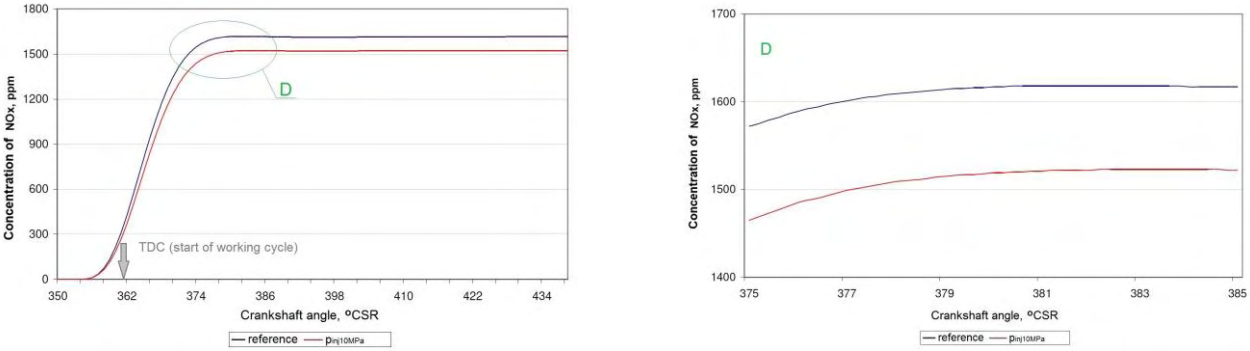

Fig. 5. Courses of changes in the concentration of NO_x particles in the exhaust gas as a function of the angle of rotation of the crankshaft, for the working stroke of the engine (a) and for the range of occurrence of the maximum value of the concentration of NO_x particles (b), achieved as a result of numerical simulation of the working process of the engine in the program DIESEL-RK under the conditions of introduced changes in the opening pressure of the injector p_{inj}

The DIESEL-RK simulation program also allowed us to deduce that for reduced injector opening pressure there is a significant effect on the value of NO_x particle concentration in the exhaust gas – lowering p_{inj} resulted in a decrease in the concentration of NO_x particles in the exhaust gas – Fig. 5. From the beginning of combustion (formation of exhaust gases), the difference in NO_x concentrations between the reference state and that for reduced injector opening pressure was about 98 ppm.

3. Results of a laboratory tests on an experimental engine Farymann Diesel type D10

The mathematical models used in computer programs that allow numerical simulation of thermodynamic processes occurring in a diesel engine contain certain simplifications (e.g., the working medium is treated as a perfect gas, and the equations of behavior do not consider mass or energy losses). Therefore, it is necessary to carry out experimental verification of simulation results, keeping in mind

that the results of laboratory tests are subject to uncertainty, which is due to interference (uniqueness) of the engine operating process and many sources of measurement uncertainty, among others, imperfection of the measurement method (measurement track), the impact of environmental conditions on the measurement result or the error of the researcher (e.g., when reading the indication of an analog instrument) [5, 12, 18]. Of course, knowledge of the thermodynamic processes and transformations occurring in the engine and in the exhaust gas channel is necessary to properly interpret the obtained measurement results and compare them with the results of numerical simulation [4].

3.1. Description of the laboratory test stand and the measurement devices used

The research was conducted on the laboratory test stand of the single-cylinder, four-stroke Farymann Diesel engine type D10 (Fig. 6), located in the Laboratory of Marine Power Plants, Faculty of Mechanical Engineering and Ship Technology, Gdansk University of Technology. The most important technical parameters of the laboratory engine include: nominal power 5.9 kW, nominal rotational speed 1500 min^{-1}, nominal torque 38 N·m, cylinder diameter 90 mm, piston stroke 120 mm, compression ratio 22:1, volume of cylinder stroke 765 cm^3.

During the research, the following were recorded: exhaust gas temperature and pressure, piston TDC signal, load current and voltage of the generator, exhaust valve opening signal, flue gas composition. In Table 1 shows the measured control parameters and the measuring equipment used during research.

A multifunctional measurement and recording module type DT-9805 from Data Translation was used to record: the quickly changing temperature and pressure of the exhaust gas and the piston top dead center signal. Matlab software was used to record the measured values. A constant crankshaft speed of 1442-1444 rpm was kept during the test. The sampling frequency was 7000 Hz. The presented research results are the average of 90 subsequent measurements recorded under the same engine operating conditions determined by the engine load, crankshaft speed and ambient parameters. A KIGAZ-310 analyzer was used to monitor the composition of the flue gas. During the tests the engine was burning marine gas fuel – MGO.

Table 1. The parameters of the Farymann type D10 single cylinder diesel engine recorded on the laboratory test stand

Item	Parameter	Measuring device	Unit	Measurement range
1.	Exhaust gas temperature – T_{sp}	Thermocouple type K, with welded joint to 0.5 mm diameter jacket, made from Inconell	K	273–1273
2.	Exhaust gas pressure in the exhaust channel – p_{sp}	Optical pressure sensor – Optrand C12296	V	0–689475.73 Pa (0–100 psi), sensitivity $6.01 \cdot 10^{-8}$ V/Pa (41.43 mV/psi)
3.	Engine speed (angular position ^{o}CA) – n Top dead center – TDC	Induction engine speed sensor and TDC sensor	min^{-1}	0–3000
4.	Load current of the generator – I_{tw}	Electric current meter	A	0–15
5.	Voltage at the armature terminals – U_{tw}	Voltmeter	V	0–250
6.	Exhaust valve opening signal	Gap type optoisolator with a comparator LM393	V mm	0–5 10 (gap)

a) b)

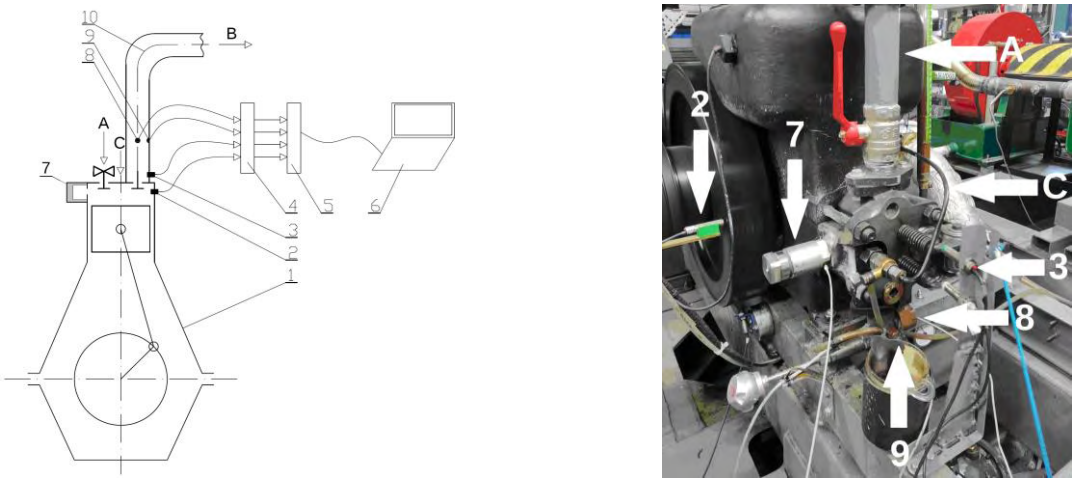

Fig. 6. a) Diagram of the laboratory test stand with the sensor mounting locations marked: 1 – Farymann D10 engine, 2 – engine rotational speed and TDC sensor, 3 – exhaust valve opening sensor, 4 – A/C converter, 5 – recorder, 6 – software, 7 – component to increase the volume of the combustion chamber, 8 – pressure sensor, 9 – water cooled thermocouple, 10 – exhaust gas channel, A – intake air with ball valve on the channel, B – exhaust gas, C – fuel line; b) view of the stand with the location of the sensors highlighted: 2 – engine speed and TDC sensor, 3 – exhaust valve opening sensor, 7 – component to increase the volume of the combustion chamber with a pressure sensor, 8 – pressure sensor, 9 – water cooled thermocouple, A – intake air with ball valve on the channel, C – fuel line

3.2. Results of the laboratory research

The experimental research was carried out on the Farymann Diesel engine type D10 (Fig. 6). Due to the limited measurement capabilities of the experimental engine, the following in-cylinder parameters were not recorded: flame temperature and the working gas medium in the combustion chamber. However, it was possible to record and compare with the result of a numerical simulation of the working process: the temperature of the exhaust gas T_{exh} and the composition of the exhaust gas (concentration of nitrogen oxide particles NO_x). The test was conducted for two different technical states of the research object. The first defined as the reference (benchmark, baseline) condition.

The second condition – partial suitability, resulting in a decrease in the opening pressure of the injector, was introduced through changes in the design structure of the injector: the thickness of the shim under the injector spring was changed. Changing the shim to a thinner one caused the spring tension force to decrease, thus simulating relaxation of the spring's structural material [2]. This is one of the most common states of operational unfitness in a marine engine. The engine under test has an injector with shims with a total thickness of δ_{inj} equal to 2.3 mm, resulting in a fuel injector opening pressure value of about 12 MPa (the value for the reference condition) – Fig. 7. During the test, shims with a total thickness of 1.8 mm were installed in the injector, resulting in a reduction of the injector opening pressure to 10 MPa, which simulated a malfunction in the fuel injection system involving too early injection of fuel into the combustion chamber.

The temperature of the exhaust gas T_{exh} values were recorded with a K-type thermocouple, with a sheath welded joint, with an outer diameter of the sheath of 0.5 mm and a time constant of 65 ms, mounted at a distance of 15 cm from the outlet valve seat. The concentration of NO_x particles was obtained by measurements in the exhaust gas channel using a KIGAZ-310 exhaust gas composition analyzer.

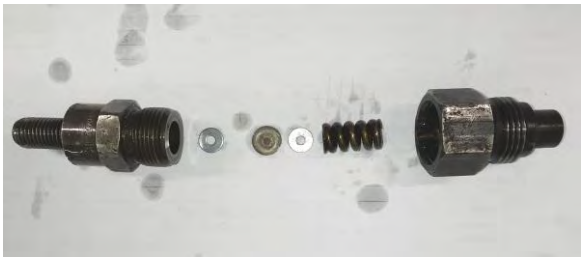

Fig. 7. View of the structural components of the injector used during the tests, including the replaceable shims under the injector spring

Table 2 shows the values obtained both by numerical simulation and measured during the active experiment, for the reference condition and for the reduced opening pressure of injector p_{inj}. In addition, the percentages of changes ΔX of these diagnostic parameters relative to the values for the engine's reference condition and the character (increase or decrease) of each change were determined, according to the relationship:

$$\Delta X = \left|\frac{X_{ref} - X_p}{X_{ref}}\right| \quad (1)$$

where: X_{ref} – value of the diagnostic parameter for the reference condition, X_p – value of the diagnostic parameter for reduced injector opening pressure.

During simulation, the average value of the exhaust gas temperature T_{exh} for the reduced injector opening pressure p_{inj} increased by 0.9% (5.52 K), while the measurement on the experimental engine showed an approximate 4% (8.3 K) decrease in the average value of this parameter. As for the concentration of NO_x particles in the exhaust gas, the lowered p_{inj} resulted in a 95% (525 ppm) increase in concentration during the laboratory test, while the simulation showed a 5,77% (93.2 ppm) decrease in the value of this diagnostic parameter. During the active experiment, the recorded diagnostic parameters are the averaged values within one cycle of the experimental engine, while the average values too were determined for the numerical simulation – Fig. 2–5.

Table 2. Average values of the diagnostic parameters for the numerical simulation of the working process and for the active experiment for two operating states, and the percentages and character of the changes of the diagnostic parameters with relation to the reference state

Operational status	Diagnostic parameter			
	Numerical simulation		Active experiment	
	Temperature of exhaust gas T_{exh}, K	Concentration of particles NO_x, ppm	Temperature of exhaust gas T_{exh}, K	Concentration of particles NO_x, ppm
State of full suitability (reference) p_{inj} = 12 MPa	889.35	1614.85	478.95	553
Condition of partial suitability (reduced injector opening pressure) p_{inj} = 10 MPa	894.87	1521.65	470.65	1078
Value and the character of the change in the value of the diagnostic parameter	↑ 5.52 K (0.9%)	↓ 93.2 ppm (5.77%)	↓ 8.3 K (4%)	↑ 525 ppm (95%)

4. Conclusions

The achieved values of selected diagnostic parameters such as the exhaust gas temperature T_{exh} and the concentration of NO_x particles, as well as the character and magnitude of their changes relative to the reference condition, differ when we compare the values obtained by numerical simulation in the DIESEL-RK program and for the experimental test. There may be many reasons for these differences, but the following should be considered the most important:

1. Simplifications used in the computer program's calculation algorithms, such as not taking into account the real

phenomena occurring in the diesel engine and exhaust gas channel, or treating the working medium as a perfect gas.
2. The presence of many sources of measurement uncertainty during the experimental test, among others, the influence of external factors on the engine operating process and the measurement track. This factor is not considered to any degree by the numerical simulation in the computer program.
3. Phenomena occurring in the exhaust gas channel, such as: heat release in the process of expansion, delay and deformation of recorded signals, flow resistance in the exhaust gas channel depending on its structural form, technical condition of the internal surface, etc., wave phenomena occurring in the channel (interference and reflection of pressure waves), adiabatic compression of the gas column located in front of successive pulses of exhaust gas leaving the engine cylinders [6].

Programs that allow the numerical simulation of the working process occurring in diesel engines, such as the presented DIESEL-RK, can be considered useful at the stage of selecting the analyzed parameters of the engine's design structure and the adequate diagnostic parameters that will respond most strongly to the introduced changes, before proceeding to tests on a laboratory engine or under operating conditions on a ship. However, this is a very multifaceted issue that requires further research and analysis.

Bibliography

[1] Bruski S. Zastosowanie metod analizy częstotliwościowej drgań skrętnych wału napędowego do identyfikacji stanu technicznego wtryskiwaczy paliwa średnioobrotowego silnika okrętowego w eksploatacji. Praca doktorska. Politechnika Gdańska, Gdańsk 2005.

[2] Dyląg Z, Jakubowicz A, Orłoś Z. Wytrzymałość materiałów, tom II. Wydawnictwo Naukowo-Techniczne, Warszawa 1997.

[3] Girtler J. Energetic aspect of diesel engine operation. Combustion Engines. 2009;137(2):84-92. https://doi.org/10.19206/CE-117183

[4] Kniaziewicz T, Zacharewicz M. Evaluation of adequacy of a model of a marine diesel engine based upon empirical research. Combustion Engines. 2020;181(2):40-45. https://doi.org/10.19206/CE-2020-206

[5] Korczewski Z. Diagnostic tolerances evaluation method of the start-up exhaust temperature of a naval gas turbine. Combustion Engines. 2011;145(2):99-105. https://doi.org/10.19206/CE-117108

[6] Korczewski Z. Diagnostyka eksploatacyjna okrętowych silników spalinowych – tłokowych i turbinowych. Wybrane zagadnienia. Wydawnictwo Politechniki Gdańskiej, Gdańsk 2017.

[7] Kuleshov AS. Diesel-RK Engine Simulation Software User Manual. Moscow 2004.

[8] Pham VV. Research on the application of diesel-RK in the calculation and evaluation of technical and economic criteria of marine diesel engines using the unified ULSD and biodiesel blended fuel. Journal of Mechanical Engineering Research and Developments. 2019;42(2):87-97. https://doi.org/10.26480/jmerd.02.2019.87.97

[9] Puzdrowska P. Evaluation of the significance of the effect of the active cross-sectional area of the inlet air channel on the specific enthalpy of the exhaust gas of a diesel engine using statistics F of the Fisher-Snedecor distribution. Combustion Engines. 2020;182(3):10-15. https://doi.org/10.19206/CE-2020-302

[10] Puzdrowska P. Identification on damages in the inlet air duct of a diesel engine based on exhaust gas temperature measurements. Combustion Engines. 2019;177(2):108-112. https://doi.org/10.19206/CE-2019-219

[11] Ta TV, Thien DM, Cang VT. Marine propulsion system reliability assessment by fault tree analysis. International Journal of Mechanical Engineering and Applications. Special issue: Transportation Engineering Technology Part III. 2017;5(4-1):1-7. https://doi.org/10.11648/j.ijmea.s.2017050401.11

[12] Trzeciak AM, Gieras M. Temperature estimating method for exhaust gases in valveless pulsejet engine. Combustion Engines. 2020;182(3):3-9. https://doi.org/10.19206/CE-2020-301

[13] Wang G, Zhou Y, Zhang Q. et al. The small sample failure distribution model of diesel engine component parts using FMECA approach. International Journal of Modeling and Optimalization. 2017;7(1):19-23. https://doi.org/10.7763/IJMO.2017.V7.551

[14] Witkowski K. Badania wpływu wybranych uszkodzeń silników okrętowych na parametry pracy silnika i skład spalin. Autobusy: technika, eksploatacja, systemy transportowe. 2016;17(4):95-101.

[15] Witkowski K. Stan diagnostyki technicznej okrętowych silników tłokowych. Diagnostyka. 2005;34:85-92.

[16] Witkowski K. The increase of operational safety of ships by improving diagnostic methods for marine diesel engine. Transnav the International Journal on Marine Navigation and Safety of Sea Transportation. 2017;11(2):317-321. https://doi.org/10.12716/1001.11.02.15

[17] Woś P, Jaworski A, Kuszewski H. et al. Technical and operating problems yielded from setting up the optimum value of geometric compression ratio in piston engines. Combustion Engines. 2016;164(1):3-14. https://doi.org/10.19206/CE-116483

[18] Document EA-4/02 M:2022. Ocena niepewności pomiaru przy wzorcowaniu. Polskie Centrum Akredytacji, 2022.

[19] Diesel-RK. www.diesel-rk.bmstu.ru/Eng/index.php (accessed on 2.04.2022).

Patrycja Puzdrowska, MEng. – Faculty of Mechanical Engineering and Ship Technology, Gdansk University of Technology, Poland.

e-mail: *patpuzdr@pg.edu.pl*

Article citation info:
Giechaskiel B, Melas A, Mamakos A. Assessment of two condensation particle counters (CPCs) in photometric mode for high concentration exhaust emission measurements. Combustion Engines. 2023;193(2):15-23. https://doi.org/10.19206/CE-161190

Barouch GIECHASKIEL
Anastasios MELAS
Athanasios MAMAKOS

Combustion Engines
Polish Scientific Society of Combustion Engines

Assessment of two condensation particle counters (CPCs) in photometric mode for high concentration exhaust emission measurements

ARTICLE INFO

Received: 31 December 2022
Revised: 12 February 2023
Accepted: 13 February 2023
Available online: 14 February 2023

Condensation particle counters (CPCs) use light scattering to count particles after they have grown to micron size in a supersaturated environment. In single counting mode each particle is counted depending on whether the scattered light exceeds a threshold value or not. In photometric mode the total scattered light is converted in particle number concentration. While for laboratory grade particle number systems, CPCs are allowed to operate only in single counting mode, there is no such requirements for portable emissions measurements systems (PEMS) for real-driving emissions (RDE) testing or for instruments for periodic technical inspection (PTI) of vehicles. In this study two CPCs of the same model were assessed in single counting and photometric modes with silver and graphite particles with sizes ranging from 10 nm to 100 nm. The results showed that the concentration was measured accurately enough for particles in the 25 nm to 50 nm size range, but was underestimated and overestimated for smaller and larger particles, respectively. The key message is that the photometric mode should be avoided or calibrated in function of concentration and particle size.

Key words: *PEMS, PTI, CPC, PNC, single counting mode, photometric mode*

1. Introduction

The particulate matter (PM) emissions from diesel vehicles are regulated since the beginning of the 1990s in the United States of America (USA), European Union (EU) and Japan. Other countries, such as China and India, introduced limits at the beginning of 2000. The method is based on (i) testing the vehicle over a prescribed test cycle on a chassis dynamometer; (ii) weighing of a filter that collected PM from a diluted part of the exhaust gas. The introduction of particulate filters at the exhaust aftertreatment of diesel vehicles rendered the filter method unsuitable due to the low mass of the collected PM. Furthermore, concerns that ultrafine particles might have more adverse health effects than bigger particles for the same mass led to assessment of a particle counting method for regulatory purposes. This was tasked in 2003 to the particle measurement programme (PMP) informal group of the United Nations Economic Commission for Europe (UNECE). Dedicated evaluations and inter-laboratory studies confirmed the suitability of the particle number (PN) counting method for introduction in the regulations [1]. The PN method was introduced in the EU regulation for light-duty diesel vehicles in 2011. The PM and PN limits were extended to gasoline vehicles with direct injection engines, heavy-duty engines, and non-road mobile machinery (NRMM) [2, 3]. A similar method has also been proposed for measurement of particles from brake emissions [4].

A further big step in the EU regulation was the control of vehicles on the road with portable emissions measurement systems (PEMS) during real-driving emissions (RDE) testing [5–8]. On-board vehicle testing requires small, lightweight instruments and consequently the technical requirements of the laboratory grade equipment were relaxed for PEMS. Laboratory grade systems require calibration of the thermal pre-treatment unit and the particle number counter (PNC) separately. On the other hand, PEMS can be calibrated as a complete unit. Most importantly, while the laboratory grade systems have condensation particle counters (CPCs) for counting the particles, PEMS can have any detector, as long as they fulfil the counting efficiency requirements. CPCs are instruments that optically count particles using light scattering after their growth to micron size in a supersaturated environment [9, 10]. The CPCs of the laboratory systems have strict linearity requirements (±5%), while the PEMS more relaxed (±15%) [2].

The previous discussion was referring to instrumentation for the type-approval and in-service conformity (ISC) of the vehicles, which is responsibility of the vehicle manufacturers. The same instrument requirements apply for the market surveillance, which is responsibility of type-approval authorities and the European Commission. Type-approval, ISC or market surveillance is conducted on a limited number of vehicles from the vehicle fleet. On the other hand, every vehicle circulating in the market needs to be tested for its roadworthiness every few years. This is responsibility of the vehicle owner, who brings the vehicle to an appropriate testing center for the periodic technical inspection (PTI). The control of the PM is conducted with an opacity meter only for diesel vehicles. The opacity measurement however, is not appropriate for particulate filters equipped vehicles, because it can hardly detect a removed or tampered particulate filter [11, 12]. A new PN methodology was introduced in Belgium in July 2022, while the Netherlands, Germany and Switzerland will introduce the new methodology in 2023. The sensors that are used are handheld devices designed for garage environment. Thus, their technical specifications are even more simplified than for PEMS. There is no requirement for the principle of operation of the detector, and the linearity accuracy requirements are ±25%.

Laboratory grade CPCs have to be used in single counting mode, while for PEMS or PTI devices there is no such

requirement, and thus, the use of the photometric mode is not excluded. In single counting mode the particle concentration is determined by counting discrete events of light scattered by a particle(s) passing through an inspection volume. The light scattered creates an electric pulse, which above a threshold value is considered a particle count. Internal corrections such as for coincidence for older CPCs, or dead/live time for newer CPCs are typically applied. In photometric mode the concentration is determined by a bulk measurement of the amount of light scattered by a particle(s) passing through the inspection volume. Corrections include functions that turn the photometric measurement into a concentration. In theory, the photometric mode could be used for single particles counting as well. However, the accuracy is not as good as with single counting mode because of the sixth power dependence of light scattering intensity on particle size for particles small compared to the wavelength of scattered light [9, 10]. Thus, the transition between the two modes is typically done at some upper limit, typically when the internal single counting mode corrections reach a 10–20% value. The transition concentration is between 10^4 #/cm^3 to 10^5 #/cm^3, depending on the CPC model. The PTI limit in Belgium and the Netherlands is 10^6 #/cm^3, thus a CPC with a 10:1 dilution, in principle, could avoid the use of the photometric mode. The tailpipe exhaust concentrations measured by PEMS can be as high as 10^8 #/cm^3 [13]. A dilution of 1000:1 could avoid the use of the photometric mode, but for typical dilutions of 100:1 there will be instances that the CPC measures in the photometric mode.

In theory, once calibrated, the photometric mode should remain in acceptable levels of accuracy (±20%) independently of the original type of particles, because all particles grow in similar sizes in the micrometer range before detection and they should have the same refractive index due to the condensed vapor of the working fluid. However, recently we found that small silver particles were underestimated at least 40% compared to soot particles [14]. There are not many studies that have examined the photometric mode range of CPCs, and even less any size dependency [15]. The knowledge on the topic is based on studies on the growth of particles in the CPCs at low particle number concentrations [9, 16], but has not been expanded to high concentrations. Furthermore, usually, CPCs are not accompanied with calibration certificates for the photometric range and thus the true uncertainty at these high levels is not well known. Current regulations for PEMS and PTI devices permit the photometric mode and different materials can be used for calibration. For example, for PEMS only soot-like particles are permitted, while for PTI additionally salt or other materials can be used. Furthermore, for PEMS calibration is done at sizes > 45 nm, while for PTI between 70 and 80 nm. Consequently, the main questions raised are (i) what is the uncertainty of the photometric mode and (ii) whether the uncertainty can be kept at low levels with specific calibration requirements. In order to address these questions, and cover this gap in the literature, in this study we compare two identical CPCs in both single and photometric counting modes with different materials (graphite, silver) and different sizes. The results of this study are not useful only for vehicle exhaust emission measurements [17–19], but any other aerosol measurement field (e.g. nanomaterials, ambient air, work exposure) [20, 21].

2. Materials and methods

Figure 1 presents the experimental setup. Two particle generators were used to generate particles of different materials (graphite or silver) and sizes: the geometric mean diameter (GMD) ranged from below 10 nm up to 100 nm. Silver particles are typically small (< 20 nm) and can be assumed that they resemble more the metal oxides from the lubricant. Graphite particles have similarities with soot particles from combustion engines [22, 23]. Furthermore, vehicle exhaust regulations require the measurement of the non-volatile (solid) particles, thus the silver and graphite particles of this study should be representative of the results expected with exhaust particles.

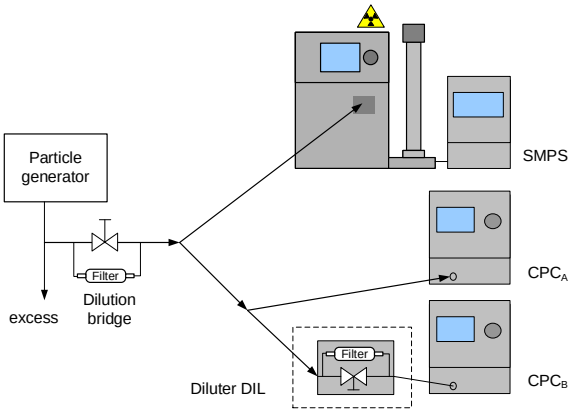

Fig. 1. Experimental setup. With dotted lines we indicate instruments that were optionally used

The concentration was further decreased in a dilution bridge. The size distributions were determined by a scanning mobility particle sizer (SMPS) with a long differential mobility analyzer (DMA) 3081, and a 3010 butanol CPC with 50% efficiency at 10 nm (SMPS model 3936, TSI Inc., Shoreview, MN, USA). Corrections for multiply charged particles and diffusion losses were applied by the manufacturer's aerosol instruments manager (AIM) software version 9.0.0. The SMPS was evaluated before the measurement campaign [14]. In parallel to the SMPS, two identical CPCs were measuring; one of them optionally with a diluter (DIL). The protocol included tests at different concentration levels adjusting the dilution bridge. The SMPS due to its lower resolution time (around 2.5 min) was not used at all concentrations steps, but at indicative intervals. For silver particles only part of the size distribution was captured by the SMPS. The missing part was taken into account by fitting the measured part (Fig. 2). The "missing" part below 7.5 nm was around 28–30%, while below 4 nm around 0.5–1.5%. The correction of the particle concentration for the "missing" part was between 1.35 and 1.55. Details for the instruments follow.

2.1. Particle generators

The DNP 3000 (Palas GmbH, Karlsruhe, Germany) produces graphite particles by high-voltage spark discharges between two graphite electrodes in a N_2 flow [24]. Sub-

sequent internal dilution with filtered air reduces the particle number concentration. The two settings used were: (i) for GMDs 25 nm to 50 nm: medium energy 3.0 kV, current 2 mA, N_2 carrier 3 dm^3/min, mixing air 8 dm^3/min; (ii) for GMDs 60 nm to 100 nm, medium energy 3.0 kV, current 5 mA, N_2 carrier 3 dm^3/min, mixing air 3 dm^3/min. The size was adjusted by modifying the residence time in the tubing between the generator and the instruments.

Silver particles were generated by an in-house tungsten glowing wire generator (GWG) [25]. Accordingly, a silver filament was placed around tungsten. The silver filament was heated resulting in silver vapors. N_2 was used as carrier gas to avoid oxidation of the tungsten wire and the silver particles. The carrier gas was further mixed with N_2 to reduce the silver particles concentration.

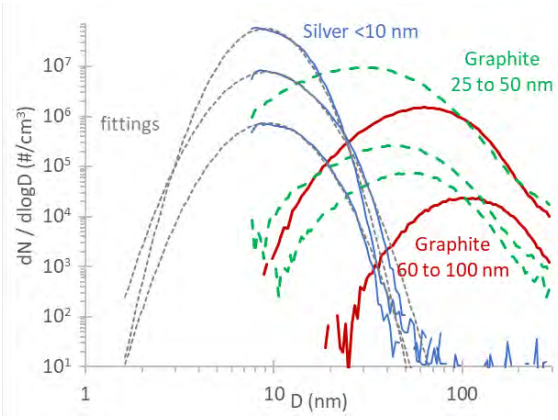

Fig. 2. Examples of particle number size distributions measured by SMPS. Grey dotted lines present the fittings to the measured silver size distributions

2.2. Condensation Particle Counters (CPCs) model 3752

Two identical butanol CPCs (model 3752, TSI) with 50% efficiency at 4 nm were measuring the particle number concentration [26, 27]. The CPCs were used with 1.5 dm^3/min flowrate. From this flow, 0.3 dm^3/min pass through the optics, while the 1.2 dm^3/min bypass the optics. Flow rate measurements confirmed that these flows were within 5% of the nominal values. One of them (CPC_A) was calibrated 10 months before the measurement campaign. The other (CPC_B) was calibrated three years before the measurement campaign. However, due to the COVID-19 lockdown, its use the last two years was limited. All calibration certificates, for the initial and subsequent calibrations, included only a single check in single counting mode at 50,000 #/cm^3, and no information on the photometric mode. This certificate calibration factor was taken into account in the results.

2.3. Diluter (DIL)

One of the CPCs (CPC_B) was also used downstream of a diluter (model DDS 560, Topas GmbH, Dresden, Germany) in order to keep the concentrations in the single counting mode. The principle was similar to the dilution bridge concept (i.e. bifurcated diluter). A fixed dilution of 50:1 was used for all tests. We calibrated the diluter (DIL) at this specific dilution 50:1 before the measurement campaign. The penetration with silver and graphite particles is given in Fig. 3. The procedure was according to the regulation for particle number systems: Regulation (EU) 2017/1151. The penetration was around 95% for 25 nm particles, 82% for 15 nm, 60% for 8 nm. Based on the fitting of the experimental data and to take into account the particle losses: a 1.05 correction was applied when 25 nm size distributions were measured with graphite particles and 1.65 for 8 nm size distributions with silver particles.

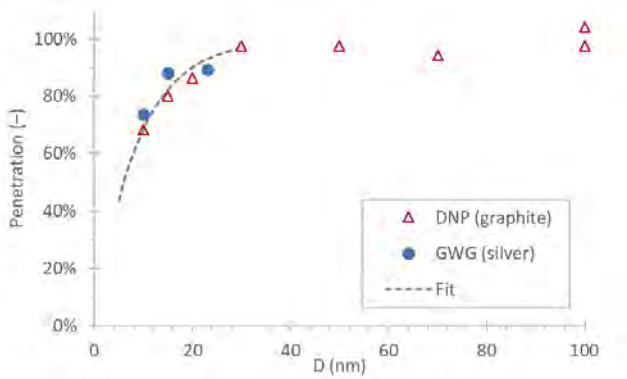

Fig. 3. Penetration of diluter DIL with silver and graphite particles at dilution ratio 50:1

3. Results

3.1. Inter-comparison of CPCs

Figure 4 plots the difference of the two CPCs at various concentrations. The tests were conducted without any dilution upstream of the CPCs, thus the "raw" concentrations refer to the readings of the CPC (including the certificate calibration factors).

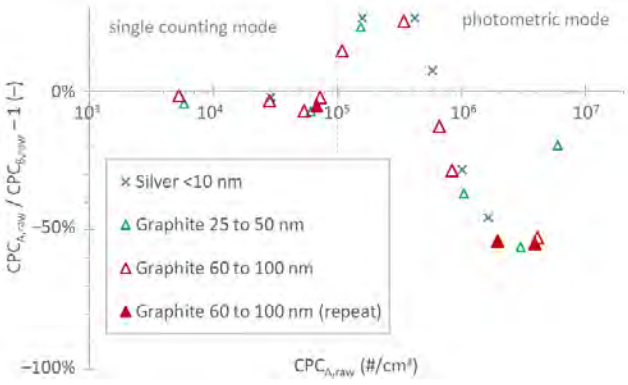

Fig. 4. Comparison of CPC_A with CPC_B. No dilution DIL was used upstream of any CPC. CPC_{raw} refers to the concentration measured by the CPC, including the certificate calibration factors

Up to 10^5 #/cm^3, the differences were within 5%. Then the differences followed a wavy curve: they increased up to 25% at concentrations 2–4×10^5 #/cm^3, then they decreased to –55% at concentrations 2–4×10^6 #/cm^3, and then they further increased. The behavior was independent of the material or the size distribution. Since these are nominally the same devices, this behavior points towards inaccurate calibration at high concentrations. The actual correction applied in photometric mode is not known. From this comparison it was not clear which CPC was the correct one, if any of the two. It should be noted that the calibration certificates of the specific CPCs included only one point in the

single counting mode at 5×10^4 #/cm^3, and no points in the photometric mode.

3.2. CPC vs. SMPS

Figure 5 and Figure 6 compare CPC_B and CPC_A, respectively, with SMPS for various materials and size distributions. The SMPS silver particle size distributions were corrected by a factor 1.35 to 1.55 depending on the missing part of the size distributions (see Fig. 2). The y-axis plots the difference of the corrected CPC concentration (i.e. certificate calibration factor, dilution ratio, diluter losses) to the SMPS. The x-axis plots the raw CPC concentration, i.e. without dilution correction (if any).

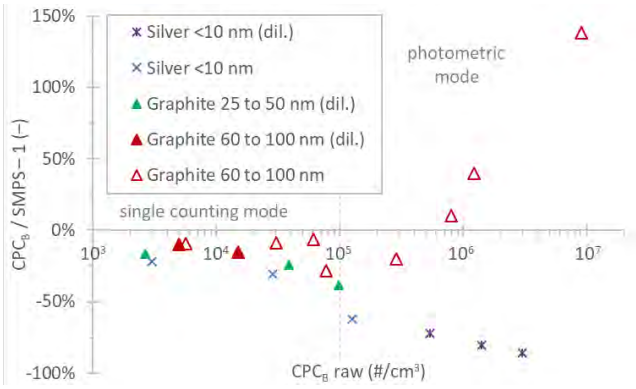

Fig. 5. Comparison of CPC_B with SMPS. "dil." indicates measurements that the CPC_B was used downstream of the diluter

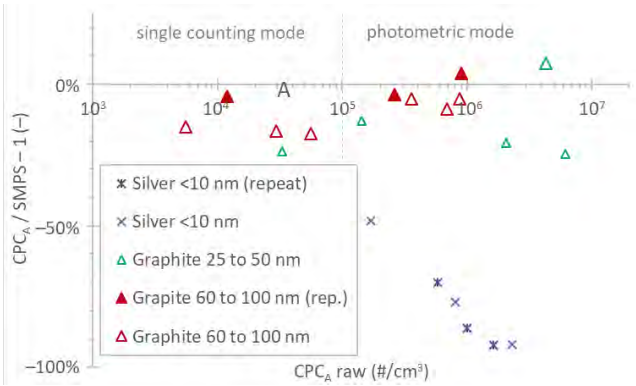

Fig. 6. Comparison of CPC_A with SMPS

The measurements with graphite particles resulted in a reasonable agreement with the SMPS (5% to 40%) [28] for both CPCs up to a concentration of 10^5 #/cm^3 and up to the maximum concentration of 10^7 #/cm^3 for CPC_A. In the photometric mode, the two CPCs showed different trends partly in agreement with their relative comparisons, as presented in Fig. 4.

The comparison to the SMPS, however, revealed a consistent effect of the aerosol in the CPC/SMPS correlations. In particular, both CPCs were found to measure systematically lower concentrations of silver particles, with the difference increasing with the concentration reaching as high as –90% at 10^7 #/cm^3 (i.e. one order or magnitude lower).

3.3. CPC_A vs. CPC_B downstream of a diluter

The uncertainties associated with the SMPS data inversion including the external correction for the undetected fraction of the silver particle distribution, can raise concerns. Furthermore, high concentrations of charged particles, if not properly neutralized, can lead to overestimation of the SMPS concentrations. For example, the graphite particles can be highly charged [29] or high charges from the glowing wire generators have been reported [30]. In order to confirm that the findings were true and not experimental errors we repeated some tests using CPC_B downstream of the diluter as reference instrument. The CPC concentrations, when used in single counting mode, should be very accurate, but CPCs, do not give size information. Figure 7 compares the readings of CPC_A without any dilution to the readings of CPC_B corrected with the dilution 50:1 of the upstream diluter. Thus, the concentrations measured by CPC_B were approximately 50 times lower than those shown in the x-axis of Fig. 7 and always in single counting mode. Furthermore, particle losses for the diluter according to Fig. 3 were applied.

For concentration levels up to 10^5 #/cm^3 the differences were within ±5% for graphite or ±10% for silver particles. When the two CPCs were compared to each other, their differences were within ±5% (Fig. 4). The higher variability with silver particles (10% vs. 5%) had to do with the uncertainty of the particle loss corrections for the diluter DIL. Nevertheless, the variability is smaller than when the CPCs were compared to the SMPS (Fig. 4 and 6).

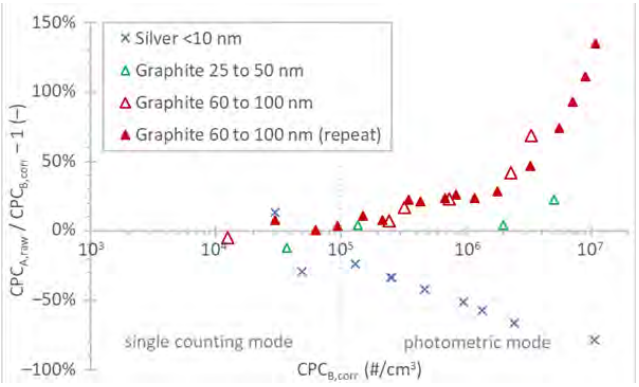

Fig. 7. Comparison of CPC_A with CPC_B downstream of diluter DIL; $CPC_{B,corr}$ refers to the concentration after correction with the dilution ratio of DIL 50:1, certificate calibration factors, and losses in the diluter DIL; $CPC_{B,raw}$ was always in the single particle mode

In the photometric mode, CPC_A underestimated the concentrations for silver particles. On the other hand, it overestimated the concentration for large graphite particles at concentrations > 10^6 #/cm^3. Only for the 25 to 50 nm graphite particles the differences remained within 20%.

The results were very similar to those of Fig. 6, where the reference was a SMPS, confirming the reliability of the data. The results and trends were also very similar with those of CPC_B (Fig. 5). However, as noted also in Fig. 4, for concentrations > 1×10^6 #/cm^3 CPC_A was measuring much lower, or as the previous results showed, CPC_B was actually measuring much higher (overestimating). Combining the information from Fig. 5–7 it can be concluded that the calibration of CPC_A in the photometric mode was more accurate.

4. Discussion

This study addressed a critical question: what is the uncertainty of the photometric mode of the CPCs. While CPCs for laboratory grade equipment are allowed to operate only in the single counting mode, there is no such requirement for PEMS and PTI. Thus, it was important to evaluate whether the uncertainty remains within 15% for PEMS and 25% for PTI instruments, as prescribed in the relative regulations. It should be emphasized that the specific CPCs that we evaluated are not used for PEMS or PTI testing, and the aim of this study was to assess the principle of photometric mode in such applications, and not the specific CPCs per se.

The results showed that in most cases, a calibrated CPC, can remain within 25% (Fig. 6), which includes also the uncertainty of the reference system. This value is close to the one typically reported as uncertainty for photometric mode (20%) from the instrument manufacturer. The results were confirmed using either a SMPS as reference instrument or a CPC downstream of a diluter measuring in single counting mode. However, the results also revealed that: (i) for very small particles (around 10 nm) the concentration was underestimated; (ii) for very large particles (> 60 nm) the concentration can be overestimated; (iii) the deviations depended on the concentration levels; (iv) the two CPCs had large differences in the photometric mode.

This is one of the few studies that have examined the high concentration (photometric) range of the CPCs, and probably the first one that covered from very small to large particle sizes (range at least 10 nm to 100 nm). It is also the first study that raises concerns for the photometric mode for large sizes. The assessment of the photometric mode (principle) at low concentrations is not something new. The first photoelectric instrument was developed early in 1940 [9]. The aerosol was saturated by diffusion of water vapor. The subsequent expansion to atmospheric pressure produced cloud by condensation. The attenuation was measured with a photoelectric cell. Such an instrument developed in 1970s was capable of reaching concentrations up to 10^6 #/cm^3 [31]. A commercially available and commonly used instrument since the 1980s was the TSI model 3020 [32]. It operated in the photometric mode for concentrations higher than 1000 #/cm^3. The photometric mode was based on the scattered light by the aerosol cloud and an empirical calibration. The successor was the TSI model 3022A using butanol as a working fluid, which was replaced by model 3775 and later by 3752, the model that was assessed in our study.

The first question would be how the photometric mode is calibrated and which are the reported deviations reported in the literature. Calibration of the first photoelectric counters was conducted with a "tube bridge" or dilution bridge in mid-1940s and polydisperse aerosol, which practically halved the aerosol concentration [33]. Since the 1970s the preferred method was, and still is, using monodisperse aerosol with a differential mobility analyzer (DMA) and determination of the concentration with an electrometer [9]. Our tests were a combination of the two methods: We used a DMA and a diluter upstream of the reference CPC. By characterizing the diluter, it was possible to minimize the measurement uncertainty.

One study [34] with a CPC model 3022 found a constant deviation of 20–30% for concentrations up to 4×10^5 #/cm^3 for polydisperse 35 nm and 92 nm NaCl, 82 nm carbon, 111 nm and 233 nm di-ethyl-hexyl-sebacate (DEHS) particles. However, higher concentrations were not tested. Others have tested the transition from single counting mode to photometric mode and noticed differences for a Grimm 5.401 CPC [35], a TSI 3022A [36] and a water CPC [37]. The only study with high concentrations, up to 10^7 #/cm^3 [15], compared many instruments with various polydisperse materials. The 3022A was within 5% of the average value for concentrations up to 10^5 #/cm^3 for all materials. At higher concentrations the deviation was much higher: -65% at 2×10^6 for 7 nm silver, –30% at 5×10^5 for 11 nm tungsten oxide, –50% at 5×10^5 for 20 nm NaCl, but +20% at 5×10^6 for 130 nm DEHS particles. However only two instruments could measure above 10^6 #/cm^3. The findings demonstrate large deviations in the photometric mode, that depend on the particle size. Thus, our results are in good agreement with the literature.

Even though there is only one study that examined the photometric mode experimentally and there was no "true" reference, insight for the measured deviations can be gained by older studies at low concentration levels. Already in the early 1980s researchers observed that pulse heights produced by the photodetector of the TSI 3020 decreased with decreasing particle size for particles smaller than 15–20 nm [9]. The super-saturation that is required to activate condensational growth increases as droplet sizes decrease (Kelvin effect). Saturation ratios increase from a value of unity near the condenser inlet to a maximum in the midsection [38–41]. Due to the Kelvin effect, smaller particles travel further in the condenser before their activation and therefore they have less time to grow, resulting in lower scattered light and pulse height. For example, when the flow rate of a TSI 3020 decreased from 300 to 200 cm^3/min, the counting efficiency of 5 nm particles increased by as much as six-fold, indicating that the particles grew more in size [42]. However, too low flowrate can result in excessive particle losses before their growth. Particles activated near the entrance of the condenser reach similar final sizes and produce similar pulse heights [43].

Extrapolating the findings of the above mentioned studies from low to high particle concentrations, it can be derived that the signal of the photometric mode depends on the initial particle size when at the steep part of the counting efficiency curve. Figure 8a plots the ratio of the CPC_A to the SMPS in function of the GMD of the measured size distributions. The data are based on Fig. 6 with a correction factor of 1.15 to bring the ratio to 100% at large sizes. The reason of this 15% correction was not investigated in detail, but is well within expected differences between SMPS and CPCs [44, 45]. The same figure plots (dotted line) the expected ratio measuring polydisperse aerosol, based on the monodisperse counting efficiencies found in the literature for the specific CPC model [27]. Small symbols are measurements in photometric mode, while big symbols in single counting mode. Figure 8b plots the same information for

CPC_B. Although the single counting mode (large) points lay on the expected curve, the measurements in photometric mode of small particles are much lower. In single counting mode the pulse height is not important because each particle is counted, as long as the pulse height is above a threshold level. In photometric mode, the total scattered light is translated into particle concentration. Since the scattered light from each particle is lower for small particles, the total scattered light and the resulting concentration will be lower.

The pulse height depends on the final particle size and consequently on the saturation profile. The saturation profile depends on the geometry and the operating conditions of the CPC, which determine the heat and mass transfer [43]. Thus, different CPC models with differences in saturator temperatures will have different super-saturation ratios (and profiles) and thus different droplet growth [38].

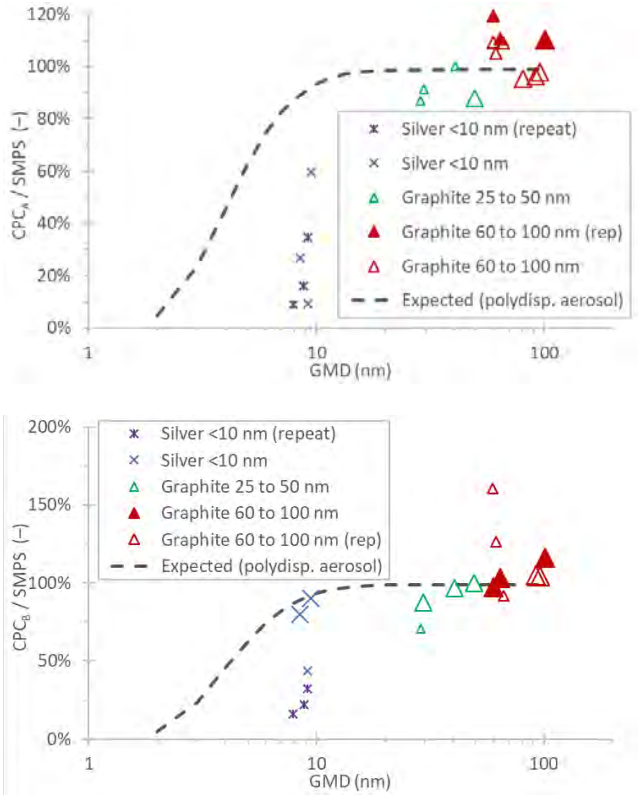

Fig. 8. Ratio of CPCs relative to SMPS for polydisperse particles in function of the geometric mean diameter (GMD). Dotted line is the expected curve for polydisperse aerosol based on the typical counting efficiency of the same model. Small symbols are concentrations in photometric mode, while larger symbols are in single counting mode: (a) CPC_A; (b) CPC_B

The previous studies can explain why there is a lower detection efficiency for smaller particle sizes, but they cannot explain why this difference varies with particle concentration (for the same size). Particle concentrations can also influence pulse-heights through vapor depletion as it was shown theoretically for the TSI 3022A [46] and for a TSI water CPC 3785 [47]. Experimentally it was found that pulse heights drop linearly with increasing concentration for all particle sizes [16]. However, the pulse height difference for particles of different initial size is a very weak function of aerosol concentration. A detailed theoretical study clearly demonstrated that at high particle number concentrations the super-saturation ratios decrease due to [48]: (i) depletion of the working fluid vapor due to the uptake by the droplets, and (ii) increase in the equilibrium vapor pressure due to warming of the flow from condensational heat release. Thus, with increasing particle number concentrations, the critical activation diameters increase and the final droplet sizes are smaller [48]. The later activation also results in smaller droplets due to less time in the condenser, as discussed previously. Concluding, the calibration should be model specific and in function of the particle concentration. Our results with the rest of the studies indicate that the calibration is valid only in the plateau region of the CPC, and attention is needed at small particle sizes.

Although less pronounced than for small sizes, why the calibration was not valid for big particles is not entirely clear. A plausible explanation is that the calibration was done at around 50 nm, for which the pulse height was not the maximum. Still some small differences of the final size can be seen for bigger particles, as they are activated earlier, although very small to fully explain this trend [41]. The linear pulse heights drop with increasing concentration probably is not taken into account correctly with the internal calibration functions. Another explanation could be the decrease of the droplet size with the temperature increase from the condenser to the optics. We are not aware of studies discussing this, and it's a topic that needs further investigation.

Finally, the influence of particle composition on pulse heights was also studied by other researchers [16]. Sulfuric acid and tungsten oxide particles had the same pulse height dependence with size below 10 nm [16, 43], while above 10 nm the dependency was very small in function of size. NaCl had differences at sizes < 10 nm, but they were attributed to the cubic shape of NaCl particles. For the same electrical mobility diameter, the length of the cube is 0.72 times the diameter of a sphere [16]. Thus, for the same electrical mobility size, the cube length is smaller and the activation more difficult. Based on these findings, the researchers concluded that the pulse height is not affected by the chemical composition, but weakly on the shape (surface area). Differences in the counting efficiencies in the cut-off curve have been reported by many researchers testing in the single counting mode [49–51]. These findings justify why there were no differences of the material in the plateau region (25 to 50 nm range) in the photometric mode for graphite, soot, and salt particles in our previous study [14].

Summarizing, the pulses depend on the size of particles and the particle number concentration. The chemical composition probably does not have any impact in the plateau region, but shape could have an effect at the steep part of the efficiency curve. However, at the sub-10 nm region, most particles are spherical so the shape impact should be negligible for most applications in practice. The key findings of this study is that the photometric mode needs detailed calibration in function of (i) the concentration and (ii) size, similar to what is done for the single counting mode for each instrument. For one of the tested CPCs the valid range (around 25 to 50 nm) was appropriate for PEMS

which measure from approximately 23 nm, but not for PTI instruments which are calibrated at 70 to 80 nm.

The key messages of this study are: (i) current calibrations in the photometric mode (if any) are not sufficient. Typically, no data are provided or in some cases a single concentration point. The material and the size is often not reported; (ii) more studies are necessary to confirm the findings of this study and whether the impact of concentration and size can be extrapolated to other designs. At the moment the use of the photometric mode for regulatory PEMS and PTI tests should be avoided; (iii) future calibration certificates should cover the concentration range of the photometric range and the size range of validity.

5. Conclusions

In this study we assessed two TSI 3752 CPCs in the photometric mode with silver and graphite particles in the size range of 10 nm to 100 nm. The two CPCs were within ±20% up to 10^6 #/cm^3 but had higher difference at higher concentrations. The differences were independent from the material indicating that one of them needed better calibration in the photometric mode. When a SMPS or a CPC downstream of a diluter (in order to keep it in single counting mode) were the reference instrument, it was found out that the silver 10 nm particles were almost linearly underestimated with increasing concentration. The underestimation was around –50% at 10^6 #/cm^3, reaching –90% at 10^7 #/cm^3. Large particles > 60 nm were overestimated around 50% at 3×10^6 #/cm^3 exceeding 100% at 10^7 #/cm^3. Only particles in the size range of 25 nm to 50 nm were accurately measured in the whole concentration range for one of the CPCs.

The behavior for small particles was attributed to the different position and time of particles activation in the condenser and consequently the different final size before optical detection. The resulting smaller final growth of smaller particles resulted in different scattered light and consequently particle number concentration. The particle concentration due to vapor depletion and condensational heat release reduced the super-saturations, and consequently resulted in larger activation diameters and smaller final droplet sizes. Consequently, smaller particles had an increasing deviation from the reference instrument in function of the concentration. The behavior for large particles needs further investigation, but it could be related to the internal calibration curve optimized for mid-sized particles. The important message is that the photometric mode should be avoided, and used only when its calibration remains unaffected in the size range of interest for the specific application.

Acknowledgements

The authors would like to acknowledge Dominique Lesueur for the support in the execution of the tests.

Disclaimer

The opinions expressed in this manuscript are those of the authors and should in no way be considered to represent an official opinion of the European Commission. Mention of trade names or commercial products does not constitute endorsement or recommendation by the authors or the European Commission.

Nomenclature

AIM aerosol instruments manager
CPC condensation particle counter
DEHS di-ethyl-hexyl-sebacate
DIL diluter
DMA differential mobility analyzer
EU European Union
GMD geometric mean diameter
GWG glowing wire generator
ISC in-service confirmity
NRMM non-road mobile machinery
PEMS portable emissions measurement system
PM particulate matter
PN particle number
PNC particle number counter
PTI periodic technical inspection
RDE real-driving emissions
SMPS scanning mobility particle sizer
USA United States of America

Bibliography

[1] Giechaskiel B, Mamakos A, Andersson J, Dilara P, Martini G, Schindler W et al. Measurement of automotive nonvolatile particle number emissions within the European legislative framework: a review. Aerosol Sci Tech. 2012;46:719-749. https://doi.org/10.1080/02786826.2012.661103

[2] Giechaskiel B, Melas A, Martini G, Dilara P. Overview of vehicle exhaust particle number regulations. Processes. 2021;9:2216. https://doi.org/10.3390/pr9122216

[3] Giechaskiel B, Lähde T, Suarez-Bertoa R, Clairotte M, Grigoratos T, Zardini A et al. Particle number measurements in the European legislation and future JRC activities. Combustion Engines. 2018;174(3):3-16. https://doi.org/10.19206/CE-2018-301

[4] Grigoratos T, Mamakos A, Arndt M, Lugovyy D, Anderson R, Hafenmayer C et al. Characterization of particle number setups for measuring brake particle emissions and comparison with exhaust setups. Atmosphere. 2023;14:103. https://doi.org/10.3390/atmos14010103

[5] Pajdowski P, Woodburn J, Bielaczyc P, Puchałka B. Development of RDE/ISC test methodology in light of Euro 6d/VI emissions limits. Combustion Engines. 2019;178(3):274-282. https://doi.org/10.19206/CE-2019-348

[6] Giechaskiel B, Bonnel P, Perujo A, Dilara P. Solid particle number (SPN) portable emissions measurement systems (PEMS) in the European legislation: a review. IJERPH 2019;16:4819. https://doi.org/10.3390/ijerph16234819

[7] Czerwiński J, Zimmerli Y, Hussy A, Engelmann D, Bonsack P, Remmele E et al. Testing and evaluating real driving emissions with PEMS. Combustion Engines. 2018;174(3):17-25. https://doi.org/10.19206/CE-2018-302

[8] Merkisz J, Pielecha J. Observations from PEMS testing of combustion engines of different applications. Combustion Engines. 2018;174(3):40-55. https://doi.org/10.19206/CE-2018-305

[9] McMurry PH. The history of condensation nucleus counters. Aerosol Sci Tech. 2000;33:297-322. https://doi.org/10.1080/02786820050121512
[10] Giechaskiel B, Maricq M, Ntziachristos L, Dardiotis C, Wang X, Axmann H et al. Review of motor vehicle particulate emissions sampling and measurement: From smoke and filter mass to particle number. J Aerosol Sci. 2014;67:48-86. https://doi.org/10.1016/j.jaerosci.2013.09.003
[11] Burtscher H, Lutz Th, Mayer A. A new periodic technical inspection for particle emissions of vehicles. Emiss Control Sci Technol. 2019;5:279-287. https://doi.org/10.1007/s40825-019-00128-z
[12] Melas A, Selleri T, Suarez-Bertoa R, Giechaskiel B. Evaluation of measurement procedures for Solid Particle Number (SPN) measurements during the Periodic Technical Inspection (PTI) of Vehicles. IJERPH 2022;19:7602. https://doi.org/10.3390/ijerph19137602
[13] Czerwiński J, Comte P. Testing emissions of passenger cars in laboratory and on-road (PEMS, RDE). Combustion Engines. 2016;166(3):17-23. https://doi.org/10.19206/CE-2016-326
[14] Giechaskiel B, Melas A. Comparison of particle sizers and counters with soot-like, salt, and silver particles. Atmosphere. 2022;13:1675. https://doi.org/10.3390/atmos13101675
[15] Ankilov A, Baklanov A, Colhoun M, Enderle K-H, Gras J, Yu J et al. Intercomparison of number concentration measurements by various aerosol particle counters. Atmos Res. 2002;62:177-207. https://doi.org/10.1016/S0169-8095(02)00010-8
[16] Saros MT, Weber RJ, Marti JJ, McMurry PH. Ultrafine aerosol measurement using a condensation nucleus counter with pulse height analysis. Aerosol Sci Tech. 1996;25:200-213. https://doi.org/10.1080/02786829608965391
[17] Tartakovsky L, Fleischman R. DPF retrofit program in Israel – effects of diesel particle filters on performance of in-use buses. Combustion Engines. 2017:176-178. https://doi.org/10.19206/CE-2017-330
[18] Olczyk M, Hejny B, Bielaczyc P. An overview of particle number emission from direct injection SI engine in scope of new legislation rules. Combustion Engines. 2015;163(4):67-78. https://doi.org/10.19206/CE-116858
[19] Czerwiński J, Comte P, Keller A, Mayer A. Investigations of nanoparticle emissions of two gasoline cars MPI & DI at stationary part load operation. Combustion Engines. 2014; 158(3):3-11. https://doi.org/10.19206/CE-116932
[20] Stabile L, Cauda E, Marini S, Buonanno G. Metrological assessment of a portable analyzer for monitoring the particle size distribution of ultrafine particles. Ann Occup Hyg. 2014;58:860-876. https://doi.org/10.1093/annhyg/meu025
[21] Jaroń A, Borucka A, Sobecki G. Assessment of the possibility of using nanomaterials as fuel additives in combustion engines. Combustion Engines. 2022;189(2):103-112. https://doi.org/10.19206/CE-143824
[22] Andres H, Lüönd F, Schlatter J, Auderset K, Jordan-Gerkens A, Nowak A et al. Measuring soot particles from automotive exhaust emissions. EPJ Web of Conferences 2014;77: 00020. https://doi.org/10.1051/epjconf/20147700020
[23] Hagen F, Hardock F, Koch S, Sebbar N, Bockhorn H, Loukou A et al. Why soot is not alike soot: A molecular/nanostructural approach to low temperature soot oxidation. Flow Turbulence Combust. 2021;106:295-329. https://doi.org/10.1007/s10494-020-00205-2
[24] Helsper C, Mölter W, Löffler F, Wadenpohl C, Kaufmann S, Wenninger G. Investigations of a new aerosol generator for the production of carbon aggregate particles. Atmos Environ A-Gen. 1993;27:1271-1275. https://doi.org/10.1016/0960-1686(93)90254-V
[25] Burtscher H, Schmidt-Ott A, Siegmann HC. Photoelectron yield of small silver and gold particles suspended in gas up to a photon energy of 10 eV. Z Physik B – Condensed Matter. 1984;56:197-199. https://doi.org/10.1007/BF01304172
[26] TSI Inc. Model 3752 Condensation Particle Counter Operation Manual, P/N 6011194, Revision D 2022.
[27] Hammer T, Irwin M, Swanson J, Berger V, Sonkamble U, Boies A et al. Characterising the silver particle generator; a pathway towards standardising silver aerosol generation. J Aerosol Sci. 2022;163:105978. https://doi.org/10.1016/j.jaerosci.2022.105978
[28] Liu PSK, Deshler T. Causes of concentration differences between a scanning mobility particle sizer and a condensation particle counter. Aerosol Sci Tech. 2003;37:916-923. https://doi.org/10.1080/02786820300931
[29] Tabrizi NS, Ullmann M, Vons VA, Lafont U, Schmidt-Ott A. Generation of nanoparticles by spark discharge. J Nanopart Res. 2009;11:315-332. https://doi.org/10.1007/s11051-008-9407-y
[30] Peineke C, Attoui MB, Schmidt-Ott A. Using a glowing wire generator for production of charged, uniformly sized nanoparticles at high concentrations. J Aerosol Sci. 2006; (37):1651-1661. https://doi.org/10.1016/j.jaerosci.2006.06.006
[31] Sinclair D, Hoopes GS. A continuous flow condensation nucleus counter. J Aerosol Sci. 1975;6:1-7. https://doi.org/10.1016/0021-8502(75)90036-1
[32] Agarwal JK, Sem GJ. Continuous flow, single-particle-counting condensation nucleus counter. J Aerosol Sci. 1980; (11):343-357. https://doi.org/10.1016/0021-8502(80)90042-7
[33] Sem GJ. Design and performance characteristics of three continuous-flow condensation particle counters: a summary. Atmos Res. 2002;62:267-294. https://doi.org/10.1016/S0169-8095(02)00014-5
[34] Asbach C, Schmitz A, Schmidt F, Monz C, Todea AM. Intercomparison of a personal CPC and different conventional CPCs. Aerosol Air Qual Res. 2017;17:1132-1141. https://doi.org/10.4209/aaqr.2016.10.0460
[35] Bau S, Toussaint A, Payet R, Witschger O. Performance study of various Condensation Particle Counters (CPCs): development of a methodology based on steady-state airborne DEHS particles and application to a series of handheld and stationary CPCs. J Phys: Conf Ser. 2017;838:012002. https://doi.org/10.1088/1742-6596/838/1/012002
[36] Gilham RJJ, Quincey PG. Measurement and mitigation of response discontinuities of a widely used condensation particle counter. J Aerosol Sci. 2009;40:633-637. https://doi.org/10.1016/j.jaerosci.2009.03.004
[37] Biswas S, Fine PM, Geller MD, Hering SV, Sioutas C. Performance evaluation of a recently developed water-based condensation particle counter. Aerosol Sci Tech. 2005;39: 419-427. https://doi.org/10.1080/027868290953173
[38] Stolzenburg MR, McMurry PH. An ultrafine aerosol condensation nucleus counter. Aerosol Sci Tech. 1991;14:48-65. https://doi.org/10.1080/02786829108959470
[39] Reinisch T, Radl S, Bergmann A, Schriefl M, Kraft M. Effect of model details on the predicted saturation profiles in condensation particle counters. Adv Powder Technol. 2019; (30):1625-1633. https://doi.org/10.1016/j.apt.2019.05.011
[40] Giechaskiel B, Wang X, Gilliland D, Drossinos Y. The effect of particle chemical composition on the activation probability in n-butanol condensation particle counters. J Aerosol Sci. 2011;42:20-37. https://doi.org/10.1016/j.jaerosci.2010.10.006
[41] Mamakos A, Giechaskiel B, Drossinos Y. Experimental and theoretical investigations of the effect of the calibration aerosol material on the counting efficiencies of TSI 3790 con-

densation particle counters. Aerosol Sci Tech. 2013;47:11-21. https://doi.org/10.1080/02786826.2012.716174
[42] Su YF, Cheng YS, Newton GJ, Yeh HC. Counting efficiency of the TSI model 3020 condensation nucleus counter. Aerosol Sci Tech. 1990;12:1050-1054. https://doi.org/10.1080/02786829008959414
[43] Weber RJ, Stolzenburg MR, Pandis SN, McMurry PH. Inversion of ultrafine condensation nucleus counter pulse height distributions to obtain nanoparticle (~3–10 nm) size distributions. J Aerosol Sci. 1998;29:601-615. https://doi.org/10.1016/S0021-8502(97)10026-X
[44] Ham S, Lee N, Eom I, Lee B, Tsai P-J, Lee K et al. Comparison of real time nanoparticle monitoring instruments in the workplaces. Safety and Health at Work. 2016;7:381-388. https://doi.org/10.1016/j.shaw.2016.08.001
[45] Watson JG, Chow JC, Sodeman DA, Lowenthal DH, Chang M-CO, Park K et al. Comparison of four scanning mobility particle sizers at the Fresno Supersite. Particuology. 2011; (9):204-209. https://doi.org/10.1016/j.partic.2011.03.002
[46] Wu C-Y, Biswas P. Particle growth by condensation in a system with limited vapor. Aerosol Sci Tech. 1998;28:1-20. https://doi.org/10.1080/02786829808965508
[47] Stratmann F, Herrmann E, Petäjä T, Kulmala M. Modelling Ag-particle activation and growth in a TSI WCPC model 3785. Atmos Meas Tech. 2010;3:273-281. https://doi.org/10.5194/amt-3-273-2010
[48] Lewis GS, Hering SV. Minimizing concentration effects in water-based, laminar-flow condensation particle counters. Aerosol Sci Tech. 2013;47:645-654. https://doi.org/10.1080/02786826.2013.779629
[49] Chen L, Zhang X, Zhang C, Raza M, Li X. Experimental investigation of a condensation particle counter challenged by particles with varying wettability to working liquid. Aerosol Air Qual Res. 2017;17:2743-2750. https://doi.org/10.4209/aaqr.2017.06.0201
[50] Giechaskiel B, Wang X, Horn H-G, Spielvogel J, Gerhart C, Southgate J et al. Calibration of condensation particle counters for legislated vehicle number emission measurements. Aerosol Sci Tech. 2009;43:1164-1173. https://doi.org/10.1080/02786820903242029
[51] Wang X, Caldow R, Sem GJ, Hama N, Sakurai H. Evaluation of a condensation particle counter for vehicle emission measurement: Experimental procedure and effects of calibration aerosol material. J Aerosol Sci. 2010;41:306-318. https://doi.org/10.1016/j.jaerosci.2010.01.001

Barouch Giechaskiel, PhD – European Commission, Joint Research Centre (JRC), Ispra 21027, Italy.
e-mail: *Barouch.Giechaskiel@ec.europa.eu*

Anastasios Melas, PhD – European Commission, Joint Research Centre (JRC), Ispra 21027, Italy.
e-mail: *Anastasios.Melas @ec.europa.eu*

Athanasios Mamakos, PhD – Corning GmbH, Wiesbaden 65189, Germany.
e-mail: *MamakosA@corning.com*

Article citation info:
Korlak PK. Comparative analysis of the heat balance results of the selected Tier III-compliant gas-fuelled two-stroke main engines. Combustion Engines. 2023;193(2):24-28. https://doi.org/10.19206/CE-158545

Piotr K. KORLAK

Combustion Engines
Polish Scientific Society of Combustion Engines

Comparative analysis of the heat balance results of the selected Tier III-compliant gas-fuelled two-stroke main engines

ARTICLE INFO

Received: 4 September 2022
Revised: 24 November 2022
Accepted: 25 December 2022
Available online: 3 January 2023

Two-stroke engines are distinguished by the highest overall efficiency among all main engines. This is not only due to the low speed, and large piston stroke, but also to the high combustion temperature, which results in an increase in nitrogen oxides (NO_x) emission. Technical solutions applied to bring main engines into compliance with current NO_x emission standards set by the Tier III limits include the use of SCR and EGR systems, the implementation of the Otto cycle, and the application of liquified natural gas (LNG) as the low-emission fuel. Impact of the available Tier III-compliant technologies on the heat balance results is analysed using the example of the currently most popular dual-fuel main engines, i.e. WinGD X92DF and MAN G95ME-C10.5-GI. The possibilities of waste heat recovery in the electricity generation process and thereby improving the ship energy efficiency are discussed.

Key words: *heat balance, two-stroke engine, LNG, SCR, EGR*

1. Introduction

Two-stroke engines, achieving an overall efficiency of more than 50% and not requiring the use of reduction gears, are unrivalled as the most efficient source of mechanical energy needed to move the ship at the set sailing speed. As such, they are widely used on all types of cargo ships (including container ships, bulk carriers, and tankers), whose geometry allows the main engine of considerable height to be installed inside the ship's engine room space in the plane of symmetry of the hull's skeg. The highest overall efficiency among all internal combustion engine types is due not only to the low speed and large piston stroke, but also to the relatively high combustion temperatures of the compressed fuel-air mixture. It promotes efficient utilisation of the chemical energy contained in the supplied fuel, but is associated with an undesirable significant increase in nitrogen oxides (NO_x) emission [7]. NO_x emission increasing with the combustion temperature of hydrocarbon fuels, especially intensively above 1300°C, are an inherent part of the operation of all internal combustion engines [3]. The negative impact of NO_x emission on the environment and human health has been recognised by the International Maritime Organisation (IMO) and MARPOL Annex VI has been expanded to include provisions obliging shipowners to implement technical solutions to reduce NO_x emission from ships. The requirements for the prevention of NO_x emission apply to engines with a rated brake power of more than 130 kW as defined in rules 2.12 and 2.14. The most stringent NO_x emission standards have been set by the Tier III limits since 2015 [13]. Despite the enduring popularity of direct-driven main propulsion systems with a two-stroke engines, publicly available analyses and studies of the heat balance results refer to an outdated state of the art. The main engine operation was then unaffected by the selective catalytic reduction (SCR) or exhaust gas recirculation (EGR), ensuring the exhaust gas composition in compliance with current NO_x emission standards, liquified natural gas (LNG) was not yet in widespread use as the low-emission fuel and there were no main engines implementing the Otto cycle instead of the Diesel cycle [10]. Thus, the purpose of this paper is to compare the percentage share of heat losses in the heat balances of the most popular dual-fuel two-stroke main engines, i.e. WinGD X92DF and MAN G95ME-C10.5-GI, operating in a Tier III-compliant gas mode under ISO ambient conditions [7]. The realisation of the chosen objective will facilitate the selection of a gas-fuelled two-stroke main engine in terms of waste heat recovery in the process of electricity generation based on the thermodynamic cycle appropriate for the parameters of available heat losses [1].

2. Heat balance of the internal combustion engine

The heat balance is a compilation of the distribution of the total heat supplied to the main engine with fuel into useful heat, equivalent to the brake power, and the sum of heat losses. To make the heat balance more readable, the percentage of all components in relation to the total heat supplied is given. The heat balance is carried out at a constant load for the contract parameters after the engine has reached thermal equilibrium, and the results obtained are presented analytically. Performing a heat balance with the presentation of results makes it possible to determine ways of increasing its efficiency, which is particularly important in terms of waste heat recovery. Equations (1)–(4), applicable to the heat balance of all internal combustion engines, are listed below [2].

$$\dot{Q}_T = \dot{Q}_u + \sum \dot{Q}_L \tag{1}$$

hence:

$$\sum \dot{Q}_L = \left(\dot{Q}_g + \sum \dot{Q}_{lt} + \dot{Q}_r\right) \tag{2}$$

hence:

$$\sum \dot{Q}_{lt} = \left(\dot{Q}_o + \dot{Q}_w + \dot{Q}_{sa} + \dot{Q}_{EGR}\right) \tag{3}$$

and:

$$\dot{Q}_T = \frac{\dot{Q}_u}{\eta_o} = \frac{P_B}{\eta_o} \quad (4)$$

thus for LNG-fuelled engines [12]:

$$\dot{Q}_T = \frac{P_B \cdot (LCV_{FO} \cdot SFOC + LCV_G \cdot SGC)}{3600} \quad (5)$$

where: $\dot{Q}_T$ – total heat supplied with fuel, kW; $\dot{Q}_u$ – useful heat, kW; $\sum \dot{Q}_L$ – sum of all heat losses, kW; $\dot{Q}_g$ – exhaust gas waste heat, kW; $\sum \dot{Q}_{lt}$ – sum of the low-temperature heat losses, kW; $\dot{Q}_r$ – radiation waste heat, kW; $\dot{Q}_o$ – cooling oil waste heat, kW; $\dot{Q}_w$ – jacket water waste heat, kW; $\dot{Q}_{sa}$ – scavenge air waste heat, kW; $\dot{Q}_{EGR}$ – EGR cooling waste heat, if applicable, kW; P_B – main engine brake power, kW; η_o – main engine overall efficiency; LCV_{FO} – lower calorific value of the pilot fuel oil, $\frac{kJ}{kg}$; SGC – specific LNG consumption, $\frac{g}{kWh}$; $SFOC$ – specific pilot fuel oil consumption, $\frac{g}{kWh}$; LCV_G – lower calorific value of the LNG, $\frac{kJ}{kg}$.

$\dot{Q}_{EGR}$ is a total heat dissipated in plate heat exchanger according to Fig. 1. This heat loss is unique to engines equipped with each of the EGR system variants [15].

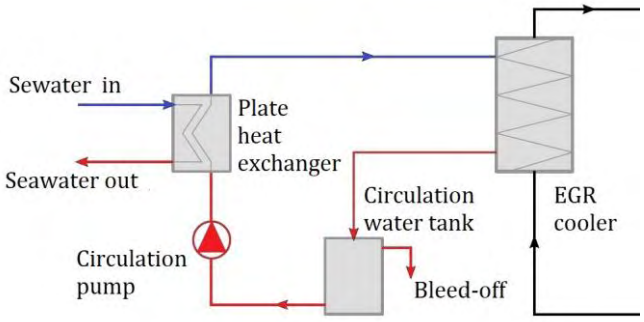

Fig. 1. Overview of the EGR cooling system [21]

The overall efficiency of the contemporary two-stroke dual-fuel main engines operating at maximum continuous load under ISO ambient conditions exceeds 50%, which means that such a proportion of the fuel-supplied energy is converted into brake power, with the rest being lost [11]. Potentially, therefore, very large amounts of heat could be recovered, which is severely hampered by the relatively low temperature of the waste heat carriers. Conventional waste heat recovery systems reach for exhaust gas characterised by sufficiently high inlet and outlet temperatures that allow the use of this waste heat carrier in electricity generation based on steam Rankine cycle (SRC), Brayton cycle (BC) or combined cycle (CC) [1]. The other waste heat carriers, i.e. scavenge air, jacket water, lubricating oil and EGR cooling water, are distinguished by significantly lower temperatures (Table 3) that preclude water steam production. Only the scavenge air gives off a portion of its heat to the feed water supplying an exhaust gas economiser in several maritime applications. Consequently, they have not yet been used in the electricity generation required to reduce the energy efficiency index for designed (EEDI) and existing (EEXI) ships [14]. The amount of the useful heat and the individual heat losses in the heat balance as well as the temperatures of waste heat carriers are subject by both the engine thermodynamic cycle and the operation of the SCR or EGR systems used [1]. The impact of the operation of the mentioned systems and thermodynamic cycle realised by the two-stroke dual-fuel main engine on the available waste heat amounts and temperatures are discussed and illustrated by the heat balance results later in the paper.

3. Methodology

The impact of technical solutions to adapt main engines to the Tier III emission standards on the heat balance results and the temperature of waste heat carriers is illustrated using the example of the currently most popular two-stroke dual-fuel main engines, i.e. WinGD X92DF and MAN G95ME-C10.5-GI. These have found the application, among others, on all the series of dual-fuel ultra-large container ships built in the last three years [7]. Table 1 contains the basic design and operating parameters of the analysed main engines.

Table 1. Basic design and operating parameters of the WinGD X92DF and MAN G95ME-C10.5-GI main engines [15]

Parameter	Unit	WinGD X92DF	MAN G95ME-10.5-GI
Piston stroke	m	3.468	3.46
Piston bore		0.92	0.95
Maximum continuous speed	min^{-1}	80	
Maximum continuous power	$\frac{kW}{cyl.}$	5320	6870
Available number of cylinders	–	6–12	
Available range of contract maximum continuous power	kW	23,520–63,840	27,120–82,440
Compression ratio	–	6.25	12
Gas supply pressure	MPa	0.75–1.5	20–30

Simulations of the operation of selected main engines were performed in the MAN Computer Engine Application System and General Technical Data for WinGD 2-Stroke Engines software for the boundary conditions indicated in Table 2. In this manner the full heat balance results of the analysed main engines were received, including the amount of all heat losses as well as the temperature and mass flow of the available waste heat carriers. The most important data are presented in graphical (Fig. 2–3) and tabular (Table 3) form later in the paper.

The reference engine load equal to 75% of the maximum continuous rating allows obtaining information useful, among other things, in calculating EEDI and EEXI and in developing how to recover available waste heat amount. In addition, it should be noted that the scope of EEDI and EEXI does not include the use of waste heat for heating services as well as in the process of domestic hot water and fresh water production. Improving the energy efficiency of a ship as defined by these technical measures, therefore requires the production of electricity in recovery turbine generator units. In this way, some of the diesel generating sets of the ship's electric power station can be set aside and

the surplus power transferred to the main engine crankshaft by means of a shaft generator operating in a PTO (Power Take-Off) mode [4].

Table 2. Boundary conditions assumed for the simulation of the selected main engines operation [4]

Boundary conditions		Remarks
Engine load	75% of maximum continuous power	Engine load is related to the calculation of energy efficiency design (EEDI) and existing ship (EEXI) index
Engine speed	91% of maximum continuous speed	Engine speed corresponds to the operation of the engine according to the propeller curve
Ambient conditions	ISO	Ambient air and scavenge air coolant temperature is 25°C
Fuels used	Regasified LNG	Gas mode in which the pilot oil dose is involved in the initiation of ignition
	MGO as a pilot oil	
Compliance with NO_x emission standards	Tier III and consequently less stringent Tier II	WinGD X92DF in a gas mode does not require the use of SCR or EGR systems

In turn, the presentation of heat losses as a percentage of the energy supplied with fuel makes it easier to relate these values to main engines with any available number of cylinders. On the other hand, the temperature of each of the waste heat carriers refers to the thermodynamic cycle whose realisation enables the production of steam to drive the steam turbine generator unit [11].

4. Results and discussion

The heat balance results of the WinGD X92DF and MAN G95ME-C10-GI operating in a Tier III-compliant gas mode under 75% maximum continuous rating and ISO ambient conditions received in the simulation carried out for the boundary conditions listed in Table 2 are shown in Fig. 2. All the symbols used are identical to those mentioned below equations (1)–(5).

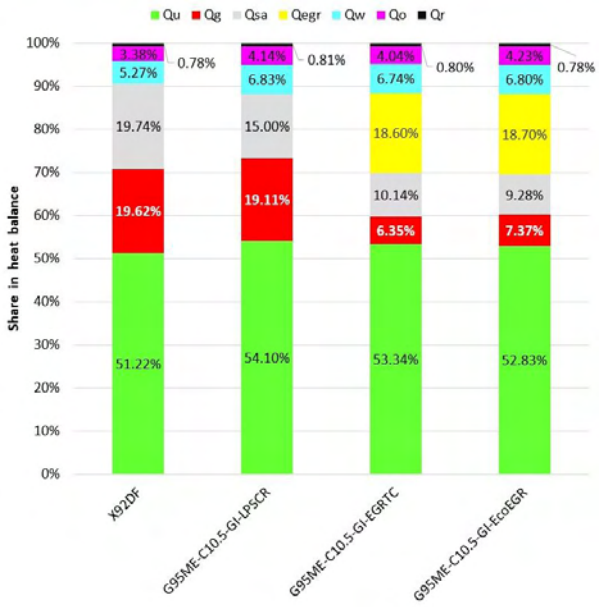

Fig. 2. Heat balance results of the gas-fuelled MAN G95ME-C10.5-GI and WinGD X92DF operating in a Tier III-compliant gas mode under 75% maximum continuous rating and ISO ambient conditions

On the basis of a comparison of the heat balance results shown in Fig. 2, it was found that the realisation of the Otto cycle by the WinGD X92DF was associated with up to 2.88 percentage points lower overall efficiency and thus much higher waste heat resources than the Diesel-cycle MAN G95ME-C10.5-GI. This was caused by a significantly lower compression ratio as well as the combustion temperature of the compressed fuel-air mixture (Table 2). Otto cycle is the most efficient thermodynamic cycle of the internal combustion engines assuming the same compression ratio. However, the almost twice lower compression ratio than in the case of the Diesel cycle determines the lower efficiency of Otto-cycle WinGD X92DF [10]. In addition, it is important to note the largest share of exhaust gas and scavenge air heat losses with the smallest share of jacket water and lube oil heat losses in the WinGD X92DF engines waste heat. This is due to the lack of any additional systems to ensure the exhaust gas composition complied with Tier III emission standards, and a slightly larger piston stroke (Table 1) than the competing MAN G95ME-C10.5-GI [21].

MAN G95ME-C10.5-GI equipped with the LPSCR system stands out for the highest overall efficiency and share of exhaust gas waste heat in the total heat loss. This was attributed to the lack of interference of low-pressure selective catalytic reduction in the combustion process and thus the highest exhaust gas temperature and mass flow values among the available main engine configurations from this manufacturer [23]. Those equipped with both EGR system variants, on the other hand, are characterised by an unique EGR cooling heat loss ($\dot{Q}_{EGR}$), which is greater the higher the percentage of exhaust gas is recirculated. The appearance of this heat loss in the heat balance is linked to the significant decrease in the contribution of exhaust gas and scavenge air heat loss to total waste heat (Fig. 2) [13].

The inlet T_i and outlet T_o temperatures of the available waste heat carriers obtained from the MAN Computer Engine Application System and General Technical Data for WinGD 2-Stroke Engines software are shown in Table 3.

Table 3. Inlet T_i and outlet T_o temperatures of the available waste heat carriers

Waste heat carrier		Exhaust gas		Scavenge air		Jacket water	
X92DF		351	206	185	31	84	75
G95ME-C10.5-GI	LPSCR	424	254	188	32	87	
	EGRTC	294	214	193	33		
	EcoEGR	290	213	192	35		
Symbol		T_i	T_o	T_i	T_o	T_i	T_o
Unit		°C					

Waste heat carrier		Lube oil		EGR cooling water	
X92DF		55	45	N/A	
G95ME-C10.5-GI	LPSCR	54			
	EGRTC			44	25
	EcoEGR			45	
Symbol		T_i	T_o	T_i	T_o
Unit		°C			

The temperature values of the available waste heat carriers shown in Table 3 are not the highest achievable due to the reduction of the main engine load to 75% of the maximum continuous rating. The exhaust gas temperatures of all the analysed main engines are among the lowest range due to the location of the operating point in the area of highest overall efficiency, when the temperatures of the rest of waste heat carriers increase proportionally to the main engine load [11]. Exhaust gas is the only waste heat carrier whose sufficiently high temperature makes it possible to use them directly in the electricity generation process on the basis of both conventional thermodynamic cycles, i.e. the steam Rankine cycle (SRC), Brayton gas cycle (BC) or combined gas-steam cycle (CC), as well as the organic Rankine cycle (ORC). Each of the other waste heat carriers, due to their temperature precluding the steam production, can only be used to generate electricity in an ORC using an organic working fluid with a sufficiently low boiling point. In this way, superheated steam can be produced using waste heat carriers with a temperature below the water boiling point [1]. So far, only waste heat recovery based on conventional (SRC, BC and CC) thermodynamic cycles adapted to the main engine output has been implemented on some ships [8]. On the basis of comparison of the data contained in Figure 2, it is concluded that the use of a main engine equipped with any of the available EGR system variants can make waste heat recovery of the exhaust gas alone unprofitable in terms of the economy and improving ship energy efficiency defined by EEDI and EEXI values. This results from the relatively small share (6.35 ÷ 7.37%) of exhaust gas waste heat from in the heat balance. This means that its amount, expressed in kilowatts, is almost 3 times smaller than that of main engines equipped with LPSCR or implementing the Otto cycle. The share of exhaust gas and low-temperature (3) waste heat in the sum of heat losses are shown in Fig. 3.

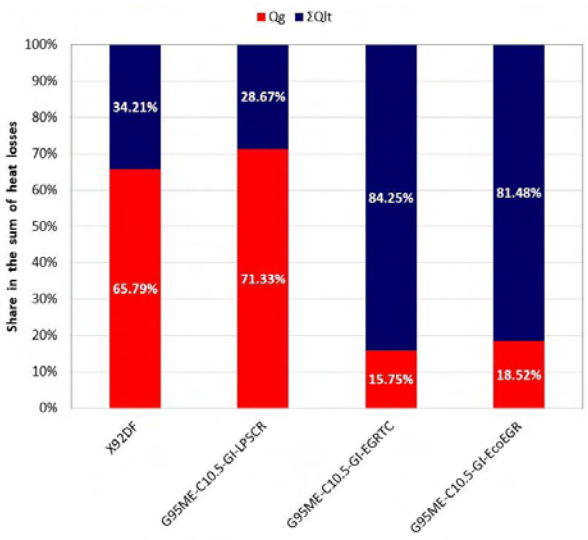

Fig. 3. Share of exhaust gas and low-temperature waste heat in the sum of heat losses

Analysis of the data contained in Fig. 3 has shown that waste heat recovery based on the ORC is particularly important for improving the energy efficiency of ships powered by main engines equipped with EGR systems. The waste heat of low-temperature carriers (3) in their case is equivalent to as much as 81.48–84.25% of the sum of heat losses, while for Diesel-cycle main engines equipped with LPSCR and Otto-cycle X92DF this share is within the limits of 28.67–34.21%. The indicated percentage of available waste heat can only be recovered in the power generation process in turbine generator units based on the ORC. It should also be emphasised that there is some waste cold amount from the LNG regasification process, which can be utilised to discharge heat from the steam in the condenser and in consequence significantly increase the ORC efficiency [1].

Conclusions

Performed analysis of the heat balance results of the two most popular two-stroke gas-fuelled main engines, i.e. WinGD X92DF and MAN G95ME-C10.5-GI, revealed that all available Tier III-compliant technologies have a significant impact on overall efficiency and the share of heat losses in the total waste heat.

Gas-fuelled Otto-cycle WinGD X92DF meets the most stringent Tier III emission standards without the use of any additional systems due to the lower combustion temperature of the less compressed fuel-air mixture. However, this is linked to the less efficient use of the chemical energy contained in the supplied fuel and therefore a decrease in overall efficiency and exhaust gas temperature (Table 3). Furthermore, it stands oud for the largest share of exhaust gas and scavenge air heat losses, while having the smallest share of cooling water and lube oil losses in total waste heat.

Gas-fuelled Diesel-cycle MAN G95ME-C10.5-GI requires the use of one of the available Tier III-compliant SCR or EGR systems due to the higher combustion temperature of the more compressed fuel-air mixture. LPSCR does not interfere with the combustion process, so main engines equipped with this system are characterised by the highest overall efficiency and exhaust gas temperature, as well as the largest share of exhaust gas waste heat in the sum of heat losses. Those equipped with both EGR system variants, on the other hand, are distinguished by their unique EGR cooling waste heat, which is greater the higher the percentage of exhaust gas is recirculated. The appearance of this EGR heat loss in the heat balance is associated with a significant decrease in the share of the exhaust gas temperature and waste heat as well as scavenge air to the total waste heat. In contrast, the temperature differences of the other waste heat carriers are negligible regardless of the Tier III-compliant technology used or lack thereof.

The reduction of EEDI and EEXI values requires the use of available waste heat in the electricity generation process. Exhaust gas is the only waste heat carrier with a sufficiently high temperature to enable its direct use in the electricity generation process on the basis of conventional thermodynamic cycles, i.e. the steam Rankine cycle (SRC), Brayton gas cycle (BC) or combined gas/steam cycle (CC), as well as the organic Rankine cycle (ORC). Any of the other low-temperature waste heat carriers, due to their temperatures precluding steam production, can only be used for power generation based on an ORC using an organic work-

ing fluid with a sufficiently low boiling point. Having regard to the dominant share of low-temperature waste heat carriers in the total heat loss of EGR-equipped main engines, it becomes ineffective to improve the energy efficiency of the ship driven by them without the use of waste heat recovery based on the ORC. Available waste cold amount from the LNG regasification process, which can be utilised to discharge heat from the steam in the condenser and consequently significantly increasing the ORC efficiency.

Nomenclature

EEDI	energy efficiency design index	EEXI	energy efficiency index for exisiting ships
EGRTC	exhaust gas recirculation turbocharger cut-out	EcoEGR	Eco-exhaust gas recirculation
LPSCR	low-pressure selective catalytic reduction	ORC	organic Rankine cycle

Bibliography

[1] Andreasen JG, Meroni A, Haglind F. A comparison of organic and steam Rankine cycle power systems for waste heat recovery on large ships. Energies. 2017;10:547. https://doi.org/10.3390/en10040547

[2] Brzeżański M, Mężyk P. Heat balance of the military vehicle. Combustion Engines. 2017;170(3):131-134. https://doi.org/10.19206/CE2017-322

[3] Hochgreb S. Handbook of Air Pollution from Internal Combustion Engines. Academic Press. San Diego 1998.

[4] International Maritime Organisation. IMO Train the Trainer (TTT) Course on Energy Efficient Ship Operation, Module 2 – Ship Energy Efficiency Regulations and Related Guidelines. https://www.imo.org/en/OurWork/Environment/Pages/IMO-Train-the-Trainer-Course.aspx (accessed on 24.11.2022)

[5] Ivanova G. Analysis of the specifics in calculating the index of existing marine energy efficiency EEXI in force since 2023. 2021 13th Electrical Engineering Faculty Conference. 2021:1-4. https://doi.org/10.1109/BulEF53491.2021.9690805

[6] Kniaziewicz T, PiasecznyL. Selected aspects of application of dual fuel marine engines. Combustion Engines. 2021; 148(1):25-34. https://doi.org/10.19206/CE-117048

[7] Korlak PK. Prediction of the ultra-large container ships' propulsion power at the initial design stage. Communications – Scientific Journals of the University of Zilina. 2022; 24(3):228-238. https://doi.org/10.26552/com.C.2022.3.B228-B238

[8] Korlak PK. Prediction of the very- and ultra-large container ships' electricity generation capacity at the initial design stage. Naše More. 2022;69(2):103-113. https://doi.org/10.17818/NM/2022/2.5

[9] Krakowski R. The emissions reduction possibility of sulphur compounds of vessel sailing in Emission Control Area (ECA). Combustion Engines. 2017;169(2):162-166. https://doi.org/10.19206/CE-2017-229

[10] Latarche M. Pounder's marine diesel engines and gas turbines. Tenth edition. Elsevier Science. Oxford 2020.

[11] Liberacki R. Niekonwencjonalne metody odzysku ciepła odpadowego na statkach. Journal of Polish CIMEEAC. 2019;14. http://www.polishcimeeac.pl/Papers1/2019/013.pdf

[12] MAN Diesel & Turbo. Costs and benefits of LNG as ship fuel for container vessels. Copenhagen 2013.

[13] MAN Diesel & Turbo. Tier III two-stroke technology. Copenhagen 2013.

[14] MAN Diesel & Turbo. Waste Heat Recovery System (WHRS) for reduction of fuel consumption, emissions and EEDI. Copenhagen 2017.

[15] MAN Energy Solutions. Marine engine programme 2022. Copenhagen 2022.

[16] Molland AF. The Maritime Engineering Reference Book. Elsevier Science. Oxford 2008.

[17] Mondejar ME, Andreasen JG, Pierobon L, Larsen U, Thern M, Haglind F. A review of the use of organic Rankine cycle power systems for maritime applications. Renew Sust Energ Rev. 2018;91:126-151. https://doi.org/10.1016/j.rser.2018.03.074

[18] Sagin S, Kuropyatnyk O, Sagin A, Tkachenko I, Fomin O, Píštěk V, Kučera P. Ensuring the Friendliness of Drillships during Their Operation in Special Ecological Regions of Northern Europe. J Mar Sci Eng. 2022;10:1331. https://doi.org/10.3390/jmse10091331

[19] Singh DV, Pedersen E, A review of waste heat recovery technologies for maritime applications. Energ Convers Manage.2016;111:315-328. https://doi.org/10.1016/j.enconman.2015.12.073

[20] Szelangiewicz T, Żelazny K. CO_2 emission level as a criterion in modern transport ship design. Combustion Engines. 2014;156(1):59-68. https://doi.org/10.19206/CE-116953

[21] WinGD. Low-pressure X-DF engines FAQ. Winterthur 2020.

[22] WinGD. Low-speed engines 2022. Winterthur 2022.

[23] WinGD. Selective Catalytic Reduction FAQ. Winterthur 2020.

[24] Wojnowski W. Okrętowe siłownie spalinowe. Cz. I. Wydawnictwo Akademii Marynarki Wojennej w Gdyni. Gdynia 1998.

Piotr Kamil Korlak, MSc. – Doctoral School of the Maritime University of Szczecin, Poland.
e-mail: *pkor@int.pl*

Article citation info:
Czarnigowski J, Trendak M. Aircraft piston engine load distribution in steady state operating conditions. Combustion Engines. 2023; 193(2):29-35. https://doi.org/10.19206/CE-160505

Jacek CZARNIGOWSKI
Michał TRENDAK

Combustion Engines
Polish Scientific Society of Combustion Engines

Aircraft piston engine load distribution in steady state operating conditions

ARTICLE INFO

Received: 29 September 2022
Revised: 3 January 2023
Accepted: 3 February 2023
Available online: 13 February 2023

The article presents the results of statistical analysis of aircraft piston engine operational parameters during normal operating conditions. Test was carried out on ultralight gyroplane Tercel produced by Aviation Artur Trendak equipped with CA 912 ULT piston engine. Research was conducted under normal operating conditions of the autogyro and data was collected from 15 independent tests including a total of 14 flight hours conducted during training flights. Engine and flight parameters were recorded at 9 Hz during each flight using on-board Flight Data Recorded system. The data collected was subjected to statistical analysis to determine the statistical distribution of parameters defining the engine's operating condition. The analysis covered engine speed, intake manifold pressure, oil temperature, head temperature and exhaust gas temperature. The results were presented in the form of histograms showing the characteristic ranges of the parameters in aviation engine operation. An analysis of the rate of change of the analysed parameters was then carried out. This was the basis for defining the engine's steady state. The results showed that the steady state of the engine under these operating conditions accounted for more than 78% of the total engine operating time. A Power Consumption Ratio indicating the load range of the engine was determined for steady states. It was shown that most of the time the motor operates at an average load of between 50% and 80% of the nominal value.

Key words: *piston engine, engine parameters, statistic, normal operating conditions*

1. Introduction

Aviation continues to be one of the leading industries and a driver of innovation [1]. The main directions of aviation development are to increase the safety of the structure and its operation, and to increase its efficiency, defined as the energy consumption to transport the load. This is particularly important in the case of the fastest growing branches of aviation is ultralight aviation, i.e. small, maximum two-seat aircraft with take-off mass not exceeding 600 kg [2–4]. These are aircraft that can be used from short grass airfields, significantly increasing their availability for recreational and utility use. In addition, the regulations to which they are subject significantly simplify the requirements for their use and maintenance, allowing low operating costs [5].

Modern technologies are widely used in ultralight aircraft. Simplified construction certification procedures allow modern solutions to be introduced into their design much more quickly than in General Aviation or Transportation Aviation [6]. The use of modern materials, such as carbon fiber, allow a reduction in empty weight, therefore increasing the payload weight [2, 7, 8]. The use of modern materials also allows the shapes of the aircraft themselves to be optimized, thereby increasing their aerodynamic efficiency [9]. This makes it possible to reduce energy requirements or increase cruise speeds [10, 11].

Optimization also extends to powertrains. For ultralight aircraft, the main propulsion system currently used is a small piston engine. They are characterized by construction simplicity, low failure rate and low weight [12, 13]. The development of that engines is mainly aimed at increasing the power-to-weight ratio. It is done by minimize the size of the engine components and reduce of its weight without changing the power or by increase power while maintaining or slightly increasing the weight of the engine. A common solution is the turbocharging systems [14] which allows to obtain higher power at similar weight. However it leads to increase of the thermal and mechanical load of the engine [15]. This requires increased attention in operation and maintenance.

The best solution would be to combine both methods or to introduce a new type of power unit that meets the criteria of a higher power-to-weight ratio than at present. This leads to ideas of using electric or hybrid systems [16–18]. Such systems have been well introduced in automotive propulsion systems [19].

In both cases, the optimization of current propulsion systems and the introduction of new ones requires the gathering of data on the range and operating conditions of these units under actual operating conditions. This is because the conditions of operation, particularly the load range of the engine and the steady-state and transient operation ratio, strongly influence the stresses on the structures and their lifetime [20–22]. However, these data cannot be translated between different types of vehicle, and especially between motor vehicles and aircraft.

The authors of the work [19, 23], highlighting the significant contribution of dynamic states under normal vehicle operating conditions. They show that dynamic conditions occupy from 20% to 50% [19]. For aircraft engines, the contribution of dynamic conditions is much smaller [16] and do not across ranges from 5% to 20% of the engine operating time [17]. The difference also are shown in the

average conditions of steady state engine operation. In the vehicles, the average conditions correspond to about 20% to 30% of the nominal power [1], while in the case of aircraft engines, they are much higher, about 50 to 70% [17, 24]. Knowledge of the exact distribution of operating parameters is therefore important for the development of propulsion systems.

This paper presents an analysis of performance of CA 912 RSTi engine, used to propel the Tercel autogyro in real operating conditions.

2. Methodology and research object

2.1. Research object

The research was carried out on a autogyro with registration number SP-XXBX type Tercel, produced by Aviation Artur Trendak. It is a two-seat ultralight autogyro, designed for recreational, training, commercial use and sport. The Tercel autogyro is shown in Fig. 1. Basic technical data of the tested autogyro are shown in Table 1.

Fig. 1. Test object: Tercel autogyro produced by Aviation Artur Trendak

Table 1. Technical data of Tercel autogyro [25]

Dimensions		
Rotor diameter	8.60	m
Rotor disc area	60.82	m^2
Rotor blade chord	0.20	m
Overall length (without rotor)	5.04	m
Hull width	2.35	m
Cabin width	2.20	m
Cabin width	1.36	m
Overall height	2.35	m
Wheel diameter	2.87	m
Weight		
Maximum take-off weight	560	kg
Empty weight	295	kg
Payload weight	265	kg
Propulsion System		
Engine gear ratio	1:2.43	
Propeller diameter	1.72	m
Propeller	Kaspar Aero 2/3 LT	
Fuel tank capacity	120	l

The Tercel is powered by a CA 912 RSTi engine. It is four cylinder boxer type engine, turbocharged with electronic injection system. The technical data of the CA 912 ULT engine are shown in Table 2.

Table 2. Technical data of CA 912 ULT engine [25]

Parameter	Value
Cylinder no.	4, boxer
Displacement	1211 cm^3
Cylinder diameter	79.5 mm
Piston stroke	61 mm
Compression ratio	9.0:1
Engine gear ratio	2.43:1
Fuelling system	Indirect, multipoint injection system Auris by Auto&Aero Technologies
Turbocharging	Turbocharger with an exhaust gas pressure control valve
Take-off power	140 HP (at 5800 rpm)
Nominal power	125 HP (at 5500 rpm)
Idle speed	2000 rpm

2.2. Scope of research

The aim of the study was to analyse the statistical distributions of the main parameters of the aircraft engine operation in real operating conditions in steady and transient state. The data was collected by Flight Data Recorder FDR K.01 produced by Auto&Aero Technologies Sp. z o.o. and built into the autogyro as standard equipment. FDR collects the information from the avionics system and the engine control system via RS485 communication (Fig. 2).

Fig. 2. Flight Data Recorder used in the research

The tests were conducted from 19.10.2021 to 28.10.2021 in Baranów airbase. There were 20 independent tests (flights) during pilots training flights – Table 3. These flights included mainly full Airfield traffic pattern with full landing or touch-and-go. In 4 cases these were navigational distance flights. The time to take one Airfield traffic pattern was about 8 to 15 minutes and the time for a single recording (single flight) ranged from 22 to 90 minutes. In total, the flights covered 1009 minutes and 88 take-offs and landings.

During the flights, the following parameters, among others, were recorded at 9 Hz:

- Air speed, km/h;
- Altitude, m. asl;
- Climb rate, m/s;
- Rotor speed, rpm;
- Crankshaft speed, rpm;
- Intake manifold pressure, kPa;
- intake manifold air temperature, °C;

– fuel pressure, kPa;
– oil pressure, kPa;
– oil temperature, °C;
– 2 × head temperature, °C;
– 2 × exhaust temperature, °C.

Table 3. Test flights

No	Date	Duration, min	Landings
1	19.10.2021	65	8
2	19.10.2021	35	4
3	19.10.2021	60	8
4	19.10.2021	88	8
5	20.10.2021	58	1
6	20.10.2021	22	2
7	20.10.2021	65	7
8	20.10.2021	64	7
9	21.10.2021	60	5
10	22.10.2021	19	1
11	26.10.2021	61	6
12	26.10.2021	57	6
13	26.10.2021	58	1
14	26.10.2021	58	4
15	27.10.2021	38	4
16	27.10.2021	36	2
17	27.10.2021	61	2
18	27.10.2021	33	4
19	28.10.2021	34	4
20	28.10.2021	37	4
	Total	**1009**	**88**

2.3. Methodology

The collected data were subjected to statistical analysis. For each parameter, an occurrence histogram was determined. In the case of speed and intake manifold pressure, a histogram of the occurrence of the dependence on these two variables was also determined.

The next step was a steady-state and transient analysis. For this purpose, an analysis of the rate of change of the analyzed parameters was carried out. According to the literature [15, 18, 26], it was assumed that steady state can be defined as such a state of engine operation in which the rate of parameters defining the operating point does not change by more than 1% of range per second. On this basis, steady-state operating points were determined. The parameters considered in this case are engine speed, manifold air pressure and the thermal state of the engine expressed by oil temperature and head temperature. The stability of all 4 parameters together define the steady-state operating point of the engine.

For such a defined steady-state operating point, a load distribution analysis of the engine was carried out. The engine load (P_{CR} – power consumption ratio) was determined as a relative value:

$$P_{CR} = \frac{n_i - n_{idle}}{n_{nom} - n_{idle}} \cdot \frac{MAP_i - MAP_{idle}}{MAP_{nom} - MAP_{idle}} \quad (1)$$

where: n_i – engine speed at the analysed point; MAP_i – manifold air pressure at the analysed point; n_{nom} – engine speed at the nominal power (5500 rpm); MAP_{nom} – manifold air pressure at the nominal power (135 kPa); n_{idle} – engine speed at the idle (1800 rpm); MAP_{idle} – manifold air pressure at the idle (30 kPa).

The value of the defined coefficient is defined in the range of engine operation from idle (value 0) to nominal power (100%). When the engine is operating at take-off power, the coefficient value will be greater than 100%. This approach is in line with the definition of engine load in the aircraft engine certification specification. The values corresponding to idle and rated power were determined from the engine manufacturer's data.

The above analyses were carried out for all flights together. The results were presented as histograms of the distribution of the analysed parameters.

3. Analysis of results

Figure 4 shows the distribution of engine operating point rates during tests. The operating points are defined by engine speed and manifold air pressure. Two groups of operating points can be seen: the idle range (n = 1500–2000 rpm and MAP = 20–40 kPa) and the engine load (n = 4000–6000 rpm and MAP = 70–140 kPa). The highest frequent engine operating points occur at idle for 1500–2000 rpm and intake manifold pressure 30–40 kPa and their rate is 28.3%. In the case of engine loads during normal flight, the frequency is 55.5% and occurs at 4000–5400 rpm and MAP = 80–120 kPa. The distribution of points is fairly uniform over this range, with the highest frequency occurring at 5000 rpm and MAP = 115 kPa and equal to 5.4%. There is also a significant occurrence of the engine starting power (n = 5500–6000 rpm and MAP = 120–140 kPa) amounting to 5.1% in the studied flights. This power is used during takeoffs and the climb after take-off. A very small proportion of intermediate conditions is also evident.

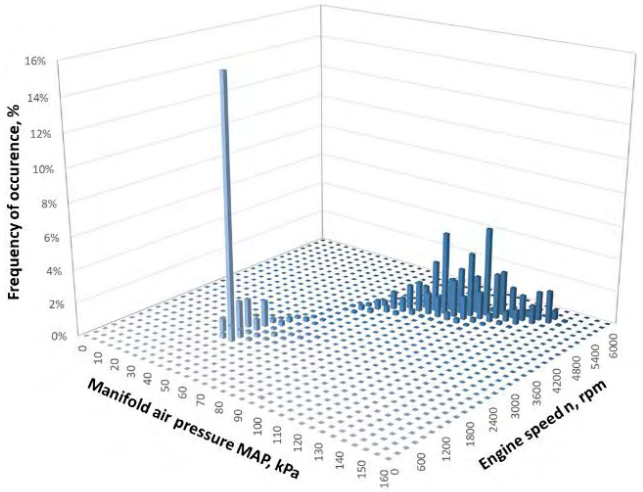

Fig. 4. Distribution of engine operating points during flights

This is more visible if we look at the distribution obtained as a map of the occurrence of work points. Figure 5 shows this distribution, assuming that the size of the circle at a given operating point corresponds to its frequency of occurrence. It can be seen that most of the working points are concentrated along one line – the propeller characteristic (marked in Fig. 5 by the line). This is a characteristic distribution for the cooperation of the engine with the propeller with constant characteristics. The concentration of

operating points in the idle, flight and take-off and climb (TOGA) range, as described earlier, is also visible.

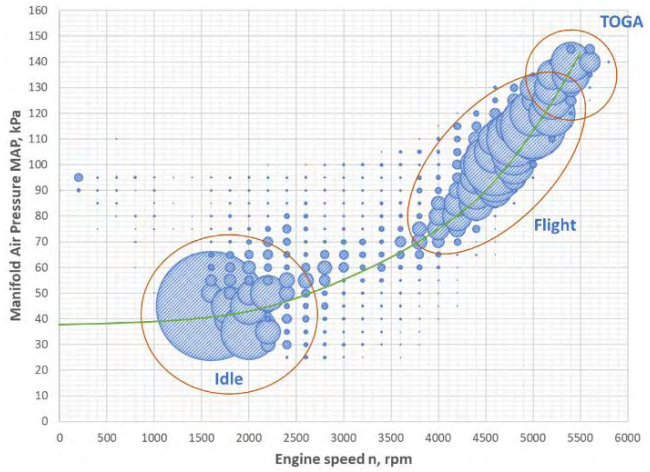

Fig. 5. Distribution of engine operating points during flights

Next the analysis was performed only for engine speed (Fig. 6) and separately for manifold air pressure (Fig. 7). For the flights, the highest frequency of occurrence was a speed around 1600 rpm corresponding to engine idle. The engine operated at this speed 17.0% of the total engine run time. The second most common speed range is around 4800 rpm. The 4600–4800 rpm range is 25.8% and the 4800–4500 rpm range is 20.1%. These ranges correspond to a cruising power of about 50% to 80% of the nominal power of the engine. The speed range 2000–2400 rpm, corresponding to the engine warm-up process, is also a significant part of the engine work and occupies a total of 12.3%. This is due to short single flights, for which the warm-up time is a significant part.

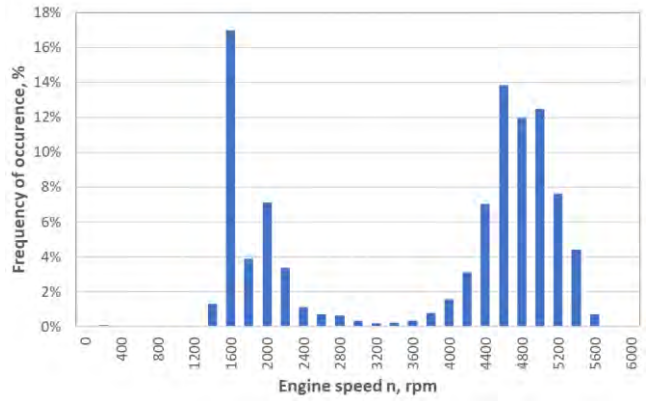

Fig. 6. Distribution of engine speed during flights

Similar distributions are seen in the manifold air pressure (MAP) (Fig. 7). The most common pressure is the range 40–50 kPa corresponding to engine idle. This occurs for 19.7% of the engine operating time. The MAP ranges from 100 kPa to 120 kPa occur with a similar frequency of about 5–8% for each 5 kPa interval considered.

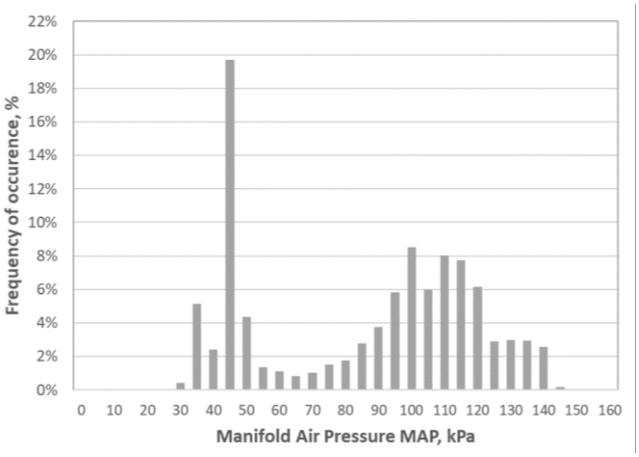

Fig. 7. Distribution of manifold air pressure during flights

Another group of analyses concerns temperatures. One of the important temperatures during engine operation is the oil temperature. Among other things, this is used as a basis for the decision to start (according to the operating manual, the oil temperature must exceed 60°C). As shown in Figure 8, the oil temperature is quite stable and after the engine warm-up was maintained in the range of 70°C to 86°C. It can be seen that the warm-up period accounted for a total of 7.3% of the total engine running time (temperatures below 62°C).

A similar stability can be observed by analysing the temperature of the cylinder heads (Fig. 9). Both sides of the engine maintain a similar temperature between 64°C and 84°C for more than 85% of the engine running time.

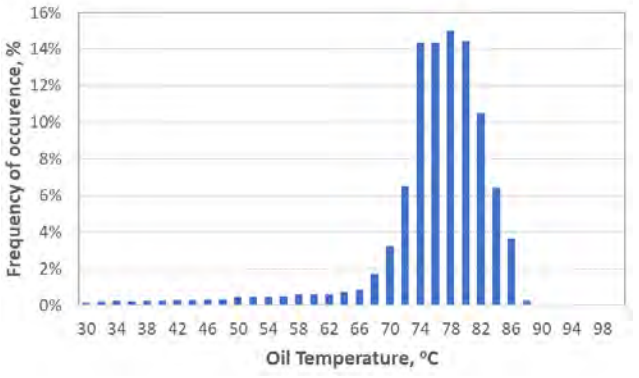

Fig. 8. Distribution of oil temperature

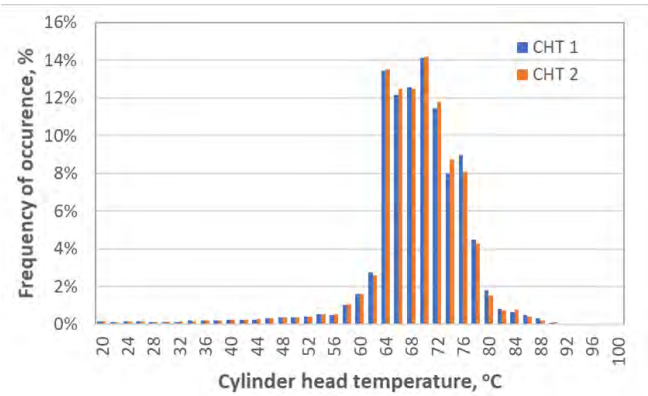

Fig. 9. Distribution of cylinder heads temperature

Similar to oil, the warm-up time (reaching 60°C) is a total of 8.0% of the engine operating time. It should be noted here that the stability of these temperatures is also related to the installation of the engine on the airframe and the proper heat dissipation from the oil and engine coolant cooling systems.

The distribution of exhaust gas temperatures (Fig. 10) shows a very high stability in the engine's operation under load. temperatures are maintained in the range of 760°C to 820°C for more than 65.3%. At lower loads, however, a significant difference in the temperature distribution for both sides of the engine (EGT 1 and EGT 2) is apparent. In this case, the right side of the engine (EGT 1) maintained about 150°C higher gas temperatures than the left side (ETG 2). This is a common case in these engines resulting from both combustion irregularities. Once the temperature exceeds 750°C (corresponding to about 50% of the nominal power), this difference practically disappears.

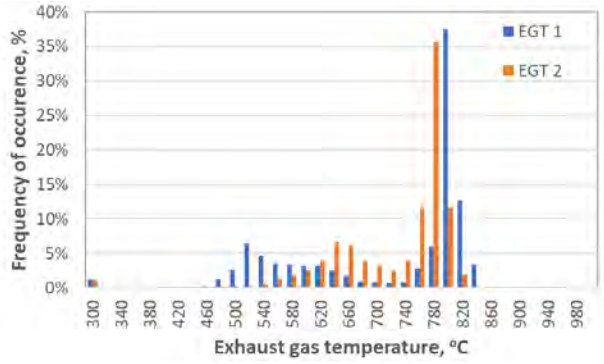

Fig. 10. Distribution of exhaust gases temperature

Another analysis included the rate of change of engine speed (Fig. 11). For analysed flights, more than 85% of the operating time is stable conditions in which the rate of change of engine speed does not exceed ±50 rpm/s. Rate of change higher than ±150 rpm/s is only 2.6% (symmetrically 1.3% decrease and increase of speed). These values are due to the landing (taking off the throttle before landing) and takeoff (rapid addition of throttle) stages. Assuming a 1% range/s limit of 58 rpm/s, it can be assumed that more than 87.5% corresponds to the steady state condition.

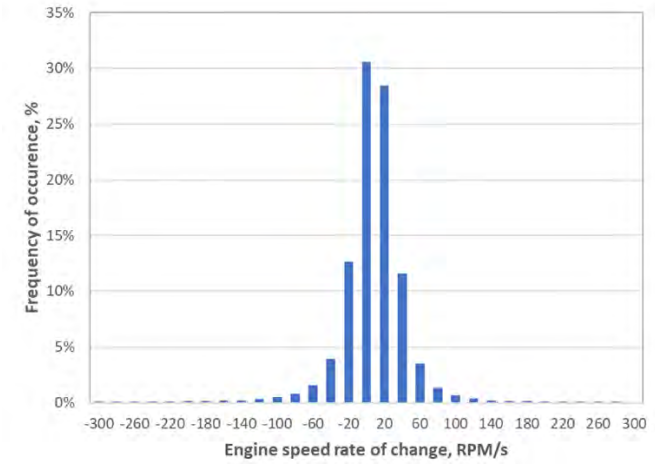

Fig. 11. Distribution of engine speed rate of change

The stability of engine operating conditions is even more apparent when the rate of change of manifold air pressure is analysed (Fig. 12). For analysed flights, the pressure practically does not change faster than ±3 kPa/s – 89.2%. Assuming a 1% range/s limit of 1.5 kPa/s, it can be assumed that more than 82.3% corresponds to the steady state condition. Maximal changes do not exceed ±9 kPa/s.

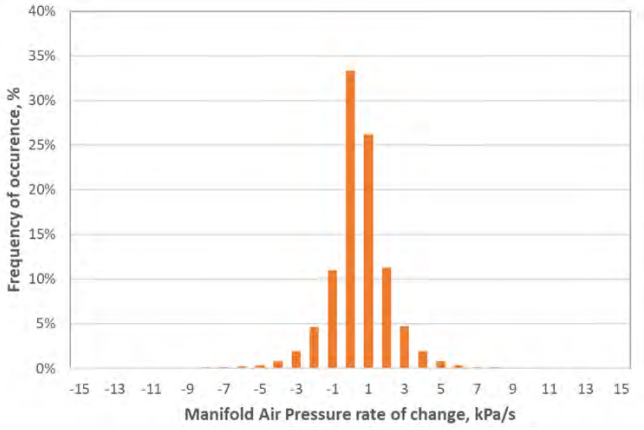

Fig. 12. Distribution of manifold air pressure rate of change

By analysing the rate of change of the oil temperature (Fig. 13), we can see that the rate of change is very low. The thermal capacity of the system causes most of the change to be in the range of ±0.2°C/s: over 87.9%. Taking 1% of the variation range kPa/s as the stability index (0.8°C/s), it can be assumed that 99.2% of the points meet the conditions for stable operation.

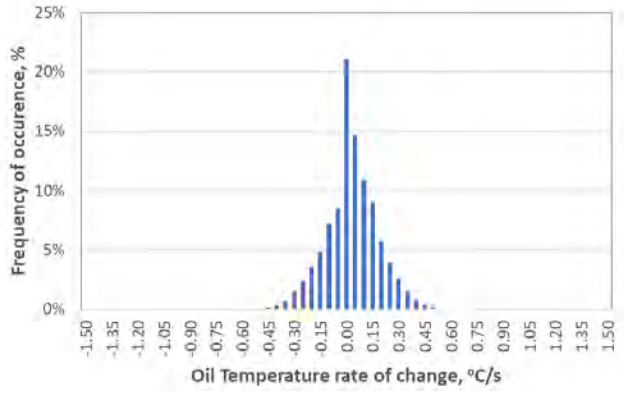

Fig. 13. Distribution of oil temperature rate of change

Similar results were observed for head temperatures (Fig. 14). Again, 99.4% of cases are within 1% (1°C/s). As for the oil, 91.7% of cases are within ±0.2°C/s. Thus, virtually all points meet the engine's steady-state condition.

On the basis of the assumed limits of engine dynamics, an analysis of engine operating states was carried out. The engine was assumed to operate as a steady state condition for four parameters: speed, intake manifold pressure, oil temperature and head temperature. On this basis, an analysis was carried out for the entire flight range. Figure 15 shows the results of the analysis. The vast majority of engine operation is at steady state: 78.9 %.

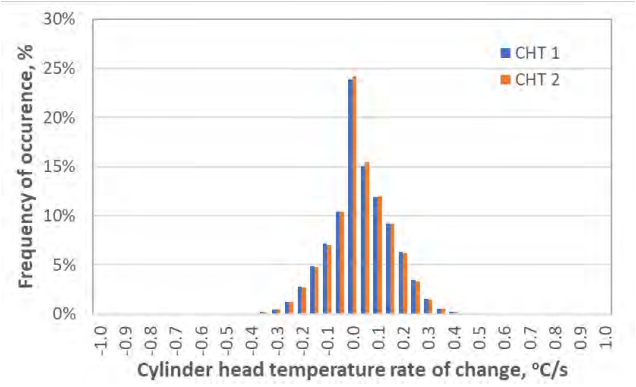

Fig. 14. Distribution of cylinder head rate of change

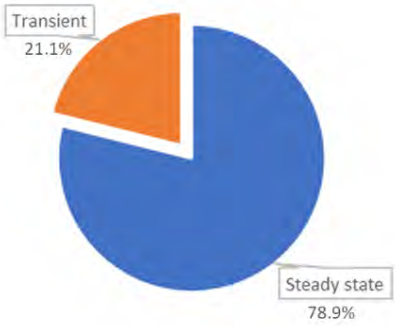

Fig. 15. Distribution of steady state and transient condition of engine work

The next step of the analyses was to analyse the Power Consumption Ratio distribution for steady-state engine operation (Fig. 16). It can be seen that idling is 18.6% and warming up (5% power) is 15.1%. The engine works very seldom in the power range between 10 and 45% of the nominal power and this applies mainly to transient conditions. The next range, covering about 55% of nominal power, is 7.8% and corresponds to stable flight at low cruise speed. Increasing speed causes an increase in power demand, which corresponds to further points in the range from 60 to 80% of nominal power. The distribution of occurrence here is quite constant and is for each range about 5 to 7%. Take-off power (above 100% nominal power) occurs a total of 3.3% of the time and nominal power 2.1%.

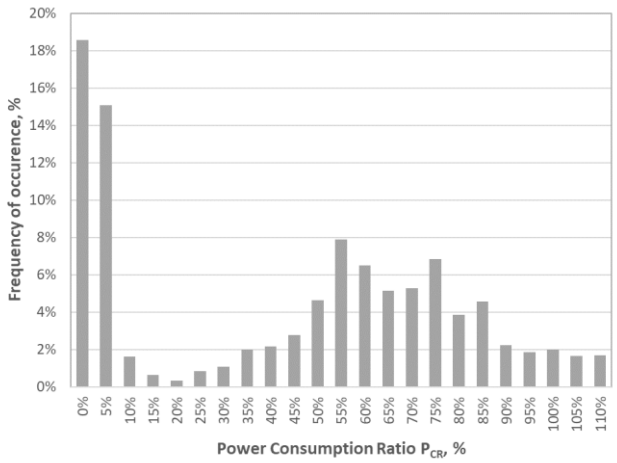

Fig. 16. Distribution of Power Consumption Ratio

Conclusions

The research shows that the aircraft engine operates in the vast majority of steady-state conditions. In the analysed flights, steady state was 78.9% of the total operating time. If we take into account that most of these flights were carried out as airport circle flights as part of pilot training, the dynamics in cruise flight use should be even lower. Changes in speed and air pressure in the intake manifold are mainly responsible for the transient. Variations in oil, head and exhaust gas temperatures are much smaller and mostly fall within the definition of steady state.

Aircraft engines operate at average high loads. During the flights, the most common operating condition was an engine load of 50–80% of nominal power – 55%. The second most frequent operating condition of the engine is idling (18.6%) and warming up (15.1%). Take-off power (above 100% nominal power) occurs a total of 3.3% of the time and nominal power 2.1%. Small engine loads (below 50%) practically did not occur during the research. Their share in the total engine operating time is marginal.

Bibliography

[1] Andrych-Zalewska M, Chłopek Z, Merkisz J, Pielecha J. Evaluation of the test drive cycle conditions impact on exhaust emissions from an internal combustion engine. Combustion Engines. 2018;175(4):3-9. https://doi.org/10.19206/ce-2018-401

[2] Czarnigowski J, Wendeker M, Jaklinski P, Nazarewicz A, Piertykowski K, Geca M, et al. Model of injection system for SI radial aircraft engine. SAE Technical Papers 2007-01-1903. 2007. https://doi.org/10.4271/2007-01-1903

[3] Markowski J. Correction of the model for assessing the emission of harmful exhaust emissions from the engine of a small aircraft during the flight. Transp Res Proc. 2018;35: 230-239. https://doi.org/10.1016/j.trpro.2018.12.025

[4] Bakholdin D, Biryukov V, Tolstobrova L. Determining parameters of electric power unit for light aircraft. AER Adv Eng Res. Proceedings of the International Conference Actual Issues of Mechanical Engineering (AIME 2018). 2018; (157):65-69. https://doi.org/10.2991/aime-18.2018.13

[5] Jakliński P, Wendeker M, Czarnigowski J, Duk M, Zyska T, Klimkiewicz J. The comparison of the operating parameters in an aircraft radial piston engine fuelled by 100LL and ES95 gasoline. Combustion Engines. 2009;136(1):52-59. https://doi.org/10.19206/CE-117220

[6] Czarnigowski J, Jakliński P, Zyska T, Klimkiewicz J. Analysis of influence of legal requirements on the design of electronic ignition system for aviation piston engine. Journal of Kones. 2017;24(1):91-100. https://doi.org/10.5604/01.3001.0010.2801

[7] Kwon H, Park Y, Shin C, Kim J-H, Kim C-G. In-flight strain monitoring of aircraft tail boom structure using a fiber bragg grating sensor based health and usage monitoring system. Int J Aeronaut Space. 2021;22(3):567-577. https://doi.org/10.1007/s42405-020-00324-0

[8] Zhu L, Li N, Childs PRN. Light-weighting in aerospace component and system design (2018) Propul Power Research. 2018;7(2):103-119. https://doi.org/10.1016/j.jppr.2018.04.001

[9] Rohani SV, Jahangirian A. A fast and efficient method for multiobjective aerodynamic optimization of a civil aircraft fuselage. J Aerospace Eng. 2022;35(6). https://doi.org/10.1061/(ASCE)AS.1943-5525.0001494
[10] Sabater C, Stürmer P, Bekemeyer P. Fast predictions of aircraft aerodynamics using deep-learning techniques. AIAA J. 2022;60(9):5249-5261. https://doi.org/10.2514/1.J061234
[11] Song C, Liu H, Zhou Z, Luo X, Li W. Inverse design of aerodynamic configuration using generative topographic mapping. Xibei Gongye Daxue Xuebao/Journal of Northwestern Polytechnical University. 2022;40(4):837-844. https://doi.org/10.1051/jnwpu/20224040837
[12] Shen Y-G, Nie K, Xu J-S, Chen G-S. Combustion and emission characteristics of compression-ignition aero piston engine at different altitudes. Tuijin Jishu/Journal of Propulsion Technology. 2022;43(4). https://doi.org/10.13675/j.cnki.tjjs.200896
[13] Zhao Z, Cui H. Numerical investigation on combustion processes of an aircraft piston engine fueled with aviation kerosene and gasoline. Energy. 2022;239:122264. https://doi.org/10.1016/j.energy.2021.122264
[14] Grabowski Ł, Karpiński P, Rudzik D. Study on operating load of the compression ignition engine. Combustion Engines. 2017;168(1):168-171. https://doi.org/10.19206/CE-2017-127
[15] Heywood JB. Internal Combustion Engine Fundamentals. McGraw Hill, New York, 1988.
[16] Bai M, Yang W, Song D, Kosuda M, Szabo S, Lipovsky P, Kasaei A. Research on energy management of hybrid unmanned aerial vehicles to improve energy-saving and emission reduction performance. Int J Env Res Pub He. 2020;17:2917. https://doi.org/10.3390/ijerph17082917
[17] Yuhimenko V, Baimel D. Sitbon M, Averbukh M, Lineykin S, Kuperman A. Hybrid internal combustion engine based auxiliary power unit. Micromachines. 2020;11:438. https://doi.org/10.3390/mi11040438
[18] Zhao X, Guerrero JM, Wu X. Review of aircraft electric power systems and architectures. Energycon 2014 – IEEE Int. Energy Conf. 2014:949-953. https://doi.org/10.1109/ENERGYCON.2014.6850540
[19] Song J, Cha J. Analysis of driving dynamics considering driving resistances in on-road driving. Energies. 2021;14: 3408. https://doi.org/10.3390/en14123408
[20] Bieniek A, Brol S, Mamala J. The system for estimation parameters of internal combustion engine in the road test. Journal of Kones. 2011;18(2):279-286.
[21] Sureshkumar J, Venkitachalam G, Mallikarjuna JM, Elayaraja R. Study on effect of engine operating parameters on flame characteristics. SAE Technical Papers 2015-01-0749. 2015. https://doi.org/10.4271/2015-01-0749
[22] Gao Y, Checkel MD. Emission factors analysis for multiple vehicles using an on-board, in-use emissions measurement system. SAE Technical Papers 2007-01-1327, 2007(724), 776-790. https://doi.org/10.4271/2007-01-1327
[23] Bera P. Torque characteristic of SI engine in dynamic operating states. Combustion Engines. 2017;171(4):175-180. https://doi.org/10.19206/CE-2017-429
[24] Wendeker M, Jakliński P, Czarnigowski J. Experimental analysis of automotive engine conditions of operation. Eksploat Niezawodn. 2000;6:19-28.
[25] Aviation Artur Trendak TERCEL Carbon RSTi aircraft maintenance manual TERCEL-C-AMM-001-EN, edition 1. 28 Oct 2020.
[26] Boriboonsomsin K, Durbin T, Scora G, Johnson K, Sandez D, Vu A, et al. Real-world exhaust temperature and engine load distributions of on-road heavy-duty diesel vehicles in various vocations. Data Brief. 2018;18:1520-1543. https://doi.org/10.1016/j.dib.2018.04.044

Jacek Czarnigowski, DSc., DEng. – Faculty of Mechanical Engineering, Lublin University of Technology, Poland.
e-mail: *j.czarnigowski@pollub.pl*

Michał Trendak, MEng. – Faculty of Mechanical Engineering, Lublin University of Technology, Poland.
e-mail: *michal@trendak.eu*

Article citation info:
Pełczyński J. Outline of history and comparative analysis of internal combustion engines for flying models. *Combustion Engines*. 2023; 193(2):36-44. https://doi.org/10.19206/CE-155865

Jakub PEŁCZYŃSKI

Combustion Engines
Polish Scientific Society of Combustion Engines

Outline of history and comparative analysis of internal combustion engines for flying models

ARTICLE INFO

Received: 24 March 2022
Revised: 10 September 2022
Accepted: 18 October 2022
Available online: 30 November 2022

The article discusses the most important facts from the history of the development of miniature aircraft engines and carries out their comparative analysis. Already in the 1930s, the structural system characteristic of model engines was established, which has hardly changed to this day. The following sections compare the various types of engines: two-stroke and four-stroke engines, spark-ignition engines, glow plug engines, engines with a push-pull cylinder arrangement, radial and in-line engines. The comparisons of the parameters and operational indicators of such engines presented in the tables allowed for the assessment of the advantages and disadvantages of individual engines, making several observations and drawing some more general conclusions.

Key words: *internal combustion engines, model engines, history of model engines, comparative, flying models*

1. Introduction

With the development of technology, more and more complex and expensive to build machines are created. In order to reduce the costs of manufacturing and testing prototypes, their smaller models are often built, on which it is possible to test various design and technological solutions. It was similar in aviation. The first flights were always associated with a high risk, which is why some designers decided to build smaller, unmanned prototypes. For them, sufficiently small power units were needed; initially, miniaturized steam engines were used, then internal combustion engines. Over time, with the development of aviation, the role of experimental models has decreased. However, they began to be used for hobby and recreational purposes [14].

The subject of model aircraft propulsion is extremely interesting, and unfortunately, over the last several decades it has been quite disregarded in domestic literature. The last monograph devoted entirely to modeling engines "Popularne mikrosilniki spalinowe" [17] was written over 40 years ago by W. Schier, a great mentor of Polish aviation modeling.

During the time of the People's Republic of Poland, new monographs in this field, which were created almost every few years, testified to the great interest in the subject of model engines. The first monograph after the war was published in 1946: "Silniki lotnicze do modeli latających" by W. Niementowski [8].

The subject of miniature aircraft engines for flying models certainly deserves a new study, mainly due to the use of new design concepts and the development of model engines that have taken place in recent years. This article attempts to conduct a comparative analysis of the most important design parameters and operational indicators of modern model engines and to assess the current level of their development.

2. The history of the development of model engines

The second half of the nineteenth century was a time of an intensive development of steam engines. Then, they were the main source of propulsion, except, of course, for draft animals. With the advancement of steam engines, the need quickly arose to test various designs and construction concepts on scaled-down prototypes. It allowed to avoid significant costs of building expensive and complicated devices in real sizes.

For the first time a steam engine to drive an aircraft structure was used by an Englishman, John Stringfellow, in 1848, Fig. 1. The engine propelled a three-meter model, which made several successful jumps at a distance of less than 40 meters [18].

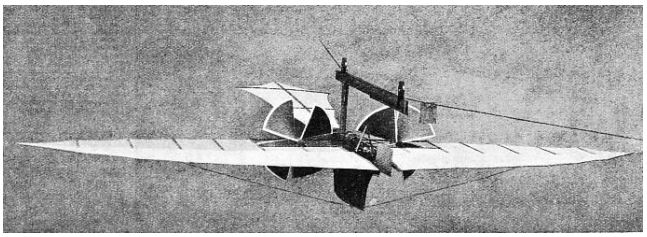

Fig. 1. John Stringfellow's airplane [41]

The steam engine of that time, however, was too heavy to be effectively used on a larger scale in aviation. Therefore, other solutions were sought. In the late 19th century, experiments were conducted with compressed air engines. The real breakthrough came with the development of internal combustion engines. In 1901, the first internal combustion miniature aircraft engine, designed by Samuel Pierpont Langley, was developed in the United States. Its power was 2 HP (about 1.5 kW) and allowed the flight of the model weighing 13.5 kg.

Soon after, the first "large" aircraft with a combustion engine was built [9]. Therefore, miniature engines began to lose their relevance. However, they quickly found a new application in aviation modeling. Initially, they were smaller and simplified versions of "large" four-stroke aircraft engines. Compressed air drive has been experimented with. A simple rubber drive was invented, which is used to this day in the simplest aircraft models. The first model engine with a classic design, similar to modern engines, was made

in 1934 in the USA; It was called Brown "Junior", Fig. 2. It was a two-stroke, single-cylinder, spark-ignition engine, also called gasoline engine in modeling terminology because of the fuel it burns. It had a displacement of 9.72 cm^3. It reached the power of 0.25 HP (approx. 0.2 kW) and the maximum speed of 6000 rpm. Currently, engines of this size can have nearly 10 times the power and 2-3 times the maximum speed. Nevertheless, at that time the Brown "Junior" engine was a breakthrough design and for those times – very modern.

Fig. 2. Engine Brown "Junior" [25]

The main problem in spark ignition engines was the considerable weight of the ignition system, especially the battery. The Swiss managed to solve this problem in 1940. They created a compression-ignition engine for model airplanes with the same layout as previously built model engines, i.e. the so-called self-ignition engine. It sucked in a fuel-air mixture from the carburetor, similar to spark ignition engines. The Swiss dubbed the new engine "Dyno 1". It had a displacement of 2.04cc. It reached the power of 0.09 HP (approx. 0.07 kW) and the maximum speed of 7500 rpm [17].

After the end of World War II, self-ignition engines spread throughout Europe, almost completely replacing spark-ignition engines by the end of the 1950s [13].

The construction of the self-ignition engine offered many possibilities that were impossible to achieve with gasoline engines. Very small engines were built, even below 1 cm^3 of cylinder capacity, which – if they had a heavy ignition system with a spark plug – would not have any practical application [15]. A model powered by such a small motor would not be able to lift the battery.

Over the years, the modeling engines have been improved more and more. New, better and better flushing systems began to be used in two-stroke engines. A good example is the 1.8cc "Elfin 1.8" engine. It reached the power of 0.11 HP (about 0.8 kW) and the volumetric power ratio of 61 HP/dm^3 (45 kW/dm^3), which was much more than in the analogous spark ignition engines of that time. Such engines were also built in Poland. An example can be the famous "Jaskółka" Fig. 3 [14].

Fig. 3. Polish self-ignition engine "Jaskółka" with a capacity of 2.5 cm^3 [26]

Despite the popularity of self-ignition engines in Europe, they never became widespread in the USA. Gasoline engines were constantly improved there, achieving a power ratio of over 100 KM/dm^3 (76 kW/dm^3), higher than most of the then engines [17]. Still, an unsolved problem was the considerable weight of the ignition system, especially the battery [22].

The breakthrough for American modeling was the invention of the glow plug by Roy Arden. He used it for the first time in his "Arden .09" engine. The model automatic engine with glow plug ignition, also referred to as a glow engine, which he created had the same structure as the rest of the model engines [14]. The only difference was the glow plug, which does not need to be permanently connected to the power source, but only during start-up. Therefore, the battery that powers it does not have to be on board an airplane model. It only needs to be connected to the plug on the ground when starting the engine, before take-off [6].

For some time, the development of model engines was different in America and Europe. Spark ignition engines in the USA were replaced by compression ignition glow engines, and in Europe by compression ignition self-ignition engines [14].

In the 1950s, further development of model drives showed the superiority of glow engines in terms of the power achieved. However, in Europe, self-ignition engines were already very common. They also burned less fuel. Glow engines slowly began to appear on the European market in the second half of the 1950s, but they were fully ousted only several dozen years later, Fig. 4.

Fig. 4. Modern ASP S52A glow engine [29]

The 1950s and 1960s were a period in which the so far built sub-square [1] engines with a large piston stroke, larger than the cylinder diameter, were more and more often replaced by engines with the same stroke as the diameter or with a stroke greater than the diameter, i.e. square motors. The stroke-to-diameter ratio is usually only slightly less than one, although in the 1960s experiments were conducted on motors with a very small ratio of these sizes. An example is the Soviet self-ignition engine by engineer Blinov, where this value was 0.27 [14].

In the 1960s, the so-called multi-range engines, i.e. with the possibility of changing the rotational speed, and not, as before, without such a possibility. In order to ensure the maximum simplification of construction, initially efforts were made to solve their operation in various unusual ways. Experiment with adjusting the engine speed only by changing the position of the needle valve (needle) of the carburetor. For some time, a popular solution was to use a special, simple, controlled shutter of the outlet opening in the cylinder. By exposing the exhaust port, the exhaust gases from the cylinder were allowed to flow out normally, and by obstructing their outflow. Eventually, development of rotary damper carburetors began. Thus, at the end of the 20th century, multi-range engines with a rotary throttle in the carburetor almost completely replaced those without the possibility of rotational speed control [17].

Interesting solutions tested in the 1960s were Wankel engines, i.e. engines with a rotating piston. Despite their short-lived popularity, they did not enter into wider use for a long time. An example can be the Polish "SW-92" engine designed by MSc. J. Falęcki from the Institute of Aviation in Warsaw. Its structure, together with executive and assembly drawings, is presented by W. Schier in the book „Miniaturowe silniki spalinowe" from 1967 [14].

By the end of the 20th century, self-ignition engines were practically out of use. Currently, virtually no one produces them. There are only rare exceptions to the solutions offered as "retro engines". Very small self-ignition engines for particularly small model aircraft are also appearing in the USA. In recent years, however, spark ignition engines have become widespread. They are designed for large aircraft models where the weight of the ignition system is of little importance. This is possible because currently used nickel or lithium batteries are much lighter than those used in the past. Therefore, no such engines are produced with displacements of less than 10 cm^3. The main advantage of spark ignition engines is the low price of gasoline that drives them in relation to methanol-based fuels used in glow engines. Currently, almost all engines with a cylinder capacity exceeding 20-30 cm3 are built as spark ignition engines, Fig. 5 [6].

Nowadays, very large, multi-cylinder model engines are also built, the power of which can exceed 20 HP (approx. 15 kW). Such engines are usually built in a system with push-pull pistons (the so-called boxer), less often in an in-line configuration.

Four-stroke engines are also being built. They have less power and a lower maximum speed than two-stroke engines, but they are considered more exclusive, and the sound they make is extremely beautiful. Manufacturers often advertise the sounds of their engines. Four-stroke radial engines and sometimes also four-stroke in-line engines are considered extremely exclusive. They are valued primarily for their aesthetic qualities. They can also be used in mock-ups of airplanes that actually had radial engines. Thanks to this, instead of inserting a mock-up of a radial engine into the engine cover, you can place a real engine there, which powers the model during flight [21].

Fig. 5. O.S.Gasoline spark ignition engine MAX GT60 [33]

3. Comparative analysis of two-stroke and four-stroke engines

Nowadays, the vast majority of aircraft engines for flying models are built as two-stroke engines, Fig. 6, Fig. 7. They have a simpler and cheaper structure than four-stroke engines and have greater power [10]. The only technical advantage of four-stroke engines is that they burn less fuel. Fuel injection and power stroke occur every second revolution of the crankshaft. Valves opened at appropriate moments prevent the formation of such large losses of the mixture during injection, as in two-stroke engines, in which, during the rinsing process, part of the mixture escapes along with the exhaust gases through the outlet port [2]. Nevertheless, with such small displacements, the difference in the fuel used is so small that the difference in the price of the fuel used is negligible in relation to the difference in the price of the engines. Therefore, four-stroke engines (Fig. 8) in modeling will probably never fully replace two-stroke engines [12].

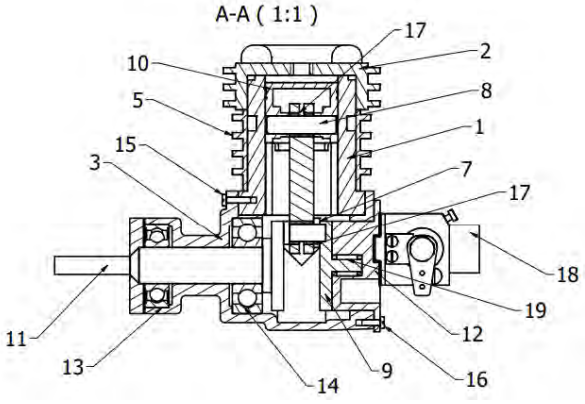

Fig. 6. Cross-section of a typical two-stroke glow engine, fragment of the assembly drawing [12]

Fig. 7. ASP 180 AR two-stroke glow ignition engine [29]

Fig. 8. The Saito FA-125 A four-stroke glow-ignition engine [36]

The only real advantage of 4-stroke engines is their clear sound when operating. It is especially appreciated by modellers. In models of real aircrafts, it allows not only to match the original appearance, but also in terms of the sounds that the plane makes during the flight. Four-stroke engines are considered more elegant and exclusive than ordinary two-stroke engines [11].

As can be seen from the comparison in Table 1 and 2, the power of two-stroke engines is much greater than the power of four-stroke engines. Two-stroke engines with small and medium displacements also have significantly higher maximum speeds. In four-stroke engines, however, they do not change significantly with increasing displacement, while in two-stroke engines they decrease significantly. Thus, large four-stroke engines (from about 15 ccm) often have higher RPMs than similarly sized two-stroke engines.

The main parameters by which two-stroke and four-stroke engines can be compared are the maximum speed and power. These are also the basic parameters provided by the producers. Tables 1 and 2 provide lists of engines for two selected cylinder capacities. Only the glow engines were selected for comparison as they are the most popular.

The unit power of two-stroke engines decreases with the displacement, and in four-stroke engines it remains unchanged. Nevertheless, for typical displacements used in single-cylinder model aircraft engines, its value is always higher for two-stroke engines.

Two-stroke engines with small displacement can generate very high power in relation to their displacement. An example is ASP 12A with a capacity of 1.94 cm^3, for which this ratio is as much as 309 KM/dm^3 (about 228 kW/dm^3) [11].

Table 1. Glow engines with a displacement of approximately 10 cm^3 [27, 28, 30, 32, 35, 38-40, 42]

Two-stroke engines	Maximum rotational speed [rpm]	Power [hp (kW)]	Specific power [KM/dm^3]	Four-stroke engines	Maximum rotational speed [rpm]	Power [hp (kW)]	Specific power [KM/dm^3]
MAX-55AX	17,000	1.68 (1.24)	188	O.S. MAX FSa-56II	13,000	0.99 (0.73)	106
ASP S61A	17,500	2.19 (1.61)	229	Saito FA-62B	11,000	1.01 (0.74)	101
MAX-65AX	12,000	1.73 (1.27)	163	ASP FS61AR	11,500	1.14 (0.84)	114
Super Tigre G-61 Ring	16,500	1.80 (1.32)	180	O.S, MAX FS-62V	11,000	1.08 (0.79)	107
Average	15,750	1.85 (1.36)	190	Average	11,625	1.06 (0.78)	107

Table 2. Glow engines with a displacement of approximately 20 cm^3 [27, 28, 30, 32, 35, 38-40, 42]

Two-stroke engines	Maximum rotational speed [rpm]	Power [hp (kW)]	Specific power [KM/dm3]	Four-stroke engines	Maximum rotational speed [rpm]	Power [hp (kW)]	Specific power [KM/dm3]
MAX-120AX Ring	9600	3.06 (2.25)	153	O.S. MAX FS-120SII	12,000	2.07 (1.52)	104
ASP 120AR	9600	3.60 (2.65)	180	ASP FS-120AR	11,500	2.13 (1.57)	107
Moki M140 RC	13,000	3.90 (2.87)	173	Saito FA-125a	11,000	2.22 (1.63)	108
Average	10,730	3.52 (2.59)	169	Average	11,500	2.14 (1.57)	106

4. Comparative analysis of glow and spark ignition engines

Currently, most of the engines for models produced are compression ignition engines with a glow plug. It is exactly the opposite of aero engines for propulsion of "large" aircraft, where compression ignition engines are a minority [5]. However, more and more often engines with a cylinder capacity exceeding 10–15 cm^3 are built with spark ignition, Fig. 9. At the beginning of the history of engines for model aircraft, only spark ignition engines were produced [14]. Their main disadvantage was the weight of the ignition system, especially the battery. Currently used nickel or lithium batteries are much lighter than those used in the past, so their weight in larger models with spark ignition engines is not a problem [6]. The use of a glow plug allows the construction of very small engines for small models. The glow plug needs to be connected to the power source only during start-up, therefore the battery does not have to be on board the model. The construction of spark ignition and glow engines is practically no different. The only significant difference, apart from the ignition system, is the compression ratio – in glow engines it is higher [17].

Spark ignition engines burn ordinary gasoline, which can be obtained, for example, at a gas station. That is why they are also called gasoline engines in modeling. Fuel for glow engines is much more expensive. Its main ingredient is methanol. Usually it also contains nitromethane, which increases the calorific value of the fuel. Usually its content is significant, it can reach even 30–40% of the total volume of the fuel consisting of pure methanol. Such fuel is produced especially for incandescent engines. Fuel with a composition of 70% methanol and 30% nitromethane has a calorific value of about 25% greater than that of pure methanol [16]. You can buy it only in stores and modeling wholesalers, which makes it much more expensive than gasoline. This is the main reason why gasoline engines are used, not just glow ones.

Fig. 9. Spark ignition engine O.S. MAX GT15 [29]

As in the case of the comparison of two-stroke and four-stroke engines, Tables 3, 4 and 5 contain lists of engines for selected cylinder volumes, giving the power and maximum rotational speed of these engines.

Table 3. Engines with a displacement of approximately 15 cm^3 [27, 28, 30, 32, 35, 38-40, 42]

Glow engines	Maximum rotational speed [rpm]	Power [KM (kW)]	Specific power [KM/dm^3]	Spark ignition engines	Maximum rotational speed [rpm]	Power [KM (kW)]	Specific power [KM/dm^3]
Super Tigre G-90 Ring	16,000	2.5 (1.84)	170	O.S. MAX GT15	15,000	2.47 (1.82)	165
ASP S91A	18,000	2.8 (2.06)	187	RCGF 15cc	15,000	2.4 (1.77)	160
MAX-95AX RING	16,000	2.86 (2.1)	184	ngh GT17	9000	2.1 (1.54)	124
Average	16,700	2.72 (2.0)	180	Average	13,000	2.32 (1.71)	150

Table 4. Engines with a displacement of approximately 20 cm^3 [27, 28, 30, 32, 35, 38-40, 42]

Glow engines	Maximum rotational speed [rpm]	Power [KM (kW)]	Specific power [KM/dm^3]	Spark ignitron engines	Maximum rotational speed [rpm]	Power [KM (kW)]	Specific power [KM/dm^3]
MAX-120AX Ring	9600	3.06 (2.25)	153	DLE20	9000	2.5 (1.84)	125
ASP 120AR	9600	3.6 (2.65)	180	RCGF 20cc	10,500	2.8 (2.06)	140
Moki M 140 RC	13,000	3.9 (2.87)	173	Valley View 20cc	9000	2.5 (1.84)	125
Average	10,600	3.45 (2.54)	169	Average	9500	2.6 (1.91)	130

Table 5. Engines with a displacement of approximately 30 cm^3 [27, 28, 30, 32, 35, 38-40, 42]

Glow engines	Maximum rotational speed [rpm]	Power [KM (kW)]	Specific power [KM/dm^3]	Spark ignitron engines	Maximum rotational speed [rpm]	Power [KM (kW)]	Specific power [KM/dm^3]
Moki M 180 RC	12,000	4.1 (3.02)	138	MVVS 30 IFS/ICU-L	9500	4.1 (3.02)	137
ASP 180 AR	10,000	6.0 (4.41)	201	DLE30	8500	3.7 (2.72)	123
Average	11,000	5.05 (3.71)	170	average	9000	3.9 (2.87)	130

As can be seen from the presented comparisons, glow engines are usually more powerful than spark ignition engines. The maximum speed is similar, although in glow engines it is usually slightly higher than in spark ignition engines. The unit power of glow engines is much greater than those of spark ignition engines. For both types of engines, it decreases as the displacement increases. It should be noted that the comparisons were made for extreme values. A displacement of 15 cm^3 is perfectly normal for glow engines, while for gasoline engines it is almost the lower limit, below which they are usually no longer built. There are only a few types of smaller displacement engines. 20cm^3 glow engines are much rarer than spark ignition engines of this size. 30cm^3 engines are very rarely built as glow engines. Here, the glow engines with the largest value of cylinder capacities and the spark ignition engines for the smallest were compared.

The smallest glow engines have very high maximum rotational speeds. An example would be the ASP AP. 061 A Wasp engine, with a rotational speed of 25,000 rpm. This engine has a displacement of 1 cm^3. Building a spark ignition engine of this size would be possible, but it would be practically pointless, as its applicability would be significantly limited by the considerable weight of the ignition system [11].

5. Engines with push-pull cylinder arrangement

The largest modeling engines are those with a push-pull cylinder arrangement, also known popularly as boxers, Fig. 10. The largest of them exceed the volume of 300 cm^3, reaching a power of 40 HP (approx. 30 kW) or more. Usually they are not smaller than 20–25 cm^3, i.e. about 10 cm^3 per cylinder.

There are several reasons why boxer engines are built. First of all, the capacity of a single cylinder cannot be increased without limit. It would be difficult to fit in the fuselage of an aircraft or in the engine nacelle, and the large and protruding cylinder would be a significant drag in flight [19]. In many models of real airplanes, a single cylinder protruding beyond the fuselage would spoil the silhouette of the model [21], especially in airplanes that also originally had a boxer engine. Engines with a push-pull cylinder arrangement are also characterized by the lowest vibrations during operation. Vibrations from opposite cylinder can cancel out partially.

Due to the fact that boxer engines usually have large displacement volumes, the vast majority of them are spark-ignited. Glow plug ignition engines are also built, usually then also four stroke. Their displacement volumes do not exceed 60 cm^3, i.e. up to 30 cm^3 per cylinder. However, they are quite rare exclusive products, in which the aesthetic values and the sound they produce outweigh the practical ones; similar to the single cylinder four-stroke engines. Pull-push cylinder arrangement engines are usually built for high horsepower, and therefore have a two-stroke cycle.

Fig. 10. Two-stroke gasoline boxer engine RCGF 70cc T [34]

Engines with a push-pull arrangement of cylinders always have at least one pair of cylinders located opposite to each other [4]. The axis of one of them is slightly shifted back to the axis of the other, which is due to the location of the connecting rods on the crankshaft. Each pair has a common crankcase and carburetor. The pistons in a pair simultaneously execute the same power stroke. As a result, the boxer engines are characterized by low vibrations during operation and good balance. Single boxer engines (i.e. with one pair of cylinders) or double boxer engines (i.e. with two pairs of cylinders) are built. Engines with three pairs of cylinders are much less common.

It is difficult to compare engines with a push-pull cylinder arrangement and single cylinder engines, as few designs have similar displacements. Table 6 presents a simplified comparison of several; push-pull (boxer) engines with single-cylinder engines of the same displacement.

Table 6. Comparison of basic indicators for single-cylinder and boxer engines with comparable displacements [27, 28, 30, 32, 35, 38-40, 42]

	20 cm^3		30 cm^3		40 cm^3		60 cm^3	
	Single-cylinder engine	Boxer	Single-cylinder engine	Boxer	Single-cylinder engine	Boxer	Single-cylinder engine	Boxer
Name	RCGF 20cc	RCGF 20ccT	DLE 30	RCGF 30ccT	Zenoah 38 cm	DLE 40	O.S. MAX GT60	DLE 60
Power [KM (kW)]	2.8 (2.06)	2.8 (2.06)	3.7 (2.72)	3.7 (2.72)	2.64 (1.94)	4.8 (3.53)	6.0 (4.41)	7.0 (5.15)
Maximum rotational speed [rpm]	10,500	8600	8500	8500	9500	8500	8000	8500
Mass [g]	798	920	1140	1145	1623	1450	1400	1950

From the list in Table 6, it can be concluded that the maximum rotational speeds of the engines with the push-pull cylinder arrangement and the single-cylinder engines do not differ significantly. But you can see some difference in the achieved power. The boxer engines have a displacement similar to that of single-cylinder engines in the region of 30 cm^3. In engines with a displacement of 40 cm^3, there is already a significant difference in favor of the boxer engines. It should also be noted that the boxer engines are usually heavier than single-cylinder engines [11].

6. Radial engines

Radial engines (Fig. 11) in modeling are used to a fairly limited extent, as they are among the most expensive reciprocating model engines. They are considered the most exclusive. Therefore, they are only built as four-stroke. Radial engines do not match the performance of engines with a similarly sized push-pull cylinder arrangement. Their use is limited primarily to models where appearance matters. An example of this is models of real aircrafts where a real radial engine adds authenticity compared to a single-cylinder or boxer engine, often hidden or integrated into a model of a radial engine.

The smallest of the model radial engines have several dozen cm^3 of displacement, the largest ones can even be up to 400 cm^3. Together with the engines with the push-pull cylinder arrangement, they are among the largest model engines. They can be built with both glow and spark ignition.

In a radial engine, connecting rods with pistons are placed radially around the crankshaft [23]. To avoid resonance of inertia forces, their number is always odd. 3-cylinder, 5-cylinder, 7-cylinder and 9-cylinder engines are built. In "real" aviation, there are engines with a greater number of cylinders, in a double or even quadruple radial system [23]. In modeling, however, motors in a multiple radial system do not exist.

Table 7 presents an illustrative comparison of spark-ignition radial engines with two-stroke boxer engines, also with spark ignition. Due to the relatively small number of model radial engine types produced, the list is simplified, as in the case of boxer engines.

On the basis of the quoted list, the following conclusions can be drawn: above all, radial engines are inferior in all respects to engines with an push-pull cylinder arrangement. Therefore, in terms of performance, the boxer engines are much more profitable as large model engines. Radial engines are always inferior to them in terms of power, usually also in terms of maximum speed and weight.

7. In-line engines

In-line engines (Fig. 12) are rarely used in modeling; there are very few designs of such engines. Two-stroke in-line engines may be an alternative to push-pull cylinder engines in airplanes which require a narrow fuselage for some reason. An example can be models of real airplanes, which in fact also had an in-line engine [21]. The four-stroke in-line engines are more exclusive. By using such engines in models of real aeroplanes, you also get pure sound, more like the original engine used in a real, original airplane.

Fig. 11. 7-cylinder Evolution Radial 260cc engine [37]

Fig. 12. MVVS 116 iL two-cylinder two-stroke in-line engine [31]

Table 7. Comparison of basic indicators for radial and boxer engines with comparable displacements [27, 28, 30, 32, 35, 38-40, 42]

	Ca. 20 cm^3		Ca. 60 cm^3		Ca. 125 cm^3		Ca. 180 cm^3	
	Radial engine	Boxer	Radial engine	Boxer	Radial engine	Boxer	Radial engine	Boxer
Name	Saito FG-19R3	RCGF 20cc TWIN	Saito FG-60R3	DLE60	UMS 5-125cc	DLA 128	UMS 5-180cc	DLA 180
Power [KM(kW)]	1.5 (1.1)	2.8 (2.06)	4.5 (3.31)	7.0 (5.15)	8.0 (5.88)	13.0 (9.56)	10.9 (8.02)	18.5 (13.61)
Maximum rotational speed [rpm]	10,000	8600	7000	8500	6000	6600	5500	6200
Number of cylinders	3	2	3	2	5	4	5	2
Mass [g]	950	920	1850	1950	3900	3780	4700	4130

Table 8. Comparison of basic indicators for in-line and two-stroke boxer engines with comparable displacements [27, 28, 30, 32, 35, 38-40, 42]

	60 cm^3		100 cm^3		116 cm^3	
	In-line engine	Boxer	In-line engine	Boxer	In-line engine	Boxer
Name	Moki G 360 RC	DLE60	DA-100I	DA-100L	DLA160i2	MVVS 116NS IRS
Power [KM (kW)]	7.3 (5.37)	7.0 (5.15)	–	9.8 (7.21)	13.0 (9.56)	11.0 (8.09)
Maximum rotational speed [rpm]	11,000	8500	6800	6800	6500	7500
Number of cylinders	2	2	2	2	2	2
Mass [g]	2450	1950	3450	2800	3744	3310

Table 9. Comparison of basic indicators for in-line and four-stroke boxer engines with comparable displacements [27, 28, 30, 32, 35, 38-40, 42]

	60 cm^3		85 cm^3	
	In-line engine	Boxer	In-line engine	Boxer
Name	ngh GF60i2	Saito FG-61TS	ROTO 85 FSI	ROTO 85 FS-NG
Power [KM (kW)]	6.3 (4.63)	–	–	–
Maximum rotational speed [rpm]	7500	7400	5800	–
Number of cylinders	2	2	2	2
Mass [g]	2940	2090	3000	2790

The pistons in an in-line engine are arranged in a row, one after the other on the crankshaft. “Large” in-line engines may have cylinders arranged in two or more rows. This happens only in the largest engines, which are no longer being built [7]. In modeling engines, however, such a solution has never been used.

The vast majority of in-line miniature aircraft engines for flying models are built with spark ignition. There are only a few designs of compression-ignition in-line engines.

Table 8 shows a simple comparison of the spark ignition two-stroke in-line engines with the push-pull cylinder two-stroke engines, also with spark ignition. The second list in Table 9 concerns four-stroke spark ignition engines.

Due to the small number of produced types of in-line engines, it is difficult to make a meaningful comparison. In addition, rarely used engine types have little data available. However, on the basis of the quoted summaries, several conclusions can be drawn. Inline and boxer engines have similar values of operational indicators. The main difference is the much greater weight of the inline engines. As a result, the use of in-line engines in modeling is unprofitable, except when it is absolutely necessary to keep a narrow fuselage.

8. Summary and conclusions

This article presents a comparative analysis of the construction of model aircraft engines. This required supplementing the information in relation to the last monographs entirely devoted to this issue from forty years ago. During this time, a lot of changes took place in the technique of miniature motors.

Currently, the modeling market is dominated by glow engines and large, more and more perfect spark ignition engines. Self-ignition engines are practically no longer used. Small internal combustion engines have been largely replaced by brushless (induction) electric motors [6]. In the past, even small engines with a displacement of 0.5 cm^3 were produced. Motors with such small capacities turn out to be heavier than electric motors of similar power together with the battery.

Model making is constantly evolving, and there are still many people in Poland who deal with it. Unfortunately, currently no one in Poland produces piston model engines. Although there is a company near Poznań that produces turbojet engines for models, they are not the most popular propulsion for model aircraft and do not fit into the subject of this study.

In the Czech Republic, however, model making is developing very intensively. Particular attention can be paid to excellent Czech gasoline engines from companies such as MVVS or ZDZ. Their products far surpass most other motors.

Bibliography

[1] Czajka J, Wisłocki K. The specificity of attached high-performance engines. Combustion Engines. 2007;131(4): 19-32. https://doi.org/10.19206/CE-117314

[2] Danilewicz L. Silnik benzynowy, część I. Opis konstrukcji i działanie. Księgarnia B. Kotuli, Cieszyn 1930.

[3] Danilewicz L. Silnik benzynowy, część II. Popularny opis konstrukcji silników benzynowych. Księgarnia B. Kotuli, Cieszyn 1931.

[4] Dziulak T, Flach R, Witkowski R. Budujemy silniki do modeli latających. Wydawnictwo Ministerstwa Obrony Narodowej, Warsaw 1954.

[5] Grabowski Ł, Karpiński P, Barański G. Experimental research of two stroke aircraft diesel engine. Combustion Engines. 2019;179(4):75-79. https://doi.org/10.19206/CE-2019-412

[6] Hlebowicz M. ABC lotniczych modeli zdalnie sterowanych. Oficyna Wydawnicza MH, Warsaw 2011.

[7] Kostia T. Silniki lotnicze. Wydawnictwo Ligii Przyjaciół Żołnierza, Warsaw 1953.

[8] Niementowski W. Silniki lotnicze do modeli latających. Universum, Katowice 1946.

[9] Opara R. History and future of turbine aircraft engines. Combustion Engines. 2006;127(4):3-18. https://doi.org/10.19206/CE-117335
[10] Orgelbrand B. Silniki spalinowe. Państwowe Zakłady Wydawnictw Szkolnych/św. Wojciech, Warsaw 1946.
[11] Pełczyński J. Zarys historii i analiza porównawcza modelarskich napędów lotniczych, Diploma thesis. Faculty of Civil Engineering and Transport, Poznań University of Technology, Poznań 2020.
[12] Pełczyński J. Studium projektowe miniaturowego tłokowego silnika do modeli latających, Engineering thesis (supervisor: K. Wisłocki), Faculty of Civil Engineering and Transport, Poznań University of Technology, Poznań 2021.
[13] Schier W. Miniaturowe lotnictwo. Wydawnictwo Komunikacji i Łączności, Warsaw 1962.
[14] Schier W. Miniaturowe silniki spalinowe Wydawnictwo Komunikacji i Łączności, Warsaw 1967.
[15] Schier W. ABC miniaturowego lotnictwa. Wydawnictwo Komunikacji i Łączności, Warsaw 1977.
[16] Schier W. Paliwa i smary w technice miniaturowych silników. Wydawnictwo Komunikacji i Łączności, Warsaw 1980.
[17] Schier W. Popularne mikrosilniki spalinowe. Wydawnictwo Komunikacji i Łączności, Warsaw 1980.
[18] Simons D, Withington T. Historia lotnictwa, od pierwszych dwupłatowców po podbój kosmosu, trans. J. Misiuna, Parragon Books Ltd/Firma Księgarska Jacek Olesiejuk, Ożarów Mazowiecki 2008.
[19] Staszek J. Aerodynamika modeli latających. Wydawnictwo Komunikacji i Łączności, Warsaw 1983.
[20] Towner HJ, Boys H. Scale models aircraft that fly. The Harborough Publishing Company Limited, Bedford 1941.
[21] Whitehead G. Budowa lotniczych makiet RC, trans. M. Hlebowicz. Oficyna Wydawnicza MH, Warsaw 2009.
[22] Wojciechowski J. Jak zbudować kierowany radiem model. Wydawnictwo Komunikacji i Łączności, Warsaw 1962.
[23] Worobiow P. Teoria silników lotniczych. Publishing house of the Ministry of National Defense, Warsaw 1951.
[24] Podręcznik mechanika lotniczego, French-Polish translation (no name of the translator) Ministry of Military Affairs, Warsaw 1928.
[25] http://cmac.synthasite.com (accessed on 1.2.2022)
[26] https://pl.wikipedia.org/wiki/Silnik_samozap%C5%82onowy (accessed on 11.2.2022)
[27] https://www.desertaircraft.com (accessed on 12.2.2022)
[28] https://www.dlengine.com/en (accessed on 16.3.2022)
[29] https://www.modelmotor.pl (accessed on 17.2.2022)
[30] https://mokiengine.com (accessed on 19.2.2022)
[31] https://www.mvvs.cz/en (accessed on 21.1.2022)
[32] https://www.nghengine.com (accessed on 12.2.2022)
[33] https://www.os-engines.co.jp/english (accessed on 19.1.2022)
[34] https://www.rcgfusa.com (accessed on 6.2.2022)
[35] https://www.rotomotor.cz (accessed on 9.2.2022)
[36] https://www.saito-mfg.com/en (accessed on 10.2.2022)
[37] https://www.scorpio-polska.pl (accessed on 25.1.2022)
[38] http://www.supertigre.com/index_html.html (accessed on 5.1.2022)
[39] https://umstech.in (accessed on 26.1.2022)
[40] https://www.valleyviewrc.com (accessed on 24.2.2022)
[41] https://www.wondersofworldaviation.com (accessed on 10.1.2022)
[42] https://www.zenoah.com/int (accessed on 25.2.2022)

Jakub Pełczyński, Eng. – Faculty of Civil and Transport Engineering, Poznan University of Technology, Poland.
e-mail: *jakubpelczynski-1999@wp.pl*

Article citation info:
Majka A, Muszyńska-Pałys J. Analysis of the performance of an aircraft powered by hybrid propulsion. Combustion Engines. 2023; 193(2):45-51. https://doi.org/10.19206/CE-161107

Andrzej MAJKA
Jagoda MUSZYŃSKA-PAŁYS

Combustion Engines
Polish Scientific Society of Combustion Engines

Analysis of the performance of an aircraft powered by hybrid propulsion

ARTICLE INFO

Received: 17 July 2022
Revised: 15 January 2023
Accepted: 10 February 2023
Available online: 16 April 2023

Travel is an inseparable part of human life. It is connected not only with private life but also with business life. People want to travel more, farther and faster. That is why air transport is currently one of the fastest-growing areas of passenger transport, and airlines carry more and more passengers from year to year. Due to the growing negative impact of air transport on the natural environment, research aimed at the development of technologies to reduce the negative impact of air transport is becoming more and more important. One of the possibilities for improving the situation is the use of alternative energy sources, limiting the emission of greenhouse gases into the atmosphere. The paper aimed to analyze the meaningfulness of replacing the classic power unit in a light transport aircraft with a hybrid, combustion-electric power unit. Analyzes were made with the use of simulation methods for the PZL M-28 aircraft.

Key words: *air transport, hybrid power unit, electric aircraft, Small Air Transport (SAT), aircraft emission*

1. Introduction

According to ICAO's annual global statistics, the total number of passengers carried by regular services in 2019 was 4.5 billion, and the number of flights reached 38.3 million [1]. 11.1 million flights were made in the ECAC area. Eurocontrol's forecast for 2027 predicts an increase in the number of flights in the ECAC area by 6 to 17% [2].

Unfortunately, the development of aviation is also associated with an increase in carbon dioxide emissions to the environment. Research shows that aviation is responsible for over 2% of global carbon dioxide emissions [3]. Carbon dioxide is not the only product of fuel combustion. Nitrogen and sulphur oxides as well as soot also have atmospheric altering properties. In 2017, air navigation was responsible for 3.4% of total green-house gas emissions [4]. Although it is not the highest source of greenhouse gas emissions, it is in this sector that the greatest increase in the production of atmospheric pollutants is noticeable. Forecasts suggest that aviation could be responsible for 20.2% of global green-house gas production in 2050 [5].

According to the Intergovernmental Panel on Climate Change (IPCC), global greenhouse gas emissions must fall by around 60% by 2050. Only thanks to this will it be possible to achieve the assumed climate goal [6]. The International Civil Aviation Organisation (ICAO) plans, after 2021, to initiate the Program of Compensation and Reduction of Carbon Dioxide Emissions in International Aviation (CORSIA) [7]. The purpose of this program is to help tackle the problem of the annual increase in CO_2 emissions from international civil aviation. Aircraft operators are tasked with monitoring and reporting the fuel consumption of international flights in order to determine their annual carbon dioxide emissions. Title offsetting is based on emissions trading, not emissions reduction – aircraft operators will have to buy carbon credits from the carbon market [8]. The International Air Transport Association (IATA) is also striving to reduce emissions of harmful gases. Its goal is to achieve net CO_2 emissions of 50% of 2005 emissions by 2050 [7].

The need to reduce the emissions of air transport was a factor that initiated work on the search for new types of power units and new fuels for transport aircraft. Aviation fuels must have certain properties, the most important of which are: excellent combustion properties, low viscosity, high energy density and low freezing point. Among the potential candidates for the fuel of the future aircraft, hydrogen seems to be the ideal solution because it has very good energy properties and is also environmentally friendly. In aviation, hydrogen can be used in two ways – as a replacement for petroleum fuels in large aircraft or in fuel cells to produce electricity. The second solution is intended for smaller transport aircraft. Unfortunately, replacing kerosene with hydrogen requires modification of both the aircraft and the entire aviation fuel production and distribution system. Hydrogen must be stored at low temperature and in well-insulated tanks, 3 times larger in volume than current kerosene fuel tanks [9, 10].

Electricity can also be a fuel substitute. Fully electric power units are popular in the automotive market, especially in cars and ships. Research typically divides electric drives into three main groups:
– fully electric drive,
– turboelectric drive,
– hybrid electric drive.

Unfortunately, only a small number of experimental aircraft use electric propulsion. This is mainly due to insufficiently developed battery technology, which limits the flight range [12]. Research conducted by Safran has shown that a small aircraft needs cells with a specific energy of at least 500 Wh/kg for flight, which is much more than lithium-ion batteries can offer. An alternative for them could be lithium-air batteries with the theoretical specific energy of 11500 Wh/kg [13], unfortunately their lifetime is insufficient when it comes to use in the aviation industry. Lithium-sulfur batteries seem to be the most promising replacement for lithium-ion batteries. It is predicted that by 2030 their specific energy may reach the value of 650 Wh/kg and their service life in the range of 1500–2500 cycles [11].

Nevertheless, in Norway it is planned that by 2040 all short-haul flights will be performed by electric aircraft [22].

The situation is a bit different in the case of a hybrid-electric aircraft, where the weight of the load carriers is smaller. On the basis of research by Geiß and VoitNitschmann, it was found that hybrid-electric general aviation aeroplanes, designed for short-range missions, are able to use less energy than conventional aircraft [14]. Airbus, in collaboration with Siemens and Rolls-Royce, proposed the creation of a hybrid airliner. Their design, called the E-Fan X, involved replacing one of the four jet engines with an electric motor [15]. Unfortunately, in 2020, a year before the first flight of the pioneering machine, the companies announced the end of the demonstration program.

The solution that can revolutionize the aviation industry is the use of fuel cell (FC) technology and a hybrid energy storage system (HESS). Fuel cells are a quiet and clean source, and additionally, the energy density of hydrogen tanks is definitely higher than in batteries [20]. Unfortunately, the power density of fuel cells is insufficient. Battery energy storages are characterized by high energy conversion efficiency (nearly 85%), high response speed and high power density (output current up to 5C) [21]. Combining fuel cells with a hybrid energy storage system can improve the mileage, dynamics and economy of vehicles. Considering the above advantages, such connections may have a promising future in aviation applications.

2. Methodology

The concept of hybrid propulsion in aviation is at a low level of technological maturity. Currently, research and development works are carried out on the development of the concept of using hybrid drives. They are supported by experimental tests carried out with the use of stationary laboratory test stands or with the use of light unmanned aircraft or motor gliders. Currently, it is not possible to conduct experimental research with the use of light, real-size transport aircraft. For this reason, the basic research method used in research on hybrid power units in aviation is the computer simulation method. It requires building, verification and validation of mathematical models, selection of appropriate tools and research methods as well as methods for analysing the obtained results.

Research problem: currently available technological solutions do not allow passenger flights with hybrid-powered planes. The main limitation is the selection of the electric motor, batteries needed to power it and a less powerful internal combustion engine so that the take-off weight (estimated) of the aircraft does not exceed its maximum take-off weight.

Hypothesis: the optimal distribution of power between the internal combustion engine and the electric motor, which together form a hybrid propulsion, can allow to fly a satisfactory distance.

Objectives: the main objective of the study is to select the components of a hybrid drive in such a way that it can replace the internal combustion drive powering the PZL M28 class aircraft, which consists of two PT6A-65B engines.

Research methods: the study used the computer simulation method. The MATLAB Simulink program was used to carry out the simulation.

General research plan:

1. Building and verification of needed mathematical models
2. Case study
3. Analysis of the obtained results
4. Analysis of the impact of new technologies on aircraft performance

3. Models definition

A hybrid drive is a combination of at least two types of drives for moving one device. A Hybrid Electric Drive (HEP) is a combination of two or more energy sources, at least one of which is electrical. Of the many types of hybrid electric drives available on the market, the most popular is the series and parallel connection of an electric motor with a combustion engine. Figure 1 shows a schematic of the hybrid drive that served as the starting point for creating the mathematical model.

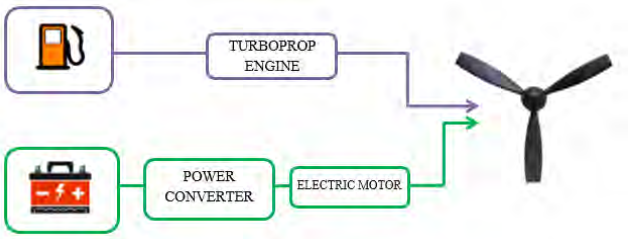

Fig. 1. Diagram of a hybrid drive

The analyzed mathematical model includes the following assumptions: the plane is not affected by any external forces, the plane is treated as a material point, and the flight takes place in the atmosphere with the parameters of a standard atmosphere.

It was assumed that the aerodynamic characteristics of an aircraft with a hybrid propulsion did not change compared to an aircraft with a traditional propulsion. The classical approximation of the aerodynamic characteristics in the aerodynamic polar, which is a square approximation of the drag coefficient as a function of the lift coefficient, was used. The minimum drag coefficient was estimated at 0.028 and the Oswald efficiency factor at 0.8.

The take-off weight of an airplane consists of the weight of the empty airplane, engines weight, fuel weight, weight of crew, batteries weight as well as the weight of passengers and their baggage. Therefore, the formula for the take-off weight of an airplane is as follows:

$$m_{to} = m_{empty} + m_{cr} + m_{pax} + m_{bag} + m_{en} + m_{fuel} + m_{bat} \quad (1)$$

The only constant value in this equation is the weight of the empty aircraft (m_{empty}), but it varies depending on the airframe model chosen. The weight of the crew (2) depends on the number of its members (n_{cr}):

$$m_{cr} = 85\, n_{cr} \quad (2)$$

Weight of passengers (3) and baggage (4) are closely related to number of passengers (n_{pax})

$$m_{pax} = 85\ n_{pax} \tag{3}$$

$$m_{bag} = 20\ n_{pax} \tag{4}$$

The weight of electric and turboprop motors depends on three variables. The first one is the power of the motors they have to replace (P). The second variable is power-to-weight ratio of the electric motor (PWR_e) and power-to-weight ratio for turboprop engine (PWR_t). The third variable is the power share between electric motors and turboprop engines. Depending on the selected variant, it will vary from 0% to 100%. So if electric motors will be responsible for x% of the total power needed, then turboprop engines will be responsible for (100–x)% of the power. Taking into account all variables, the weight of the engines (5) can be calculated from the following formula that takes into account the assumed power split between the electric and the turboprop engine:

$$m_{en} = \frac{x\%\cdot P}{PWR_e} + \frac{(100-x)\%\cdot P}{PWR_t} \tag{5}$$

The weight of fuel, as well as weight of engines, depends on the power share between the electric motors and turboprop engines, but also on the flight distance (s), flight speed (V) and the specific fuel consumption (SFC). The created model analyzes only a horizontal flight at a constant altitude with a constant speed. Additionally, it does not take into account the change in fuel weight during the flight to compensate for the first assumption, a 20% fuel reserve is made, and then to compensate for the second assumption, the weight of the fuel is averaged by dividing it in half. Taking into account all variables, the fuel weight can be calculated from the following formula which only considers the fuel consumed by the turboprop engine for the assumed power split:

$$m_{fuel} = \frac{1.2\cdot\left(\frac{s}{V}\cdot SFC\cdot*(100-x)\%\cdot P\right)}{2} \tag{6}$$

The weight of batteries largely depends on the selected battery type and its specific energy (E_{wb}), but it is also dependent on the efficiency of the electric motor (η_e), flight distance (s) and flight speed (V). As in the case of fuel weight, a reserve of 20% is taken to compensate for the lack of calculations for the take-off, climb and landing phases. Therefore, the weight of the battery can be calculated from the formula which takes into account the mass of the battery resulting from the power required of the electric motor for the assumed power split:

$$m_{bat} = 1.2 \cdot \frac{\frac{x\%\cdot P}{\eta_e}\cdot\frac{s}{V}}{E_{w_b}} \tag{7}$$

Using the formulas (2)–(7) and (1) the take-off weight of the airplane can be calculated. The necessary condition that must be met in order for the combustion engine to be replaced with a hybrid propulsion is such that the calculated take-off weight of the airplane cannot be higher than its maximum permissible take-off weight:

$$m_{to} \leq MTOM \tag{8}$$

The formulas presented above were used to create a computer simulation model in the MATLAB Simulink. The diagram of the above-mentioned model is presented in Fig. 2.

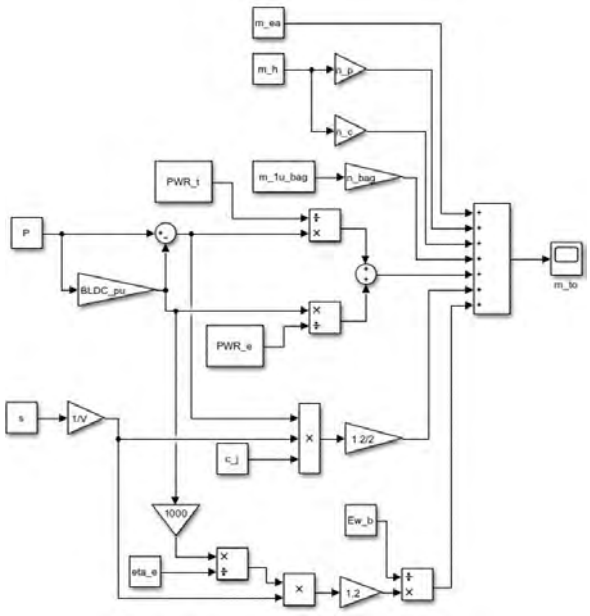

Fig. 2. Simulation model

4. Case study

Computer simulation in MATLAB Simulink has been performed for the PZL M28 class aircraft powered by two PT6A-65B turboprop engines from Pratt&Whitney Canada with a total power of P = 1640 kW. The crew of the selected aircraft consists of 3 people. Despite the fact that the maximum permissible number of passengers is 19, the research assumed that there would be 10 people on board. As part of the research carried out for the purposes of this article, three variants of the percentage power share into electric motors and turboprops are analyzed. Variant „A" assumes that 25% of the power will come from electric motors and 75% from turboprop engines. In variant „B" an equal division of 50% was assumed. Variant „C", on the other hand, assumes that 75% of the power will be generated by electric motors and 25% by turboprops. The weight of empty airplane is equal to m_{empty} = 3654 kg.

In order to be able to count the weight of electric motors and turboprop engines for consecutive variants, it is necessary to know the PWR_e and the PWR_t. There are various types of electric motors available on the market, but due to the reliability and high specific power values, the best choice is the high power density brushless motor. The power-to-weight ratio of the selected type of electric motor is [16]:

$$PWR_e = 2.68\ \frac{kW}{kg} \tag{9}$$

The power-to-weight ratio of the turboprop engine was calculated with the use of generally available data concerning the turboprop engines available on the market. It is:

$$PWR_t = 3.64\ \frac{kW}{kg} \tag{10}$$

For the calculation purposes, it was assumed that the speed of the aircraft will be V = 270 km/h, and the flight

distance s = 80 km. The SFC was calculated on the basis of data from several different turboprop engines. It is:

$$\mathrm{SFC} = 0.328\,\frac{\mathrm{kg}}{\mathrm{kWh}} \tag{11}$$

A lithium-ion battery was selected to power the electric motor, the specific energy of which is [17]:

$$\mathrm{E_{w_b}} = 250\,\frac{\mathrm{Wh}}{\mathrm{kg}} \tag{12}$$

The efficiency of the electric motor was assumed to be η_e = 0.95. The necessary condition that must be met in order for the combustion engine to be replaced with a hybrid propulsion is such that the calculated take-off weight of the aircraft cannot be greater than its maximum take-off weight. The maximum take-off weight of the PZL M28 is:

$$\mathrm{MTOM} = 7500\ \mathrm{kg} \tag{13}$$

Calculations were made using the simulation model created and the data collected above concerning the discussed case. The obtained results are presented in Table 1.

Table 1. Calculation results

Symbol		Value
m_{empty}		3654 kg
m_{cr}		255 kg
m_{pax}		859 kg
m_{bag}		200 kg
variant „A”	m_{en}	491 kg
variant „B”		531 kg
variant „C”		572 kg
variant „A”	m_{fuel}	71.7 kg
variant „B”		47.8 kg
variant „C”		23.9 kg
variant „A”	m_{bat}	613.8 kg
variant „B”		1227.6 kg
variant „C”		1841.4 kg
variant „A”	m_{to}	6135.5 kg
variant „B”		6765.7 kg
variant „C”		7395.9 kg

5. Results and discussion

5.1. Dependence of take-off weight on flight distance for different power splits

Figure 3 shows the dependence of the airplane take-off weight on the flight distance. The calculations were carried out assuming that there are 3 crew members and 10 passengers with baggage on board, and the cruising speed of the plane is 270 km/h.

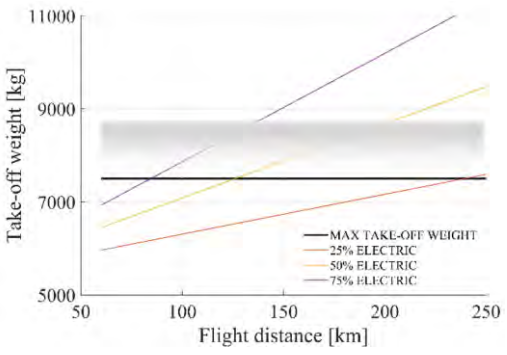

Fig. 3. Graph of dependence of take-off weight on flight distance for different power share

The chart shows that an airplane powered in 25% by electric motors and 75% by turboprop engines can fly the greatest distance. This distance is 239 km, which is about 16% of the maximum distance that the PZL-M28 can travel. The aircraft powered in 50% by electric engines and 50% by turboprop engines can fly only 126 km. Increasing the share of electric motors to 75% will reduce the flight distance to 84 km.

5.2. Dependence of take-off weight on flight distance for different number of passengers

Figures 4–6 show the dependence of the airplane take-off weight on the flight distance for a different number of passengers taken on board for three variants of the power splits into electric motors and turboprop engines. In each of the following cases, the plane is flying at a speed of 270 km/h and there are three crew members on board.

The number assigned to a specific line in the graphs represents the number of passengers taken on board. The maximum take-off weight of an airplane is a limit that cannot be exceeded with the specific number of passengers on board. This means that everything on the graphs above the black line representing the maximum take-off weight of the airplane does not meet the necessary condition and must be discarded.

A. power share – 25% electric motor 75% turboprop engine

Figure 4 shows the dependence of the airplane take-off weight on the flight distance for a different number of passengers for variant "A". It is clear that the longest flight can be with one passenger on board, although even in this case it will not be possible to travel a route longer than 375 km.

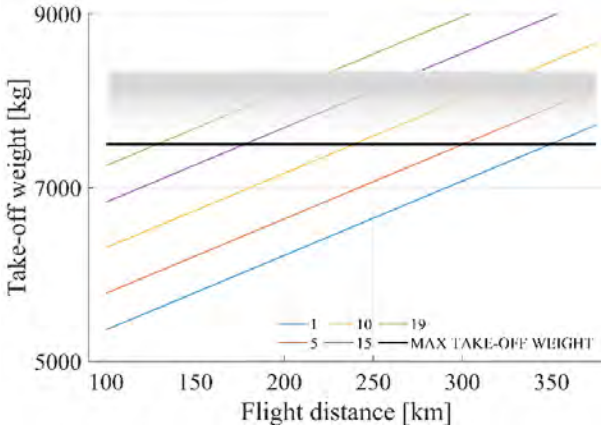

Fig. 4. Graph of the dependence of take-off weight on the flight distance for a different number of passengers– variant „A”

B. power share – 50% electric motor 50% turboprop engine

Figure 5 shows the dependence of the airplane take-off weight on the flight distance for a different number of passengers for variant „B”. Increasing the consumption of power from electric motors is associated with reducing the distance that the plane can fly. Taking 19 passengers on board, the plane can fly no longer than 67 km.

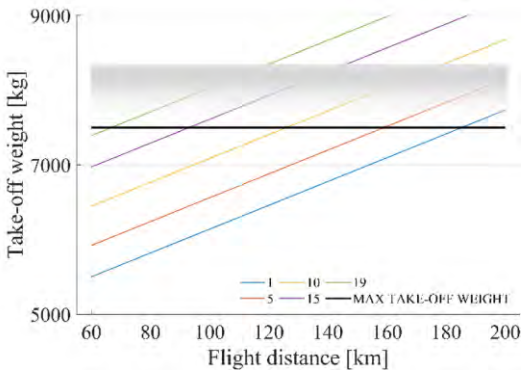

Fig. 5. Graph of the dependence of take-off weight on the flight distance for a different number of passengers– variant „B"

C. power share – 75% electric motor 25% turboprop engine

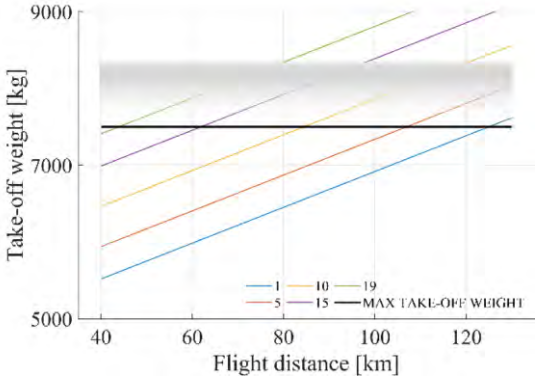

Fig. 6. Graph of the dependence of take-off weight on the flight distance for a different number of passengers– variant „C"

Figure 6 shows the dependence of the airplane take-off weight on the flight distance for a different number of passengers for variant „C". Where most of the power comes from electric motors, an airplane with one passenger can fly over 125 km. If there are 15 passengers on board, the distance drops to about 60 km.

6. The impact of new technologies

The main factor that inhibits the growth of interest in airplanes powered by fully electric or hybrid engines is the low specific energy of the battery and the insufficiently high power-to-weight ratio for the electric motor. This chapter focuses on the analysis of the dependence of the airplane take-off weight on the flight distance for three different percentage power splits, assuming that the lithium-ion battery was replaced with a lithium-air battery with specific energy:

$$E_{w_b} = 11{,}680\,\frac{Wh}{kg} \tag{14}$$

and that the power-to-weight ratio for the electric motor is:

$$PWR_e = 5\,\frac{kW}{kg} \tag{15}$$

Figure 7 consists of 3 graphs and shows the dependence of the airplane take-off weight on the flight distance at three different power splits. It was assumed that there are 3 crew members and 10 passengers with their baggage on board, and the cruising speed of the plane is 270 km/h. Calculations were made for the following four variants:

- Variant I
  - $PWR_e = 2.86\,\frac{kW}{kg}$
  - lithium-ion battery, $E_{w_b} = 250\,\frac{Wh}{kg}$
- Variant II
  - $PWR_e = 5\,\frac{kW}{kg}$
  - lithium-ion battery, $E_{w_b} = 250\,\frac{Wh}{kg}$
- Variant III
  - $PWR_e = 2.86\,\frac{kW}{kg}$
  - lithium-air battery, $E_{w_b} = 11{,}680\,\frac{Wh}{kg}$
- Variant IV
  - $PWR_e = 5\,\frac{kW}{kg}$
  - lithium-air battery, $E_{w_b} = 11{,}680\,\frac{Wh}{kg}$

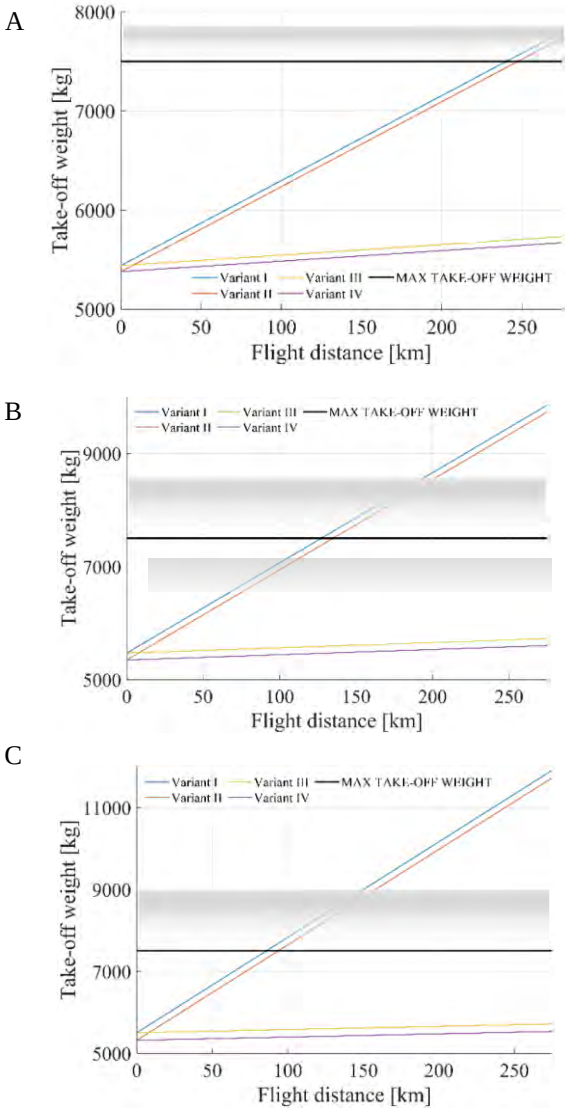

Fig. 7. Graph of the dependence of the take-off weight on the flight distance for the power split of: A – 25% from electric motors and 75% from turboprop engines, B – 50% from electric motors and 50% from turboprop engines, C – 75% from electric motors and 25% from turboprop engines

The graphs show that changing the electric motor, whose power-to-weight ratio is 2.86 kW/kg, to one whose ratio is 5 kW/kg, will slightly extend the distance that the plane can fly. The comparison of these distances is shown in Fig. 8. The biggest difference in distance that can be travelled when a lithium-ion battery is changed to an air-lithium battery. In these two cases, for the first time, increasing the share of power from electric motors increases the distance that the plane can fly. It is enough for electric motors to be responsible for 50% of the required power so that the maximum distance that the PZL-M28 would be able to fly exceeds the maximum distance of this aircraft according to the Flight Manual.

Table 2. Maximum distance for maximum take-off weight for different variants and different power share

25% electric, 75% turboprop	
variant	Distance [km]
I	169
II	176
III	1358
IV	1434
50% electric, 50% turboprop	
variant	Distance [km]
I	88
II	97
III	1522
IV	1676
75% electric, 25% turboprop	
variant	Distance [km]
I	59
II	69
III	1730
IV	1999

Summary

The calculations which was made as part of this study were to prove that it is possible to replace the internal combustion engine of a small passenger aircraft with a hybrid electric drive.

The conducted analyzes are intended to demonstrate the reasonableness of the development of hybrid power units in small transport aviation. Technological progress in the field of batteries will make the analyzed solutions even more attractive from the point of view of reducing transport aircraft emissions. They may also justify undertaking further research and experimental work, which will be characterized by higher costs and workload.

The presented results complement the research conducted so far, which mainly focuses on fully electric aircraft. The analyzed solution seems to be more attractive, due to the level of technological development of electric drives, concerning commuter-class transport aircraft.

The performed calculations, taking into account the adopted assumptions, showed that such a replacement is possible. However, it should be remembered that the change of the type of propulsion may, to some extent, limit the throughput of the aircraft or the number of passengers taken on board will have to be reduced, for example, the aircraft powered in 25% by turboprop engines and in 75% by electric motors with 10 passengers on board is able to overcome only 84 km, while when there are only 3 passengers on board, this distance increases by 36.9% to 115 km. In the case of an aircraft powered by in 50% by turboprop engines and in 50% by electric motors, the same change in the number of passengers will increase the travel distance by 36.5% from 126 km to 172 km. In the case of an aircraft powered in 75% by turboprop engines and in 25% by electric motors, the increase will be 35.9% with an increase in distance from 239 km to 325 km. This means that regardless of the percentage power share into electric motors and turboprops, a change in the number of passengers has the same effect on extending or shortening the travel distance.

An aircraft powered to a greater degree of turboprop engines can travel more than twice as far as its counterpart powered by more green energy. This is due to the lack of a battery with the appropriate specific energy.

Nevertheless, the research carried out for the air-lithium battery clearly shows that with the development of the battery, hybrid drives can be used more and more in the aviation industry. The calculations show that when the lithium-ion battery is replaced with a lithium-air battery, the aircraft powered as described above with 10 passengers on board will be able to cover 1730 km, which is more than the PZL M28 powered only by internal combustion engines can overcome.

Nomenclature

Ewb specific energy [Wh/kg]
m_{to} takeoff weight [kg]
m_{empty} aircraft empty weight [kg]
m_{cru} crew weight [kg]
m_{pax} passengers weight [kg]
m_{bag} baggage weight [kg]
m_{en} engines weight [kg]
m_{fuel} fuel weight [kg]
m_{bat} battery weight [kg]
MTOM maximum teakoff mass [kg]
n_{cru} number of crew
n_{pax} number of passengers
P power of the engine [kW]
PWR_e power-to-weight ratio of the electric motor [kW/kg]
PWR_t power-to-weight ratio for turboprop engine [kW/kg]
V speed of flight [km/h]
η_e efficiency of the electric motor

Bibliography

[1] International Civil Aviation Organization (ICAO). ICAO website. https://www.icao.int (accessed on 06.2022).
[2] Eurocontrol Forecast Update 2021-2027, European Flight Movements and Service Units – Three Scenarios for Recovery from COVID-19. Eurocontrol edition. (accessed on 15.10.2021). https://www.eurocontrol.int/sites/default/files/2021-10/eurocontrol-7-year-forecast-2021-2027.pdf

[3] Pornet C, Isikveren AT. Conceptual design of hybrid-electric transport aircraft. Prog Aerosp Sci. 2015;79:114-135. https://doi.org/10.1016/j.paerosci.2015.09.002
[4] Guillot JD. Emissions from planes and ships: facts and figures. Directorate General for Communication, European Parliament. 2022. https://www.europarl.europa.eu
[5] Staples MD, Malina R, Suresh P, Hileman JI, Barrett SRH. Aviation CO_2 emissions reductions from the use of alternative jet fuels. Energ Policy. 2018;114:342-354. https://doi.org/10.1016/j.enpol.2017.12.007
[6] Larsson J, Kamb A, Nässén J, Åkerman J. Measuring greenhouse gas emissions from international air travel of a country's residents methodological development and application for Sweden. Environ Impact Assess. 2018;72:137-144. https://doi.org/10.1016/j.eiar.2018.05.013
[7] Chao H, Agusdinata DB, Delaurentis D, Stechel EB. Carbon offsetting and reduction scheme with sustainable aviation fuel options: Fleet-level carbon emissions impacts for U.S. airlines. Transportation Res D-TR E. 2019;75:42-56. https://doi.org/10.1016/j.trd.2019.08.015
[8] Strouhal M. Corsia – Carbon Offsetting and Reduction Scheme for International Aviation. Magazine of Aviation Development. 2020;8(1):23-28. https://doi.org/10.14311/MAD.2020.01.03
[9] Saynor R, Bauen A, Leach M. The potential for renewable energy sources in aviation. Imperial College Centre for Energy Policy and Technology. 2003. http://www.iccept.ic.ac.uk
[10] Baroutaji A, Wilberforce T, Ramadan M, Olabi AG. Comprehensive investigation on hydrogen and fuel cell technology in the aviation and aerospace sectors. Renew Sust Energ Rev. 2019;106:31-40. https://doi.org/10.1016/j.rser.2019.02.022
[11] Gogolák L, Csikós S, Molnár T, Szuchy P, Bíró I, Sárosi J. Possibilities of optimizing fuel consumption in hybrid and electronic airplanes. The Analecta Technica Szegedinensia. 2019;13(2):65-76. https://doi.org/10.14232/analecta.2019.2.65-76
[12] Finger DF, Bil C, Braun C. Initial sizing methodology for hybrid-electric general aviation aircraft. J Aircraft. 2020; 57(2):245-255. https://doi.org/10.2514/1.C035428
[13] Voskuijl M, Van Bogaert J, Rao AG. Analysis and design of hybrid electric regional turboprop aircraft. CEAS Aeronautical Journal. 2018;9(1):15-25. https://doi.org/10.1007/s13272-017-0272-1
[14] Finger DF, Braun C, Bil C. Impact of battery performance on the initial sizing of hybrid-electric general aviation aircraft. J Aerospace Eng. 2020;33(3):04020007. https://doi.org/10.1061/(ASCE)AS.1943-5525.0001113
[15] Drop N. Airbus' electrically powered aircraft as an answer to the European Union's low-carbon policy. Transport Economics and Logistics. 2019;81:81-89. http://dx.doi.org/10.26881/etil.2019.81.07
[16] Sudha B, Vadde A, Sachin S. A review: high power density motors for electric vehicles. J Phys Conf Ser. 2020;1706(1). https://doi.org/10.1088/1742-6596/1706/1/012057
[17] Schäfer AW, Barrett SRH, Doyme K, Dray LM, Gnadt AR, Self R et al. Technological, economic and environmental prospects of all-electric aircraft. Nature Energy. 2019;4(2): 160-166. https://doi.org/10.1038/s41560-018-0294-x
[18] Easa Type-Certificate Data Sheet. PZL M28. EASA publication. 2014. https://www.easa.europa.eu
[19] Jaroszyński L. Akumulatory litowe w pojazdach elektrycznych. Przegląd Elektrotechniczny. 2011;87(8):280-284. ISSN 0033-2097.
[20] Li S, Gu C, Xu M, Li J, Zhao P, Cheng S. Optimal power system design and energy management for more electric aircrafts. J Power Sources. 2021;512:230473. https://doi.org/10.1016/j.jpowsour.2021.230473
[21] Li S, Gu C, Zhao P, Cheng S. A novel hybrid propulsion system configuration and power distribution strategy for light electric aircraft. Energ Convers Manage. 2021;238: 114171. https://doi.org/10.1016/j.enconman.2021.114171
[22] Fuć P, Kardach M, Maciejewska M. Analysis of the availability of aircrafts with alternative propulsions. Combustion Engines. 2019;179(4):220-225. https://doi.org/10.19206/CE-2019-437

Prof. Andrzej Majka, DSc., DEng. – Faculty of Mechanical Engineering and Aeronautics, Rzeszow University of Technology, Poland.
e-mail: *andrzej.majka@prz.edu.pl*

Jagoda Muszyńska-Pałys, MEng. – Faculty of Mechanical Engineering and Aeronautics, Rzeszow University of Technology, Poland.
e-mail: *j.muszynska@prz.edu.pl*

Article citation info:
Hamid M, Wesołowski M. Waste-to-energy technologies as the future of internal combustion engines. Combustion Engines. 2023; 193(2):52-63. https://doi.org/10.19206/CE-161650

Mohamad HAMID
Mateusz WESOŁOWSKI

Combustion Engines
Polish Scientific Society of Combustion Engines

Waste-to-energy technologies as the future of internal combustion engines

ARTICLE INFO

Received: 13 January 2023
Revised: 14 February 2023
Accepted: 24 February 2023
Available online: 11 March 2023

Syngas has a promising future as alternative to petroleum products and as a fuel for combustion engines. This study provides an overview on the feasibility of using syngas to power internal combustion engines. It presents technological process solutions for producing syngas toward minimizing the formation of tars as the most undesirable component for engine applications.. The combustion process characteristic of syngas composition has been tackled including critical criteria such as the flammability limit, ignition delay, laminar velocity, turbulent velocity, and the subsequent challenges in determining a numerical methods that best matches the experimental datas. The syngas usage as alternative resource, while tackling the uncertainty issue of its composition, for Compression Ignition (CI) and Spark Ignition (SI) with the emission and performance effectiveness has been studied as well. The results of the review showed that syngas can be a viable alternative for some stationary applications, such as advanced integrated systems (ICCG), but its application is, however, relatively limited, for example as a secondary fuel in engines (CI) for automotive applications. However, significant discrepancies between numerical (simulation) and experimental results have been noted. This suggests that there are many scientific and experimental challenges in the area of syngas combustion processes in internal combustion engines. However, given the potential of this group of fuels, especially in the face of the energy crisis, this research is highly desirable and has a significant application perspective.

Key words: *syngas, gasification, physicochemical properties, applications*

1. Introduction

The fast depletion of fossil fuels has resifted the focus towards alternative renewable fuel resources, such as syngas which is produced from biomass or waste [1]. Although current figures show that only 0.5% of syngas is produced from renewable and waste [2], production rate has increased significantly in the recent years with a great prospect for the future as it is expected to grow at 9.3% from 2022 to 2029, reaching nearly US$ 376.7 Bn [3]. This positive trend in the syngas interest was not followed closely by the literature in the past 10 years. Thus there was few researches has been conducted on syngas, and the recently published review papers were mainly referencing more than 10 years old results obtained. In our research we focused on presenting up-to-date results and consolidate the work that has been done by pervious research studies concerning specific topics such as the discrepancy between numerical and experimental results, toward drawing conclusion about the current state of the art in the syngas production and usage.

Currently there is globally almost 2.24 billon tones of municipal waste, and 140 billion metric tons of biomass wastes are generated every year from agriculture, which creates many challenges both on managemental and environmental aspects. As most of the waste goes to landfill, utilizing that waste to produce syngas would produce less emissions than otherwise if would go through incineration while reducing the landscapes allocated for landfills [2].

Gasification and pyrolysis are the main process by which the conversion of the hydrocarbons into syngas is been done, although as efficacy and reliability gasification process standout among all other conversion processes.

Gasification is a thermochemical process where carbonaceous materials conversion into gases occur at elevated temperatures above 600°C. It is done by breaking the carbon bonds and adding hydrogen to the gaseous product [4]. The conversion process occurs when solid carbon fuel reacts with a gasifying agent such as air, oxygen, water vapor or mixtures of air and water vapor.

In case oxygen or water vapor is used in the gasifying process the product is called medium calorific value gas, or as known simply syngas, which typically having a range of 10 to 20 MJ/Nm^3 heating value. The other name given to the gas product in case of using air as gasifying agent is producer gas, or lower caloric value gas which typically have a heating value range between 4 to 6 MJ/Nm^3 [5].

It produces hydrogen (H_2) and carbon monoxide (CO) mainly, and other components such CO_2, H_2O, tar, hydrogen sulfide, water vapor, hydrocarbon such as methane, and other trace species [6].

The inconsistency in the products of gasification process of waste to produce syngas is particularly difficult to control due to the varying source of the feedstock. Though many solutions are available at the industry such as closely monitoring by infrared sensors the gas composition during the conversion process [7].

The gasification process itself involves multiple complex reaction processes which also contributes to the varying composition of syngas. The generalized and specific chemical reactions involved is presented in the Table 1 [8].

Table 1. Gasification chemical reactions [9]

General chemical reaction:	Hydrocarbon feedstock → CO(g) + H_2(g) + CO_2 (g)
Char-oxygen reaction	$2C + O_2 \rightleftharpoons 2CO$
Boudouard	$C + CO_2 \rightleftharpoons 2CO$
Steam gasification/water-gas	$C + H_2O \rightleftharpoons CO + H_2$
Methanation	$C + 2H_2 \rightleftharpoons CH_4$
Shift reaction	$H_2O \rightleftharpoons H_2 + CO_2$

Other factors that affect the production of syngas from waste feedstock are residence time, temperature, pressure and the atmosphere during the gasification process. All above factors along with the varying feedstock composition and the complex gasification chemical process can be handled using many solutions that will be tackled in the following chapter.

The syngas can be use as intermediary to produce other chemicals, or for direct usage as fuel, the latter is our topic of concern. From integrated gasification combined cycle (IGCC) to internal combust engines (ICE) there is a wide range of application for syngas.

The technology of using syngas from biomass is relatively old, during WWII when there was shortage of gasoline, wood gas vehicles reached almost 7 million vehicles with countries like Sweden, Germany France and Denmark were on top of producers list. The technology was disregarded as there was a boom in gasoline availability. Strict environmental regulation and phasing out the use of fossil fuels revived the interest in synthetic gases [10–12].

In power generation/syngas has a very promising futures some studies suggest that typical incinerators of 1 tone of waste can produce 530 kWh, gasification system with integrated generation can produce from 650 kWh up to 1100 kWh [13].

2. Waste to syngas production solutions

Different types of gasification process can be achieved depend on the design and intended quality and content of the product. Since feedstocks vary significantly thus the product outcome, it's of a high importance to select the right gasifier to insure a consistency of the gasification product with minimal contamination and reduced tar output values.

The varying composition of the waste feedstock and the chemical process complexity of gasification presented challenges that is been overcame by the introduction of multiple solutions that would ensure the consistency of the gasification products and removal of impurities such as tar, Sulphur and particulate matter, etc.)

Tar is a condensable hydrocarbon formed of single and multiple aromatics compounds along with polycyclic aromatic hydrocarbons. The challenge of removing tar from the syngas product is one of the main challenges that need to be overcome in order to make the valorization technologies such as syngas production through gasification economically feasible [14].

The tar can lead to engine fouling and catalyst deactivation due to polymerization characteristics and condensation [15].

A number of solutions has been proposed in order to reduce the tar content during the gasification process. For instance, injecting CO_2 during gasification process can reduce the tar formation resulting in close to zero CO_2 process [16].

Typically, there is four types of gasifiers: updraft and downdraft fixed bed, bubbling or circulating fluidized bed reactors. Figure 1 show the principle upon which the four gasifiers work.

Each type of gasifiers has its own advantages and disadvantages which will be presented. Along with the results of some studies that tackled the issue of tar in syngas production from biomass waste and the solution it was provided for each gasifier type.

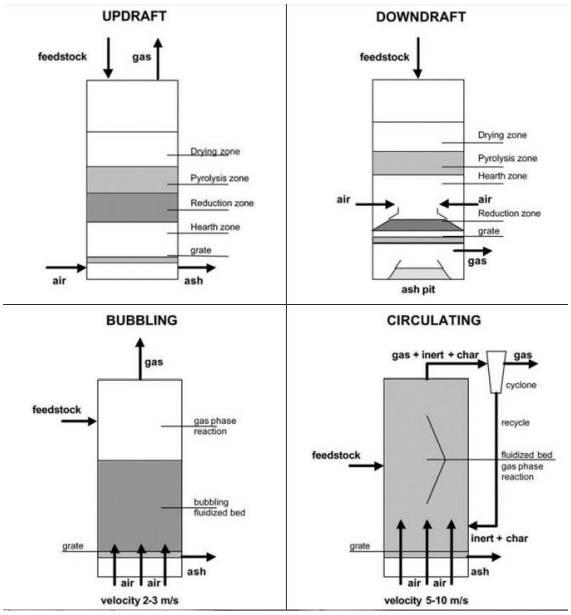

Fig. 1. Four gasifier operation principles, fixed bed (updraft, down draft) and Fluidized bed (circulation, bubbling) [14]

2.1. Fixed-bed gasifier

As for fixed-bed (updraft, downdraft) gasifier the challenge in maintaining the desired temperature and mixture composition in the process area which can lead to inconsistency in the products.

2.1.1. Updraft type

The particle size range of feedstocks for updraft type range between 2 to 50 mm under pressure range 0.15 to 2.45 MPa, with a residence time 15 to 30 min. The long residency time result in low efficiency and throughput and high tar content, thus it is not recommended for internal combustion engines instead its more suitable for heat generation. In one of the studies which used wood chips for an 8.5 MWh updraft gasifier to produce syngas, and without modifying the normal operation conditions of the gasifier or the properties of the feedstock. It recommended the usage of updraft gasifier when the fuel moisture is 20% with particles that is larger than 6.3 mm, since it would achieve a higher syngas quality and lower tar concentration [17]. Another solution presented in another study where a comparison between an updraft and downdraft type gasifier was conducted to produce syngas out of municipality green waste. It showed that incorporating a circulating cyclone to updraft type yield a higher gas output by 10–15% to downdraft type which is normally have a higher yield and lower tar formation performance. This is mainly due to recirculating the syngas inside the reactor back to the combustion zone which lead to higher rate of thermal decomposition of volatile organic substance, thus reducing tar collection [18].

Another major advantage is the ability of the updraft to handle biomass with high inorganic content with high moisture which is mainly suitable for municipal waste feedstock [19].

2.1.2. Downdraft type

The second type of fixed bed gasifier is the downdraft, where the typical size of feedstock ranges between 1 to 30

cm with moisture content up to 30% and its mostly suitable for high volatile fuel for power generation. It usually suffers from high ash content when compared to the updraft type, but when its compared to updraft type its much suitable for combustion engines since 99.9% of the tar is been removed in the process [19]. In a study that utilized agricultural waste in Scotland using the typically used downdraft gasifier type in a combine gasification with CHP engines for power generation. It tackled the design constraints and optimization of downdraft gasifier to achieve better yield from the gasification process as well as reduction in tar formation. It was found that with a moisture content of less than 10% and an equivalence ratio (Φ) of 0.3–0.35 would yield a higher syngas output efficiency. The equivalence ratio also has favored gasification temperature thus leading to lower tar formation. According to the study the highest heating value was found for barely dust which is the main crop in Scotland and barely screening (6.4 MJ/Nm^3) with tar content circa 2%mole % of produced gas) [20].

2.2. Fluidized bed gasifiers

Fluidized bed gasification main advantage is maintaining the uniformity of temperature in the combustion zone.

2.2.1. Bubbling fluidize gasifier

It has many advantages since it can accept a wide range of particle sizes, Main advantage its high yield with low tar content produced from this type < 1–3 g/Nm^3 and low unconverted carbon, as well as yield a uniform syngas as it also achieves a uniform temperature distribution throughout the reactor between 700 and 1000°C by controlling the air/biomass ratio [19]. In a study that used a bench-scale fluidized bed reactor, and feedstock from biomass waste (switchgrass, pine residues) at operating temperature circa 780°C, equivalence ratio (Φ) = ~0.32. They investigated the effect of the be materials such as sand, Al_2O_3 and CaO on the overall yield of containment, and tar reduction. It was found that the usage of Al_2O_3or CaO has reduced tar production circa 5.8 to 6.5 gtar/kg dry biomass through thermal cracking and oxidation reactions [21].

2.2.2. Circulating fluidized bed gasifier

The gasifier operates at high pressure, this would be ideal for usage of the gas that is require to be compressed in the later stages, such as in applications for gas turbines. It has many advantages in term of the speed by which the reaction occurs, and provide products with high yield, low tar and unconverted carbon. Although there is some technical downfall on the gasifier due to the rapid production rate, which can also be limited by the fuel particles size that determine the speed of the flow and the stability of the production becomes a concern after long operating duration and the bed materials should have strong abrasive materials [22]. In a study that investigated the potential of using a combination of synthetic and mineral catalysts to achieve better syngas yield production and lowering tar was able to achieve promising results. The catalysts used in the gasifier is of an importance factor in increasing the reaction rate at low-temperature, and the conversion of tar into valuable syngas via thermal cracking, steam reforming, and dry reforming.

The synthetic catalysts give better results but the downfall its high cost, while minerals can achieve good results but it could not yield in satisfactory results. The feedstock used in that study was pine sawdust collected from wood treatment plant, feed to a circulating gasifier operating under 750°C to 950°C temperature with the gasification medium was air. At first the experiment compared the reduction percentage of tar by using non-active bed material (silica sand) to a Raw-olivine, the results show a 40.6% reduction using Olivine, and a far much better results were achieved when using synthetic catalysts Fe (5%) in combination with Olivine to reach 81.5% reduction in tar compared to raw-Olivine because of the existence of because of existence of Fe_2O_3, NiO and NiO-Mg [23].

2.2.3. Syngas composition and applications

Understanding the effect of each component in the syngas along with their physicochemical properties on the combustion process in internal combustion engine would facilitate the understanding of the application methods for syngas in the different types of combustion engines.

In the following sections each component role and effect on the combustion process and thus the expected impact on the efficiency of the engine will be tackled. In the next section the specific application of syngas in Compression Ignition (CI), Spark ignition (SI) and homogenous charged compression (HCCI) engines will be discussed.

3. The physicochemical properties of typical syngas

The laminar flame speed and flammability limits are two elements that favor syngas as secondary fuel for internal combustion engines over other fuels such as hydrogen, biogas, methane or fossil fuels. In the following section we shall tackle the main burning characteristics of syngas, better understand the behavior of each component of the syngas effect on the combustion process, and subsequent challenges that arise in modeling this behavior in numerically form that can be generalized.

3.1. The laminar flame velocity

The laminar flame speed is one of the most important properties of the combustion process specially when operating an engine at fuel-lean conditions. The higher values promote for stable operation at lean conditions, and in ultra-lean spark ignition engines when syngas used as secondary fuel [24]. The laminar flame speed serves as basis to turbulent combustion, also contain fundamental information on diffusivity, reactivity, and exothermicity. The propensity of a flame, flashback and blowoff are heavily impacted by the laminar flame speed among other important combustion characteristics such as flame spatial distribution [25].

The importance of laminar flame speed led to various methods in obtaining its measurements, such as constant volume combustion bomb, heat flux method, Bunsen burner and externally heated diverging channel method [26].

There have been multiple tests published in the past about the laminar flame speed of syngas but they only tackle the combustion mixture at stoichiometric or at rich conditions, which is not suitable for modern combustion engines which favor lean-mixture [25].

The same issue could be said about the pervious published works regarding the kinetic schemes. The reaction

model predictions that give numerical predictions of laminar velocities was found to have a lot of discrepancy between the calculated and experimental data [27].

In more recent research that studied the demarcation of reaction effects on laminar burning velocities of diluted syngas–air mixtures. Results showed that using modified Davis mechanism with lower third-body efficiencies can predict accurately laminar burning velocities of mixtures with high dilution of CO_2 and N_2 mixture. As for FFCM-1 showed comparable results at all dilutions except for high dilution of CO_2 circa 70%.

The final outcome of this study showed among other results the effect of dilution of CO_2, N_2 on the burning velocities. Where dilution of CO_2 specially at higher temperatures where N_2 had much less impact on the burning velocity [28].

The pervious study [28] was mainly concerned about tackling the discrepancy of LFS for high temperature and pressure (HTP) applications for Syngas. In another study [29] that tackled the discrepancy in the LFS data provided by literature under Normal Temperature and Pressure (NTP).

The discrepancies from different group of studies were presented in Fig. 2 between the results obtained from the OPF method vs David et al. using CHEMKIN-PREMIX code chemical mechanism for predicting LFS. As it can be seen in the Fig. 2 the discrepancies are very large at very lean and very rich mixtures, and with the discrepancy about 8 percent between equivalence ration (Φ) 1 and 3.

The source of uncertainty has been investigated, and the effect of the initial conditions and equivalence ratio has been presented. The results showed that the mixture preparation had insignificant impact on the measure LFS, such as slight perturbation in equibalance ratio, temperature an pressure. It was concluded that the linear extrapolation is more sensitive to the flame radius range than nonlinear extrapolation, which can strengthen the impact of the flame radius range selected on the uncertainty, in particularly at the very lean or very rich mixtures. The study ended by declaring that there is still a lot effort needed to reduce the uncertainties in measuring LFS [29].

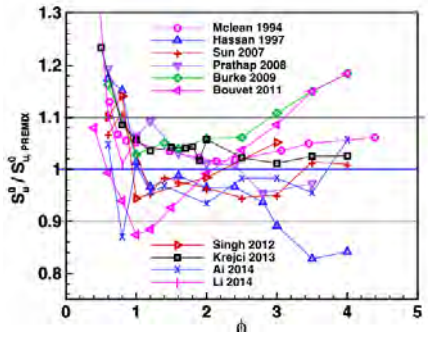

Fig. 2. Deviation of laminar speed measured by different studies in literature from the predicted laminar speed by simulation (PREMIX) based on the mechanism of David et al. for H_2/CO/air (H_2:CO = 50%:50%) at NTP [29]

3.2. Ignition delay time (IDT)

In an effort to solve the same issues of laminar flame velocity discrepancy between the measured and reaction model prediction calculations of IDTs. In addition to the emergence of advanced integrated systems such as ICCG as replacement to coal-fired conventional power plants. This promoted researches to reproduce the experiments using rapid compression machines and shock-tubes at higher temperature and pressures, whereas such data was only available at low temperature and pressured using mostly a shock-tube tube confined to a limitation up to 2.2 bar pressure and 2850 K temperature [30].

Following the effect of Pressure, Temperature and Equivalence ratio, CO, CH_4 on the Ignition Delay Time shall be discussed.

3.3. Pressure and syngas components effects on ignition delay

The influence of pressure on ignition delay was studied on multi-component syngas with and without ammonia having the following. The baseline mixture and the additional components were studied at 3 different pressures 1.6, 12.5, and 32 atm, at equivalence ratio (Φ) equal to 0.5 [31].

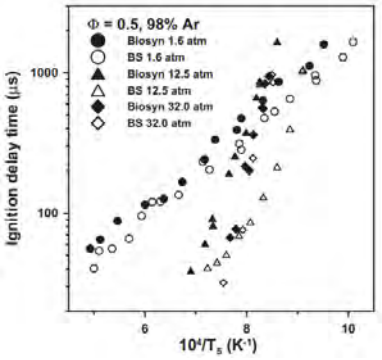

Fig. 3. Effect of the pressure on the ignition delay time [30]

In Fig. 3, a selected fuel composition was presented since the other compositions exhibited similar results, for example BS results where close to (Neat-H_2, BS-H_2O, BS-CO_2) and Biosyn to (BS-CH_4). The result shows an important effect of pressure on ignition delay values between 1.6, 12.5 and 32 atm [31].

At pressure 1.6 atm (Fig. 4) the following has been concluded that neat H_2 and BS (around 15% longer than neat H_2) exhibit similar ignition delay values, while the addition of H_2O to BS only slightly decreased ignition delay. As for temperature below 1550 K the results showed that ignition delay is further increased, compared to BS CH_4.

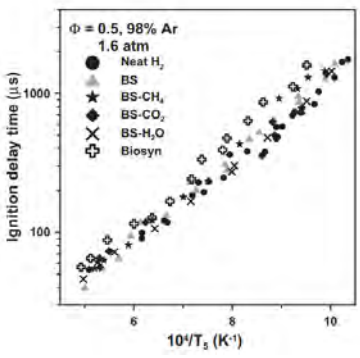

Fig. 4. Effect of the composition on the ignition delay time for a syngas with a H_2/CO ratio set to 1 and at a pressure around 1.6 atm [30]

3.4. Turbulent flame speed (TFS)

The inconsistency in the feedstock and different fuel composition of syngas by which it would replace traditional fuel. It mandates the investigation of all the combustion characteristics, such as TFS which is an important criterion in the combustion process. The high values of laminar flame speed due to high mass diffusivity of H_2 and subsequently lower Lewis number, required different operating conditions for engines to gives the intended performance and emissions of using syngas as alternative fuel. Such as improving the flammability limits, and enhancing the burning velocity and reducing the CO_2 emission [32].

Thus Turbulent flame speed is of high interest just as the LFS. In literature regarding the topic of measuring the TFS of syngas-air mixture focus on investigating the pressure, fuel composition due to concern of inconstancy in the feedstock supply, and obtaining (ST) coloration from experimental data at certain operating conditions and generalize them.

In a study that investigated the TFS of syngas at different compositions of hydrogen volumetric fractions (20%, 50% and 80%), at turbulence intensities of (0 to 3.54 m/s) and pressure (0.5 to 5 bar), and concluded with unified scaling of turbulent burning velocity. The experiment was conducted on spark ignition engine with constant volume, and to create the effect of turbulence inside a regular engine, fan-stirred turbulent combustion chamber was used.

At first the test was conducted under different turbulence intensities and initial pressures where the turbulent flame velocity where determined, secondly the turbulent flame velocity where compared under different hydrogen fraction in the syngas.

The results of the effect of pressure at constant turbulence intensity and vice versa is shown in Fig. 5.

The general understanding that the turbulent burning velocity increased as pressure and intensity increased. This relation is almost linear in case of intensity, but in reality (which is not covered as a range in this study) the turbulent velocity would reach a climax before it would actually start to decrease gradually due to local extinction. As seen in the Fig. 5b the growth becomes slower at higher pressures. This phenomenon is due to laminar flame thickness and Kolmogorov length scale which can be studied further in this reference [33]. In principle as the turbulence intensity and initial pressure increase, the flame surface wrinkles more intensely which leads increase in turbulence stretch and flame intrinsic. Thus, increasing the flame surface area.

The effect of hydrogen fraction in the syngas composition on turbulent flame speed is shown in Fig. 6, where the error bars represent the standard deviation of five loops.

The results show that the global turbulent velocity is more sensitive to hydrogen fraction with the increase in turbulence intensity as shown in (Fig. 6a). The same could be found in relation to the sensitivity of turbulent velocity to the turbulence intensity with the increase of hydrogen fraction. This could be explained due to the fact that the flamelets becomes more wrinkled with higher turbulence intensity, which in turn strengthened the diffusional-thermal instability [34]. As of result the turbulent burning velocity becomes sensitive to the hydrogen fraction in the syngas. The same could be said about the non-equal diffusion which is strengthened with the higher hydrogen fraction. Thus, the turbulent burning velocity will becomes sensitive to the flamelets wrinkling which is in turn dependent on the turbulence intensity.

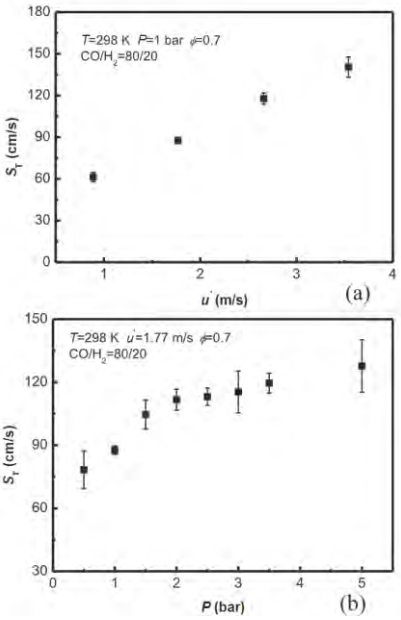

Fig. 5. Global turbulent burning velocity: (a) P = 1 bar under different u'; (b) u' = 1.77 m/s under different P [33]

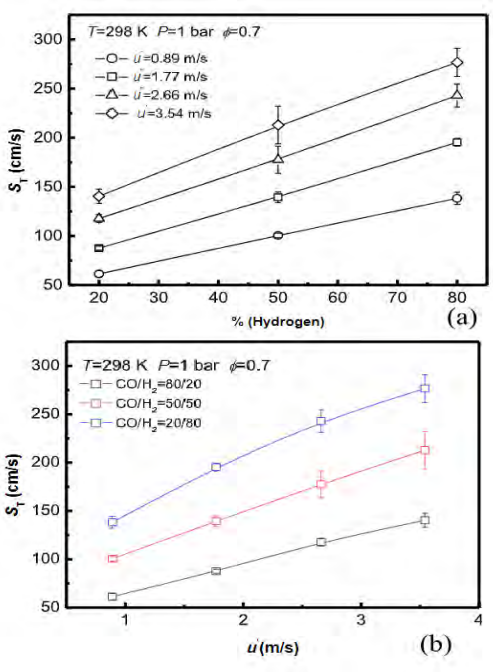

Fig. 6. Global turbulent burning velocity under different hydrogen fractions: (a) x-axis is hydrogen fraction; (b) x-axis is u' [33]

The obtained results match another research conducted to study the effect of higher hydrogen proportions of H_2/CO (5/95, 25/75, and 50/50 to 75/25) in syngas on turbulent flame speed, which indicated also an increase in OH radicals concentration. OH radical is a fundamental radical in the flame. Its concentration level can characterize the com-

bustion intensity [35]. The setup used was a water-cooled McKenna burner, and mass flow controllers. In addition, their results showed that dilution of syngas with Nitrogen (varied from 0, 10%, and 30% to 50%) was found to give the reverse effect on turbulent burning speed.

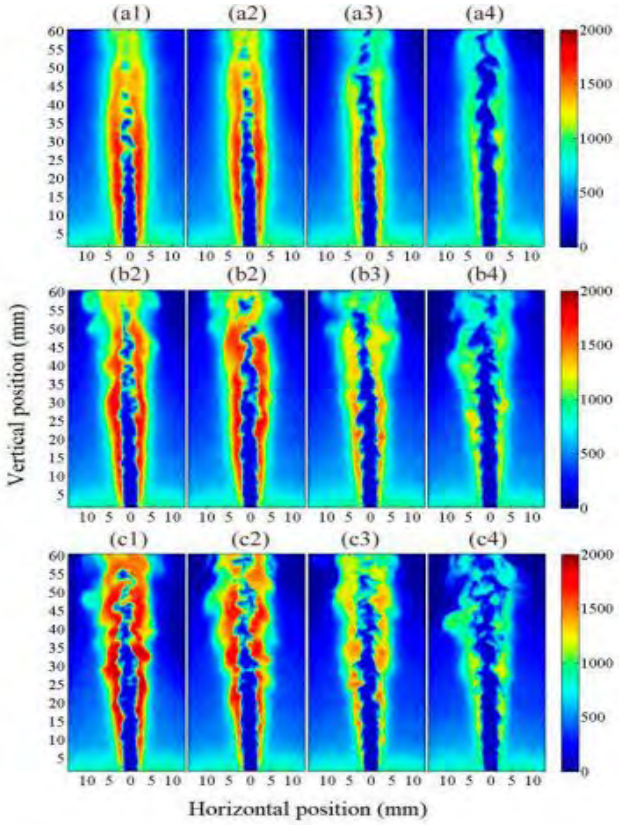

Fig. 7. OH distribution instantaneous image of syngas with volumetric ratio of 5% H_2–95%CO under different dilutions and Reynolds numbers: (a1–a4) Re = 6110; (b1–b4) Re = 10,690; (c1–c4) Re = 15,270. 1,2,3, and 4 indicate nitrogen dilution volumetric proportions of 0%, 10%, 30%, and 50%, respectively [36]

A unified scaling was conducted through dimensionless parameters to the turbulent burning velocity in order to extract general correlation of (ST) from experimental data.

The laminar flame and turbulence characteristics are two main elements that defines the turbulent burning velocity and thus it must be included in the unified scaling. The kinematic viscosity which is a dimensionless parameter in the turbulent Reynold number equation ($Re = VD\rho/\mu$) was used to reflect turbulence characteristics. Along with the ratio normalization of turbulent over laminar flame speed as show in Fig. 8, which was correlated with turbulent Reynold number ratio, suggesting that turbulent Reynolds number is a suitable to correlate turbulent burning velocity.

In quantitative level, the power exponent which 0.46 as show in Fig. 8, was found to be close to the experimental result 0.53 done by Shy et al. [37] and another theoretical result 0.5 of Chaudhuri et al. [38]. This indicated the validity of the unified scaling method regardless of initial pressures and type of fuels, so for the different turbulence intensities. The correlation obtained gave such satisfactory results due to the fact that most experimental results are at 20% hydrogen fraction and Lewis number around unity.

In another study they utilized the results obtained in the current study to verify their modified correlation for butanol/air flames $S_T \sim Da^{0.49}\ Le^{-0.35}$. With the difference between their correlation and the current study to having the Lewis number included in the equation [39].

The unified scaling method which includes Lewis number other than unity could be represented as follows with $ST/SL \sim Re_T^{0.36}\ Le^{-0.36}$, where the value of 0.36 close to 0.46 suggested by the current study. Additionally it was suggested that Da modified correlation (Damkohler number correlation) $ST \sim Da^{0.49}\ Le^{-0.35}$ is not only applicable to butanol/air flames, but also for syngas/air flames of different molecular transport effects as show in the Fig. 9.

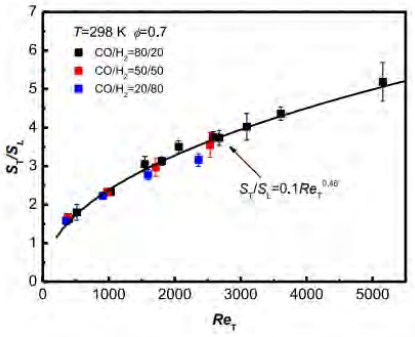

Fig. 8. A unified scaling of global turbulent burning [33]

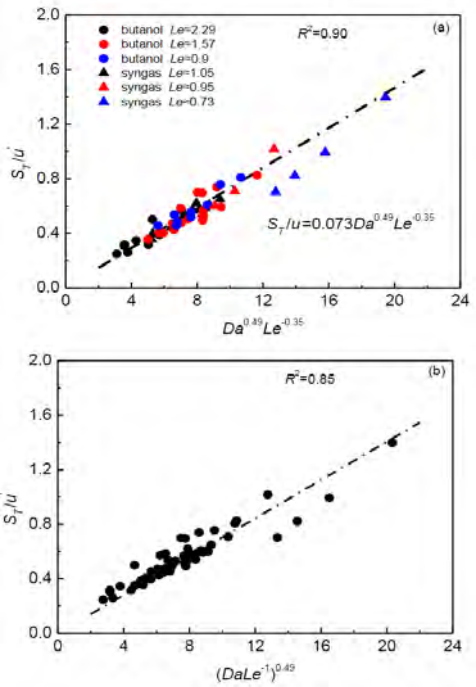

Fig. 9. Validation of modified correlation: (a) $Da^{0.49}Le^{-0.35}$, (b) $(Da\ Le^{-1})^{0.4}$ [39]

4. Syngas in internal combustion engine

Syngas has many applications in stationery and transport energy sector. It has been used a primary or secondary fuel depend on the type of engine, its operating conditions, performance requirements, and the phychemical properties of syngas. An important aspect for example is the autoignition in compression ignition engines (CI), which is difficult to achieve with syngas. Thus, diesel fuel

is used as secondary fuel to help ignite the syngas-air mixture. The challenge then is to replace the highest percentage of fuel mixture with syngas, where literature providing wide range of solutions from 25% up to 90%. The necessity is to reach a better understanding of the behavior of syngas in combustion engines based on the many criteria that define those limitations. Among many applications we shall discuss about the usage of syngas in Compression Ignition engines (CI), Spark Ignition engines (SI), Homogenous compression engines (HCCI) and advanced dual engines called reactivity-controlled compression ignition (RCCI).

4.1. Spark ignition engines

The research on spark ignition engines utilizing syngas as alternative to gasoline mainly on the aspect of fuel consumption and emissions. Spark ignition engines operating with fossil fuel at lean or even extremely lean condition has been the focus of researchers, with main goal is to achieve higher thermal efficiency due to lesser heat losses a pumping energy requirements, as well as lowering NO_x with lesser combustion temperatures [40]. This trend continued with the current experimental which utilizing syngas as an alternative fuel, where the syngas serves as an extender to the lean limits of SI engine operation. This is mainly achievable by direct injection strategies and the dilution of intake charge. The improving of the engine performance through implementing the typical strategies such as boosting, utilizing EGR, and engine downsizing is under investigating for the syngas application in SI engines.

The usage of syngas in spark ignition engines can vary depend on the engine type. For instance, the syngas applications on direct injection SI, carbureted and port fuel injection, and modified CI engines into SI engines. Also, whether the syngas would be used as primary, dual or as secondary fuel, but more importantly the applicability of the syngas usage in term of its advantages and disadvantages.

Many considerations such as combustion process, the typical engine operating range, and the LHV of syngas which is lower than gasoline, causes droppage in engine performance. Therefore, it has led to favoring the usage of 100% syngas as primary fuel for portal port fuel injection and carburetor SI engines in power generation rather than for vehicular applications. Since the operating point of fixed engines are limited, thus it can be optimized and the possibility of engine modification is more suitable.

This has been demonstrated in a study that replaced gasoline with syngas for a 650 W Yamaha 950 generator set. The syngas was derived from wood pellets through gasification which had lower heating value of 4.5 MJ/kg. The modification was done on the engine included the lubrication system, the air and fuel flow control, and the ignition timing. The Ignition timing had to be advanced by 13 degree to compensate, as we explained in pervious section, due to the high laminar velocity of syngas. Whereas the 45% decrease in power output compared to gasoline of 360 W [41].

Despite the negative impact on engine performance, utilizing syngas in Spark Ignition engines has significant impact on reduction of emissions [42]. A study done using a laboratory scale gasifier and portable gasoline generator of 8.5 compression ratio and 2.8 kW. Their emission results showed consistency with another study done on generator running at 740 Watt [43], with maximum power output of 1392 W. It is worth mentioning that there is scarcity in experimental work which compares generators running on gasoline vs syngas since the year 2010 onwards. Table 2 shows comparison between gasoline and syngas emission results. The CO emission was less by 20 times compared to gasoline, and reduced of NO_x emission by one-third. In totality the emission flow amount was about 25% less when operated on syngas.

Table 2. Gasoline and syngas emission comparison [42]

Fuel	O_2 in exhaust [%]	CO [mg/m³] @13% O_2	NO [mg/m³]@ 13% O_2	NO_x [mg/m³ @13% O_2	SO_2 [mg/m³ @13% O_2
Gasoline	8.93	24,700	45.4	69.7	50
Syngas	8.5	14,000	22.8	35	n.d.
Syngas	8.8	3100	24	38	n.d.
Syngas	9.12	1250 I	21.0	32	n.d.
Syngas	10.1	1120	16.6	25.6	n.d.
Syngas	10.8	1700	15.9	24.6	n.d.
Syngas	11.4	4000	16.8	26	n.d.

4.2 Syngas for dual-fuel CI engines

Due to high self-ignition temperature of syngas, typically about 500°C [44], syngas cannot be ignited by compression ignition diesel engines, combined with the the low reactivity of syngas-air mixture in CI engines. Thus the solution is typically dual fueling method is used, where diesel is injected as a pilot fuel to initiate the ignition while syngas injected into the induction system.

The dual fueling where a premixed fuel and piolet fuel is injected is gaining moment in the research area due to the ever-strict emission regulation for diesel engines. Literature shows that utilizing syngas in dual system is to certain degree beneficial as the other alternatives in term of performance and emission such as compressed natural gas and liquefied petroleum gas, with the advantage over them being a renewable energy.

In term of performance, its been reported that there is a decrease in power output due to lower volumetric efficiency of syngas [45]. As for emission CO and HC reduction was mainly observed under medium load conditions, but in general there is an increase in emissions including soot and NO_x. Other studied resulted in concluding that the incomplete combustion and excessively high Ringing Intensity (RI) are the major challenges of RCCI engines with lean premixed syngas [46].

Many strategies are being developed to reduced emission and enhance engine performance, one of which the Reactivity Controlled Compression Ignitions, where an early pilot injection during compression cycle is introduced.

In a study that tested syngas-diesel fueled RCCI engine was numerically investigated using KIVA-3V code, which was validated with experimental work [47]. The influence of syngas composition on RCCI combustion were investigated. Eight typical syngas compositions at Initial temperature valve closing and 360 K and syngas premixed ratio 60%. It was found that the H_2 from 50% in syngas 4 to 75%

in syngas 8 as show in Fig. 10 inhibits the autoignition of the mixture due to the active OH radicals being consumed which is required by the diesel low-temperature oxidation. Therefore, it leads to a retarded initiation of combustion shown in the heat release graph, Fig. 10.

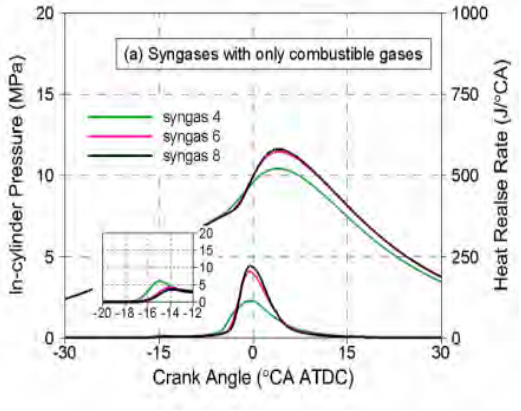

Fig. 10. In cylinder pressure and heat release graphs for pure H_2 and CO syngas. Syngas 4 (50/50), Syngas 6 (66.6/33.3), Syngas8 (75/25) [47]

The increase of H_2 lead to a decrease in combustion duration and higher thermal heat release rate which in turn lead to an increase in the combustion efficiency. Another syngas compositions were tested and it was found that the impurities for example CH_4 which transform OH to H_2O_2 can lead to a further increase in reduction of OH radicals which leads to lesser combustion efficiency. Soot reduction was also observed with the increase in syngas where the soot precursors H_2 and CO are mainly responsible for the soot reduction as show in Fig. 11.

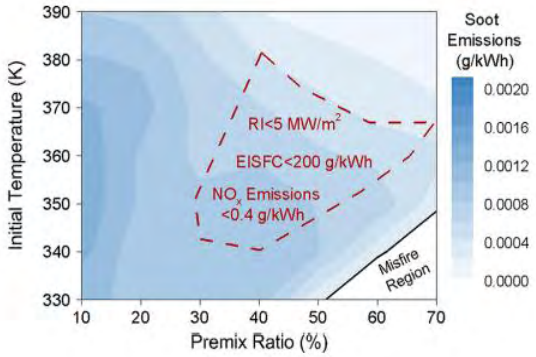

Fig. 11. Soot distributions under different initial temperatures [47]

The study concluded with suggesting an optimal syngas premixed ratio of 60% and H_2 volume fraction of 75% for best RCCI engine performance and lower emissions [47]. Similar results were obtained by another study where the H_2 optimal ratio range given was between 60–80% [46].

4.3 Syngas for HCCI engines

In the previous section syngas for spark ignition engines, we have mentioned that the usage of syngas for power generation is more suitable than vehicular application due the limitation syngas imposes on the operation of SI engines. Still syngas causes reduction in power by almost up to 40%.

Another major issue is the knock, which makes HCCI engine favorable as a solution for knock for syngas as fuel alternative in power generation applications.

For syngas to operate in SI engines it requires cooling to avoid knock, which leads to condensation of tar impurities that clog up critical process components. The tar removal procedure is costly and can make the usage of syngas economically unfeasible. HCCI which requires normally higher intake temperatures could be a solution to this critical issue in normal spark ignition engines. Thus the biomass syngas can leave the gasifier without having to go through cooling process to the HCCI power generator [48].

The knock limitation of syngas is mainly the topic that is been researched to identify the maximum compression ratio of HCCI engine, where the higher the compression ratio the better is the engine performance. According to the literature, for HCCI engines the low volumetric efficiency due to the addition of gas in the premixed charge, and the trade off between NO_x and CO remains an unsolved issues needed to be researched.

In a study done on an 435 cc mono-cylinder HCCI 12 compression ratio engine, tolerant to tar impurities above the tar dew point, they tested the sensitivity of HCCI to the ratio variation of H_2:CO from 30:70 to 55:45%.

Moisture up to 12% by volume, and tars (from 3 to 17 g/Nm^3) at the intake temperatures of around 250°C. The 250°C for the intake temperature experiment was chosen due to the fact that it the dew point of class 5 tar at a concentration of about 1 g/Nm^3, where there is mainly 6 classes of tar been identified, and class 5 dominating the tar dew point [48].

The results of the CO emission is shown in (Fig. 12b). Where the CA 10–90 represent combustion duration defined as the difference between the CA90 and the CA10, represented as the heat release duration. Since there is not any significant amount of hydrocarbon to contribute for the emission of CO, its considered that the CO emission is directly correlated with the unburned CO.

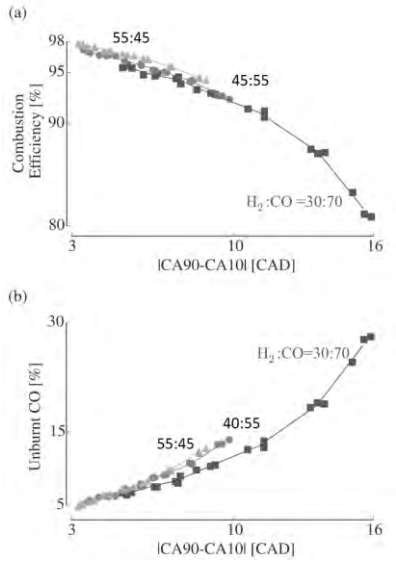

Fig. 12. Combustion efficiency and unburnt portion of CO measured in the emissions as a function of the combustion duration CA90–CA10 for various H_2:CO mixture ratios [48]

The similarity in the shape of the curve of the engine efficiency and CO is due to the slowing down effect on the combustion of the CO component.

It was also reported an increase in the NO_x emission as the combustion duration decrease, due an increase of the combustion temperature. The combustion temperatures in HCCI are still less when it's compared to SI and CI engines, thus NO_x emissions results are better for HCCI. It was also observed that the H_2:CO ratio did not have any significant effect on the NO_x emissions.

Besides the NO_x, CO trade-off issue in HCCI engines run on syngas, the volumetric efficiency issue has been investigated. The low heating value (LHV) of syngas along with high inlet temperature caused a significant reduction in the volumetric efficiency of the engine, thus low indicated mean effective pressure.

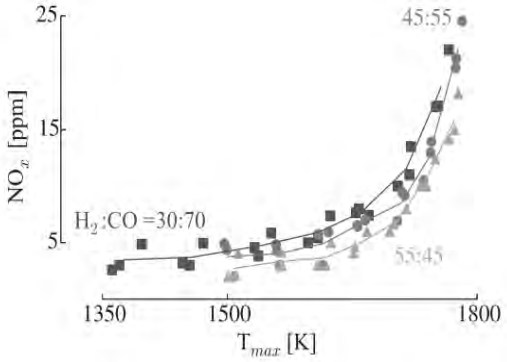

Fig. 13. Experimental NO_x measurements as a function of peak cycle temperature [48]

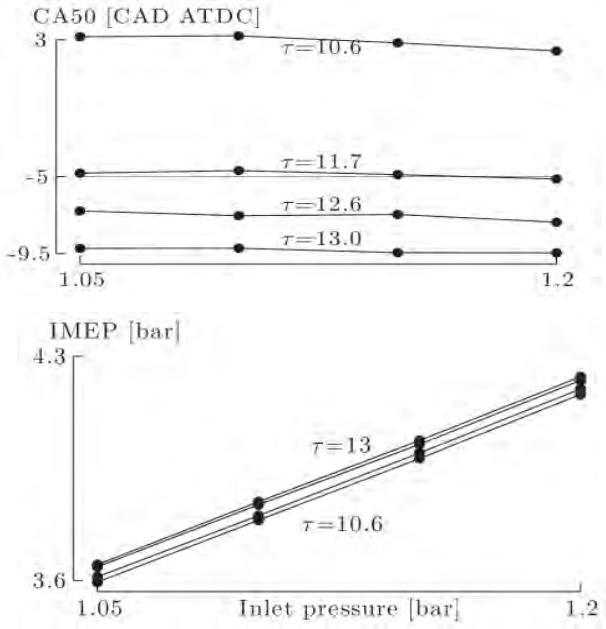

Fig. 14. Inlet pressure effect at different compression ratios on IMEP and CA50 [48]

For this purpose, researchers investigated the effect of pressure inlet effect. Satisfactory results were obtained which indicates that the workout of the engines could be controlled by adjusting the pressure inlet. Changing the compression ratio on the other hand showed a minimal impact on the IMEP, due to to high Maximum Pressure Rise Rate (MPRR) and improper phasing CA50. The best result for the whole range of pressure inlet where found to be at compression ratio 12, where the whole range of pressure inlet fulfilled the constraints they set for this study in term of CA50 (–5 and 10 CAD), engine knock MPRR (max 10 bar/CAD), and maximum cylinder pressure (100 bars) as it can be seen in Fig. 14.

Similarly, the temperature inlet had a significant impact on the (230, 250 and 270°C). The higher the temperature the earlier CA50 is achieved and the shorter the combustion duration. For instance, an increment by 20 degree in inlet temperature advanced the CA50 by about 8 degrees, with an increase in MPRR by 3.6 bar/CAD. Thus, it was concluded that As Inlet temperatures increases, the bad phasing decreases both the indicated efficiency and the indicated mean effective pressure (IMEP).

5. Summary and conclusion

This paper provided an in-depth review of the current syngas production processes and its applications, along with their utmost critical issues been tackled by the literature. Syngas as an alternative fuel has drawn recently increasing attention with the ever-stricter environmental regulations. The research area regarding syngas has mainly focused on the possible ways of achieving high production yields while reducing tar during the gasification process instead of being processed at later stages. This is mainly due to higher costs that makes syngas economically and technically invalid. Besides, the inconsistency of the feedstock components plays a major role in the combustion process of syngas as fuel in combustion engines, thus creating a greater challenge in accurately anticipating the combustion behavior of syngas at different loads, equivalence ratios, and initial conditions. Thus it necessitates to study each components and its effect on the combustion process. Based on the learned behavior of syngas during the combustion process, and the possible applications was discussed. The most important conclusions will be summarized as follows:

The main four types of gasification process as the mostly used tools to produce syngas from waste biomass feedstock has shown many advantages and disadvantages alike. Thus, it been recommended different applications to each type based on many criteria and their subsequent possible issues they could create in the engines. Multiple possible way was suggested to tackle those issues to reduce for instance their tar production and increases their yield production rate. For instance, incorporating a circulating cyclone to updraft type shown to yield a higher gas output by 10–15%, which is due to its feedstock long residency time, result in low efficiency and throughput and high tar content. Thus, it was not recommended for internal combustion engines, instead it was found to be more suitable for heat generation engine applications. Whereas the downdraft gasifier being the favored method so far in term of tar production rate with 99.9% being removed, which makes it suitable for engine combustion engines, mainly for high volatile fuel for power generation applications.

Unlike circulation fluidized bed, budding type is capable to acquire larger feedstock particle size, whereas for circulation gasifier type the particles size becomes a hindering criterion since larger sizes lowers and cause unstable production rate. Thus, the advantage of the bubbling gasifier bed is the uniformity in syngas production, where it maintains a uniform temperature distribution throughout the reactor between 700 and 1000°C by controlling the air/biomass ratio.

The physicochemical properties of a syngas in terms of laminar flame, turbulence flame speed, ignition delay, and knock limitation are considered to be the most important aspects has been researched in the effort to better understand the combustion behavior of syngas in combustion engines. The current literatures all agree that the discrepancy between the numerical and experimental data results need more investigation to tackle the reasons behind it, in an effort to speed up the study of syngas as an alternative fuel for combustion engines. In that regard the effect of highly diluted syngas (CO_2 and N_2) on the laminar flame speed was investigated. Results showed that using modified Davis mechanism can predict with high accuracy the LFS for application which requires high temperature and pressures such as for advanced technologies IGCC. Whilst FFCM-1 method resulted in comparable results except for high dilution of CO_2 circa 70%. In case of low temperature and pressures application, an investigation was done to better under the reasons behind the discrepancies between the results presented in the literature which used Davis mechanism and the measurements obtained using OPT method. The source of discrepancies was found to be mainly at very lean and very rich mixtures, with about up to 45% percent difference. It was due to the ignition which has strong impact on the uncertainty, as well as the extrapolation method used to study the LFS at early stage of spherical flame propagation, where the nonlinear method were found more sensitive to the linear extrapolation method.

The different production processes of syngas that constitute the product components and the physicochemical properties defines the applicability of syngas in different combustion engine type. Compression ignition engines self-ignition requirements cannot be met for syngas at about 500°C, thus it usually used in dual mode where the challenge to increase the ratio of syngas as the primary fuel. Such applications have been investigate and literature is giving a wide range of solutions from 25% up to 90%. The higher the percentage the lower the volumetric efficiency, thus the lower power out can be achieved. Besides the reduction of emission is limited to CO and HC at particularly medium loads while there is generally an increase in soot and NO_x. To overcome these issues advanced technologies such as RCCI engines can be more suitable for syngas application, although their main challenges when operating with syngas is the high ringing intensity and incomplete combustion, which requires further investigation for a complete adaptivity. For RCCI engines multiple studied suggested that the optimal syngas premixed ratio of 60% and H_2 volume fraction of 75% for best RCCI engine performance and lower emissions [47]. In spark ignition engines (SI) the syngas is mainly been investigated as an extender to the lean limits, since the advanced engine technologies already been designed to operate on very lean mixtures. Thus, the typical strategies such as boosting, utilizing EGR, and engine downsizing is under investigating for the syngas application in SI engine, taking into consideration the lower LHV of syngas compared to gasoline which leads to lower of engine performance. Syngas in that regard were mostly found to be useful in power generation rather than vehicular applications since the engine calibration can be easily modified to fit the limited operation points in stationary engine applications, with an advantage of reducing CO and NO_x emissions by up to 25%. Another main concern in spark ignition engines is knock. As a solution HCCI engines serves as viable alternative to regular SI engines when operating on syngas fuel. This in turns solves the tar major issue in syngas usage. Unlike SI engines, HCCI operates at higher intake temperatures which avoid the necessity to cool syngas which causes tar formation. As of result the combustion temperatures in HCCI could increase affecting the NO_x emissions but when its compared to SI and CI engines its of a lower NO_x emission values. The main challenges been investigated in such types of engines is the effect of initial pressure and temperature on the combustion duration to achieve the lowest emission with highest engine output power.

Syngas has a promising protentional to be usage as alternative to traditional fossil fuels when its physicochemical properties can be fully studied and numerical models are established. This would help facilitate the speed up of the investigation of syngas behavior in different engine applications to set the recommended percent usage and initial conditions. It can be concluded that:

- Downdraft gasification is the most preferable type currently been used to produce almost tar free syngas.
- Other gasification types showing an improved and promising tar and yield production rates with newly proposed solutions, yet it requires further investigation and research.
- The physicochemical properties of syngas in term of turbulent, laminar flame speed, and ignition delay time is not fully yet comprehended. Which explains the significant gap and discrepancies between the numerical models and the experimental results.
- Although there has been a significant progress in establishing a reliable models that can speed up the research of syngas as alternative fuel.
- Syngas has wide range of application in ICE, although its limited due to its physicochemical properties such as self-ignition temperature, where it could only be used in dual fuel CI engines.
- The applicability of syngas in stationary engines were found to be more favorable than in vehicular engine application due to the limited operation ranges that can be modified and controlled.

Nomenclature

Al_2O_3 aluminium oxide
Ar argon
BS baseline syngas
CA crank angle
CH_4 methane
CI compression ignition engines
CO carbon monoxide
Da Damkohler number correlation
EGR exhaust gas recirculation
Fe iron
FFCM foundational fuel chemistry model
H_2 hydrogen
HCCI homogenous charged compression
HTP high temperature and pressure
ICE internal combustion engines
IDT ignition delay time
IGCC integrated gasification combined cycle
IMEP indicated mean effective pressure
Le Lewis number
LFS laminar flame speed
LHV lower heating value
Mg magnesium
MPRR maximum pressure rise rate
NiO nickel oxide
NTP normal temperature and pressure
OPF outwardly propagating spherical flame method
Re rhenium
RCCI reactivity-controlled compression ignition
SI spark ignition
Φ equivalence ratio

Bibliography

[1] Grzelak P, Żółtowski A. Environmental assessment of the exploitation of diesel engines powered by biofuels. Combustion Engines. 2020;180(1):31-35. https://doi.org/10.19206/CE-2020-105

[2] Sikarwar VS, Zhao M, Fennell PS, Shah N, Anthony EJ. Progress in biofuel production from gasification. Prog Energ Combust. 2017;61:189-248. https://doi.org/10.1016/j.pecs.2017.04.001

[3] Syngas & Derivatives Market: Global Industry Analysis (2022-2029) by Technology, Gasifier Type, Feedstock, Application and Region. https://www.maximizemarketresearch.com

[4] Ahmad AA, Zawawi NA, Kasim FH, Inayat A, Khasri A. Assessing the gasification performance of biomass: A review on biomass gasification process conditions, optimization and economic evaluation. Renew Sust Energ Rev. 2016;53:1333-1347. https://doi.org/10.1016/j.rser.2015.09.030

[5] Gupta AK, Cichonski W. Ultra-high temperature steam gasification of biomass and solid wastes. Environ Eng Sci. 2007;24(8):1179-1189. https://doi.org/10.1089/ees.2007.0120

[6] Basu P. Gasification Theory and Modeling of Gasifiers. Biomass Gasification Design Handbook. Elsevier; 2010.

[7] Aydin ES, Yucel O, Sadikoglu H. Numerical and experimental investigation of hydrogen-rich syngas production via biomass gasification. Int J Hydrogen Energ. 2018;43(2):1105-1115. https://doi.org/10.1016/j.ijhydene.2017.11.013

[8] Basu P, Kaushal P. Modeling of pyrolysis and gasification of biomass in fluidized beds: A review. Chemical Product and Process Modeling. 2009;4(1). https://doi.org/10.2202/1934-2659.1338

[9] Wang Q-D. An updated detailed reaction mechanism for syngas combustion. RSC Adv. 2014;4(9):4564-4585. https://doi.org/10.1039/C3RA45959D

[10] Stępień Z. Synthetic automotive fuels. Combustion Engines. 2023;192(1):78-90. https://doi.org/10.19206/CE-152526

[11] Bielaczyc P, Woodburn J, Gandyk M. Trends in automotive emissions, fuels, lubricants, legislation and test methods – a global view, with a focus on the EU & US – summary of the 5th International Exhaust Emissions Symposium (IEES). Combustion Engines. 2016;166(3):76-82. https://doi.org/10.19206/CE-2016-342

[12] Mckendry P. Energy production from biomass (part 3): gasification technologies. Bioresource Technol. 2002;83(1): 55-63. https://doi.org/10.1016/S0960-8524(01)00120-1

[13] Waldheim L. Gasification of waste for energy carriers : a review. IEA Bioenergy. 2018;12. https://www.ieabioenergy.com/

[14] Bosmans A, Wasan S, Helsen L. Waste-to-clean syngas: avoiding tar problems. 2nd International Enhanced Landfill Mining Symposium. 2013:181-201.

[15] Liu L, Zhang Z, Das S, Kawi S. Reforming of tar from biomass gasification in a hybrid catalysis-plasma system: A review. Appl Catal B-Environ. 2019;250:250-272. https://doi.org/10.1016/j.apcatb.2019.03.039

[16] Bastos AK, Torres C, Mazumder A, de Lasa H. CO_2 biomass fluidized gasification: thermodynamic and reactivity studies. Can. J. Chem. Eng. 2018;96:2176-2184. https://doi.org/10.1002/cjce.23316

[17] Oveisi E, Sokhansanj S, Lau A, Lim J, Bi X, Preto F et al. Characterization of recycled wood chips, syngas yield, and tar formation in an industrial updraft gasifier. Environments. 2018;5(84):1-13. https://doi.org/10.3390/environments5070084

[18] Tezer O, Karabag N, Ozturk MU, Ongen A, Ayol A. Comparison of green waste gasification performance in updraft and downdraft fixed bed gasifiers. Int J Hydrogen Energ. 2022;47(74):31864-31876. https://doi.org/10.1016/j.ijhydene.2022.04.077

[19] Couto N, Rouboa A, Silva V, Monteiro E, Bouziane K. Influence of the biomass gasification processes on the final composition of syngas. Energy Proced. 2013;36:596-606. https://doi.org/10.1016/j.egypro.2013.07.068

[20] Salem AM, Dhami HS, Paul MC. Syngas production and combined heat and power from scottish agricultural waste gasification – a computational study. Sustainability. 2022; 14(3745). https://doi.org/10.3390/su14073745

[21] Nam H, Wang S, Sanjeev KC, Seo MW, Adhikari S, Shakya R et al. Enriched hydrogen production over air and air-steam fluidized bed gasification in a bubbling fluidized bed reactor with CaO: Effects of biomass and bed material catalyst. Energy Convers Manag. 2020;225:113408. https://doi.org/10.1016/j.enconman.2020.113408

[22] Kurkela E, Kurkela M, Tuomi S. Development of a bubbling circulating fluidized-bed reactor for biomass and waste gasification. Chem Eng Trans. 2022;92:385-390. https://doi.org/10.3303/CET2292065

[23] Meng J, Wang X, Zhao Z, Zheng A, Huang Z, Wei G et al. Highly abrasion resistant thermally fused olivine as in-situ

catalysts for tar reduction in a circulating fluidized bed biomass gasifier. Bioresour Technol. 2018;268:212-220. https://doi.org/10.1016/j.biortech.2018.07.135
[24] Zhang W, Gou X, Kong W, Chen Z. Laminar flame speeds of lean high-hydrogen syngas at normal and elevated pressures. Fuel. 2016;181:958-963. https://doi.org/10.1016/j.fuel.2016.05.013
[25] Lee HC, Jiang LY, Mohamad AA. A review on the laminar flame speed and ignition delay time of Syngas mixtures. Int J Hydrogen Energ. 2014;39(2):1105-1121. https://doi.org/10.1016/j.ijhydene.2013.10.068
[26] Varghese RJ, Kumar S, Kolekar H. Effect of CO_2 dilution on the burning velocity of equimolar syngas mixtures at elevated temperatures. 26th ICDERS, Boston 2017. http://www.icders.org/ICDERS2017/abstracts/ICDERS2017-1033.pdf
[27] Jithin E, Raghuram GKS, Keshavamurthy T v., Velamati RK, Prathap C, Varghese RJ. A review on fundamental combustion characteristics of syngas mixtures and feasibility in combustion devices. Renew Sust Energ Rev. 2021;146:111178. https://doi.org/10.1016/j.rser.2021.111178
[28] Varghese RJ, Kolekar H, Kumar S. Demarcation of reaction effects on laminar burning velocities of diluted syngas–air mixtures at elevated temperatures. Int J Chem Kinet. 2019; 51(2):95-104. https://doi.org/10.1002/kin.21232
[29] Han W, Dai P, Gou X, Chen Z. A review of laminar flame speeds of hydrogen and syngas measured from propagating spherical flames. App Energ Combust Sci. 2020;1-4:100008. https://doi.org/10.1016/j.jaecs.2020.100008
[30] Chaos M, Dryer FL. Syngas combustion kinetics and applications. Combust Sci Technol. 2008;180(6):1053-1096. https://doi.org/10.1080/00102200801963011
[31] Mathieu O, Kopp MM, Petersen EL. Shock-tube study of the ignition of multi-component syngas mixtures with and without ammonia impurities. P Combust Inst. 2013;34(2): 3211-3218. https://doi.org/10.1016/j.proci.2012.05.008
[32] Samiran NA, Ng JH, Mohd Jaafar MN, Valera-Medina A, Chong CT. Swirl stability and emission characteristics of CO-enriched syngas/air flame in a premixed swirl burner. Process Saf Environ. 2017;112:315-326. https://doi.org/10.1016/j.psep.2017.07.011
[33] Zhao H, Wang J, Cai X, Dai H, Bian Z, Huang Z. Flame structure, turbulent burning velocity and its unified scaling for lean syngas/air turbulent expanding flames. Int J Hydrogen Energy. 2021;46(50):25699-25711. https://doi.org/10.1016/j.ijhydene.2021.05.090
[34] Kim JS, Williams FA, Ronney PD. Diffusional-thermal instability of diffusion flames. J Fluid Mech. 1996;327:273-301. https://doi.org/10.1017/S0022112096008543
[35] Chen Z, Jiang Y. Numerical investigation of the effects of H_2/CO/syngas additions on laminar pre-mixed combustion characteristics of NH_3/air flame. Int J Hydrogen Energy. 2021;46(21):12016-12030. https://doi.org/10.1016/j.ijhydene.2021.01.054
[36] Yang L, Weng W, Zhu Y, He Y, Wang Z, Li Z. Investigation of hydrogen content and dilution effect on syngas/air premixed turbulent flame using OH planar laser-induced fluorescence. Processes. 2021;9(11):1894. https://doi.org/10.3390/pr9111894
[37] Liu CC, Shy SS, Peng MW, Chiu CW, Dong YC. High-pressure burning velocities measurements for centrally-ignited premixed methane/air flames interacting with intense near-isotropic turbulence at constant Reynolds numbers. Combust Flame. 2012;159(8):2608-2619. https://doi.org/10.1016/j.combustflame.2012.04.006
[38] Chaudhuri S, Akkerman V, Law CK. Spectral formulation of turbulent flame speed with consideration of hydrodynamic instability. Phys Rev E Stat Nonlin Soft Matter Phys. 2011;84(2). https://doi.org/10.1103/PhysRevE.84.026322
[39] Zhao H, Wang J, Cai X, Dai H, Huang Z. Turbulent burning velocity and its unified scaling of butanol isomers/air mixtures. Fuel. 2021;306:121738. https://doi.org/10.1016/j.fuel.2021.121738
[40] He X, Zhou Y, Liu Z, Yang Q, Sjöberg M, Vuilleumier D et al. Impact of coolant temperature on the combustion characteristics and emissions of a stratified-charge direct-injection spark-ignition engine fueled with E30. Fuel. 2022; 309:121913. https://doi.org/10.1016/j.fuel.2021.121913
[41] Gitano-Briggs HW, Kean KL. Genset optimization for biomass syngas operation. renewable energy – utilisation and system integration. InTech. 2016. https://doi.org/10.5772/62727
[42] Puglia M, Morselli N, Pedrazzi S, Tartarini P, Allesina G, Muscio A. Specific and cumulative exhaust gas emissions in micro-scale generators fueled by syngas from biomass gasification. Sustainability. 2021;13(6):3312. https://doi.org/10.3390/su13063312
[43] Shah A, Srinivasan R, D. Filip To S, Columbus EP. Performance and emissions of a spark-ignited engine driven generator on biomass based syngas. Bioresour Technol. 2010; 101(12):4656-4661. https://doi.org/10.1016/j.biortech.2010.01.049
[44] Stolecka K, Rusin A. Analysis of hazards related to syngas production and transport. Renew Energy. 2020;146:2535-2555. https://doi.org/10.1016/j.renene.2019.08.102
[45] Guo H, Neill WS, Liko B. The combustion and emissions performance of a syngas-diesel dual fuel compression ignition engine. Proceedings of the ASME 2016 Internal Combustion Engine Division Fall Technical Conference. Greenville. October 9-12, 2016. https://doi.org/10.1115/ICEF2016-9367
[46] Xu Z, Jia M, Li Y, Chang Y, Xu G, Xu L et al. Computational optimization of fuel supply, syngas composition, and intake conditions for a syngas/diesel RCCI engine. Fuel. 2018;234: 120-134. https://doi.org/10.1016/j.fuel.2018.07.003
[47] Xu Z, Jia M, Xu G, Li Y, Zhao L, Xu L et al. Potential for reducing emissions in reactivity-controlled compression ignition engines by fueling syngas and diesel. Energy Fuels. 2018;32(3):3869-3882. https://doi.org/10.1021/acs.energyfuels.7b03265
[48] Bhaduri S, Contino F, Jeanmart H, Breuer E. The effects of biomass syngas composition, moisture, tar loading and operating conditions on the combustion of a tar-tolerant HCCI (Homogeneous Charge Compression Ignition) engine. Energy. 2015;87:289-302. https://doi.org/10.1016/j.energy.2015.04.076

Mohamad Hamid, PhD student – Faculty of Mechanical Engineering, Wrocław University of Science and Technology, Poland.
e-mail: *mohamad.hamid@pwr.edu.pl*

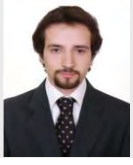

Mateusz Wesołowski, Eng. – Faculty of Mechanical Engineering, Wrocław University of Science and Technology, Poland.
e-mail: *mateusz.wes12@wp.pl*

Article citation info:
Andrych-Zalewska M. Research of pollutant emissions from automotive internal combustion engines in conditions corresponding to the actual use of vehicles. Combustion Engines. 2023;193(2):64-70. https://doi.org/10.19206/CE-162621

Monika ANDRYCH-ZALEWSKA

Combustion Engines
Polish Scientific Society of Combustion Engines

Research of pollutant emissions from automotive internal combustion engines in conditions corresponding to the actual use of vehicles

ARTICLE INFO

Received: 20 March 2023
Revised: 24 March 2023
Accepted: 25 March 2023
Available online: 27 March 2023

The subject of the article is the study of pollutant emissions from automotive combustion engines that operate in conditions corresponding to the actual use of vehicles. Includes information on the properties of exhaust gas parameters characterizing the following features: energy, economic, environmental impact and serviceability, additional and constant. Reference was also made to the possibility of determining driving tests on the basis of the similarity of the frequency characteristics of the speed processes in both driving tests and in the real use of vehicles. The article presents the results of research on pollutant emissions from a passenger car during the RDE test. The emission of carbon monoxide, hydrocarbons, nitrogen oxides, particulate matter and carbon dioxide, as well as the number of particulate matter, were examined. The process of pollutant emission intensity and particle number intensity was presented. Tests were carried out on the statistical properties of the car speed, the intensity of pollutant emissions, and the intensity of the number of particulate matter. Correlation studies were carried out on the speed of the vehicle, the intensity of pollutant emissions, and the intensity of the number of particulate matter.

Key words: *pollutant emission, vehicles, internal combustion engines*

1. Introduction

The article considers the problem of pollutant emissions from automotive internal combustion engines in conditions corresponding to the actual use of vehicles. The emission of pollutants from internal combustion engines is treated as one of their functional properties.

In order to be able to test the emission of pollutants from an internal combustion engine in conditions corresponding to its use in a vehicle, it is necessary to ensure the engine's operating states using the following methods [2, 3]:

– driving the vehicle in conditions corresponding to real use – such tests may be carried out either on a chassis dynamometer or in road conditions,
– simulating engine operating states in conditions corresponding to actual use in the vehicle – tests are carried out on an engine dynamometer.

For light vehicle engines (passenger cars, light trucks, minibuses and L-category vehicles – motorcycles, mopeds, quads and microcars), the tests may be carried out under comparable conditions on a chassis dynamometer. It is also possible to conduct tests in road conditions thanks to the use of the PEMS (Portable Emissions Measurement System) mobile emission testing system [16, 18, 19]. This type of research is carried out using type-approval tests of light vehicles in order to determine the emission of nitrogen oxides and the number of particulate matter [11, 20].

Heavy vehicles (trucks and buses) are mainly tested in road conditions. This is mainly due to the difficulty of accessing large-sized chassis dynamometers, of which there are very few. The tradition of testing heavy vehicles in road conditions is due to the fact that the operational fuel consumption of buses is determined using SORT (Standardized On-Road Test) and UITP (The International Association of Public Transport) tests [1].

In this work, the methods of creating driving tests that simulate the movement of vehicles have been systematized. The results of empirical tests of pollutant emissions from the internal combustion engine of a passenger car during the RDE (Real Driving Emissions) test in real driving conditions are also presented.

2. Performance characteristics of automotive internal combustion engines

The operational properties of internal combustion engines relate primarily to [2]:

– energy characteristics,
– economic features,
– impact on the environment,
– serviceability, reliability and durability.

Energy features are characterized primarily by useful power and dynamic properties – in the case of a car engine, it is the maximum speed and maximum acceleration of the vehicle. The economic features are characterized by the overall efficiency of the engine. Due to the impact on the environment, pollution and noise emissions are primarily considered.

These properties are strongly dependent on the operating states of internal combustion engines in both their static and dynamic states.

The following operating states of internal combustion engines are described in [2, 3, 5]:

– rotational speed,
– load,
– thermal state.

The measure of load is usually the engine's torque or net power. The thermal state is most often characterized by the temperature of operating factors: engine oil or engine coolant. In a stabilized thermal state of the engine, its operating states are therefore described by rotational speed and load.

In the case of car engines, the main factor determining engine operating states is the vehicle speed process [1–6]. For this reason, in order to simulate the operating states of car engines, they are tested in conditions corresponding to the movement of the vehicle.

3. Performance characteristics of automotive internal combustion engines

Driving tests are developed to simulate the operating states of internal combustion engines in conditions corresponding to the real use of road vehicles. Driving tests are processes of driving speed.

A process is a state quantity defined on a certain normed space. The domain in which the process is defined is usually time or a monotonic function of time (process – time function, time series) or an area of space (process – field). In this article, a process is treated as a numerical function whose argument is time or a monotonic function time. The zero-dimensional characteristic of the process is the functional of this process, e.g. the mean value of the process, standard deviation of the process, extreme values of the process relative to speed, etc.

There are two basic ways to create driving tests. The first method of developing driving tests involves simulating the speed process in the time domain [1, 6–8]. On the basis of empirical tests of vehicles in real traffic conditions, speed processes are recorded. Then, the registered velocity processes are analyzed in terms of their selected properties, e.g. the average value, the average value of the absolute value of the product of velocity and acceleration, or the probability density. There are two options for developing driving tests in this way. The first option is to adopt the selected recorded speed process as the driving test, with the second being to create the driving test as a combination of fragments of recorded processes. Examples of tests created on the basis of simulating the time domain are the homologation FTP-75 (Federal Test Procedure) and WLTC (Worldwide Harmonized Light Vehicles Test Cycle) [11, 20] tests, as well as special tests for simulating traffic conditions in traffic jams – Stop&Go, or for traffic on motorways and expressways – Autobahn [6].

Tests created on the basis of simulating the time domain can be treated as stochastic processes in the form of a set of realizations [15].

The second method of developing driving tests is the arbitrary adoption of the speed process, and then the selection of the parameters of this process in accordance with the principle of the similarity of these parameters with the parameters of the processes recorded in the conditions of the actual use of vehicles. The arbitrary adoption of the speed process consists in adopting the character of the process similar due to certain properties to the speed processes actually occurring in the use of vehicles. Such parameters are, for example, the average speed value, the maximum speed value, or extreme acceleration values. Examples of such tests are the following homologation tests: NEDC (New European Driving Cycle), which consists of both driving tests in cities – UDC (Urban Driving Cycle) and driving tests outside cities – EUDC (Extra Urban Driving Cycle) or Japanese 10-15 Mode [11, 20].

It is also possible to create driving tests based on the similarity of frequency characteristics [9].

The developed tests are used for the following purposes:

- testing the compliance of the properties of light vehicles; tested on a chassis dynamometer and in road conditions using the RDE test. There are applicable legal acts in approval procedures – the evaluation criterion is the emission of pollutants and the number of particulate matter [11, 20];
- an inventory of pollutant emissions carried out over the course of 1 year – the result is the national annual pollutant emission [5, 12];
- forecasting the state of environmental pollution by determining the intensity of pollutant emissions and, by modeling the spread of pollutants, determining the concentration of pollutants.

While the conditions of vehicle movement in the approval procedures are strictly defined, in the other two applications, driving tests must simulate different traffic conditions. Traffic models are usually distinguished: in traffic jams, in cities (no traffic jams), outside cities, and on motorways and expressways [5, 10]. Numerous tests have been developed for these purposes as part of extensive research programs. For example, under the ARTEMIS (Assessment and Reliability of Transport Emission Models and Inventory Systems) program, numerous CADC (Common Artemis Driving Cycles) tests [1] have been developed, which correspond to the movement of vehicles in driving conditions in cities, outside cities, and on highways and expressways.

Thanks to the study of pollutant emissions and fuel consumption using various tests, it was possible to develop software that allows the emission of pollutants and the number of particulate matter for various vehicle traffic conditions to be determined. This software contains, for elementary and cumulative vehicle categories, formulas for the emission of pollutants and the number of particulates with regards to the average speed.

A category is a class of objects that have specific characteristics and which are related to each other. Categories of road vehicles are determined according to the following criteria: application, contractual size, construction properties, fuel, and technical level [10].

The elementary category of road vehicles includes vehicles with all the same criteria. The cumulative category of motor vehicles includes vehicles with not all the same criteria.

Examples of emission simulation software are: COPERT (Computer Program to Calculate Emissions From Road Transport) [10], normally used for pollutant inventory [5, 12], and HBEFA (Handbook Emission Factors for Road Transport) INFRAS AG (Infrastructure, Umwelt- und Wirtschaftsberatung) [13].

4. Empirical studies of pollutant emissions from an internal combustion engine in conditions corresponding to the actual use of vehicles

Empirical studies of pollutant emissions from an internal combustion engine in conditions corresponding to the actual use of vehicles were carried out using the RDE test.

The subject of the research was a passenger car with a spark-ignition engine, which was equipped with an automatic gearbox at the Euro 6 level due to road emissions. The car was tested for pollutant emissions and fuel consumption using the RDE test. The test is performed with a cold engine start-up. The PEMS mobile pollutant emission testing system was used in the research [16]. The Semtech DS analyzer [18] and the TSI 3090 EPSS™ (Engine Exhaust Particle Sizer™ Spectometer) analyzer [19] were used for the pollutant emission tests.

The recorded processes were subjected to low-pass filtration using the second-order Savitzky-Golay filter [17] in order to reduce the share of high-frequency noise in the signals.

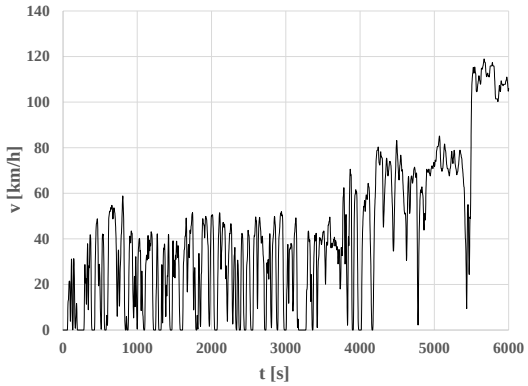

Fig. 1. Car speed process – v during the RDE test

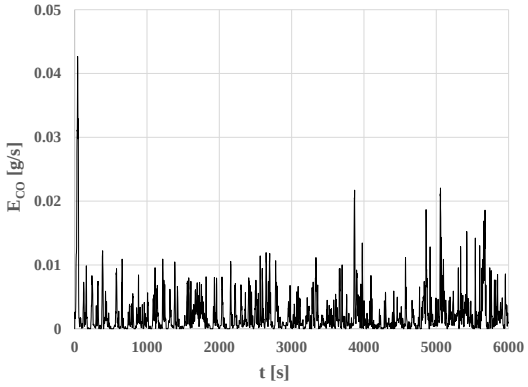

Fig. 2. The process of carbon monoxide emission intensity – E_{CO} from the car engine during the RDE test

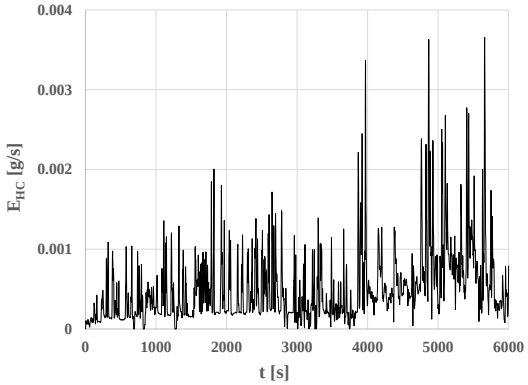

Fig. 3. The process of hydrocarbon emission intensity – E_{HC} from the car engine during the RDE test

Figure 1 shows the car speed process during the RDE test. Figures 2–5 show the processes of the emission intensity of pollutants: carbon monoxide, hydrocarbons, nitrogen oxides and carbon dioxide from the car engine during the RDE test.

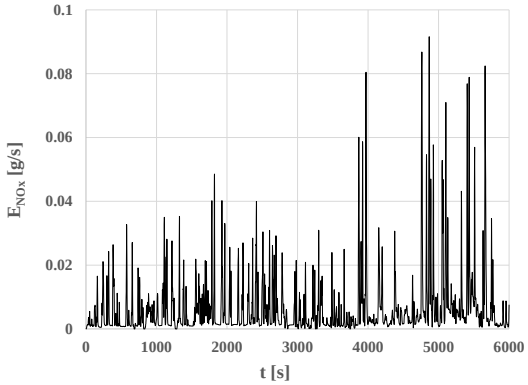

Fig. 4. The process of nitrogen oxide emission intensity – E_{NOx} from the car engine during the RDE test

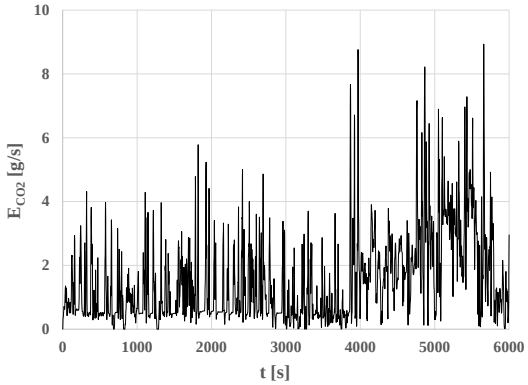

Fig. 5. The process of carbon dioxide emission intensity – E_{CO2} from the car engine during the RDE test

Figure 6 shows the particle number intensity process during the RDE test.

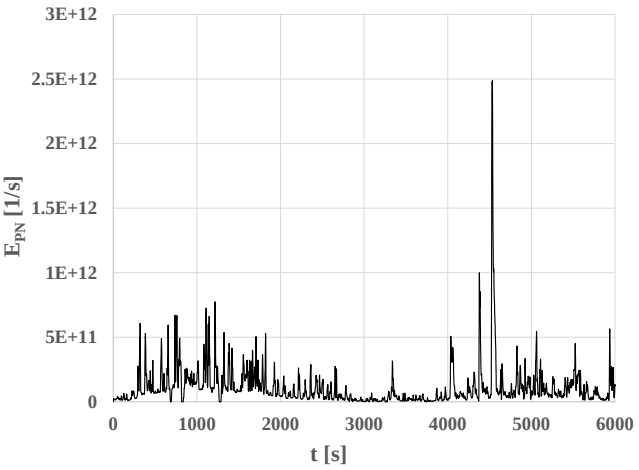

Fig. 6. Process of particle number intensity – E_{PN} from the car engine during the RDE test

The statistical properties [14] of the velocity process and the processes of pollutant emission intensity and parti-

cle number intensity were also tested. The following were designated:

- minimum value – Min,
- maximum value – Max,
- range – R,
- average value – AV,
- median – M,
- standard deviation – D,
- coefficient of variation – W.

Figure 7 shows the zero-dimensional statistical characteristics of the car speed process, Fig. 8–11 – the processes of pollutant emission intensity, and Fig. 12 – the particle number intensity process.

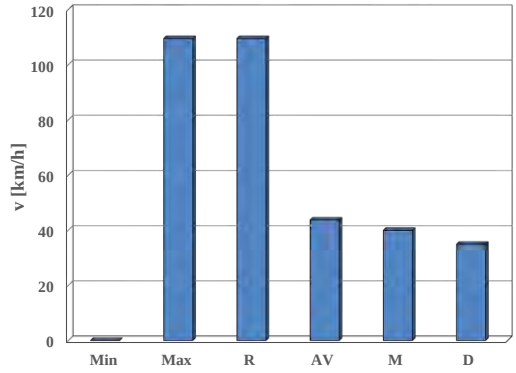

Fig. 7. Statistical characteristics of the car speed process – v

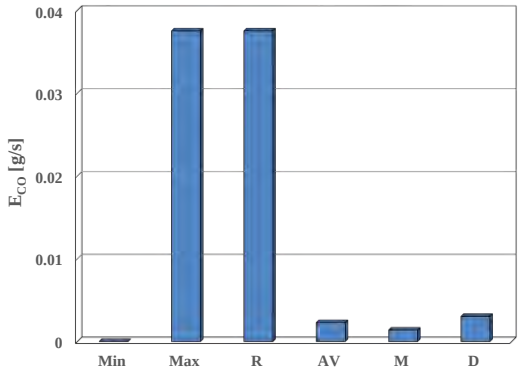

Fig. 8. Statistical characteristics of the carbon monoxide emission intensity process – E_{CO}

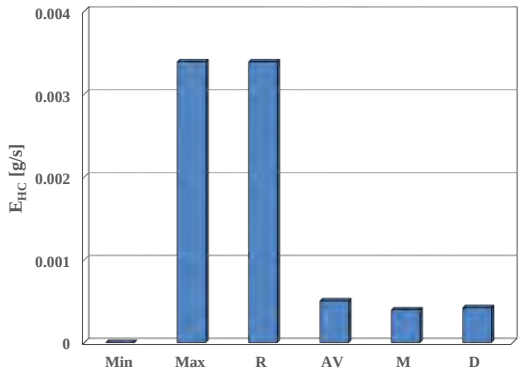

Fig. 9. Statistical characteristics of the hydrocarbon emission intensity process – E_{HC}

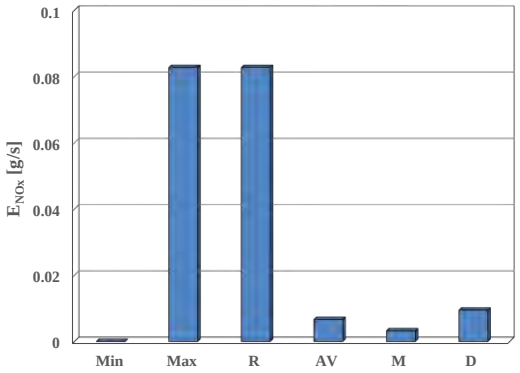

Fig. 10. Statistical characteristics of the nitrogen oxide emission intensity process – E_{NOx}

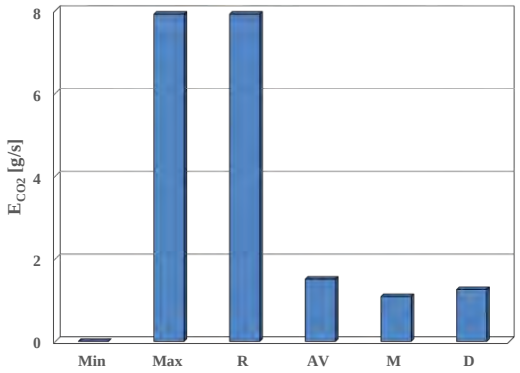

Fig. 11. Statistical characteristics of the process of carbon dioxide emission intensity – E_{CO2}

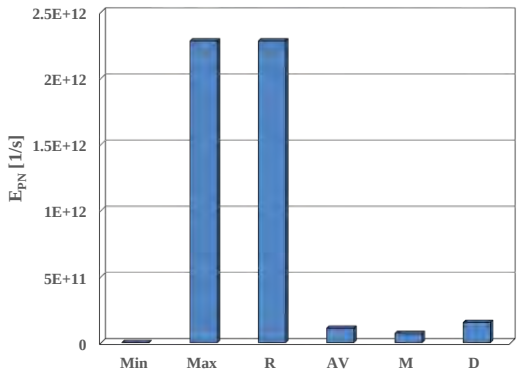

Fig. 12. Statistical characteristics of the particle number intensity process – E_{PN}

For all the processes, the average value is greater than the median.

Figure 13 shows the coefficient of variation of the examined processes.

The coefficient of variation characterizes the dynamic properties of processes [14]. The processes of carbon monoxide and nitrogen oxide emission intensity, as well as the intensity of the number of particulate matter, are characterized by the strongest dynamic properties.

Correlation studies [14] of the following processes were carried out: pollutant emission intensity and particle number intensity – the test results are presented in Table 1.

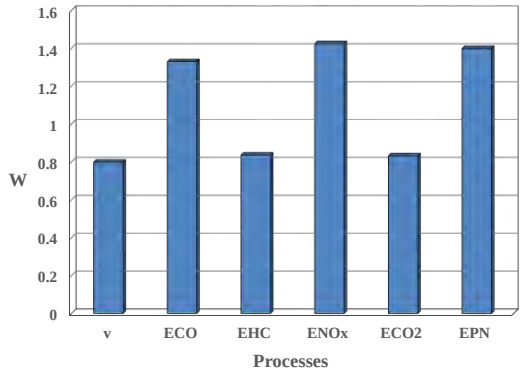

Fig. 13. Coefficient of variation of the examined processes – W

Table 1. Coefficient of determination – R^2 between the tested processes during the RDE test

	v	E_{CO}	E_{HC}	E_{NOx}	E_{CO2}	E_{PN}
E_{CO}	0.0011					
E_{HC}	0.0639	0.1428				
E_{NOx}	0.0063	0.1339	0.8360			
E_{CO2}	0.0903	0.1026	0.8573	0.6534		
E_{PN}	0.0043	0.0115	0.0723	0.0646	0.0926	

The processes of the pollutant emission intensity and the intensity of the number of particulate matter are weakly correlated with the process of car speed – the weakest in the case of carbon monoxide emission intensity, and the strongest in the case of carbon dioxide emission. This results from the fact that with increasing speed, fuel consumption also increases, and consequently carbon dioxide emissions.

The process of particle number intensity is the least correlated with all the pollutant emission intensity processes. The most strongly correlated is the intensity of hydrocarbon emissions with the intensity of emissions of carbon dioxide and nitrogen oxides.

An exemplary correlation relationship between pollutant emission intensity processes during the RDE test is shown in Fig. 14.

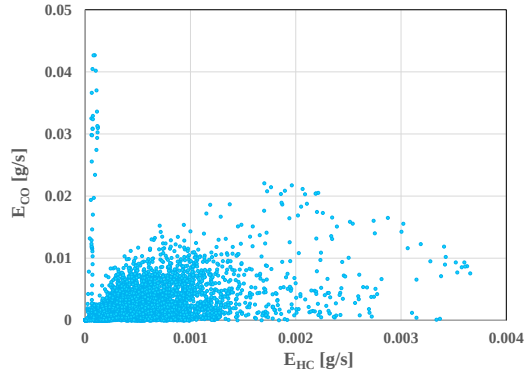

Fig. 14. Correlation relationship between the carbon monoxide emission intensity – E_{CO} and the hydrocarbon emission intensity – E_{HC} during the RDE test

On the basis of the recorded pollutant emission intensity and particle number rate, as well as the vehicle speed process, the average values during the RDE test were determined: emission of pollutants and number of particulate matter.

The average emission – b of pollutants during the RDE test is the ratio of the emission of pollutants in the test – m and the length of the road covered by the car in the test – L.

$$b = m/L \tag{1}$$

The mean particle number during the RDE test – b_PN is the ratio of the number of particles in the test – PN and the distance traveled by the car in the test.

$$b\_PN = PN/L \tag{2}$$

The pollutant emission during the RDE test is the integral of the pollutant emission intensity – E.

$$m = \int_0^T E(t)dt \tag{3}$$

where: t – time, T – test duration.

The particulate number during the RDE-PN test is the integral of the particulate number intensity – EPN.

$$PN = \int_0^T E_{PN}(t)dt \tag{4}$$

The length of the road covered by the car during the RDE test – L is the integral of the car's speed – v.

$$L = \int_0^T v(t)dt \tag{5}$$

Table 2 presents the zero-dimensional pollutant emission characteristics during the RDE test.

Table 2. Zero-dimensional characteristics of pollutant emissions and fuel consumption during the RDE test

b_{CO}	b_{HC}	b_{NOx}	b_{CO2}	b_{PN}
g/km				1/km
0.1994	0.04387	0.5796	131.2	9.500E+12

In relation to the emission limits of pollutants and the number of particulate matter at the Euro 6 level, the relative values of the emission determined during the RDE test are as follows: for carbon monoxide – 0.199, for hydrocarbons – 0.439, for nitrogen oxides – 9.66, for the number of particles – 15.8.

5. Conclusions

Based on the conducted research, the following conclusions can be drawn:

1. The processes characterizing the emission of pollutants are mostly poorly correlated with each other. These processes are also weakly correlated with the car speed process. The most strongly correlated is the intensity of hydrocarbon emissions with the intensity of emissions of carbon dioxide and nitrogen oxides.
2. For all the examined processes, the average value is greater than the median.
3. In relation to the emission limits of pollutants and the number of particulate matter at the Euro 6 level, the relative values of the emission determined during the RDE test are as follows: for carbon monoxide – 0.199, for

hydrocarbons – 0.439, for nitrogen oxides – 9.66, for the number of particles – 15.8.

4. The strongest dynamic properties, assessed on the basis of the coefficient of variation, are characterized by the processes of carbon monoxide and nitrogen oxide emission intensity and the intensity of the number of particulate matter.
5. The processes of pollutant emission intensity and the process of particle number intensity are characterized by strong maxima for small process values.

It is expedient to continue working in the following directions:

1. It is advisable to treat the stages of the car velocity process, and consequently the operating states and the internal combustion engine during the RDE test, as stochastic processes that are represented by sets of realizations. Empirical studies that are performed for many implementations of the car speed process during the RDE test enable the waveforms of the engine's operating states, which are actually the processes of these states, to be obtained. Conducting empirical research in individual implementations of stochastic processes enables research results to be statistically elaborated.
2. It is advisable to conduct separate tests for each phase of the RDE test. The test results would enable the assessment of the specificity of the car's traffic conditions on the engine operating states and, consequently, on the intensity of pollutant emissions and the intensity of the number of particulate matter.
3. It is interesting to compare the impact of the technical level of cars in terms of pollutant emissions with the results of the RDE test.
4. It is useful to compare the test results of the same car during the RDE test and the WLTC test.

Acknowledgements

The article was written in cooperation with Autocomp Management Sp. z o.o. from Szczecin, Research and Development Center-Producer of simulators on the military and civilian market from Poland.

Nomenclature

CI	compression ignition
CNG	compressed natural gas
DI	direct injection
LPG	liquified petrolum gas
SI	spark ignition
ARTEMIS	Assessment and Reliability of Transport Emission Models and Inventory Systems
Autobahn	driving test on highways and expressways
AV	average value
b	average road emission of the pollutant/average road number of particulates
CADC	Common Artemis Driving Cycles
CO	carbon monoxide
CO2	carbon dioxide
COPERT	Computer Programme to Calculate Emissions From Road Transport
D	standard deviation
E	pollutant emission intensity/particle number intensity
EPSS™	Engine Exhaust Particle Sizer™ Spectometer
EUDC	Extra Urban Driving Cycle
FTP	Federal Test Procedure
HBEFA	Handbook Emission Factors for Road Transport
HC	hydrocarbons
Japanese 10-15 Mode	homologation test in Japan
L	distance traveled by the car
m	emission of pollution
M	median
Max	maximum value
Min	minimum value
NEDC	New European Driving Cycle
NOx	nitrogen oxides
PEMS	Portable Emissions Measurement System – portable emission testing system
PN	particle number
R	range
RDE	Real Driving Emissions – test in the conditions of real use of the road vehicle
SORT	Standardised On-Road Test
Stop&Go	driving test in traffic jams
t	time
UDC	Urban Driving Cycle
UITP	The International Association of Public Transport
v	vehile velocity
W	coefficient of variation
WLTC	Worldwide Harmonized Light Vehicles Test Cycle

Bibliography

[1] André M. The ARTEMIS European driving cycles for measuring car pollutant emissions. Sci Total Environ. 2004;334-335:73-84. https://doi.org/10.1016/j.scitotenv.2004.04.070

[2] Andrych-Zalewska M, Chłopek Z, Merkisz J, Pielecha J. Determination of characteristics of pollutant emission from a vehicle engine under traffic conditions in the engine test. Combustion Engines. 2022;191(4):58-65. https://doi.org/10.19206/CE-147327

[3] Andrych-Zalewska M, Chłopek Z, Merkisz J, Pielecha J. Research on exhaust emissions in dynamic operating states of a combustion engine in a Real Driving Emissions test. Energies. 2021;14(18):1-15. https://doi.org/10.3390/en14185684

[4] Andrych-Zalewska M, Chłopek Z, Merkisz J, Pielecha J. Investigations of exhaust emissions from a combustion engine under simulated actual operating conditions in Real Driving Emissions test. Energies. 2021;14(4):935. https://doi.org/10.3390/en14040935

[5] Bebkiewicz K, Chłopek Z, Sar H, Szczepański K, Zimakowska-Laskowska M. Assessment of impact of vehicle traffic conditions: urban, rural and highway, on the results of pollu-

tant emissions inventory. Archives of Transport. 2021;60(4): 57-69. https://doi.org/10.5604/01.3001.0015.5477
[6] Buwal, Infras AG: Luftschadstoffemissionen des Strassenverkehrs 1950–2010. Buwal–Bericht Nr. 255. 1995.
[7] Chłopek Z, Biedrzycki J, Lasocki J, Wójcik P. Examination of pollutant emissions and fuel consumption at tests simulating the real conditions of operation of a passenger car. The Archives of Automotive Engineering. 2014;65(3):3-18.
[8] Chłopek Z, Biedrzycki J, Lasocki J, Wójcik P. Investigation of pollutant emissions from a motor vehicle engine in tests simulating real vehicle use in road traffic conditions. Combustion Engines. 2013;154(3):202-207.
[9] Chłopek Z. Synthesis of driving cycles in accordance with the criterion of similarity of frequency characteristics. Eksploat Niezawodn. 2016;18:572-577. https://doi.org/10.17531/ein.2016.4.12
[10] Copert – Computer Programme to Calculate Emissions From Road Transport.
[11] DieselNet: Engine & Emission Technology Online. https://dieselnet.com (accessed on 2022.03.11).
[12] EEA/EMEP Emission Inventory Guidebook 2019.
[13] Infras AG: Handbuch für Emissionsfaktoren des Strassenverkehrs; Version 24.2. Bern 2022.
[14] Lane DM et al. Introduction to statistics – Open Textbook Library (www.umn.edu).
[15] Papoulis A, Pillai SU. Probability, random variables, and stochastic processes. Tata McGraw-Hill, 2002:852.
[16] PEMS Testing – Portable Emissions Measurement Systems (www.horiba.com).
[17] Savitzky A, Golay MJE. Smoothing and differentiation of data by simplified least squares procedures. Analytical Chemistry. 1964;36(8):1627-1639. https://doi.org/10.1021/ac60214a047
[18] Semtech-DS On Board Vehicle Emissions Analyzer. User Manual. Document: 9510-086, Revision: 2.01, October 2010.
[19] TSI 3090 EEPS™ (Engine Exhaust Particle Sizer™), User Manual, 2008.
[20] Worldwide emission standards. Passenger cars and light duty vehicles. Delphi. Innovation for the real world. 2020/2021.

Monika Andrych Zalewska, DEng. – Faculty of Mechanical Engineering, Wroclaw University of Science and Technology, Poland.
e-mail: *monika.andrych@pwr.edu.pl*

Article citation info:
Lisowski M, Gołębiewski W, Prajwowski K, Danilecki K, Radwan M. Modeling the fuel consumption by a HEV vehicle – a case study. Combustion Engines. 2023;193(2):71-83. https://doi.org/10.19206/CE-157112

Maciej LISOWSKI
Wawrzyniec GOŁĘBIEWSKI
Konrad PRAJWOWSKI
Krzysztof DANILECKI
Mirosław RADWAN

Combustion Engines
Polish Scientific Society of Combustion Engines

Modeling the fuel consumption by a HEV vehicle – a case study

ARTICLE INFO

Received: 13 October 2022
Revised: 23 November 2022
Accepted: 4 December 2022
Available online: 26 December 2022

The article presents a mathematical model demonstrating the synergy of HEV energetic machines in accordance with the model predictive control. Then the results of road tests are presented. They were based on the factory control of the above-mentioned system. The results of the operating parameters of the system according to the factory control and the results of the operating parameters according to the model predictive control were compared. On their basis, it could be concluded that the model predictive control contributed to changes in the power and electrochemical charge level of the energy storage system from 50.1% (the beginning) to 56.1% (the end of course) and for MPC from 50.1% (the beginning) to 59.9% (the end of the course). The applied MPC with 13 reference trajectories (LQT) of power machines of the series-parallel HEV allowed for fuel savings on the level of 4%.

Key words: *hybrid electric vehicle, fuel consumption, model predictive control, factory control, energy consumption*

1. Introduction

The fuel consumption of HEVs is an important parameter depending on the method of controlling the internal combustion engine, generator and the electric motor. The main purpose of this control is to increase the energy efficiency of the HEV drive system. This control can be defined as the cooperation of assemblies/components remaining in continuous interaction with each other. This can also be considered as energetic machines energy management system [3, 10, 24].

The origins of HEV energy management systems are seen in a control method based on heuristic hypotheses. They assumed the expected operating conditions of the drive system – commencement of operation and its continuation in electrical mode to the set speed or reaching the maximum torque. Within the range that the torque of the electric motor decreased, the drive was supported by an internal combustion engine [14, 17].

Another solution of the energy management system was the use of statistical optimisation. This method did not require knowledge of the actual power demand, but was based only on taking into account its average value [3].

The low accuracy of the mentioned method resulted in the development of the HEV drive energy management system based on stochastic-dynamic programming (DP) [2, 10, 18, 19, 36]. In the model of the hybrid powertrain energy management system, the power demand, determined by the driver, was of a stochastic process characteristics. In the concept, however, the model of a hybrid vehicle was determined. The optimisation of the target function was based on the power demand in general road conditions and not on a specific driving cycle. This resulted in low accuracy of the method [19].

An interesting approach to the issue of energy management of HEVs can be found in [24, 25]. They contain algorithms of the equivalent fuel consumption strategy (ECMS), among others, in HEVs equipped with fuel cells.

Such a control strategy presented as a function of cost (the sum of fuel consumption and energy consumption of a hybrid vehicle) also appears in [11, 30]. The main disadvantage of this type of control is the use of information *a priori* regarding road conditions or conditions for conducting laboratory tests (according to the adopted driving cycle).

Modification of fuel consumption optimisation algorithms (ECMS) for series-parallel electric hybrid vehicles was undertaken by Liu and Peng [19]. The experimental tests carried out by them using the SDP and ECMS strategies resulted in an improvement in the dynamic properties of HEV. They also contributed to the reduction of fuel consumption of the HEV. The energy model of the HEV vehicle powertrain system created by them automatically generated dynamic equations of the system. The demonstrated algorithms implemented an effective synergy of the internal combustion engine with electric machines ensuring a reduction in fuel consumption [20].

Another solution assumed the use of PSO (*particle swarm optimisation*) [1, 6–8, 15, 31]. It was used in a hybrid vehicle enabling charging the traction battery from a power socket (plug-in HEV) [6, 30]. This energy management strategy was based on a real-time algorithm used to reduce fuel consumption. The result of Hwang and Chen's research was an improvement in fuel consumption to 9.4% compared to the base control model [15].

In parallel, research was conducted on the model predictive control in energy management in HEVs [16]. The control applied enabled optimal torque distribution for the parallel hybrid powertrain of the vehicle. The cost function used in the strategy was minimised thanks to telemetric estimation of vehicle speed [16].

Research was also carried out using model predictive control in parallel-series HEVs equipped with a supercapacitor [5].

Simultaneously, experiments were carried out with HEVs equipped with a series powertrain system. A strategy

to minimise fuel consumption was developed thanks to the use of stochastic optimisation of the management process using the Markov chain [23].

Model predictive control was also used to determine exits from the system (economical driving reducing fuel consumption) and also relied on information provided by the Intelligent Transport System [36].

This energy management system was developed in [34, 35]. Linear square tracking (LQT) was applied to the model predictive control. It supported the effective control of power distribution in a series-parallel HEV. At the same time, the LQT controller minimised the cost function, maintaining the level of charge of the energy storage system at the desired level [34, 35].

Another method of exercising model predictive control in the energetic machines energy management model of a HEV was also invented. Non-linear predictive control (NMPC) has saved up to 8.8% of fuel consumption according to the NEDC cycle. This result was obtained by comparing the values to the Factory Vehicle Energy Management System [31].

The energy model of a series-parallel HEV is also presented in the article [6]. It was characterised by high accuracy; however, it was based on NEDC and HWYCOL road tests.

It is also important to mention about the other actual effective energy management systems proposed in HEVs. It was based on distributed deep reinforcement learning (DRL). Paper presented DRL algorithms just like: a deep q-network (DQN), asynchronous advantage actor-critic (A3C) and distributed proximal policy optimalization (DPPO). Simulation results show that tree DRL based control strategies can achieve near optimal fuel economy but also outstanding computational efficiency [32].

It is worth noting that above all presented energy management systems, the MPC is a proven and effective method used by many researchers [28, 34–36]. But the main problem of MPC is that it is useless to achieve a lower level of HEV fuel consumption without reference trajectory (infinite prediction horizon). So, as it was mentioned, LQT with MPC can reduce fuel consumption [34, 35]. But it was proven only for maximum load of ICE. It was only one reference trajectory. An important aspect is how to reach the lower level of HEV fuel consumption? Maybe the use of dozen reference trajectories, not only for maximum power but also for partial loads of ICE, would solve this problem? To reach this, it is required to collect operational points of ICE under real conditions. Only a few works were carried out in road conditions, e.g. [4, 27–29] not based on simulations or observations and measurements in stationary (laboratory) conditions [15, 30, 32–35].

In real life operation, it is possible to get more necessary information useful to optimise the HEV energy management control. This translates into its mileage of fuel consumption.

The vast majority of the publications cited outline the study of the mileage fuel consumption of the HEV in stationary conditions. The experiments are then carried out on the basis of specific road tests (often poorly reflecting the actual road conditions). However, there is no information on changes in the mileage fuel economy of the HEV in actual road operation using the model predictive control mode. Hence, it seemed necessary to carry out tests of the mileage fuel consumption value of the HEV vehicle with the model predictive control. For this purpose, a diagnostic computer for a specific car model was used. Such research is a novelty in this field. The above observations became the basis for formulating the main purpose of the work.

2. Purpose and scope of research

The aim of the study was to assess the fuel consumption of HEV with model predictive control in real road conditions (case study).

Raising this issue was due to the insufficient level of knowledge about the impact of the change in the energetic machines management control in the HEV concerned on its fuel consumption (in real road conditions). The additional purpose of the research was to verify the energetic machines operating parameters of the series-parallel HEV powertrain system.

The basic study questions were as follows: 1) does MPC strategy with 13 reference trajectories really contribute to improving the fuel economy of a HEV? 2) does this EMS have an good effect on the battery state of charge (SOC)?

The aim of the work is considered to be achieved when the answers to the research questions are obtained. The values of operational parameters during real vehicle traffic conditions should be taken as the basic evaluation criterion. Within the framework of the defined objective of the work the following specific objectives were implemented: – determination of percentage differences in the course of fuel consumption according to MPC with 13 reference trajectories (LQT) and factory control, – comparison of the obtained values with the values provided by the vehicle manufacturer. Experimental assessment of HEV fuel consumption in real road conditions as the main scientific goal will allow to prove the rightness and to indicate the benefits of the MPC with 13 reference trajectories application of the HEV working machines.

The scope of research will be based on the experimental method. It will include tests of the fuel consumption of the HEV with factory control in real road conditions. Then, the values of the parameters of the internal combustion engine and electrical machines will be simulated. This will be implemented in accordance with the energy management strategy for model predictive control – also in real road conditions.

The studies will be carried out in urban and extra-urban traffic conditions with the use of a specific HEV vehicle. They will be carried out in accordance with the presented HEV energy consumption model.

The subject of the studies will be a Toyota Prius 3 car (produced in 2012), a HEV equipped with a series-parallel hybrid powertrain system.

The technical and operational characteristics of the test object are presented in Table 1 [13, 19].

3. HEV energy consumption model

In order to determine the value of the mileage fuel consumption of the HEV according to the predictive control, it was necessary to determine the type of parameters related to the cost function. These included:

a) power of the internal combustion engine,
b) angular speed of the internal combustion engine,
c) power of the generator,
d) angular speed of the generator,
e) power of the electric motor,
f) the angular speed of the electric motor,
g) power of the traction battery,
h) the level of charge of the traction battery.

The indicated parameters are related to the power transmission in the powertrain system of the HEV.

Table 1. Specifications of Toyota Prius 3 2012 vehicle [13]

Parameter	Unit	Value
Total mass	kg	1630
Wheel dynamic radius	m	0.29
Wheels moment of inertia	kg m^2	2.7
Facing Surface	m^2	1.62
Rolling resistance coefficient	–	0.0084
Air drag coefficient	–	0.25
Drive system type	–	Series and parallel
Internal combustion engine		
Ignition type		spark ignition
Capacity	dm^3	1.8
Number of cylinders		4
Max. power	kW	73
Max. power rotational speed	rpm	5200
Max. torque	Nm	142
Max. torque rotational speed	rpm	4000
Mass moment of inertia	kg m^2	0.18
Generator (MG1)		
Type	–	three-phase synchronous AC
Function	–	generator, ICE starter
Rated voltage	V	650
Maximum output power	kW	42
Max torque	Nm	45
Current at max torque	A	75
Max. rotational speed	rpm	10,000
Mass moment of inertia	kg m^2	0.023
Electric motor (MG2)		
Type		three-phase synchronous AC
Function		generator, wheel drive
Rated voltage	V	650
Maximum output power	kW	60
Maximum torque	Nm	207
Current at max torque	A	230
Max. rotational speed	rpm	13000
Mass moment of inertia	kg m^2	0.05
Electrochemical accumulation system and inverter		
Battery type		NiMH
Nom. voltage	V	201.6
Capacity	Ah	6.5

3.1. Power transmission in the powertrain system

The power generated by the internal combustion engine is transferred to the yoke of the satellite wheels. Then it is directed onto the planetary gear crown wheel. After exiting the planetary gearbox, the power drives the axles of the vehicle's wheels using the counter drive gear and the final drive gear. The MG1 generator, connected to the sun gear, acts as a starter and is used to charge the battery while driving. The MG2 electric machine is connected to the sun gear of the second planetary gear. It is designed to support the internal combustion engine in generating power, but also to ensure energy recovery during braking [22] (Fig. 1).

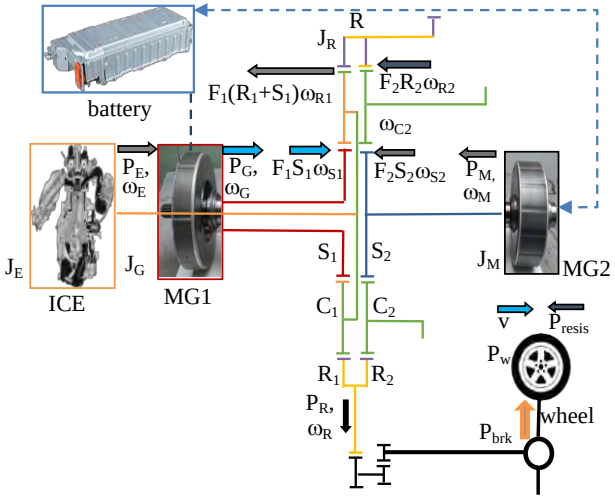

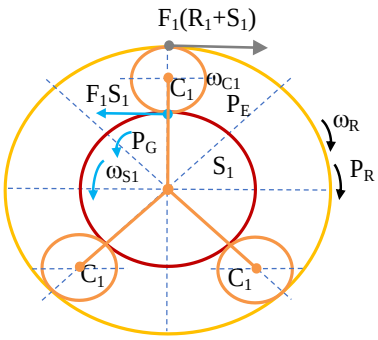

a) first planetary gear (ICE side)

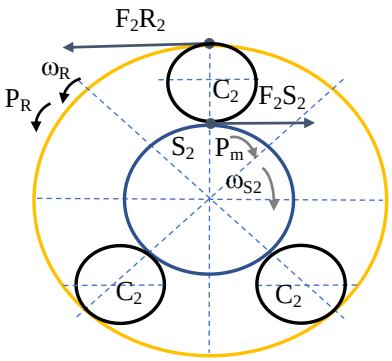

b) second planetary gear (MG2 side)

Fig. 1. Power transfer dynamics in the series-parallel powertrain system of the HEV

The operation of the above system is described by the following angular speed relationships [22]:

$$\omega_{C1} = \frac{R_1}{S_1 + R_1}\omega_R + \frac{S_1}{S_1 + R_1}\omega_{S1} \quad (1)$$

$$\omega_{C2} = \frac{R_2}{S_2 + R_2}\omega_R + \frac{S_2}{S_2 + R_2}\omega_{S2} \quad (2)$$

The yoke of the second gear's satellites is blocked, therefore $\omega_{C2} = 0$.

$$0 = \frac{R_2}{S_2 + R_2}\omega_R + \frac{S_2}{S_2 + R_2}\omega_{S2} \quad (3)$$

$$\frac{R_2}{S_2+R_2}\omega_R = -\frac{S_2}{S_2+R_2}\omega_{S2} \tag{4}$$

$$\omega_R = -\frac{S_2}{R_2}\omega_{S2} \tag{5}$$

$$\omega_{S2} = \omega_M,\ \omega_{C1} = \omega_E,\ \omega_{S1} = \omega_G \tag{6}$$

$$\omega_R = -\frac{S_2}{R_2}\omega_M \tag{7}$$

$$\omega_E = \frac{R_1}{S_1+R_1}\omega_R + \frac{S_1}{S_1+R_1}\omega_G \tag{8}$$

$$\omega_E = -\frac{R_1}{S_1+R_1}\cdot\frac{S_2}{R_2}\omega_M + \frac{S_1}{S_1+R_1}\omega_G \tag{9}$$

$$\omega_M = -\frac{R_2}{S_2}\omega_R \tag{10}$$

$$\omega_G = \frac{\omega_E(R_1+S_1)}{S_1} + \frac{R_1}{S_1}\frac{S_2}{R_2}\cdot\omega_M \tag{11}$$

As it can be seen from the above relationships, the angular speeds of individual HEV energy machines are closely related.

The angular speed at the output of the gearbox results from the angular speeds of individual energetic machines. The vehicle speed is described by the following relationship [35]:

$$v = \frac{\omega_R \cdot r_d}{i_{FD}} \tag{12}$$

Limitations of power transmission in the powertrain system:

a) power of the internal combustion engine:

$$0 \le P_E \le P_E^{max} \tag{13}$$

b) angular speed of the internal combustion engine:

$$\omega_E^{min} \le \omega_E \le \omega_E^{max} \tag{14}$$

c) power of the generator (MG1):

$$P_G^{min} \le P_G \le P_G^{max} \tag{15}$$

d) angular speed of the generator (MG1):

$$\omega_G^{min} \le \omega_G \le \omega_G^{max} \tag{16}$$

(e) power of the electric motor (MG2):

$$P_M^{min} \le P_M \le P_M^{max} \tag{17}$$

(f) rotational speed of the electric motor (MG2):

$$\omega_M^{min} \le \omega_M \le \omega_M^{max} \tag{18}$$

The propulsion system of the HEV is characterised by different relationships when the vehicle is in the steady conditions or unsteady conditions.

3.2. Movement of the HEV under steady state conditions

During the steady movement of the vehicle, there is no resistance to inertia forces, hence the mass moments of inertia of individual energetic machines are not taken into account. Then the operation of the powertrain system (Fig. 1) describe the following equations [26, 32]:

$$P_E \cdot \eta_{C_1/R} \cdot \omega_E^{-1} = F_1(R_1+S_1) \tag{19}$$

$$P_G \cdot \eta_{S_1/C_1} \cdot \omega_G^{-1} = -F_1 S_1 \tag{20}$$

$$P_M \cdot \eta_{R_2/R} \cdot \omega_M^{-1} = F_2 S_2 \tag{21}$$

It can also be noted that the output power of the system depends on the power of individual power machines:

$$P_E \cdot \eta_{C_1/R} + P_M \cdot \eta_{R_2/R} = P_R \tag{22}$$

Hence, the power acting on the wheels of the vehicle, taking into account the output power of the system and the efficiency of the main transmission, takes the form of:

$$P_W = P_R \cdot \eta_{fd} = (P_E \cdot \eta_{C_1/R} + P_M \cdot \eta_{R_2/R}) \cdot \eta_{fd} \tag{23}$$

The movement of the HEV under steady state conditions is characterised by a constant speed. In such conditions, when driving on a smooth, straight road (without bends), the HEV overcomes rolling resistance, air resistance, or hill resistance. Then, the relation of the HEV movement, expressed by the power acting on the wheels, is as follows:

$$P_w = F_p \cdot v \tag{24}$$

$$P_w = P_{resis} \tag{25}$$

$$P_w = F_{resis} \cdot v = (F_r + F_s + F_a) \cdot v \tag{26}$$

$$P_w = \left(mgf_r \cos\alpha + mg\sin\alpha + \frac{1}{2}\rho_A \cdot C_d A_f v^2\right) \cdot v \tag{27}$$

3.3. Vehicle movement under unsteady (transient) state conditions

During the transient movement of the vehicle there are inertia resistances, hence in this case the mass moments of inertia of individual energetic machines are taken into account. This is described in the following equations [28, 34]:

$$J_E \cdot \dot{\omega_E} = P_E \cdot \eta_{C_1/R}\omega_E^{-1} - F_1(R_1+S_1) \tag{28}$$

$$J_G \cdot \dot{\omega_G} = P_G \cdot \eta_{S_1/C_1} \cdot \omega_G^{-1} + F_1 S_1 \tag{29}$$

$$J_M \cdot \dot{\omega_M} = P_M \cdot \eta_{R_2/R} \cdot \omega_M^{-1} - F_2 S_2 \tag{30}$$

$$\begin{aligned} J_R \cdot \dot{\omega_R} &= F_1 R_1 + F_2 R_2 - P_R \omega_R^{-1} \\ &= \frac{R_1}{R_1+S_1} P_E \cdot \eta_{C_1/R}\omega_E^{-1} + \frac{R_2}{S_2} \cdot P_M \\ &\cdot \eta_{R_2/R} \cdot \omega_M^{-1} - P_R \omega_R^{-1} \end{aligned} \tag{31}$$

The movement of the HEV in transient conditions is characterised by variable speed. In such conditions, when

driving on a smooth, straight road (without bends), the HEV overcomes rolling resistance, air resistance, inertia resistance, or potentially hill resistance. Then the relation of the movement of the HEV, expressed through the power on the wheels, takes the form of:

$$P_w = \int_{v1}^{v2} F_{resis} dv = \int_{v1}^{v2} (F_r + F_s + F_i + F_a) dv \quad (32)$$

$$P_w = \int_{v1}^{v2} (mgf_r \cos\alpha + mg \sin\alpha + \delta \cdot m \cdot a + \frac{1}{2}\rho_A \cdot C_d A_f v^2) dv \quad (33)$$

When overcoming inertia resistance by the vehicle, an important parameter is the rotating mass coefficient. Taking into account the mass moments of inertia of energetic machines, it takes the following form:

$$\delta = w_1 + w_2 \cdot i_G^2 + w_3 \cdot i_E^2 + w_4 \cdot i_M^2 \quad (34)$$

$$w_1 = 1 + \frac{g}{G} \cdot \frac{J_k}{r_d^2} \quad (35)$$

$$w_2 = \frac{g}{G} \cdot \frac{J_G \cdot \eta_{fd} \cdot i_{fd}^2}{r_d^2} \quad (36)$$

$$w_3 = \frac{g}{G} \cdot \frac{J_E \cdot \eta_{fd} \cdot i_{fd}^2}{r_d^2} \quad (37)$$

$$w_4 = \frac{g}{G} \cdot \frac{J_M \cdot \eta_{fd} \cdot i_{fd}^2}{r_d^2} \quad (38)$$

Using relations from (28) to (31) with the assumptions of the model ($J_R \approx 0$), a simplified version of the predictive control model is presented below:

$$\left[J_E + J_G \left(\frac{R_1+S_1}{S_1}\right)^2\right] \cdot \dot{\omega}_E - \left[J_G \frac{R_1 \cdot S_2 \cdot (R_1+S_1)}{R_2 \cdot S_1^2}\right] \cdot \dot{\omega}_M = P_E \cdot \eta_{C_1/R} \cdot \omega_E^{-1} + P_G \cdot \frac{(R_1+S_1)}{S_1} \cdot \eta_{S_1/C_1} \cdot \omega_G^{-1} \quad (39)$$

$$\left[J_E \cdot \frac{R_1}{R_1+S_1}\right] \dot{\omega}_E + \left[J_M \frac{R_2}{S_2} - m \cdot \left(\frac{r_d}{f_d}\right)^2 \cdot \frac{S_2}{R_2}\right] \cdot \dot{\omega}_M = P_E \cdot \frac{R_1}{R_1+S_1} \eta_{\frac{C_1}{R}} \cdot \omega_E^{-1} + P_M \cdot \frac{R_2}{S_2} \eta_{\frac{R_2}{R}} \cdot \omega_M^{-1} + \frac{T_{brk} \cdot \eta_{fd}}{f_d} + \frac{1}{2} \cdot \rho_A \cdot C_d \cdot A_f \cdot \frac{{S_2}^2 \cdot {\omega_M}^2 \cdot r_d^3}{{R_2}^2 \cdot f_d^3} - mg \cdot \frac{r_d}{f_d} (f_r \cos\alpha + \sin\alpha) \quad (40)$$

3.4. Operation of the electrochemical energy storage system

The full electric hybrid powertrain system of the vehicle assumes the efficient use of an electric power source. The status of available electricity is reflected in the battery charge level (SOC) [12, 20, 34, 35]:

$$SOC = \frac{Q_{max} - Q_{used}}{Q_{max}} \cdot 100\% \quad (41)$$

The used electrical capacity of the battery is described by the following relation:

$$Q_{used} = \begin{cases} \int_0^t I_{bat} \cdot dt \\ \int_0^t I_{bat} \eta_{coulomb} dt \end{cases} \quad (42)$$

Please note that $I_{bat} > 0$ (discharging), $I_{bat} < 0$ (charging). Hence, the derivative of the electrochemical charge level of the energy storage system can be presented as follows:

$$\dot{SOC} = -\frac{I_{bat}}{Q_{max}} \quad (43)$$

Power of the electrochemical energy storage system:

$$P_{bat} = U_{bus} \cdot I_{bat} = (V_{oc} - I_{bat} \cdot r_{bat}) \cdot I_{bat} = V_{oc} I_{bat} - I_{bat}^2 \cdot r_{bat} \quad (44)$$

Ultimately, the charging or discharging current of the battery takes the following form:

$$\dot{SOC} = -\frac{V_{OC} - \sqrt{V_{OC}^2 - 4 r_{bat} P_{bat}}}{2 r_{bat} Q_{max}} \quad (45)$$

The power of the energy storage system P_{bat} is used during all driving modes. Both during the drive or recuperation process. To cover the power demand generated by the generator and/or the electric motor according to the following relation:

$$P_{bat} = P_G \cdot \eta_G^k \cdot \eta_{C1}^k + P_M \cdot \eta_M^k \cdot \eta_{C2}^k = P_{des} - P_E \quad (46)$$

P_{des} is the power expected through pressing the accelerator or brake pedal. The power of the energy storage system shall be either a positive value during discharge or a negative value during charging.

3.5. Restrictions to the energy storage system

The applied energy management strategy – the predictive control is characterised by specific limitations of the energy storage system:

a) traction battery power:

$$P_{bat}^{min} \le P_{bat} \le P_{bat}^{max} \quad (47)$$

(b) the level of charge of the traction battery:

$$SOC^{min} \le SOC \le SOC^{max} \quad (48)$$

The mathematical model has been linearised to the specific conditions. The linear form of the MPC model is represented by the matrices:

$$\begin{bmatrix} E_{11} & -E_{12} \\ E_{21} & E_{22} - \rho_A \cdot C_d \cdot A_f \cdot \frac{S_2^2 \cdot r_d^3}{R_2^2 \cdot f_d^3} \end{bmatrix} \cdot \begin{bmatrix} \dot{\omega}_E \\ \dot{\omega}_M \end{bmatrix} = \begin{bmatrix} \eta_{C_1/R} \cdot \omega_E^{-1} & \frac{R_1}{R_1+S_1} \cdot \eta_{S_1/C_1} & 0 \\ \frac{R_1}{R_1+S_1} \eta_{C_1/R} & 0 & \frac{R_2}{S_2} \eta_{R_2/R} \end{bmatrix} \begin{bmatrix} P_E \cdot \omega_E^{-1} \\ P_G \cdot \omega_G^{-1} \\ P_M \cdot \omega_M^{-1} \end{bmatrix} \quad (49)$$

where:

$$E_{11} = J_E + J_G \left(\frac{R_1+S_1}{S_1}\right)^2, \quad E_{12} = \left[J_G \frac{R_1 \cdot S_2 \cdot (R_1+S_1)}{R_2 \cdot S_1^2}\right],$$
$$E_{21} = \left[J_E \cdot \frac{R_1}{R_1+S_1}\right], \quad E_{22} = \left[J_M \frac{R_2}{S_2} - m \cdot \left(\frac{r_d}{f_d}\right)^2 \cdot \frac{S_2}{R_2}\right] \quad (50)$$
$$E_D = E_{11}(E_{22} - \rho \cdot C_d \cdot A_f \cdot \frac{S_2^2 \cdot r_d^3}{R_2^2 \cdot f_d}) + E_{12} \cdot E_{21}$$

3.6. Mileage fuel consumption

The mileage fuel consumption of the HEV is a result of several other parameters. Not only the fuel consumption of the internal combustion engine, but also the equivalent fuel consumption of the electric motor should be taken into account here. This is described in the following relations showing the relationships between the required power values of the internal combustion engine and the electric motor [28, 35]:

$$b = \frac{\dot{m}}{P_E} \tag{51}$$

$$\dot{m} = b \cdot P_E = \frac{P_{Edes}}{\eta_E \cdot W_u} \tag{52}$$

The calorific value of the fuel (petrol) was equal to $44 \cdot 10^6$ J/kg. The equivalent fuel consumption, calculated on the basis of the consumed energy of the traction battery, has been determined in accordance with the formula:

$$\dot{m_{eq}} = C_{bat} \cdot P_{bat} = C_{bat} \cdot V_{oc} \cdot I_{bat} \tag{53}$$

Ultimately, the equivalent fuel consumption takes the form of:

$$\dot{m_{eq}} = \frac{C_{bat}}{2r_{bat}}\left[V_{oc}^2 - V_{oc} \cdot \sqrt{V_{oc}^2 - 4r_{bat}P_{bat}}\right] \tag{54}$$

The value of the equivalent fuel consumption coefficient C_{bat} was determined and equalled 0.0000227. The parameter was determined on the basis of the equivalent fuel consumption. As the power of the traction battery to the calorific value of the fuel coefficient. According to [11], the values of b1 and the coefficient a1 were adopted from 0.0000227 to 0.0000237.

Taking into account the above relationships, the instantaneous fuel consumption of the HEV (related to the distance) can be described using the formula:

$$\mathbf{Q} = \frac{\mathbf{100} \cdot (\dot{\mathbf{m}} + \dot{\mathbf{m}}_{\mathbf{eq}})}{\mathbf{3600} \cdot \boldsymbol{\rho}_{\boldsymbol{F}} \mathbf{v}} = \frac{\dot{\mathbf{m}} + \dot{\mathbf{m}}_{\mathbf{eq}}}{\mathbf{36} \cdot \boldsymbol{\rho}_{\boldsymbol{F}} \mathbf{v}} \tag{55}$$

The mileage consumption of the HEV is related to the cost function, which is associated with the predictive control model of the HEV's powertrain system energetic machines. The main objective of the presented energy management system is to minimise fuel consumption and equivalent fuel consumption. The parameter describing the total fuel consumption of the vehicle is determined by the relation [16]:

$$J = \sum_{s=0}^{N-1}(fuel_s + \alpha_E \Delta_{SOC}^2) \rightarrow \min \tag{56}$$

$$\Delta_{SOC} = \begin{cases} SOC_s - SOC_d & SOC_s < SOC_d \\ 0 & SOC_k \geq SOC_d \end{cases} \tag{57}$$

Using the previous dependencies, the cost function takes the following form:

$$J = \int_0^{N \cdot t_d} \rho(\left[\dot{m}(P_{E\_des}, \tau)\right]^2 + \left[\dot{m}_{eq}(P_{G\_des}, P_{M\_des}, \tau)\right]^2)\}d\tau \rightarrow \min \tag{58}$$

The expected value of the torque in the function of cost is related to the value of the output power from the system. Relation (58) takes the form of [34, 37]:

$$J = \int_0^{N \cdot t_d}\left[P_{pre}(\tau) - P_R\right]^2 + \rho(\left[\dot{m}(P_{E\_des}, \tau)\right]^2 + \left[\dot{m}_{eq}(P_{G\_des}, P_{M\_des}, \tau)\right]^2)\}d\tau \rightarrow \min \tag{59}$$

Since the function of cost is non-linear, according to relation (59) the control of the output parameters must be converted to the category m and m_{eg}:

$$P_{E\_des} = \eta_E \cdot W_u \cdot \dot{m} \tag{60}$$

Equations (51) and (53) take the form:

$$P_{des} = \frac{\dot{m}_{eq}}{C_{bat}} - \frac{r_{bat} \cdot \dot{m}_{eq}^{\ 2}}{V_{oc}^2 \cdot C_{bat}^{\ 2}} + P_E \tag{61}$$

The linear model of the operational points themselves is as follows:

$$\dot{T_E} = -\frac{1}{\tau_E}T_E + \Gamma_{e\omega e} \cdot \omega_E + \Gamma_{em} \cdot \dot{m} \tag{62}$$

$$\dot{T_G} = \Gamma_{GTE} \cdot T_E - \frac{1}{\tau_G}T_G \tag{63}$$

$$\dot{T_M} = \Gamma_{MTE} \cdot T_E - \frac{1}{\tau_M}T_M + \Gamma_{M\omega_E} \cdot \omega_E + \Gamma_{M\omega_M} \cdot \omega_M + \Gamma_{Meq} \cdot \dot{m_{eq}} \tag{64}$$

where:

$$\Gamma_{e\omega e} = -\frac{1}{\tau_E} \cdot \frac{\eta_e \cdot W_u \cdot \dot{m}_0}{\omega_{E0}^2}, \Gamma_{em} = \frac{1}{\tau_E} \cdot \frac{\eta_e \cdot W_u}{\omega_{E0}} \tag{65}$$

$$\Gamma_{GTE} = -\frac{1}{\tau_G} \cdot \frac{S_1}{R_1 + S_1} \tag{66}$$

$$\Gamma_{MTE} = -\frac{1}{\tau_M} \cdot (\frac{R_1}{S_1 + R_1} \cdot \frac{S_2}{R_2} - \frac{\omega_{E0}}{\omega_{M0}}) \tag{67}$$

$$\Gamma_{M\omega E} = \frac{1}{\tau_M} \cdot \frac{T_{E0}}{\omega_{M0}} \tag{68}$$

$$\Gamma_{M\omega_M} = -\frac{1}{\tau_M \cdot \omega_{M0}^2} \cdot (\frac{\dot{m}_{eq0}}{C_{bat}} - \frac{r_{bat} \cdot \dot{m}_{eq0}^2}{V_{0C}^2 \cdot C_{bat}^2} + T_{E0} \cdot \omega_{E0}) \tag{69}$$

$$\Gamma_{M_{eq}} = -\frac{1}{\tau_M \cdot C_{bat} \cdot \omega_{M0}} \cdot (1 - 2\frac{r_{bat}}{V_{0C}^2 \cdot C_{bat}}) \tag{70}$$

The linear form of the energy management model is as follows:

$$\begin{cases} \dot{x} = A_c x + B_c \mathbf{u} \\ y = C_c x + D_c \mathbf{u} \end{cases}, \mathbf{u} = \begin{bmatrix} \dot{m} \\ \dot{m_{eq}} \end{bmatrix} \mathbf{y} = P_R \tag{71}$$

Equation describing A_c:

$$\mathbf{A_c} = \begin{bmatrix} -\frac{1}{\tau_E} & 0 & 0 & \Gamma_{e\omega e} & 0 & 0 \\ \Gamma_{GTE} & -\frac{1}{\tau_G} & 0 & 0 & 0 & 0 \\ \Gamma_{MTE} & 0 & -\frac{1}{\tau_M} & \Gamma_{M\omega E} & \Gamma_{M\omega M} & 0 \\ \frac{E_{22}}{E_D} - \rho \cdot C_d \cdot A_f \cdot \frac{S_2^2 \cdot r_d^3}{R_2^2 \cdot f_d^3 \cdot E_D} + \frac{E_{12}}{E_D}\left(\frac{R_1}{R_1+S_1}\right) & \frac{E_{22}}{E_D} - \rho \cdot C_d \cdot A_f \cdot \frac{S_2^2 \cdot r_d^3}{R_2^2 \cdot f_d^3 \cdot E_D}\left(\frac{R_1}{R_1+S_1}\right) & \frac{E_{12}}{E_D}\frac{R_2}{S_2} & 0 & 0 & 0 \\ -\frac{E_{21}}{E_D} + \frac{E_{11}}{E_D}\left(\frac{R_1}{R_1+S_1}\right) & -\frac{E_{21}}{E_D}\left(\frac{R_1}{R_1+S_1}\right) & \frac{E_{11} \cdot R_2}{E_D \cdot S_2} & 0 & 0 & 0 \\ 0 & \Gamma_{sG} & \Gamma_{sM} & \Gamma_{s\omega e} & \Gamma_{s\omega M} & 0 \end{bmatrix} \quad (72)$$

$$\mathbf{x} = \begin{bmatrix} P_E \\ P_G \\ P_M \\ \omega_E \\ \omega_M \\ SOC \end{bmatrix} \quad (73)$$

$$\mathbf{B_c} = \begin{bmatrix} \Gamma_{em} & 0 \\ 0 & 0 \\ 0 & \Gamma_{Meq} \\ 0 & 0 \\ 0 & 0 \\ 0 & 0 \end{bmatrix} \quad (74)$$

$$\mathbf{C_C^T} = \begin{bmatrix} \frac{R_1}{R_1 + S_1} \\ 0 \\ \frac{R_2}{S_2} \\ 0 \\ 0 \\ 0 \end{bmatrix} \quad (75)$$

$$\mathbf{D_c} = 0 \quad (76)$$

$$\dot{\mathbf{x}} = A_c x + B_c \mathbf{u}$$
$$\mathbf{y} = C_c x \quad (77)$$

where A_c described in (72):

The solution of the mathematical model presented above is the use of the LQT controller (Fig. 2) and the conversion of the analytical version of the model to a discrete version.

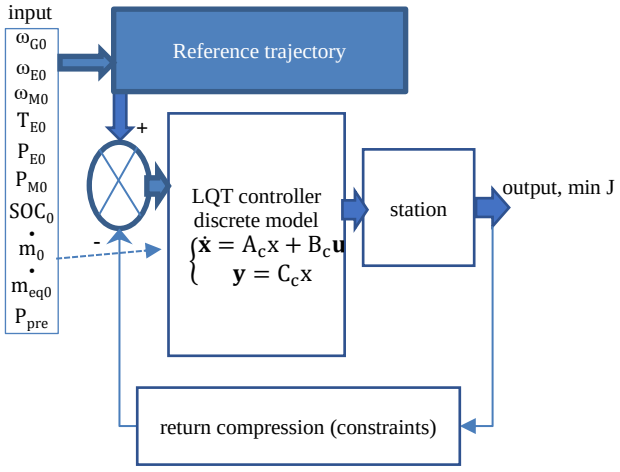

Fig. 2. LQT algorithm architecture

The LQT controller uses input parameters that are the parameters of the model. Also, the linear form of the model (discrete) in order to search for the optimal (minimum) solution of the cost function J. The return compression is supposed to provide the optimal value of the cost function.

The values of the input parameters for the implementation of the presented LQT algorithm are presented in Table 2.

Table 2. Simulation parameters

Machine	Parameter	Value
Vehicle	total weight	1630 kg
combustion engine	start delay	0.5 s
	time constant	1 s
	max. output power	73 kW
electric motor	output power	60 kW
electrochemical energy storage system	SOC upper level	0.75
	SOC lower level	0.45
	SOC objective	0.60

4. Test results

4.1. Statistics of ICE

The most important parameter that affects power was the torque of ICE. Within 616 seconds of travel, in the test it was measured 241 ICE operating points. This parameter has been ordered from the minimum to maximum value. After that, the created series was divided into groups. After calculating the frequency of occurrences in a given group, we obtained a distributive series. Each distributive series was characterized by the class intervals of groups and the number of cases occurring in subsequent groups. These are the parameters of the ICE statistics (Table 3) that were used to describe the distributive series.

Table 3. ICE statistics parameters

Distributive series – torque of the ICE	
Parameter	Value
Number of observations (n)	241
Number of classes (k)	$\sqrt{241} = 15.52 \sim 16$
Minimum value (Min)	0.01 Nm
Maximum value (Max)	142 Nm
Max-min	141.99 Nm
(Max-min)/k	8.87~9
Descriptive statistics – torque of the ICE	
Average	23.36 Nm
Median	12.23 Nm
Variance	670.93 Nm
Standard deviation	25.90 Nm
Lower Quartile	2.78 Nm
Upper Quartile	36.83 Nm
Skewness	1.33
Kurtosis	1.14

According to the presented graph (Fig. 2), the values of the ICE torque were divided into 16 classes. But in the last 3 classes (117…142 Nm) there were no torque operating points. For this reason, 13 value classes have been selected to declare 13 reference trajectories.

13 reference trajectories were described in Table 4 (below) and were used in LQT algorithm architecture (Fig. 2).

There were estimated based the equations of trend curves (values of ICE torque).

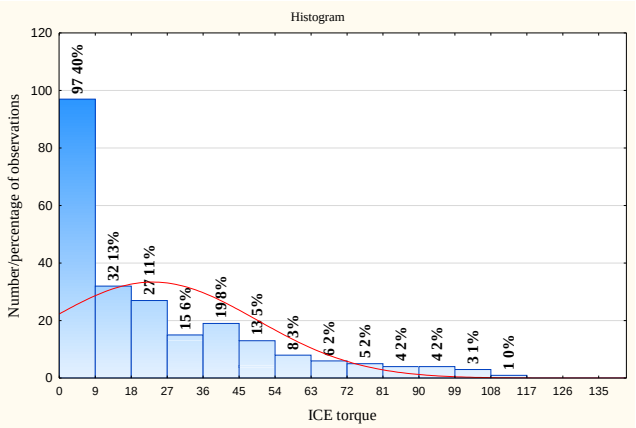

Fig. 2. Histogram of ICE torque (red line – expected normal)

Table 4. Reference trajectory

IF $0 < T_E \leq 9$ Nm THEN:	$T_{Edes} = -7 \cdot 10^{-7} \cdot n_E{}^2 + 0.0033 \cdot n_E - 0.3969$ $P_{Edes} = T_{Edes} \cdot \omega_E$ $P_{Edes} = P_E$
IF $9 < T_E \leq 18$ Nm THEN:	$T_{Edes} = 3 \cdot 10^{-8} \cdot n_E{}^2 - 0.0016 \cdot n_E + 14.903$ $P_{Edes} = T_{Edes} \cdot \omega_E$ $P_{Edes} = P_E$
IF $18 < T_E \leq 27$ Nm THEN:	$T_{Edes} = -1 \cdot 10^{-6} \cdot n_E{}^2 + 0.0053 \cdot n_E + 16.245$ $P_{Edes} = T_{Edes} \cdot \omega_E$ $P_{Edes} = P_E$
IF $27 < T_E \leq 36$ Nm THEN:	$T_{Edes} = -1 \cdot 10^{-6} \cdot n_E{}^2 - 0.0058 \cdot n_E + 38.056$ $P_{Edes} = T_{Edes} \cdot \omega_E$ $P_{Edes} = P_E$
IF $36 < T_E \leq 45$ Nm THEN:	$T_{Edes} = -1 \cdot 10^{-6} \cdot n_E{}^2 + 0.001 \cdot n_E + 42.293$ $P_{Edes} = T_{Edes} \cdot \omega_E$ $P_{Edes} = P_E$
IF $45 < T_E \leq 54$ Nm THEN:	$T_{Edes} = 4 \cdot 10^{-7} \cdot n_E{}^2 - 0.0008 \cdot n_E + 48.387$ $P_{Edes} = T_{Edes} \cdot \omega_E$ $P_{Edes} = P_E$
IF $54 < T_E \leq 63$ Nm THEN:	$T_{Edes} = -6 \cdot 10^{-6} \cdot n_E{}^2 + 0.0196 \cdot n_E + 46.391$ $P_{Edes} = T_{Edes} \cdot \omega_E$ $P_{Edes} = P_E$
IF $63 < T_E \leq 72$ Nm THEN:	$T_{Edes} = -2 \cdot 10^{-6} \cdot n_E{}^2 + 0.0069 \cdot n_E + 59.273$ $P_{Edes} = T_{Edes} \cdot \omega_E$ $P_{Edes} = P_E$
IF $72 < T_E \leq 81$ Nm THEN:	$T_{Edes} = -1 \cdot 10^{-5} \cdot n_E{}^2 + 0.00457 \cdot n_E + 42.177$ $P_{Edes} = T_{Edes} \cdot \omega_E$ $P_{Edes} = P_E$
IF $81 < T_E \leq 90$ Nm THEN:	$T_{Edes} = -3 \cdot 10^{-5} \cdot n_E{}^2 + 0.0859 \cdot n_E + 27.572$ $P_{Edes} = T_{Edes} \cdot \omega_E$ $P_{Edes} = P_E$
IF $90 < T_E \leq 99$ Nm THEN:	$T_{Edes} = -0.0002 \cdot n_E{}^2 + 0.3827 \cdot n_E - 130.24$ $P_{Edes} = T_{Edes} \cdot \omega_E$ $P_{Edes} = P_E$
IF $99 < T_E \leq 135$ Nm THEN:	$T_{Edes} = 5 \cdot 10^{-5} \cdot n_E{}^2 - 0.1633 \cdot n_E + 240.11$ $P_{Edes} = T_{Edes} \cdot \omega_E$ $P_{Edes} = P_E$
IF $135 < T_E \leq 142$ Nm THEN:	$T_{Edes} = -4 \cdot 10^{-6} \cdot n_E{}^2 + 0.035 \cdot n_E + 73.868$ $P_{Edes} = T_{Edes} \cdot \omega_E$ $P_{Edes} = P_E$

4.2. Speed profile

On Figure 3 it was presented speed profile during the road tests.

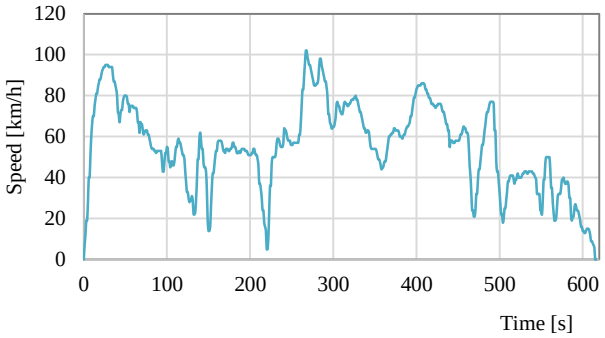

Fig. 3. Speed profile during the road tests

The HEV's speed varied from 0 km/h to 102 km/h over the entire period of time. The values of this parameter were characteristic for urban driving (less than or equal to 50 km/h) and extra-urban driving (greater than 50 km/h). When driving below 50 km/h, the electric drive mode of the HEV was frequently engaged. Above this speed, the electric hybrid powertrain was operating in the Normal Drive Mode (NORMAL)

4.3. Power of energetic machines

On Figure 4, the degree of electrochemical charge of the energy storage system is presented. It is worth noting that the applied model predictive control contributes to a higher level of charge of the traction battery while driving.

Fig. 4. Level of charge of the traction battery

This is due to the energy accumulation system power values (Fig. 5), which translate into the level of battery charge. Negative power indicates charging of the energy storage system, while positive power indicates the discharging thereof.

For the factory control, the power of the traction battery varies from –17.87 to 26.96 kW. For the model predictive control, the power of the traction battery varies from –20.16 to 27.85 kW.

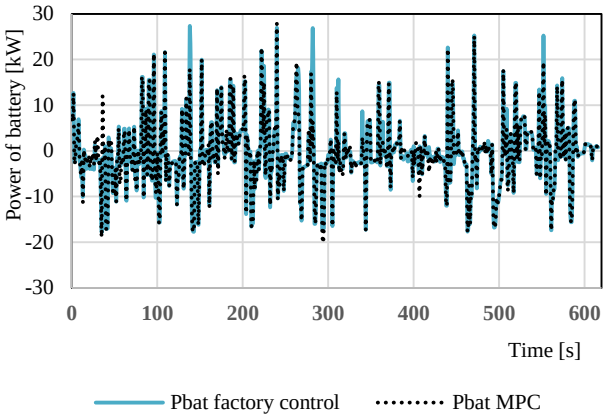

Fig. 5. Power of battery

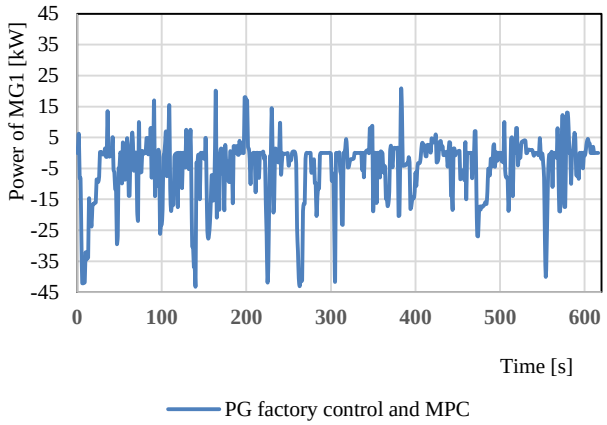

Fig. 6. Power of MG1

For the factory control and for model predictive control, the power of the MG1 varies from –43.09 to 20.49 kW.

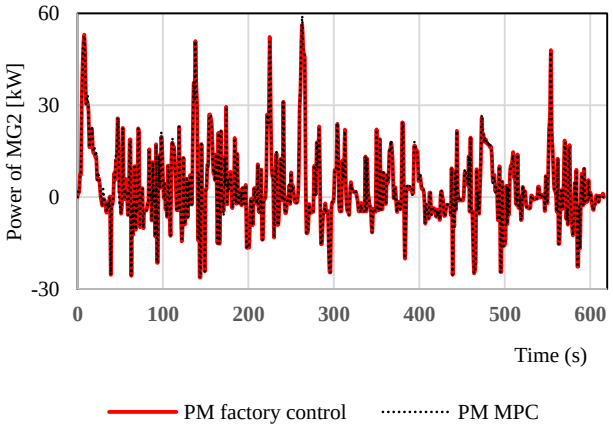

Fig. 6. Power of MG2

For the factory control, the power of the MG2 varies from –26.19 to 56.24 kW. For the predictive control, the power of the traction battery varies from –26.19 to 59.16 kW.

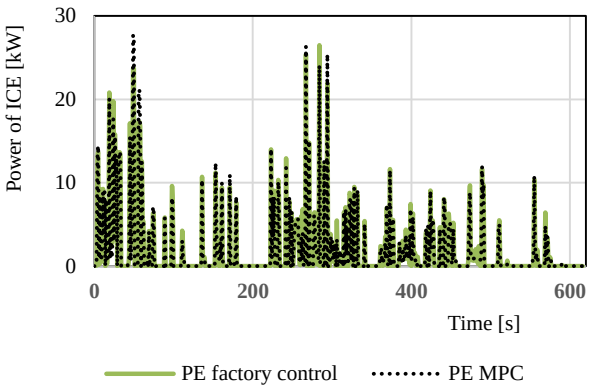

Fig. 7. Power of ICE

For the factory control, the power of the internal combustion engine varies from 0 to 26.50 kW. For the model predictive control, the power of the internal combustion engine varies from 0 to 27.58 kW. It can be concluded that the change of control type has an impact on the change of the power value of the internal combustion engine.

An important fact is that the power of the battery depends on the power balance of the generator and the electric motor. Hence, the negative power values of the electrochemical energy storage system indicate that the power is being recovered. This can be achieved during regenerative braking of the vehicle. Positive values of battery power indicate the use of energy accumulated in it.

4.4. Rotational velocities of energy machines

Rotational velocities of energetic machines (Fig. 8) are the same for both factory control and model predictive control of the system.

factory control, MPC

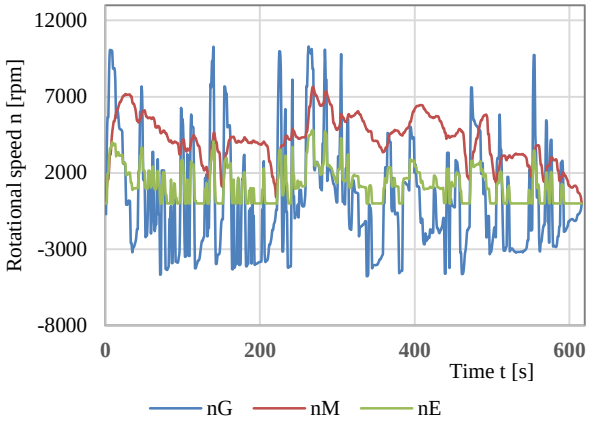

Fig. 8. Rotational speeds of energetic machines

The rotational speed of the internal combustion engine is between 0 and 4800 rpm. The rotational speed of the generator is between –4769 and 10,292 rpm. The rotational speed of the electric motor is between 0 and 7630 rpm.

4.5. Fuel consumption of internal combustion engine and electric motor

Figure 9 and Fig. 10 show the equivalent consumption of fuel of the battery and the fuel consumption of the internal combustion engine.

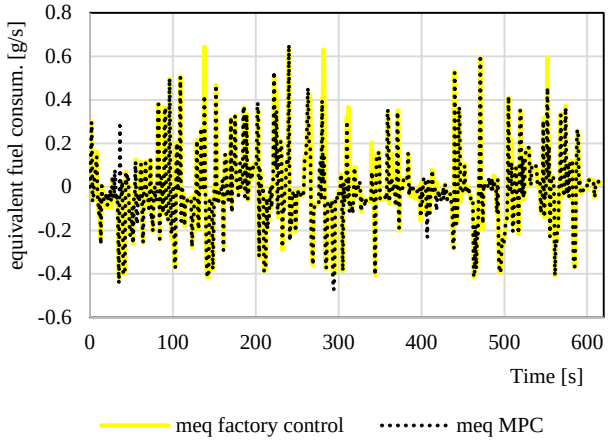

Fig. 9. Equivalent fuel consumption

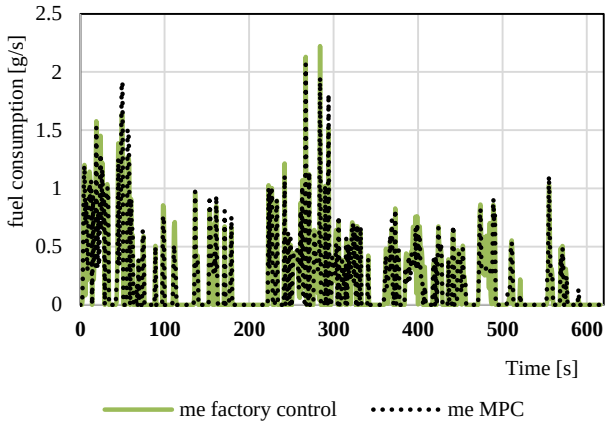

Fig. 10. Fuel consumption

In the course of the factory control mode, the equivalent fuel consumption is between –0.42 g/s and 0.63 g/s. For model predictive control equivalent fuel consumption values range from –0.47 g/s to 0.65 g/s.

The fuel consumption of the internal combustion engine reaches values from 0 to 2.22 g/s (factory control) and from 0 to 2.06 g/s (MPC).

4.6. Power map of the internal combustion engine

Figure 11 presents power maps of the internal combustion engine in the course of factory and model predictive control.

On the basis of the graphs, some differences can be noticed in the location of the useful power values of the engine (with factory control and model predictive control).

In the case of the factory control, the useful power values are distributed in the range from 0 to 26.5 kW. This corresponds to an overall engine efficiency from 0 to 34%. In the case of the model predictive control, most of the useful power of the internal combustion engine is concentrated in the range from 0 to 27.6 kW. For this type of control, the overall efficiency values of the internal combustion engine are between 0 and 34%.

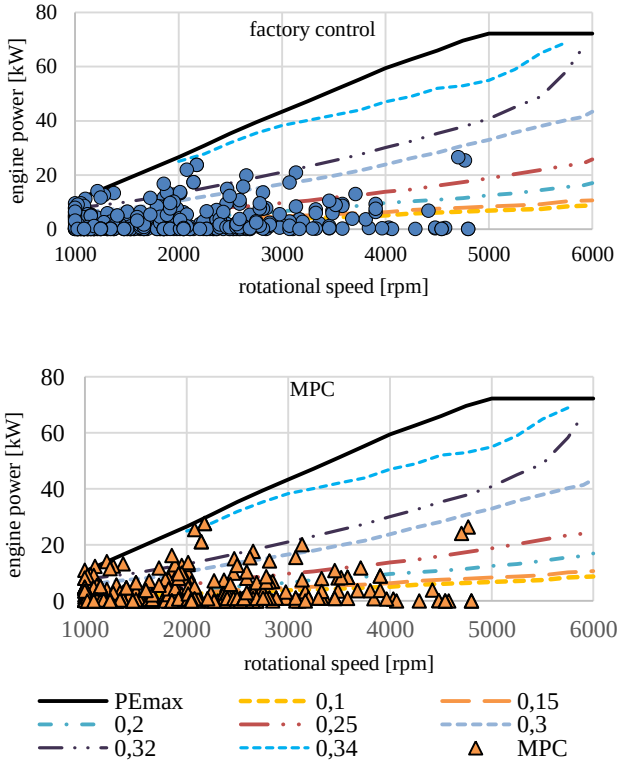

Fig. 11. Power map of the internal combustion engine

5. Model validation

Model validation was based on comparison of fuel consumption value of the HEV according to the manufacturer, factory control and MPC with LQT (Table 5).

Table 5. Mileage fuel consumption

	mileage fuel consumption	
	[dm^3/100 km]	[mpg]
factory control	1.90	123.78
MPC	1.79	130.98
Manufacturer	2.10	111.87

The mileage consumption of the Toyota Prius 3 (2012) HEV provided by the manufacturer was determined on the basis of tests in established laboratory conditions (for a mixed cycle). It is 10% higher than the value of the mileage consumption of the HEV obtained on the presented route. The difference may be due to different measurement conditions. This could have been caused by other speed and acceleration values in road conditions, additional electric receivers turned off on the route, etc. The simulation of energy management of energetic machines according to MPC allowed to reduce the mileage fuel consumption from 1.90 to 1.79 dm^3/100 km. This is the HEV fuel consumption savings of 4%.

6. Conclusion

The mileage consumption of the Toyota Prius 3 (2012) HEV provided by the manufacturer was 10% higher than the value of the mileage consumption of the HEV obtained on the presented route. The evaluation of the HEV mileage fuel consumption in real road conditions according to MPC with 13 reference trajectories showed total fuel savings of 4%. The energy management system used have good effect on SOC in comparison to factory control. Under MPC (with 13 reference trajectories) at the end of the course SOC was 6.7 % higher than under factory control. Changes of SOC – factory control: from 50.1% (the beginning) to 56.1% (the end of course); for MPC from 50.1% (the beginning) to 59.9% (the end of the course). The research method used was a case study. The values of the mileage fuel consumption were considered for one specific HEV model (and one specific route). Due to the great similarity in the design of the drive system of the test object and other HEVs, it can be assumed that the test results were general in nature. The percentage improvement in fuel economy in MPC can also translates into other HEVs. The adopted work methodology contained certain limitations. They included, among others road tests in urban and extra-urban conditions (motorway conditions have not been taken into account) as well as considering only mileage fuel consumption. The directions of future research follow directly from the limitations. It would be worth carrying out road tests of HEV fuel consumption with MPC not only in urban and extra-urban conditions, but also in highway conditions. An interesting idea would also be road tests of HEV exhaust emissions with MPC.

Nomenclature

HEV hybrid electric vehicle
ICE internal combustion engine
MPC model predictive control
MG1 generator
MG2 electric motor
A_f frontal area of vehicle (m^2)
b specific fuel consumption (kg/Ws)
C_d air drag resistance coefficient
C_1 number of teeth of the first set satellites (m)
C_2 number of teeth of the second set of satellites (m)
f_d total gear ratio
f_r rolling resistance coefficient
F_a air resistance (N)
F_i inertia resistance (N)
F_p propelling force (N)
F_r rolling resistance (N)
F_s slope resistance (N)
F_1 internal force between teeth of the first gear (N)
F_2 internal force teeth force of the second gear (N)
$fuel_s$ fuel consumption (g)
g gravitational acceleration (m/s^2)
I_{bat} battery charging/discharging current (A)
J cost function (g)
J_E mass moment of inertia of the ICE (kgm^2)
J_G mass moment of inertia of the MG1 (kgm^2)
J_R mass moment of inertia of the planetary gear ring wheel (kgm^2)
J_M mass moment of inertia of the MG2 (kgm^2)
m total mass of vehicle (kg)
$\dot{m}$ actual fuel consumption (kg/s)
$\dot{m}_{eq}$ equivalent fuel consumption (kg/s)
N number of steps
P_{bat} power of battery (W)
P_E power of the ICE (kW)
P_G generator power (kW)
P_M electric motor power (kW)
P_R power of the ring gear of the planetary gear (kW)
P_{Edes} desired power of the ICE (kW)
P_{Gdes} desired power of the generator (kW)
P_{Mdes} desired power of the electric motor (kW)
P_{pre} expected system power (kW)
P_{resis} resistance power (kW)
Q_{max} maximum battery capacity (Ah)
Q_{used} battery capacity used (Ah)
r_{bat} internal battery resistance (Ω)
r_d dynamic wheel radius (m)
R number of teeth of the ring gear (m)
R_1 number of crown wheel teeth (m)
R_2 number of ring wheel teeth on the electric motor side (m)
s step
SOC state of charge (%)
SOC_d desired state of charge (%)
S_1 number of teeth of the first sun gear (m)
S_2 number of teeth of the second sun gear (m)
t time (s)
t_d jump (step level)
T_{brk} brake torque (Nm)
T_{des} desired torque (Nm)
U_{bus} voltage in the battery circuit (V)
v_{veh} vehicle speed (m/s)
V_{OC} open-circuit voltage of the battery (V)
W_u calorific value of fuel (J/kg)
α slope of elevation (^{0})
α_E penalty factor
ω_{C1} angular speed of the satellite yoke C_1 (1/s)
ω_E angular speed of the ICE (1/s)
ω_G angular speed of the generator (1/s)
ω_M angular speed of the electric motor (1/s)
ω_R angular speed of the crown wheel R (ring) (1/s)
ω_{s1} angular speed of the sun wheel S1 (1/s)
ω_{s2} angular speed of the sun wheel S2 (1/s)
ρ coefficient occurring between the tracking error and the equivalent fuel consumption
ρ_A air density (kgm^{-3})
$\eta_{coulomb}$ Coulomb efficiency
η_{C1} generator efficiency
η_{C2} motor efficiency
$\eta_{C1/R}$ efficiency between the first set satellites and the ring gear
η_E overall engine efficiency
η_{fd} final drive efficiency

$\eta_{R2/R}$ efficiency between the second ring wheel teeth and the ring gear
$\eta_{S1/C1}$ efficiency between the first sun gear and the first set of satellites
τ_E internal combustion engine operation time (s)
τ_G generator operation time (s)
τ_M electric motor operation time (s)

Bibliography

[1] Abido MA. Optimal power flow using particle swarm optimization. Int J Elec Power. 2002;24:563-571. https://doi.org/10.1016/S0142-0615(01)00067-9

[2] Back M. Pradikitive Antriebregulung zum Energieoptimalen Betrieb von Hybridfahrzeugen. 2004. Dissertation, Univ. Karlsruhe.

[3] Barsali S, Miulli C, Possenti A. A control strategy to minimalize fuel consumption of series hybrid electric vehicles. IEEE Trans Veh Technol. 2004;19(1):187-195. https://doi.org/10.1109/TEC.2003.821862

[4] Bieniek A, Graba M, Mamala J, Prażnowski K, Hennek K. Energy consumption of a passenger car with a hybrid powertrain in real traffic conditions. Combustion Engines. 2022;191(4):15-22. https://doi.org/10.19206/CE-142555

[5] Borhan HA, Vahidi A. Model predictive control of a power-split hybrid electric vehicle with combined battery and ultracapacitor energy storage. Proceedings of the 2010 American Control Conference. 2010:5031-5036. https://doi.org/10.1109/ACC.2010.5530728

[6] Cao J, Peng J, He H. Modeling and simulation research on power-split hybrid electric vehicle. Energy Proced. 2016;104:354-359. https://doi.org/10.1016/j.egypro.2016.12.060

[7] Chen S-Y, Hung Y-H, Wu C-H, Huang S-T. Optimal energy management of a hybrid electric powertrain system using improved particle swarm optimization. Appl Energy. 2015;160:132-145. https://doi.org/10.1016/j.apenergy.2015.09.047

[8] Chen Z, Xiong R, Cao J. Particle swarm optimization-based optimal power management of plug-in hybrid electric vehicles considering uncertain driving conditions. Energy. 2016;(96):197-208. https://doi.org/10.1016/j.energy.2015.12.071

[9] Chen Z, Xiong R, Wang K, Jiao B. Optimal energy management strategy of a plug-in hybrid electric vehicle based on a particle swarm optimization algorithm. Energies. 2015;8:3661-3678. https://doi.org/10.3390/en8053661

[10] Delprat S, Lauber J, Guerra TM, Rimaux J. Control of a parallel hybrid powertrain: optimal control. IEEE Trans Veh Technol. 2004;53(3):872-881. https://doi.org/10.1109/tvt.2004.827161

[11] Gao J, Zhu G, Strangas E, Sun F. Equivalent fuel consumption optimal control of a series hybrid electric vehicle. P I Mech Eng D-J Aut. 2009;23:1003-1018. https://doi.org/10.1243/09544070JAUTO107

[12] Golebiewski W, Lisowski M. Theoretical analysis of electric vehicle energy consumption according to different driving cycles. IOP Conf Ser Mater Sci Eng. 2018;421:022010. https://doi.org/10.1088/1757-899X/421/2/022010

[13] Grudzinski P. Toyota Hybrid Drive System. Toyota Motor Poland. 2022.

[14] Guzzella L, Sciarretta A. Vehicle Propulsion Systems. Introduction to Modeling and Optimalization. Berlin: Springer-Verlag. 2005, 190.

[15] Hwang H-Y, Chen J-S. Optimized fuel economy control of power – split hybrid electric vehicle with particle swarm optimization. Energies. 2020;13:2278. https://doi.org/10.3390/en13092278

[16] Kim TS, Manzie C, Sharma R. Model predictive control of velocity and torque split in a parallel hybrid vehicle. IEEE Sys Man Cyber. 2009:2014-2019.

[17] Kleimaier A, Schroder D. An approach for the online optimized control of a hybrid powertrain. 7th International Workshop on Advanced Motion Control. 2002:215-220. https://doi.org/10.1109/AMC.2002.1026919

[18] Lin CC, Peng H, Grizzle JW, Kang J-M. Power management strategy for a parallel hybrid electric truck. IEEE T Contr Syst T. 2003;11(6):839-849. https://doi.org/10.1109/TCST.2003.815606

[19] Lin CC, Peng H, Grizzle JW. A stochastic control strategy for hybrid electric vehicles. P Amer Contr Conf. 2004;(5):4710-4715. https://doi.org/10.23919/ACC.2004.1384056

[20] Liu J, Peng H. Modeling and control of a power-split hybrid vehicle. IEEE T Contr Syst T. 2008;16(6):1242-1251. https://doi.org/10.1109/TCST.2008.919447

[21] Liu J, Peng H. Automated modelling of a power-split hybrid vehicles. IFAC P Vol. 2008;41(2):4648-4653. https://doi.org/10.3182/20080706-5-KR-1001.00782

[22] Merkisz J, Pielecha I. Uklady mechaniczne pojazdow hybrydowych. Wydawnictwo Politechniki Poznanskiej. Poznan 2015.

[23] Moura SJ, Fathy HK, Callaway DS, Stein JL. A stochastic optimal control approach for power management in plug-in hybrid electric vehicles. IEEE T Veh Technol. 2011;19:545-555. https://doi.org/10.1109/TCST.2010.2043736

[24] Musado C, Rizzoni G, Guezennec Y, Staccia B. A ECMS: an adaptive algorithm for hybrid electric vehicle energy management. Eur J Control. 2005;11(4-5):509-524. https://doi.org/10.3166/ejc.11.509-524

[25] Paganelli G, Delprat S, Guerra T, Rimaux J, Santin J. Equivalent consumption minimization strategy for parallel hybrid powertrains. IEEE Vehicular Technology Conference. 2002;4:2076-2081. https://doi.org/10.1109/VTC.2002.1002989

[26] Paganelli G, Guezennec Y, Rizzoni G. Optimizing control strategy for hybrid fuel cell vehicle. SAE Technical Paper 2002-01-0102, 2002. https://doi.org/10.4271/2002-01-0102

[27] Pielecha I, Cieślik W, Fluder K. Analysis of energy management strategies for hybrid electric vehicles in urban driving conditions. Combustion Engines. 2018;173(2):14-18. https://doi.org/10.19206/CE-2018-203

[28] Prajwowski K, Golebiewski W, Lisowski M, Abramek KF, Galdynski D. Modeling of working machines synergy in the process of the hybrid electric vehicle acceleration. Energies. 2020;13:5818. https://doi.org/10.3390/en13215818

[29] Prajwowski K, Golebiewski W, Lisowski M, Eliasz J. Road tests of selected electrical parameters of hybrid vehicle accumulation system. IEEE Trans Veh Technol. 2021;70(1):203-211. https://doi.org/10.1109/TVT.2020.3043852

[30] Sciarretta A, Back M, Guzzella L. Optimal control of parallel hybrid electric vehicles. IEEE T Contr Syst T. 2004;12(3):352-363. https://doi.org/10.1109/TCST.2004.824312

[31] Shi DH, Wang SH, Pisu P, Chen L, Wang RC, Wang RG. Modeling and optimal energy management of a power split hybrid electric vehicle. Sci China Technol Sc. 2017;60:713-725. https://doi.org/10.1007/s11431-016-0452-8

[32] Tang X, Chen J, Liu T, Qin Y, Cao D. Distributed deep reinforcement learning- based energy and emission management strategy for hybrid electric vehicles. IEEE T Veh Technol. 2021;70(10):9922-9934. https://doi.org/10.1109/TVT.2021.3107734
[33] Wu X, Cao B, Wen J, Bian Y. Particle swarm optimization for plug-in hybrid electric vehicle control strategy parameter. 2008 IEEE Vehicle Power. 2008:1-5. https://doi.org/10.1109/VPPC.2008.4677635
[34] Yang J, Zhu G. Adaptive recursive prediction of the desired torque of hybrid powertrain. IEEE T Veh Technol. 2015; 64(8):3402-3413. https://doi.org/10.1109/tvt.2014.2357395
[35] Yang J, Zhu G. Model predictive control of a power split hybrid powertrain. Amer Contr Conf. 2016:617-622. https://doi.org/10.1109/ACC.2016.7524982
[36] Yu K, Yang J, Yamaguchi D. Model predictive control for hybrid vehicle ecological driving using traffic signal and road slop information. Control Theory Technol. 2015; 13(1):17-28. https://doi.org/10.1007/s11768-015-4058-x
[37] Zhu Y, Chen Y, Tian G, Wu H, Chen Q. A four-step method to design an energy management strategy for hybrid vehicles. P Amer Contr Conf. 2004;1:156-161. https://doi.org/10.23919/ACC.2004.1383596
[38] Zhu D, Pritchard E, Dadam SR, Kumar V, Xu Y. Optimization of rule-based energy management strategies for hybrid vehicles using dynamic programming. Combustion Engines. 2021;184(1):3-10. https://doi.org/10.19206/CE-131967

Wawrzyniec Gołębiewski, DEng. – Faculty of Mechanical Engineering, West Pomeranian University of Technology in Szczecin, Poland.
e-mail: *wawrzyniec.golebiewski@zut.edu.pl*

Prof. Krzysztof Danilecki, DSc., DEng. – Faculty of Mechanical Engineering, West Pomeranian University of Technology in Szczecin, Poland.
e-mail: *krzysztof.danilecki@zut.edu.pl*

Konrad Prajwowski, DEng. – Faculty of Mechanical Engineering, West Pomeranian University of Technology in Szczecin, Poland.
e-mail: *konrad.prajwowski@zut.edu.pl*

Mirosław Radwan, MSc., Lieutenant Colonel – Command of Territorial Defense Forces, Poland.
e-mail: *mirek_swir@poczta.onet.pl*

Prof. Maciej Lisowski, DSc., DEng. – Faculty of Mechanical Engineering, West Pomeranian University of Technology in Szczecin, Poland.
e-mail: *maciej.lisowski@zut.edu.pl*

Article citation info:
Kaźmierski B, Kapusta ŁJ. Numerical evaluation of urea-mixing devices for close-coupled selective catalytic reduction systems. Combustion Engines. 2023;193(2):84-93. https://doi.org/10.19206/CE-162624

Bartosz KAŹMIERSKI
Łukasz Jan KAPUSTA

Combustion Engines
Polish Scientific Society of Combustion Engines

Numerical evaluation of urea-mixing devices for close-coupled selective catalytic reduction systems

ARTICLE INFO

Received: 14 January 2023
Revised: 13 March 2023
Accepted: 26 March 2023
Available online: 7 April 2023

The following research presents a numerical evaluation of existing and conceptual urea-mixing devices used in close-coupled (to the engine) selective catalytic reduction (SCR) systems. The analysis was aimed at the assessment of urea-mixing devices that could considerably enhance the reduction of nitrogen oxides from the diesel-engine combustion process under a wide range of operating conditions, including cold starts. The analysis showed that replacing blade-equipped static mixers with perforated stationary mixing devices may provide a more uniform spatial distribution of ammonia at the inlet to the SCR catalyst and reduce pressure drops generated by mixing devices. Moreover, the conceptual mixing devices, based on combinations of the blade and perforated mixers to develop intensive turbulence, enabled the increase of the mixing length leading to effective decomposition of the urea-water solution (UWS), and provided uniform spatial distribution of ammonia, even for the small-sized mixing systems. However, the intensive mixing was often associated with a significant rise in the pressure drop.

Key words: *urea-water solution, urea mixer, selective catalytic reduction, SCR*

1. Introduction

The continuing use of diesel engines has become questionable due to the emission of harmful substances such as nitrogen oxides (NO_x). However, current exhaust gas aftertreatment systems enable a significant NO_x reduction, providing that they work under proper conditions, including the appropriate system temperature. One of the most effective NO_x abatement methods is selective catalytic reduction [25]. However, SCR systems are efficient only if the temperature of the substrate lies within a specific range [4, 34], which is dependent on the catalytic coating. Additionally, the temperature of the flue gas needs to be high enough to provide water evaporation and thermal decomposition of urea.

In a typical automotive SCR system, UWS is supplied upstream to the SCR catalyst using low-pressure injectors and immediately mixes with the relatively hot exhaust gas. Each single UWS droplet undergoes a process in which the water evaporates first [38, 48]. When a particle mostly composed of urea reaches a sufficiently high temperature (higher than 152°C [45]), chemical reactions occur. The primary reaction is thermolysis, expressed by Eq. (1):

$$(NH_2)_2CO \rightarrow NH_3 + HNCO \quad (1)$$

The generated ammonia (NH_3) and isocyanic acid (HNCO) are mixed with the exhaust gas, and the mixture enters the SCR catalytic converter, where the HNCO is converted into ammonia in a hydrolysis reaction (Eq. (2)):

$$HNCO + H_2O \rightarrow NH_3 + CO_2 \quad (2)$$

The ammonia developed in the thermolysis and hydrolysis is used to reduce the ammonia oxides to water and nitrogen, according to the governing chemical reactions (Eq. (3–5)):

$$4NO + 4NH_3 + O_2 \rightarrow 4N_2 + 6H_2O \quad (3)$$

$$2NO_2 + 4NH_3 + O_2 \rightarrow 3N_2 + 6H_2O \quad (4)$$

$$NO + NO_2 + 2NH_3 \rightarrow 2N_2 + 3H_2O \quad (5)$$

In order to reduce heat losses, the current SCR systems are combined into close-coupled modules containing diesel oxidation catalysts (DOC), diesel particulate filters (DPF), SCR converters and ammonia clean-up catalysts (CUC). Moreover, DPF and SCR catalysts are commonly integrated into one catalyst, referred to as an SDPF (SCR-coated diesel particulate filter). This SCR system's size reduction and location close to the engine both enable a decrease in the time required to achieve a suitable temperature inside a catalytic converter [31]. Moreover, an increased operating temperature before the SDPF catalyst favours UWS decomposition [4]. However, the system's size reduction shortens the droplets' pathlines, adversely affecting UWS decomposition before reaching the SCR catalyst.

The concept of the SCR system implies that accurate dosing of the UWS to properly match the amount of NO_x could lead to the complete conversion of nitrogen oxides into non-toxic substances. Therefore, assuming the perfectly uniform distribution of the velocity of the exhaust gas entering the SCR catalyst, it is also important to reach a uniform distribution of ammonia, achieved by the mixing process of UWS droplets and their by-products with the flue gas. However, the uniformity of gas velocity or ammonia distribution is often far from ideal, particularly regarding the wide span of operating conditions of diesel engines used in vehicles and transportation machines. Moreover, the efficiency of the conversion of UWS to ammonia (reactions (1)–(2)) is imperfect. Finally, the reactions (3)–(5) are not the only reactions occurring in the SCR systems as biuret, ammelide and other by-products are produced under certain conditions [17, 54], and they may occur as solid deposits

[54]. Payri et al. [42] also pointed out the importance of the UWS injector's position and its direction in aftertreatment system-relevant conditions, which affect the ammonia generation. The importance of the injector's direction is in accordance with our previous numerical study [21], which showed that it needs to be altered when the spray properties (most importantly, droplet size distribution) are changed. This was caused by the momentum exchange between droplets and cross-flowing gas, leading to the spray drift [13].

An effective way to enable more complete UWS decomposition is the application of static mixers [14], which also enhance spatial mixing of UWS droplets and their by-products with exhaust gas. The most common forms of static mixers are blade-based and baffle mixers aimed at vortex generation [50]. The advantage of blade mixers is their simplicity and the possibility of the use of the blades as impingement plates for droplets [47]. This may lead to droplet break-ups and the reduction of their size [28]. Additionally, static mixers reduce the velocity deviations of the gas entering the SCR catalyst [39]. On the other hand, blade-equipped mixers tend to work properly only under specific operating conditions [49], including with a suitable gas mass flow rate and temperature. While the first aspect influences the mixing (too strong or weak vortices may increase the local concentration of ammonia at the SCR's inlet), the temperature governs the UWS decomposition and evaporation of potentially occurring liquid film. Moreover, the blade-equipped mixers may not be easily adaptable to different spray characteristics, such as those attained through flash boiling [21].

Tan et al. [47] stressed the positive influence of the turbulence intensity increased by mixers on the UWS decomposition. Capetillo et al. [7] carried out numerical research to assess the impact of the blade angle, blade number and mixer's location in an SCR system equipped with a static mixer. In the case of the considered conditions, the biggest influence on the ammonia uniformity, pressure drop and liquid film's formation was observed to come from the angle of the blades. Shortening the distance between the injector and mixer also had a positive effect on NH_3 uniformity; however, this factor was of low importance. This shorter distance additionally enabled a slight reduction in the pressure drop. Ye et al. [50] analysed the influence of the mixer type, the number of mixers and the injector's position in the SCR system. Two types of mixers were considered – a conventional blade mixer and a conventional baffle mixer. The application of a single baffle mixer downstream to the injection or any two mixers enabled the increase of the ammonia uniformity index even by 136.4%, as well as an increase in ammonia generation. Nevertheless, the double-mixer configurations resulted in a considerable rise in overpressure. Mehdi et al. [33] performed a numerical study on blade and baffle mixers' performance in a marine SCR system. A combination of two mixers ensured the best uniformity of velocity and ammonia concentration. Even though the UWS residence time was the shortest for this configuration, the urea conversion was the most efficient. Two types of mixers were numerically tested by Park et al. [40], namely, a regular baffle-shaped mixer and a version generating swirl. The latter provided the best compromise between the ammonia uniformity index and the pressure drop.

Hui et al. [18] pointed out that it is difficult to achieve the uniform distribution of NH_3 using hole-type UWS injectors. While, Jang et al. [19] observed a decrease in exhaust gas temperature in a marine SCR system equipped with a mixer, along with a rise in the ammonia concentration. This was attributed to the endothermic thermolysis reaction and the increased area where the reaction took place. The application of a mixer particularly enhanced the uniformity of the NH_3 distribution, while its impact on the uniformity of the velocity distribution and ammonia concentration was much lower.

Another solution proposed for SCR mixers is a perforated tube inside which the UWS injection takes place, with only a part of the exhaust gas entering the tube. Therefore, the momentum exchange between the UWS droplets and gas is reduced, which in turn reduces the impact of the gas mass flow rate on the trajectories of the droplets. The main advantage of perforated mixers is their versatility. It is assumed that the adequately designed perforated mixer may enable more efficient UWS decomposition under a wider range of operating conditions than a blade mixer. The main drawback, in turn, is an increased tendency to liquid film deposition within the perforations, as well as raised manufacturing complexity. Zhang et al. [51] numerically analysed baffle-type and blade-based mixers, using a perforated tube as a secondary mixer at the inlet to the diffuser. The combination of the main, baffle-type mixer with additional blades at the circumferential part and the secondary perforated-tube-mixer provided the most uniform ammonia distribution, the lowest pressure drop and the lowest mass of the solid deposit under the tested conditions. Different mixers were also numerically tested and compared in an SCR system employing blade or baffle mixers with an additional perforated tube by Fu et al. [11]. The simple double-bladed design generated much higher backpressure and film deposition than other designs. The baffle mixer led to the lowest uniformity index of ammonia at the SCR's inlet, which was attributed to the least intense turbulence. However, this design generated the lowest pressure drop and provided the highest NO_x conversion efficiency due to the lowest film generation and the most complete droplet evaporation. Zhao et al. [52] presented an SCR mixer that generates spiral flow, elongating the droplets' pathlines, despite the small overall volume of the mixer. The mixer was enclosed by the perforated diffuser with a baffle-type mixer in the central part, which was aimed at uniform dispersing of the ammonia and balancing the centrifugal effect caused by the spiral part. In their numerical analysis, Kaźmierski et al. [24] utilised the concept of the perforated mixer equipped with guiding vanes outside the tube to develop the washing flow of the exhaust gas. This mixing device was used in a close-coupled SCR system providing a relatively high NH_3 uniformity index and low liquid film formation. The complex perforated mixer equipped with the vanes and the spinning disk was used by Huang et al. [16] in their numerical analysis of an SCR system, in which they determined the uniformity index of the ammonia, the pressure drop and the solid deposit formation, including the

species' analysis. The authors stated that additional holes in the ring baffle enabled the reduction of the system's overpressure. Interestingly, the number of vanes had a low impact on the pressure drop. Moreover, it was found that the number of swirling vanes could improve the ammonia uniformity at the SCR's inlet; however, exceeding a certain number would deteriorate it [16]. Therefore, the careful design process of mixers is crucial for beneficial selective catalytic reduction. The liquid film and solid deposit formation process was numerically investigated by Li et al. [30] for the perforated mixer. The authors observed that in the case of relatively high temperatures the mixer's geometry had a primary influence on the deposit's location; while at lower temperatures, its location was more dependent on the position and orientation of the UWS injector.

This efficient mixing performance with low deposit formations has also been attained with unconventional mixers by other researchers. Millo et al. [37] presented two unconventional SCR mixers generating separated vertices at gas and spray zones that provided an NH_3 uniformity index of 96–98%, and a time-averaged NO_x conversion efficiency of 98–99%, for the gas mass flow rate of 125 kg/h and temperature of 250°C. Michelin et al. [35] developed and tested an innovative design of an SCR mixing device, characterised by its minimised volume to enable maximum compactness of close-coupled systems. The operating principle was the development of a spiral gas trajectory and subsequent increase in the evaporation length for the UWS droplets. The evolution of innovative SCR mixers was also presented by Michelin et al. [36], comprising asymmetric vortex generation from a U-shaped design with swirling vanes or symmetric-vortex generation via an internal catcher and baffles. Moreover, the underfloor SCR layouts, including additional heating, were compared with close-coupled systems. The modern close-coupled layout provided the highest NO_x conversion efficiency for the same mixing device [36]. Another example of an unconventional solution was a mixer-less SCR system dedicated to close-coupled layouts [23]. Efficient mixing was attained at diverse mass flow rates of the flue gas and different spray set-ups (conventional and flash-boiling injections). The mixing performance was assessed by the uniformity index of the ammonia distribution; it was attributed to the intensive turbulence reached in the mixing chamber, and due to the abrupt change of the flow direction. Zheng et al. [53] developed conical-blade, two-stage and butterfly mixers for SCR applications. The butterfly-shaped mixer provided particularly high ammonia uniformity and NO_x reduction, as well as relatively low pressure drops at the same time. The authors stressed that SCR mixers are incapable of reaching a high performance in all applications and conditions. Kulkarni et al. [28] proposed reducing UWS surface tension by adding surfactant. The authors stated that this addition might improve mixing in urea-SCR systems due to the enhanced evaporation, attributed to the increased spreading factors of the droplets (ratios of a lamella size to the droplet diameter before the collision) and the narrower droplet size distributions reached for the secondary droplets.

The aforementioned investigations indicate there is no single, unquestionably best solution for a urea-SCR mixer intended for close-coupled applications. Therefore, the aim of this research was to find the answer to the following problem: what form of a urea-SCR mixer is the most efficient in terms of mixing performance and pressure drop? For this reason, seven different mixing devices were numerically tested in the same simplified close-coupled SCR system. All the mixing devices were supposed to be universal solutions; hence, specific, unconventional designs adjusted to any particular applications were not considered. The conclusions, including the greatest overall performance of the perforated mixers, are expected to orient the future design process of SCR mixers and increase the effectiveness of selective catalytic reduction systems.

2. Methods

The following research comprises a numerical analysis of the distinct forms of static mixers placed in the same close-coupled SCR system. The system was simplified to exclude the influence of complex geometrical shapes on the results. The presented analysis was performed numerically based on the Reynolds-averaged Navier-Stokes (RANS) approach with the k-ζ-f turbulence model [15], and the hybrid (compound) wall treatment [15, 43] applied.

2.1. Simulated system

The considered SCR system design was based on the close-coupled systems which have recently been widely used in the automotive industry, due to their provision of reduced heat losses [31], faster heating of the system and improved NO_x conversion efficiency [36]. The first component of the computational domain was the stabilisation volume followed by the diesel oxidation catalyst (DOC). Downstream from the DOC, there was an investigated mixing device, inside which UWS was injected. The external shape of the system was unchanged. The only difference between the investigated solution was the design and arrangement of the internal mixing elements. In the base model M0 (Fig. 1a), a simple elbow connected the DOC and SDPF catalysts with no additional mixing device placed inside. In the M1 model (Fig. 1b), the mixing element was a simple blade-based mixer, with a 45° inclination angle of each blade. In the M2 model (Fig. 1c), a combination of two analogous mixers was used, with the second mixer being counter-rotating. Such a layout aimed to increase the turbulence intensity by reversing the direction of the vortex generated by the first mixer. In the M3 model (Fig. 1d), the perforated tube was applied. The tube was equipped with holes around the bottom part. The upper part contained two symmetrical slots, which were shifted towards the inlet to work as a gas intake for the mixer's tube. Therefore, it was intended that only a minor fraction of the exhaust gas would enter the mixing tube so that diverse operating mass flow rates of gas would not cause a spray drifting effect. The UWS droplets were thereby formed in the high-temperature zone, without a too excessive momentum exchange between gas and droplets, favouring reduction of the liquid film and UWS decomposition. Then, the mixture of the flue gas and urea or decomposed by-products escaped the tube via the holes, forcing changes in flow

direction and increasing the ammonia spatial uniformity. The analogous mixer was employed in the M4 model (Fig. 1e), however the perforations were made exclusively in its lower part located farther from the inlet and outlet. Hence, the escaping mixture of the flue gas and urea/ammonia was forced to change its flow direction completely, and the pathlines became elongated and more uniformly spread. The mixers M5 (Fig. 1f) and M6 (Fig. 1g) were the hybrid mixing devices that posed combinations of M1 with M3, and M1 with M4, respectively. They were aimed at the generation of the swirling flow exclusively outside the tube.

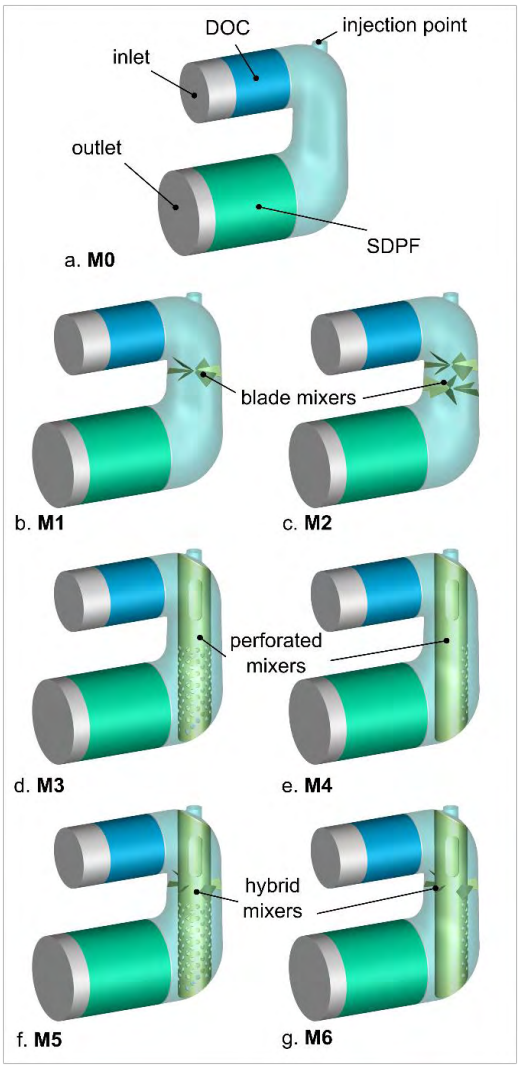

Fig. 1. The geometrical models of close-coupled SCR systems used in the simulation: a. system without mixing elements; b. single-bladed mixer; c. double, counter-rotating blade mixers; d. perforated mixer; e. partially perforated mixer; f. hybrid, blade-perforated mixer; g. blade-partially-perforated mixer

2.2. Computational mesh

A numerical mesh was generated in the AVL FAME™ M 2021 meshing module. The mesh consisted of polyhedral cells to reduce their sensitivity to numerical diffusion and reproduce sharp edges, while simultaneously maintaining their adequate quality. The boundary layer consisted of six layers with a total thickness of approximately 3 mm with automatic adjustments. The base cell size of the polyhedral cells was 5 mm, reduced to 3 mm in proximity of the walls. The mixers' surfaces were refined to reach the cell size of approximately 2 mm to properly simulate the behaviour of impinging droplets and the possible liquid film. Additionally, the mesh was refined with 1-mm cells within the primary injection zone (see. Fig. 2):

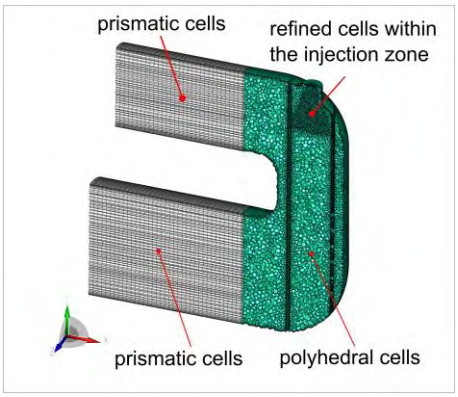

Fig. 2. The cross-section of the computational mesh of the SCR system

2.3. Numerical cases

The operating conditions were selected to reflect the conditions in exhaust systems of medium-sized passenger cars under high and medium loads [20]. The considered mass flow rate of exhaust gas was 300 kg/h (OP1) and 150 kg/h (OP2). In the case of both operating points (OPs), the gas temperature was the same: 400°C. The relatively high temperature favoured the evaporation of water from UWS droplets and accelerated urea decomposition, therefore, minimising the risk of liquid film occurrence. For this reason, the comparison of various types of SCR mixers was focused exclusively on the mixing performance and not on the tendency to generate liquid or solid deposits. Since the spray was modelled according to the Eulerian-Lagrangian approach (see section 2.4), spray properties were used as input data, and they were derived from previous experimental measurements of the two-hole injector (Bosch 0444025030) [21, 22], working under the injection pressure of 5 bar. The constant injection frequency of 4 Hz was assumed in accordance with the previous injector's mass flow measurements [21]. The amount of the urea-water solution per single injection was dependent on the injector's opening time. The UWS mass per injection was calculated based on the assumed NO_x concentration (specifically: nitric oxide concentration) of 150 ppm, corresponding to the medium load of a mid-sized passenger car (with exhaust gas recirculation) in urban traffic conditions [9]. The replacement of NO_x only with nitric oxide was based on the experimental measurements [32] that indicated the prevailing composition of NO over NO_2 at the catalyst's inlet. Nonetheless, the NO_x conversion was not simulated; hence, the exact NO_x composition had a negligible effect on the results. The summary of the operating conditions, including the UWS dosing, is presented in Table 1.

Table 1. The summary of operating conditions

Operating point	Gas mass flow rate	Gas temperature	Injector's opening time	UWS mass per injection
OP1	300 kg/h	400°C	22.77 ms	9.99 mg
OP2	150 kg/h	400°C	11.39 ms	5.00 mg

The dimensions of the catalytic converters, namely the DOC and SDPF, were defined based on similar catalytic converters used in mid-sized passenger cars. They were modelled as porous zones with a predefined, longitudinal flow direction. The pressure drops in the substrates were determined by Forchheimer's formula [10], which in the case of unidirectional flow, is expressed by Eq. (6).

$$\frac{dP}{dx} = -\alpha \cdot \mu \cdot u - \zeta \cdot \frac{\rho}{2} \cdot u^2 \tag{6}$$

where: x – distance along the flow direction; α – viscous loss coefficient; μ – dynamic viscosity; u – local gas velocity (unidirectional) inside the porous object; ζ – inertial loss coefficient; ρ – gas density. In the case of the following analysis, the α and ζ coefficients were also adopted based on similar catalytic converters from mid-sized passenger cars, with an adaptation to the specific porosity fraction.

The porosity fraction (ratio of the open volume to the whole volume of a substrate) was assumed as unity to simplify the simulated system to the maximum extent and focus exclusively on the differences caused by the various mixers. The properties of the substrates (in this case: porous objects) are presented in Table 2.

Table 2. Properties of the substrates

Catalytic converter	Length	Diameter	Viscous loss coefficient	Inertial loss coefficient	Porosity fraction
DOC	150 mm	100 mm	$2 \cdot 10^7 \frac{1}{m^2}$	$40 \frac{1}{m}$	1
SDPF	180 mm	140 mm	$10^8 \frac{1}{m^2}$	$500 \frac{1}{m}$	1

Multiple parameters can be used to evaluate the performance of SCR systems. These are: the efficiency of NO_x conversion; the uniformity of the ammonia (reducing agent) and gas velocity entering the SCR catalyst; the total pressure drop; the liquid film formation; and the risk of deposit formation.

While the NO_x conversion efficiency reflects the overall effectiveness of the system, it also depends on the NH_3 uniformity and liquid film deposition. Hence, the uniformity of the reducing agent is a direct and independent parameter, and it was indicated as the most important criterion by Zheng et al. [53]. Moreover, Xu et al. [49] showed that the ammonia uniformity at the SCR's inlet is linked with NO_x conversion efficiency. In the present analysis, the comparison of different mixer designs in close-coupled SCR systems was made based on the uniformity index of the ammonia concentration in the inlet to the SCR catalyst (approximately 10 mm behind the front surface of the porous zone – see Fig. 3). The uniformity index of the velocity was also determined in the same control section according to Eq. (7):

$$\gamma = 1 - \frac{\sum(|u_i - \bar{u}| \cdot A_i)}{2 \cdot \bar{u} \cdot A} \tag{7}$$

where: u_i – local velocity component in the i-th cell; $\bar{u}$ – area-averaged velocity within the whole control surface; A_i – area of the i-th cell; $A = \sum A_i$ – total area of the control surface.

It is to be noted that the calculation of the NH_3 uniformity index was based on Eq. (7); however, it was averaged in time and space. Moreover, the pressure drop of the mixing device was evaluated (defined here as the difference between the total pressure at the outlet at the DOC and inlet to the SDPF catalyst). Since negligible liquid film formation was expected, and the velocity uniformity index was close to 100%, the NO_x conversion would depend mostly on the spatial distribution of NH_3 within the SDPF's inlet and the urea-to-ammonia conversion. Therefore, the NH_3 uniformity index was assumed as the most accurate indicator of the mixer's effectiveness. Additionally, considering the hydrolysis reaction, Eq. (2) or NO_x reduction was unnecessary. Hence, the assumed concentration of NO_x was used exclusively to determine the dosing of UWS.

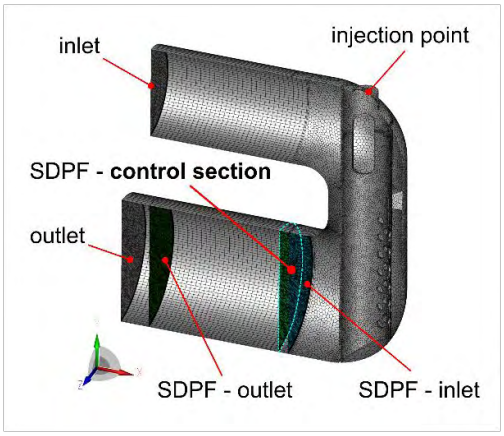

Fig. 3. The cross-section of the SCR system with the visible control section located 10 mm downstream from the SDPF's inlet

2.4. Computational mesh

The injection of the urea-water solution was simulated employing a discrete droplet model (DDM) [8], which is the Eulerian-Lagrangian particle tracking method. Droplets were randomly dispersed in the space starting from the predefined nozzles' locations. To reduce the numerical effort, droplets of similar properties are grouped into parcels in the DDM approach, and such parcels are tracked instead of single droplets. In a typical DDM approach in low-pressure UWS sprays, it is assumed that the size of the introduced droplets is the size reached after the primary break-up. The secondary break-up is not present due to low Weber numbers [1], and the application of the break-up models for such low Weber numbers can be unsuccessful [41].

Therefore, droplet size measurements are required to model the droplet size distribution properly. The most suitable measuring methods are optical laser techniques, including phase Doppler anemometry, high-resolution laser backlight imaging and high-speed microscopic imaging [6]. In this study, a pre-calibrated spray model was taken from previous work [21]. The calibration was done for the commercial two-hole UWS injector (Bosch 0444025030) experimentally tested in [21,22] using optical methods. The spray parameters used in the study here are shown in Table 3.

In order to increase the accuracy of the spatial droplet dispersion, two separated conical zones with individual droplet size distributions were defined for each spray plume, as initially proposed in [44]. These individual droplet size distributions (for each spray zone) were also derived from the research [21, 22] (Fig. 4).

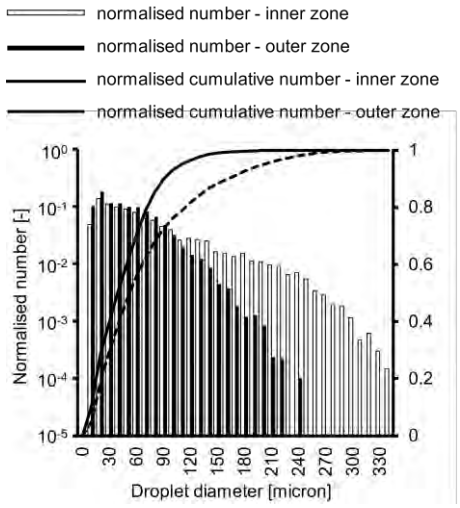

Fig. 4. The droplet size distributions of the two-zone representation of the spray used in simulations [21, 22]

The dynamics of the droplet was evaluated employing the Schiller-Naumann drag-estimation approach [46] and the Kuhnke splashing model [27] extended by Birkhold [2] to ultimately account for the droplet deposition, splashing, rebound, and break-up, but also partial rebound and partial break-up. Both spray and liquid film decomposition were modelled by the approach proposed by Birkhold [3] with the reaction's (thermolysis) activation energy and frequency factor fitted to Kim's experiment [26]. Moreover, the turbulent dispersion model was taken into account in terms of the droplets' behaviour [12].

Table 3. The summary of spray properties

Spray property	Value
Initial velocity	31.1 m/s
Inner cone angle	2°
Outer cone angle	5°
UWS mass ratio (outer-to-inner conical zones)	0.266

3. Results

A comparative analysis of the universal mixing devices dedicated to close-coupled SCR systems was performed. The effectiveness of a particular mixer was assessed based on the uniformity index of the ammonia 10 mm after the SDPF's (SCR's) inlet, and on the pressure drop of the mixing device. Additionally, the values of the velocity uniformity index measured 10 mm behind the SDPF's inlet were compared. The results showed that no liquid film was observed in any of the considered cases, which was expected due to the relatively high temperature of the exhaust gas.

3.1. The ammonia uniformity

The time-averaged concentration of the ammonia at the SDPF's control section (Fig. 3), obtained after four UWS injections, is presented in Fig. 5 (operating point 1) and Fig. 6 (operating point 2). The number of simulated injections was selected as a compromise between the computational time and the stabilisation of the investigated parameters. Lee [29] addressed the different behaviour of the droplets after the first injection compared to after the following injections. Droplets from the first injection flowed backwards and mixed with the droplets from the second injection. Later, the droplets from the following injections were mixed, and many of them were registered at the inlet of the mixer. However, the increased residence time was reported as advantageous for water evaporation and urea thermolysis [29].

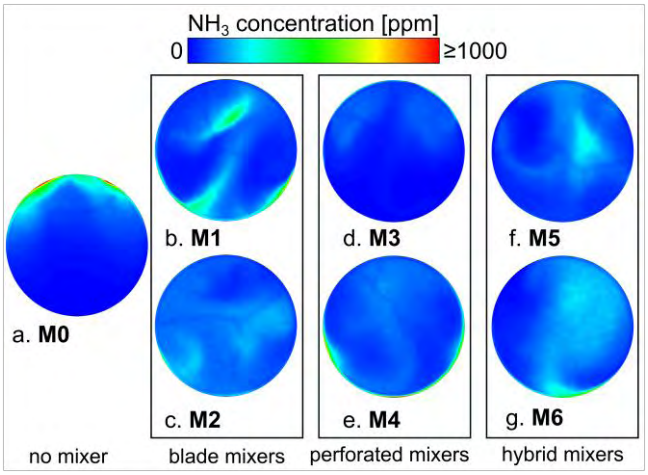

Fig. 5. Ammonia distribution at the control section located 10 mm downstream from the SDPF's inlet; OP1

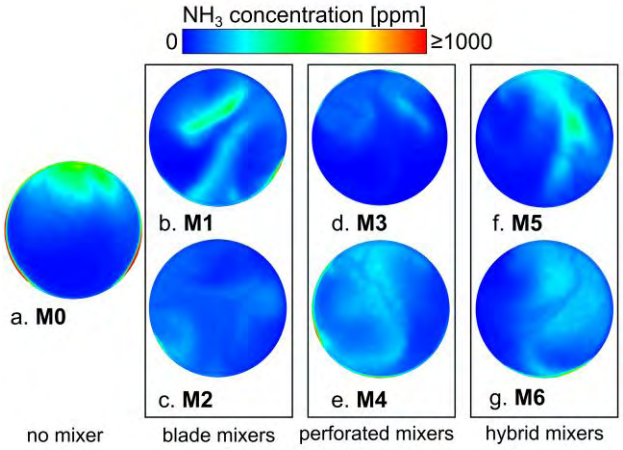

Fig. 6. Ammonia distribution at the control section located 10 mm downstream from the SDPF's inlet; OP2

It is seen that there were highly concentrated ammonia spots at the circumference of the SCR system without any mixing element; and those locations were completely different in the cases of the high (Fig. 5a) and low (Fig. 6a) mass flow rates of flue gas. This suggests that the distribution of ammonia resulted from the intensive momentum exchange between droplets and gas; since the velocity distribution maps (Fig. 7) did not indicate significant differences between operating points 1 and 2. Moreover, the higher velocity values in Fig. 7 did not correspond with the high-ammonia-concentration spots (Fig. 5a and Fig. 6a).

The application of the blade mixer (Fig. 5b and Fig. 6b) significantly improved the spatial distribution of ammonia. However, the diagonal traces of the increased NH_3 concentration were visible as a result of the generated swirl (Fig. 5b and Fig. 6b). The double-bladed mixer (M2) and the fully perforated mixer (M3) left the least distinguishable

traces of high-ammonia concentration, except for the circumference of the control section (Fig. 5c, d and Fig. 6c, d). The partially perforated mixer (M4) and hybrid mixers (M5, M6) caused the occurrence of undulated ammonia traces (Fig. 5e–g and Fig 6e–g), which were the effect of the sudden deflection of UWS/ammonia pathlines due to perforations (M4) or due to the single blade mixer (M5, M6).

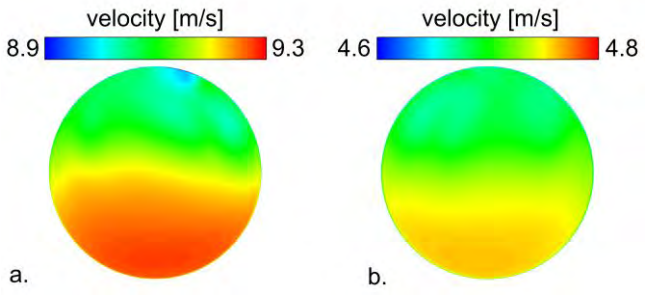

Fig. 7. Velocity distribution at the control section located 10 mm downstream from the SDPF's inlet; M0; a. OP1, b. OP2

The registered ammonia uniformity index reached similar values for both operating points 1 and 2 (Fig. 8). Additionally, the common relationships between those values for different mixing devices remained similar in the case of OP1 and OP2 (Fig. 8). The SCR system without any mixing elements (M0) resulted in an ammonia uniformity index of approximately 50%, which is an unacceptably low result. The application of the conventional, blade-equipped mixer (M1) raised the γ_{NH3} index to 72–74%. In the case of the double-bladed mixer (M2), with the second mixer generating a swirling flow in the opposite direction, γ_{NH3} was considerably increased to approximately 86% for both OP1 and OP2, which is an acceptable value in industrial applications [5]. However, it is to be noted that the presented SCR systems were simplified to the maximum extent to compare exclusively the mixer's performance, which explains the relatively low overall scoring. The application of the perforated mixer, with the holes around the whole of the lower part of the tube's surface, did not improve the γ_{NH3} much (64%). Nonetheless, in the case of perforations made exclusively at a further distance from the SDPF (M4), which hindered the direct outflow from the tube's interior to the catalyst and elongated the pathlines of the flue gas-UWS mixture, it led to a rise in the NH_3 uniformity index to 74–79%.

Finally, the blade mixer used in model M1 was combined with perforated mixers (M3 and M4, respectively). The first combination (M5) resulted in γ_{NH3} of the same level as for the partially-perforated mixer (M4) – approximately 75–77%. A slightly positive influence from the combination of the blade mixer with the fully perforated tube was observed. However, the improvement was minor compared to the blade mixer alone ($\gamma_{NH3} \approx 73\%$ for blade mixer vs. $\gamma_{NH3} \approx 76\%$ for the first hybrid mixer).

Almost the same value of γ_{NH3} as in the case of the M5 was reached by the last mixer (M6). The combination of the partially perforated tube with the blade mixer was ineffective as it significantly increased the manufacturing complexity, while it did not bring an improvement compared to the partially perforated mixer alone. This is in accordance with the analysis by Xu et al. [49], who tested not only single, unconventional urea mixing devices, but also their combinations. They reported that the single, counter-swirl mixer produced a superior performance compared to other unconventional mixers and provided the highest NO_x conversion efficiency, the lowest ammonia non-uniformity index, and a relatively low pressure drop.

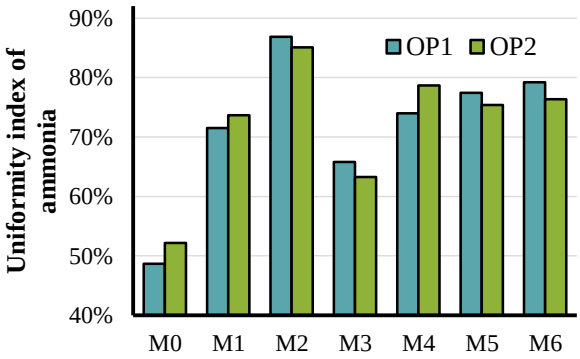

Fig. 8. Ammonia uniformity index at the control section located 10 mm downstream from the SDPF's inlet

3.2. Pressure drop

The second-ranked criterion in the following research was the pressure drop generated by the mixing devices, which was calculated as the difference between the total pressure at the outlet of the DOC and at the inlet to the SDPF catalyst. The results are presented in Fig. 9. According to the expectations, the common relationships between the pressure drops generated by the individual mixers are analogous for both operating points 1 and 2. It is seen that the pressure drop generated by the single blade mixer (M1), fully perforated mixer (M3) and partially perforated mixer (M4) are almost the same: ~200 Pa at operating point 1 and ~60 Pa at operating point 2. The negligible influence of the number of perforations on the pressure drop resulted from the fact that only a certain amount of the flue gas entered the perforated tube, while the majority washed over it from the outside. The increase of the number of blade mixers to two, with the forced change in the swirl's direction by the second mixer (M2) led to a tremendous increase in the pressure drop – more than twofold compared to the version with a single blade mixer (M1). The combination of the single blade mixer with perforated mixers (M5 and M6) also led to a significant rise in the pressure drop (from ~200 Pa for M1 at operating point 1 to ~360 Pa and ~430 Pa for M5 and M6, respectively). However, it is to be noted that the ammonia uniformity index was not improved noticeably by the hybrid mixing devices, which makes this type of design questionable. Moreover, in the case of the hybrid mixers, the number of perforations resulted in a difference in the pressure drop, being higher for the reduced number of perforations (M6). This might have come from the synergy between the swirling flow outside the tube and the outflow from the tube's holes. Additionally, the increased sensitivity of this type of hybrid design (M5, M6) to the working conditions could occur during real driving cycles.

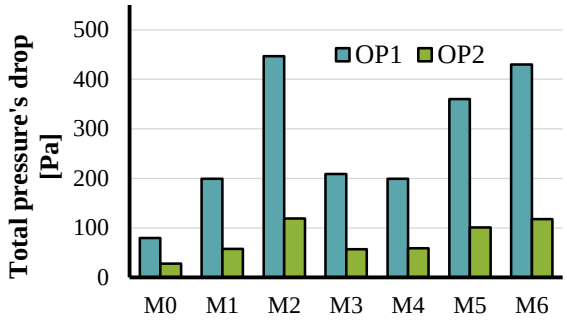

Fig. 9. Pressure drop generated by each UWS mixing device

3.3. Uniformity of velocity

Even though the analysed SCR systems were simplified to the maximum extent, the velocity uniformity index determined 10 mm after the SDPF's inlet exceeded 99% in all the considered cases (Fig. 10). Similarly to the ammonia uniformity index, the relationship between the values reached by specific mixers is analogous at operating points 1 and 2. Surprisingly, the uniformity index registered for the M0 geometry is the second highest, which may result from the lack of geometrical contractions and highly uniform velocity field within the system's inlet and DOC catalyst. However, the achievement of the highly uniform velocity and temperature fields at the catalyst surface requires a lower effort compared to the uniformity of the reducing agent, as reported by Zheng et al. [53]. Nonetheless, all the values of the velocity uniformity index are close to unity, and the exact comparison requires caution, since the differences might be a result of numerical solutions.

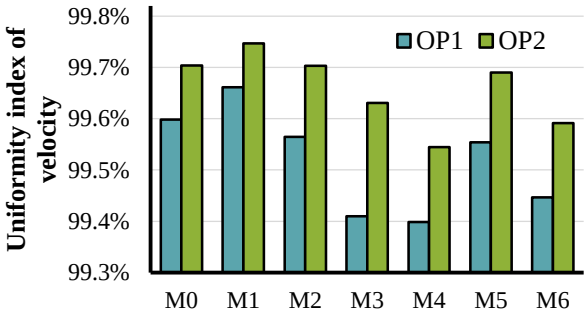

Fig. 10. Velocity uniformity index at the control section located 10 mm downstream from the SDPF's inlet

4. Conclusions

This research was aimed at an evaluation of urea-mixing devices that could considerably enhance the reduction of nitrogen oxides in close-coupled SCR systems. Seven different mixing devices were numerically tested in the same aftertreatment system and under the same operating conditions corresponding to high- and medium-load engine operation. The analysis led us to the following conclusions:

- Each mixing device improved the ammonia uniformity index.
- All mixing devices provided a velocity uniformity index exceeding 99%.
- All systems were almost insensitive to changes in the operating conditions (exhaust gas mass flow rates).
- The SCR system without mixing elements (M0) provided a highly uniform velocity field; however, the uniformity index of ammonia measured in the same control section was only 50%.
- The biggest improvement in the ammonia uniformity index was observed for the double counter-rotating mixer ($\gamma_{NH3} \approx 86\%$). However, this design (M2) generated the highest pressure drop (more than twofold compared to the version with the single blade mixer).
- The partially perforated mixer (M4) enabled the achievement of a high ammonia uniformity index (74–79%), while generating a relatively low pressure drop; which was the same as for the single blade mixer (M1).
- The hybrid mixers provided a relatively high but not improved ammonia uniformity index compared to the single blade or perforated mixers, but they did cause a significant rise in the pressure drop.
- Perforated mixers alone are expected to be used as one of the leading solutions in future SCR systems, providing a compromise between great mixing performance and manufacturing complexity.

Acknowledgements

The work was supported by the National Centre for Research and Development (NCBiR), grant no. MAZOWSZE/0101/19-00, programme "Ścieżka dla Mazowsza", project budget: 9 880 490.25 PLN.

Numerical analysis was conducted under the AVL University Partnership Program.

Nomenclature

A	total area of the control surface
A_i	area of the i-th cell
CUC	clean-up catalyst
DOC	diesel oxidation catalyst
DPF	diesel particulate filter
HNCO	isocyanic acid
NO_x	nitrogen oxides
SCR	selective catalytic reduction
SDPF	SCR-coated diesel particulate filter
u	local gas velocity (unidirectional) inside the porous object
$\bar{u}$	area-averaged velocity within the whole control surface
u_i	local velocity component in the i-th cell
UWS	urea-water solution
x	distance along the flow direction
α	viscous loss coefficient
ζ	inertial loss coefficient
μ	dynamic viscosity
ρ	gas density

Bibliography

[1] Bai C, Liu K, Zhao T et al. Study on spray characteristics and breakup mechanism of an SCR injector. Appl Sci. 2022;12(18). https://doi.org/10.3390/app12189387

[2] Birkhold F. Selektive katalytische Reduktion von Stickoxiden in Kraftfahrzeugen: Untersuchung der Einspritzung von Harnstoffwasserlösung. Dissertation. Shaker Verlag GmbH, 2007.

[3] Birkhold F, Meingast U, Wassermann P et al. Modeling and simulation of the injection of urea-water-solution for automotive SCR DeNOx-systems. Appl Catal B: Environmental. 2007;70(1-4):119-127. https://doi.org/10.1016/j.apcatb.2005.12.035

[4] Börnhorst M, Deutschmann O. Advances and challenges of ammonia delivery by urea-water sprays in SCR systems. Prog Energ Combust. 2021;87:100949. https://doi.org/10.1016/j.pecs.2021.100949

[5] Boruc Ł, Rogoz R, Bachanek J et al. An experimental facility for rapid testing of SCR systems. SAE Technical Paper 2020-01-2192. 2020. https://doi.org/10.4271/2020-01-2192

[6] Bracho G, Postrioti L, Moreno A et al. Experimental study of the droplet characteristics of a SCR injector spray through optical techniques. Int J Multiphas Flow. 2021;135:103531. https://doi.org/10.1016/j.ijmultiphaseflow.2020.103531

[7] Capetillo AJ, Ibarra F, Stepniewski D et al. Multiphase modelling of SCR systems: using the Taguchi method for mixer optimisation. SAE Int J Engines. 2017;10(1):61-71. https://doi.org/10.4271/2017-26-0113

[8] Dukowicz JK. A particle-fluid numerical model for liquid sprays. J Comput Phys. 1980;35(2):229-253.

[9] Fernández E, Ortego A, Valero A et al. Suitability assessment of NO_x emissions measurements with PTI equipment. Vehicles. 2022;4(4):917-941. https://doi.org/10.3390/vehicles4040050

[10] Forchheimer P. Wasserbewegung durch boden. Zeitschrift des Vereins deutscher Ingenieure, 45th edition. 1901.

[11] Fu H, Huang Z, Tang C et al. Effect of mixer structure on liquid film formation and NO_x conversion efficiency in selective catalytic reduction system. Fuel. 2022;330:125405. https://doi.org/10.1016/j.fuel.2022.125405

[12] Gosman AD, Loannides E. Aspects of computer simulation of liquid-fueled combustors. J Energy. 1983;7(6):482-490. https://doi.org/10.2514/3.62687

[13] Górka K, Kaźmierski B, Kapusta ŁJ. Numerical analysis of the flow rig for UWS spray examination in exhaust system-relevant conditions. Combustion Engines. 2021;186(3):103-112. https://doi.org/10.19206/CE-141182

[14] Grout S, Blaisot J-B, Pajot K et al. Experimental investigation on the injection of an urea–water solution in hot air stream for the SCR application: evaporation and spray/wall interaction. Fuel. 2013;106(x):166-177. https://doi.org/10.1016/j.fuel.2012.09.022

[15] Hanjalić K, Popovac M, Hadžiabdić M. A robust near-wall elliptic-relaxation eddy-viscosity turbulence model for CFD. Int J Heat Fluid Fl. 2004;25(6):1047-1051. https://doi.org/10.1016/j.ijheatfluidflow.2004.07.005

[16] Huang H, Chen Y, Li Z et al. Analysis of deposit formation mechanism and structure optimization in urea-SCR system of diesel engine. Fuel. 2020;265:116941. https://doi.org/10.1016/j.fuel.2019.116941

[17] Huang H, Zhang L, Chen Y et al. Study on decomposition and by-products formation mechanism of urea solution impinging on heated plate in SCR system. Chemosphere. 2022;(309):136620. https://doi.org/10.1016/j.chemosphere.2022.136620

[18] Hui Z, Boyan X, Chuansheng W. Numerical simulation to reduce NO_x of diesel engine urea-SCR system. Open Mechanical Engineering Journal. 2014;8(2):643-647. https://doi.org/10.2174/1874155x01408010643

[19] Jang J, Na S, Roh H et al. Spraying and mixing characteristics of urea in a static mixer applied marine SCR system. Energies. 2021;14(18). https://doi.org/10.3390/en14185788

[20] Kandylas IP, Stamatelos AM. Engine exhaust system design based on heat transfer computation. Energ Convers Manage. 1999;40(10):1057-1072. https://doi.org/10.1016/S0196-8904(99)00008-4

[21] Kapusta ŁJ, Rogoz R, Bachanek J. Experimental and numerical study to evaluate the effect of flash boiling on urea-water solution sprays and SCR system performance. Atomization Spray. 2021;31(5):89-117. https://doi.org/10.1615/AtomizSpr.2021035461

[22] Kapusta ŁJ, Rogoz R, Bachanek J et al. Low-pressure injection of water and urea-water solution in flash-boiling conditions. SAE Int J Adv Curr Pract Mobility. 2020;3(1):365-377. https://doi.org/10.4271/2020-01-2110

[23] Kaźmierski B, Górka K, Kapusta ŁJ. A conceptual design and numerical analysis of the mixerless urea-SCR system. Combustion Engines. 2021;187(4):12-20. https://doi.org/10.19206/CE-140539

[24] Kaźmierski B, Kapusta ŁJ. The importance of individual spray properties in performance improvement of a urea-SCR system employing flash-boiling injection. Appl Energ. 2023;(329):120217. https://doi.org/10.1016/j.apenergy.2022.120217

[25] Kim HJ, Lee SH, Kwon SI et al. Investigation of the emission characteristics of light-duty diesel vehicles in Korea based on Euro-VI standards according to type of aftertreatment system. Energies. 2020;13(18). https://doi.org/10.3390/en13184936

[26] Kim JY, Ryu SH, Ha JS. Numerical prediction on the characteristics of spray-induced mixing and thermal decomposition of urea solution in SCR system. Proceedings of the ASME 2004 Internal Combustion Engine Division Fall Technical Conference. 2004:165-170. https://doi.org/10.1115/ICEF2004-0889

[27] Kuhnke D. Spray/Wall-Interaction Modelling by Dimensionless Data Analysis. Shaker Verlag GmbH, 2004.

[28] Kulkarni AP, Megaritis T, Ganippa LC. Impact dynamics and morphology of urea-water-solution droplets impinging on a hot plate under urea-SCR relevant conditions: influence of surface tension. Fuel. 2021;298:120671. https://doi.org/10.1016/j.fuel.2021.120671

[29] Lee C. Numerical and experimental investigation of evaporation and mixture uniformity of urea–water solution in selective catalytic reduction system. Transport Res D-Tr E. 2018;60:210-224. https://doi.org/10.1016/j.trd.2017.04.015

[30] Li M, Zhang Y, Liu X et al. Numerical investigation on the urea deposit formation process in a selective catalytic reduction system of a diesel engine based on a fluid–solid coupling method. ACS Omega. 2021;6(8):5921-5932. https://doi.org/10.1021/acsomega.1c00021

[31] Maizak D, Wilberforce T, Olabi AG. DeNOx removal techniques for automotive applications – a review. Environ Adv. 2020;2:100021. https://doi.org/10.1016/j.envadv.2020.100021

[32] Majewski WA, Ambs JL, Bickel K. Nitrogen oxides reactions in diesel oxidation catalyst. SAE Technical Paper 950374. 1995. https://doi.org/10.4271/950374

[33] Mehdi G, Zhou S, Zhu Y et al. Numerical investigation of SCR mixer design optimization for improved performance. Processes. 2019;7(3). https://doi.org/10.3390/pr7030168
[34] Mera Z, Fonseca N, López J-M et al. Analysis of the high instantaneous NO_x emissions from Euro 6 diesel passenger cars under real driving conditions. Appl Energ. 2019;242: 1074-1089. https://doi.org/10.1016/j.apenergy.2019.03.120
[35] Michelin J, Guilbaud F, Guil A et al. Advanced compact SCR mixer: BlueBox. SAE Technical Paper 2014-01-1531. 2014. https://doi.org/10.4271/2014-01-1531
[36] Michelin J, Nappez P, Guilbaud F et al. Advanced close coupled SCR compact mixer architecture. SAE Technical Paper 2015-01-1020. 2015. https://doi.org/10.4271/2015-01-1020
[37] Millo F, Sapio F, Paradisi BP et al. Experimental and numerical analysis of an innovative mixer geometry for urea injection in SCR applications. Emiss Control Sci Technol. 2022;8(1-2):78-95. https://doi.org/10.1007/s40825-022-00207-8
[38] Musa SNA, Saito M, Furuhata T et al. Evaporation characteristics of a single aqueous urea solution droplet. ICLASS. 2006.
[39] Pang Z, Chen R, Cao Y. Performance analysis and optimization for static mixer of SCR denitration system under different arrangements. Energies. 2022;15(23). https://doi.org/10.3390/en15238977
[40] Park T, Sung Y, Kim T et al. Effect of static mixer geometry on flow mixing and pressure drop in marine SCR applications. Int J Nav Arch Ocean. 2014;6(1):27-38. https://doi.org/10.2478/IJNAOE-2013-0161
[41] Payri R, Bracho G, Martí-Aldaraví P et al. Computational study of urea–water solution sprays for the analysis of the injection process in SCR-like conditions. Ind Eng Chem Res. 2020;59(41):18659-18673. https://doi.org/10.1021/acs.iecr.0c02494
[42] Payri R, Marti-Aldaravi P, Bracho G et al. Numerical analysis of the injection angle of urea-water sprays for the ammonia generation in realistic test conditions. SAE Technical Paper 2022-01-0584. 2022. https://doi.org/10.4271/2022-01-0584
[43] Popovac M, Hanjalic K. Compound wall treatment for RANS computation of complex turbulent flows and heat transfer. Flow Turbul Combust. 2007;78(2):177. https://doi.org/10.1007/s10494-006-9067-x
[44] Rogóż R, Kapusta ŁJ, Bachanek J et al. Improved urea-water solution spray model for simulations of selective catalytic reduction systems. Renew Sust Energ Rev. 2020;120:109616. https://doi.org/10.1016/j.rser.2019.109616
[45] Schaber PM, Colson J, Higgins S et al. Thermal decomposition (pyrolysis) of urea in an open reaction vessel. Thermochim Acta. 2004;424(1-2):131-142. https://doi.org/10.1016/j.tca.2004.05.018
[46] Schiller L, Naumann Z. A drag coefficient correlation. In: Z Ver Deutsch Ing. 1935;77(13-14):318-320.
[47] Tan L, Feng P, Yang S et al. CFD studies on effects of SCR mixers on the performance of urea conversion and mixing of the reducing agent. Chem Eng Process – Process Intensif. 2018;123:82-88. https://doi.org/10.1016/j.cep.2017.11.003
[48] Wang TJ, Baek SW, Lee SY et al. Experimental investigation on evaporation of urea-water-solution droplet for SCR applications. AIChE Journal. 2009;55(12):3267-3276. https://doi.org/10.1002/aic.11939
[49] Xu Z, Liu J, Fu J. Experimental investigation on the urea injection and mixing module for improving the performance of urea-SCR in diesel engines. Can J Chem Eng. 2018; 96(6):1417-1429. https://doi.org/10.1002/cjce.23082
[50] Ye J, Lv J, Tan D et al. Numerical analysis on enhancing spray performance of SCR mixer device and heat transfer performance based on field synergy principle. Processes. 2021;9(5). https://doi.org/10.3390/pr9050786
[51] Zhang C, Sun C, Wu M et al. Optimisation design of SCR mixer for improving deposit performance at low temperatures. Fuel. 2019;237:465-474. https://doi.org/10.1016/j.fuel.2018.10.025
[52] Zhao C, Lou D, Zhang Y et al. Application study on a new hybrid canning structure of after-treatment system for diesel engine. Energies. 2020;13(3). https://doi.org/10.3390/en13030734
[53] Zheng G, Palmer G, Salanta G et al. Mixer development for urea SCR applications. SAE Technical Paper 2009-01-2879. 2009. https://doi.org/10.4271/2009-01-2879
[54] Zhu N, Lv L, Ye C. Component analysis of deposits in selective catalytic reduction system for automotive diesel engine. MATEC Web Conf. 2016;51:03006. https://doi.org/10.1051/matecconf/20165103006

Bartosz Kaźmierski, MEng. – Faculty of Power and Aeronautical Engineering, Warsaw University of Technology, Poland.
e-mail: *bartosz.kazmierski.dokt@pw.edu.pl*

Łukasz Jan Kapusta, DEng. – Faculty of Power and Aeronautical Engineering, Warsaw University of Technology, Poland.
e-mail: *lukasz.kapusta@pw.edu.pl*

Article citation info:
Dziubak T, Karczewski M, Dziobek I. Empirical study of the effect of the air filter on the performance and exhaust emissions of a diesel engine. Combustion Engines. 2023;193(2):94-111. https://doi.org/10.19206/CE-161881

Tadeusz DZIUBAK
Mirosław KARCZEWSKI
Ilona DZIOBEK

Combustion Engines
Polish Scientific Society of Combustion Engines

Empirical study of the effect of the air filter on the performance and exhaust emissions of a diesel engine

ARTICLE INFO

Received: 3 February 2023
Revised: 1 March 2023
Accepted: 4 March 2023
Available online: 7 March 2023

The results of an experimental study of the effect of the pressure drop of the air filter pf on the operating parameters and exhaust emissions of a modern CI internal combustion engine of a truck equipped with an electronically controlled power system are presented. The tests were carried out for an air filter with a clean filter cartridge Δp_{f0} = 0.58 kPa and with a cartridge contaminated after a service mileage (about 50 thousand km) Δp_{fD} = 2.024 kPa. In each test, engine performance, exhaust emissions and relative change in emissions were determined: CO, NO_x, HC, CO_2, H_2O. It was found that an increase in the filter resistance pf causes a decrease in the filling degree by 12%, engine useful power by almost 10%, exhaust gas temperature by a maximum of 30°C and an increase in specific fuel consumption by almost 5%. Air filter resistance has no significant effect on NO_x emissions and HC concentration. There is a reduction in H_2O emissions by up to 7%, CO by up to 13% and CO_2 by up to 4%, and an increase in oxygen emissions by 15%, depending on operating conditions.

Key words: *internal combustion engine, air filter pressure drop, engine power, specific fuel consumption, exhaust emissions*

1. Introduction

The basic component of the working medium of any internal combustion engine is air drawn from the atmosphere. The engine's intake system is responsible for supplying ambient air to the engine's cylinders with the right purity [1], in the right quantities and at the right pressure and temperature to ensure proper fuel combustion in the cylinders [2] and minimize wear on engine components [3, 4]. In addition, the intake system, has the task of suppressing the noise caused by the flow of the air stream [5] and forcing the wave phenomena of the flowing air causing resonant charging, which increases the filling pressure p_N in the cylinders, resulting in an increase in engine power [6].

Along with the ambient air, various impurities are drawn into the cylinders of internal combustion engines, mainly mineral dust. About 10–20% of the mass of dust that enters the engine with the air is retained on the walls of the cylinder liner, penetrates between the friction surfaces of the association: piston-piston rings-cylinder (P-PR-C) of the engine, causing abrasive wear [7]. SiO_2 (silica) and Al_2O_3 (alumina) grains are the basic components of mineral dust [8, 9]. The mass share of these two components in the dust reaches up to 95%. Other components in mineral dust: Fe_2O_3, (iron oxide), MgO (manganese oxide), CaO (calcium oxide) [10]. The chemical composition of mineral dust is influenced by: the type of substrate [11], climatic factors (wind, rain, snow, drought, etc.) [12], as well as industrial dust, forest fire dust and volcanic dust [13]. Dusts from the wear of clutch friction linings and pads [14] and car brake discs [15, 16], as well as tires and road surfaces [17], have a large impact on dust emissions into the environment.

Mineral dust grains are lumps with very irregular shapes and sharp edges, usually characterized by high hardness. Silica has a hardness of 7, and alumina has a hardness of 9 according to the 10-point Mohs scale. Abrasive wear of engine components is mainly caused by particles of 1–40 μm [18] with the most damaging particles having a diameter in the range of 1–20 μm [19]. The author of the paper [20] states that about 30% of the pollutants entering the engine cylinders with the air can escape unchanged with the exhaust gas, thus increasing particulate matter (PM) emissions from the engine. The primary way to prevent particulate matter from entering the environment with the exhaust gases is to use special filters [21].

The most dangerous for the two mating components are dust particles, whose diameter dp is equal to the thickness of the oil film h_{min} between the two friction surfaces. In typical internal combustion engine associations, oil film thicknesses take on varying values in the range of h_{min} = = 0.3–50.0 μm [22].

Progressive abrasive wear of the piston-piston rings-cylinder assembly is the cause of significant blowing of fresh charge into the crankcase during compression of the medium. This reduces the mass of the charge, decreases the compression pressure, resulting in a decrease in engine power and an increase in specific fuel consumption [23]. In order to reduce frictional losses and wear in the components of a reciprocating internal combustion engine, wear-resistant coatings are appropriate, which are applied to the sliding surfaces of piston rings and cylinder faces [24]. A decisive role in reducing friction losses in the friction pairs of an internal combustion engine can be achieved by ensuring the continuity and thickness of the oil film. This is realized by properly selecting the shape of the sliding surfaces of the upper as well as the lower sealing ring [25, 26].

It is the responsibility of the air filter to supply the cylinders of an internal combustion engine with air of sufficient purity. For the filtration of air of passenger car engines, which are used in conditions of low concentrations of dust in the air (highways 0.04–10 mg/m^3) [27], single-stage filters with a paper panel cartridge characterized by low dust absorption (200–250 g/m^2), but high (φ = 99.5%) fil-

tration efficiency are used. Trucks, work machinery and special vehicles that are operated under conditions of high dust concentration in the air of 2–10 g/m^3 are equipped with two-stage filters [28]. The first stage of filtration is then a battery of cyclones (multicyclone) [29, 30], and the second, a porous baffle set in series behind it in the form of a cylindrical cartridge made of pleated filter paper with an appropriately sized surface [31–33] or a PowerCore cartridge [34].

An inherent phenomenon during the operation of a baffled air filter is an increase in its pressure drop, resulting from the continuous influx and retention of dust in the filter bed (Fig. 1).

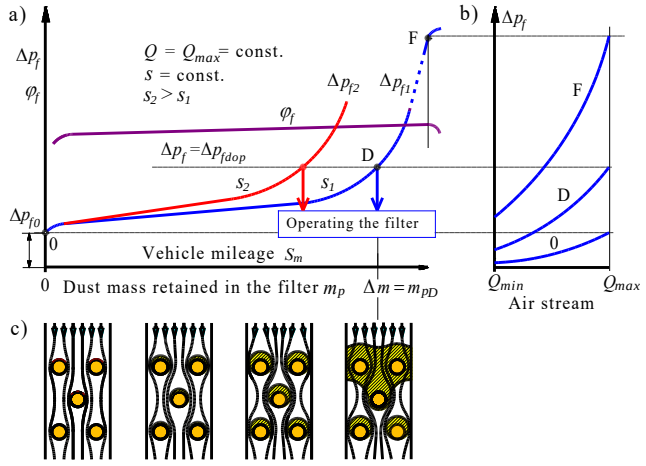

Fig. 1. The essence of baffle filters: a) filtration efficiency φ and pressure drop Δp_f of the air filter with filter media during use (1 – low dust concentration, 2 – high dust concentration), b) aerodynamic characteristics Δp_f = = f(Q) of the air filter, c) changes in the absorptive capacity of the filter bed when loaded with dust

Due to their small thickness, on the order of g_p = 0.4–0.8 mm, filter papers have limited dust absorption. After the dust fills the free spaces between the fibers (depletion of the bed's absorbency), the dust settles on the surface of the bed obstructing the flow of air, which manifests itself in an additional increase in pressure drop.

The intensity of the increase in air filter pressure drop depends on the conditions under which the vehicle is used, including the concentration of dust in the air, the fractional and chemical composition of the dust, and the duration of engine operation. The higher the value of dust concentration in the air drawn into the engine, the faster the filter bed fills with dust and the faster the filter reaches the permissible pressure drop value – Δp_{fdop} (Fig. 1), which has a different value for each engine and air filter mated with it [35, 36]. For the vehicle operator, reaching the value of the filter's permissible resistance determines the need to perform filter maintenance – replacing the filter element with a new one [37, 38].

The value of the permissible pressure drop p_{fdop} of the air filter of a passenger car engine is determined from the condition of a 3% decrease in engine power and is at the level of 2.5–4.0 kPa [39, 40]. For truck engines, the value of Δp_{fdop} is 4–7 kPa [41]. For special-purpose vehicle engines, the Δp_{fdop} value is determined from the condition of a 5% decrease in engine power and is in the range of 9–12 kPa [42, 43]. Operation of the vehicle after the Δp_{fdop} value of the air filter is possible, but not advisable.

After the Δp_{fdop} value is reached, the air filter continues to undergo the filtration process, which is characterized by an increasing increase in pressure drop while maintaining a high value of filtration efficiency. This stage of air filter operation creates two unfavorable phenomena for the engine: accelerated wear of its components and excessive power loss. Firstly, the air filter flow resistance, which is significantly increased above Δp_{fdop}, and the high air flow velocity in the filter bed, can cause "secondary emission" of dust grains. This is the detachment of dust grains from agglomerates and their movement toward the filter outlet. This phenomenon results in an increased number of large dust grains (about 10–25 μm) in the air downstream of the filter and reduced efficiency, resulting in accelerated wear of P-PR-C association elements.

Operation of the air filter after the Δp_{fdop} value is reached is not advisable due to the adverse effect of filter pressure drop on engine operation and performance and exhaust emissions. Increasing air filter pressure drop during operation lowers the value of mass air flow, which can cause a decrease in the engine's fresh charge. Deficiency of oxygen in the fuel-air mixture is the cause of disruption of the mixture preparation and combustion process, prevents the combustion of an adequate mass of fuel, which is the direct cause of a decrease in engine power (torque) an increase in specific fuel consumption and an increase in exhaust smoke [44]. These phenomena increase in intensity when the permissible resistance value is exceeded. Hence the need to replace the filter element when a certain pressure drop Δp_{fdop} is reached. The operation of an air filter is a technical compromise between pressure drop (car mileage), separation efficiency and accuracy, and engine wear and durability, as well as facility reliability [45, 46].

The primary fuel of modern compression-ignition engines is diesel fuel. Due to the depletion of fossil fuels, especially oil, climate change, economic problems, population growth and energy demand, intensive research work is being carried out to obtain alternative fuels to diesel [47–52]. For this reason, research on compression-ignition engines fueled by fuel blends as an alternative to diesel fuel is gaining great importance in the direction of performance and emissions. In addition, during the study of engines with alternative fuels, the influence of various design and operational parameters is evaluated in the direction of reducing exhaust emissions. For example, in [47], a study was conducted on a common-rail diesel engine to evaluate the effect of a diesel-butanol blend on particulate matter (PM) emissions using a pilot injection strategy. The addition of n-butanol can improve the mixing of fuel and oxidizer and lower the average temperature in the combustion chamber and consequently reduce NO_x emissions (up to 25%) and PM emissions (up to 69%). A study [48] examined the suitability of diesel-biodiesel and diesel-biodiesel-hexanol fuel blends as alternatives to diesel fuel. The results showed that the most suitable alternative fuel to diesel was a binary diesel-biodiesel fuel blend. On the other hand, the paper [49] investigated the effect of cyclohexanol mixed with diesel fuel at different volume ratios on the emissions per-

formance of a Diesel engine at different degrees of exhaust gas recirculation and injection times. The cyclohexanol-diesel mixture significantly reduced particulate matter (PM) and volumetric concentration at the expense of higher NO_x emissions. Cyclohexanol, which is derived from biomass, has been shown to be a promising alternative fuel for diesel engines. The paper [50] presents the effect of the heating time of a catalyst-covered glow plug on the exhaust emissions from a compression-ignition engine. Placing the catalyst in the combustion chamber, the place where the combustion process takes place, allows reducing emissions of: carbon monoxide, hydrocarbons and particulate matter. An improvement in the efficiency of oxidation of exhaust gas components was observed with an increase in the heating time of the glow plug. The authors of the paper [51] presented an experimental study of a common-rail diesel engine fueled by diesel fuel and a mixture of diesel and alcohol (butanol and hexanol). Engine performance and emissions of NO_x, CO, HC and soot were studied for five different ambient pressures (0.12; 0.1; 0.08; 0.07; 0.06 MPa) and for two loads (average effective pressure p_e = 0.45 MPa and 0.55 MPa). Adding butanol and hexanol (20% and 40% by volume) to diesel fuel, significantly reduced particulate matter and CO emissions, especially when the ambient pressure was below 0.1 MPa. However, the combustion of alcohol-diesel mixtures resulted in higher NO_x emissions than the combustion of diesel under the same conditions, which is also confirmed by other studies reported in [52, 53].

From the above analysis, the air filter pressure drop, which increases its value during operation and has a significant impact on engine performance and exhaust emissions, is not taken into account during experimental testing of engines. In addition, the authors of the test results do not state whether the experiment was performed with or without the presence of an air filter in the intake system.

The available literature does not provide enough information regarding the effect of air filter pressure drop on engine performance. There is mainly a lack of information regarding changes in engine emissions. The authors studied the description of studies of the effect of air filter pressure drop on the operation of naturally aspirated internal combustion engines: carburetor and diesel engines, but equipped with a classic injection system with an in-line piston (sectional) injection pump [54–59]. Today, engines of this type are not used in motor vehicles. The paper [54] presents the effect of three values of air filter flow resistance (Δp_f = 2.3; 6 and 12 kPa at n_N = 2800 rpm) on the characteristics of: filling ratio η_υ = f(n), power N_e = f(n) and torque M_o = f(n) and specific fuel consumption g_e = = f(n) of a naturally aspirated (V_{ss} = 6,84 dm^3) Diesel engine with a classical injection system. Operation of the engine in the speed range n = 1200–2800 rpm shifts the characteristics of η_υ = f(n), power N_e = f(n) and M_o = f(n) almost in parallel towards lower values of η_υ, N_e, M_o, and g_e = f(n) towards higher values of g_e. An increase in air filter pressure drop from 2.3 kPa to 12 kPa during engine operation at n = 2800 rpm and 100% load, results in a decrease in: fill factor η_υ by 25.7%, power N_e by 7.16% and increase in g_e by 8.49%.

The results of a study of the effect of air filter pressure drop Δp_f on the external characteristics of N_e effective power and specific fuel consumption ge of a special vehicle Diesel engine are presented in [55]. An increase in air filter pressure drop in the range Δp_f = 6–30.7 kPa causes a significant decrease in engine power and an increase in specific fuel consumption. There is a parallel shift of N_e power characteristics towards lower N_e speed power values. An increase in filter pressure drop causes a shift in the characteristics of specific fuel consumption g_e toward higher values of g_e and lower rotational speeds. For pressure drop Δp_f = 26.7 kPa, the decreases in N_e power take on values of: 11.75% at 2000 rpm and 20.6% at n = 1400 rpm and 32.7% for 1200 rpm.

The authors of the paper [56] presented an experimental study of the effect of air filter pressure drop on the fill factor and smoke opacity of a Diesel engine used to power a truck. Air filter pressure drop was modeled for four technical states in the range of Δp_f = 3.1–24.7 kPa at an engine speed of n = 2400 rpm. For an air filter with a clean filter element (Δp_f = 3.1 kPa), the fill factor has a value of $\eta_\upsilon \approx$ $\approx$ 1.02. For subsequent technical states of the air filter (increase in pressure drop Δp_f), the fill factor takes on smaller and smaller values, respectively: $\eta_\upsilon \approx$ 0.90; 0.81; 0.75. For the same values of Δp_f, the smoke opacity (light absorption coefficient) assumes the following values, respectively: k = = 0.42 m^{-1}, k = 0.49 m^{-1}, k = 0.62 m^{-1}, k = 0.81 m^{-1}. The obtained smoke opacity values do not exceed the permissible value, which for the T359E engine is k_{max} = 3.0 m^{-1}.

The effect of baffle filter pressure drop on the performance characteristics of a special vehicle's compression-ignition engine was presented in [57]. The effect of two filters differing in pressure drop was studied: an original air filter (Δp_f = 13.2 kPa) and an upgraded filter (Δp_f = 4.9 kPa). The engine with the upgraded filter was fed by an injection pump with an increased fuel dose of about 7%. In the latter variant, a significant (more than 2% for n = 1600 rpm and more than 10% for the n = 2200–2600 rpm range) increase in horsepower and torque was obtained compared to the basic filter variant.

Yang et al [58] studied the effects of two different air filter designs with different pressure drop (A – standard filter, B – upgraded filter with lower pressure drop), on effective power, torque, specific fuel consumption, exhaust smoke, oil temperature, engine exhaust temperature. The engine operating without an air filter obtained the highest power and torque and the lowest fuel consumption. Running the engine sequentially with filter B and A shifted the N_e = f(n) and M_o = f(n) characteristics almost in parallel toward smaller values, and the g_e = f(n) characteristics toward larger values, over the entire engine speed range. As expected, the engine operating with a type B air filter (lower pressure drop) achieved increases in torque and power, respectively: 1.6% and 1.1%, and a decrease in fuel consumption of 1.5% with respect to operation of the engine with a Type A air filter The maximum value of the smoke opacity (light absorption coefficient) increases with increasing load, and during operation of the engine without an air filter, with a Type A and Type B air filter is: k = 1.7; 2.36 and 2.0 m^{-1}, respectively. After replacing the Type A air

filter with a Type B filter, a reduction in smoke opacity of 11% was obtained.

Plotnikov et al. [59] numerically studied the effective parameters of a turbocharged diesel engine by changing the length of the inlet duct L and the internal diameter D mm. Increasing the diameter to D = 250–330 mm leads to a decrease in pressure drop, and an increase in the fill factor by an average of 0.5%. As a result, engine power increased by 0.7% and specific fuel consumption decreased in the range of 0.50–0.75%.

Abdullah et al [60] evaluated the fuel consumption and exhaust emissions of a carburetor engine as the intake system pressure drop increased. The engine was operated with and without an air filter. The tests were performed while the engine was running with and without an air filter. In the speed range of 1500–2500 rpm during engine operation at a constant load, hourly fuel consumption with an air filter increases by 49.6%, and without an air filter by 35.2%. In the absence of an air filter, CO_2 and NO_x concentrations in the exhaust gas at n = 2500 rpm are 22% and 17% higher, respectively, than when the engine is operated with an air filter.

Shannak et al. [61] studied the exhaust emissions of a gasoline engine as a function of the pressure drop of the intake system, the value of which was modeled by using different diameters of the intake pipes of the ambient air. The study was carried out by varying the engine speed in the range of n = 1000–4000 rpm. As flow resistance decreases (intake pipe diameter increases), hydrocarbon (HC) and carbon monoxide (CO) emissions decrease, while carbon dioxide (CO_2) and oxygen (O_2) remain constant.

There are only a few papers in the literature addressing the effect of air filter pressure drop on engine performance and exhaust emissions [62–65]. Thomas et al [62] studied the effect of air filter pressure drop on changes in engine emissions of three modern trucks. The vehicles were powered by turbocharged diesel engines of different displacement and design. The results showed that a change in the condition of the air filter (an increase in pressure drop) does not significantly affect the performance and exhaust emissions of modern Diesel engines. Example test results for a Volkswagen Jetta TDI 2.0 L car with a turbocharged inline four-cylinder engine, with a diesel particulate filter (DPF) and LNT emission system are shown in Fig. 2. An increase in air filter pressure drop from 1.7 kPa to 4.1 kPa and then to 6.7 kPa does not cause significant changes in CO_2 and specific fuel consumption, while there is a systematic decrease (more than 90%) in NO_x emissions.

The effect of panel pressure drop (filter paper) of the air filter after the vehicle run on selected engine and vehicle parameters: power and specific fuel consumption, exhaust emissions and vehicle dynamics, is presented in [63]. Measurements were carried out on a chassis dynamometer using two vehicles, where the power unit was a turbocharged compression-ignition engine with air cooling, and in two vehicles with a SI engine, one naturally aspirated and the other turbocharged and air-cooled.

The results indicate a relatively small effect of air filter pressure drop on the studied parameters of turbocharged engines, where a decrease in engine power in the range of 2–3% was registered. In contrast, the power loss of a naturally aspirated engine with ZI was twice as large – 6.2% [63].

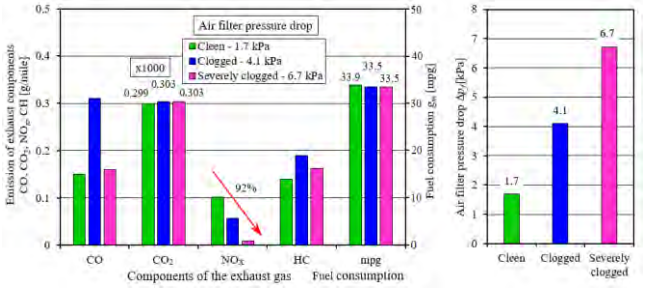

Fig. 2. The effect of an increase in baffled air filter flow resistance on emissions of exhaust components: CO, CO_2, NO_x and fuel consumption of the engine of a Dodge Ram 2500 Truck 6.7 L. Figure made by the authors based on data from the paper [62]

The paper [64] presents, in the speed range of n = 1000–2100 rpm, the results of a study of the effect of three technical states of the air filter (different pressure drop of the filter element) on the performance parameters (power, hourly and specific fuel consumption, boost pressure and exhaust gas temperature) of a modern Diesel truck internal combustion engine. It is shown that an increase in air filter resistance causes a decrease in power (9.31%), hourly fuel consumption (7.87%), exhaust gas temperature (5.1%) and boost pressure (3.11%). At the same time, there is an increase in specific fuel consumption (2.52%), smoke opacity, which does not exceed the permissible values resulting from the technical conditions for vehicle approval.

The above analysis confirmed that the air filter in the engine intake system is a device that ensures the delivery of high-purity air to the cylinders, which minimizes the wear of components working in frictional associations. An undesirable effect of a porous baffle air filter is the increase in pressure drop during its use, which results from the accumulation of dust inside the baffle. This results in a decrease in boost pressure in the intake system, resulting in a decrease in the effective performance of the engine and an increase in exhaust emissions. The negative effects worsen as the value of pressure drop increases above the value of the permissible resistance Δp_{fdop}. Hence the need to replace the filter element with a new one. Determining the value of pressure drop at which this should be done is the subject of many studies. The analysis shows that the results of studies from the 1970s, which show the effect of air filter pressure drop on the performance of carburetor internal combustion engines and diesel engines equipped with a classic injection system with an in-line piston injection pump, cannot be used to assess the effect of air filter pressure drop on the performance of modern engines. Fuel dosage control in old-style engines was not coupled to the technical condition (pressure drop) of the intake system. The results of these studies are now of limited use to vehicle manufacturers and users, as motor vehicle technology has changed and developed significantly.

Mechanical power systems (carburetor, in-line injection pump) have been eliminated from the engine's fuel supply system and replaced with multipoint, direct, electronically controlled fuel injection. Mechanical single-parameter

control has been replaced by electronic multi-parameter control, which takes into account a number of operating parameters of the engine as well as the vehicle itself. The CI engine as well as the SI engine are equipped with a turbocharger and a charge air chiller. The engine ECU controls all the quantities that affect the value of the torque generated by the engine, while meeting the requirements in the area of exhaust emissions and fuel consumption throughout the life of the vehicle. The analysis shows that the available literature practically does not present the results of experimental studies of the influence of the pressure drop of the intake system, including the air filter, on the performance of a modern internal combustion engine, and in particular on the composition and changes in exhaust emissions. Studies of this type are carried out by experimental method using an engine dynamometer. These are costly and labor-intensive studies, which explains the scant number of available results. However, despite the high cost of conducting such research, it is the most reliable research method at the moment.

Therefore, the purpose of this paper is to try to partially fill this gap and determine, by conducting experimental tests on an engine dynamometer, the quantitative and qualitative effects of air filter pressure drop on the performance parameters (fill factor, effective power, specific fuel consumption), and in particular on exhaust emissions, of a modern CI engine with electronic fuel injection control, which is applied to the drive of truck tractors. This problem is particularly important, due to the fact that modern engines with CI use a multi-parameter fuel injection and dosage strategy aimed at minimizing exhaust smoke and preventing an increase in emissions of toxic exhaust components, rather than at obtaining maximum power. The obtained test results can be used by designers to appropriately select an air filter for the engine and program the permissive resistance sensor to such a value Δp_f, at which the engine obtains an acceptable value of smoke opacity, rather than a fixed decrease in power.

2. Experimental study of the engine

2.1. Purpose and object of the study

The purpose of the study was to experimentally evaluate the effect of the increased in-service air filter pressure drop Δp_f on the useful parameters of the engine of a modern truck – useful power, hourly and specific fuel consumption, charge air pressure, exhaust gas temperature and smoke, as well as changes in the concentration and emission of the main components of the exhaust gas: carbon dioxide, carbon monoxide, oxides of nitrogen as the sum of NO, NO_2 and N_2O, oxygen and water vapor treated as a greenhouse gas.

The test object was an inline six-cylinder compression-ignition engine with direct fuel injection and electronically controlled injectors. This is a Volvo D13C460 EURO V EEV engine with a maximum power of 338 kW, which is the power unit of a Volvo FH13 truck tractor. Prior to testing, the engine was removed from the vehicle and mounted on a dynamometer bench. The technical condition of the engine up to the time of the tests was determined by its total operating time, which amounted to 11,800 hours and a mileage of 773,800 kilometers. The change in engine power and torque is shown in the external factory characteristics (Fig. 3) [65]. The tested engine met the requirements of the EURO V standard.

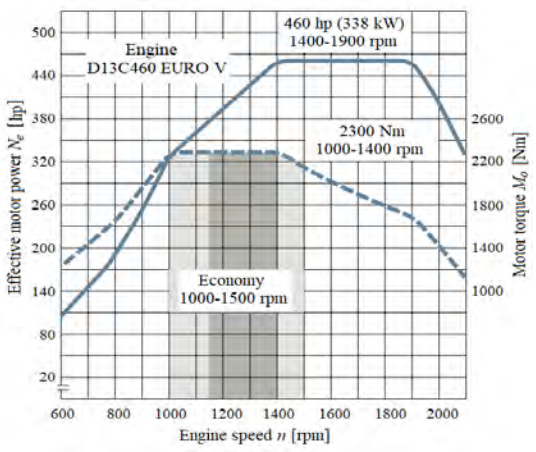

Fig. 3. Variation of power and torque on the external characteristics of the VOVLO DC13C460 motor (338 kW) given by the manufacturer [65]

The economical operation of the engine is between 1000–1500 rpm, which corresponds to the range of maximum torque, which is kept constant at around 2300 Nm in this range. The speed range at which the engine reaches its maximum power of 338 kW is 1400–1900 rpm.

The intake air flow to the engine from the environment is provided by an air supply system (Fig. 4), where its first element is an air intake located on the right side of the cab at its highest height.

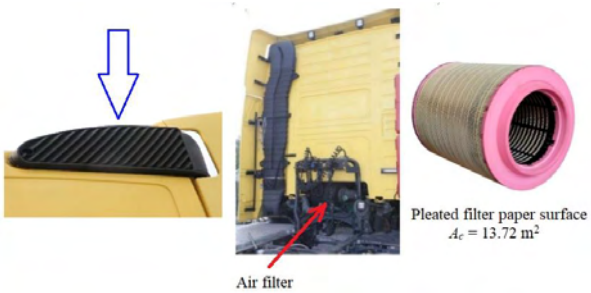

Fig. 4. Air supply system for the engine of a Volvo FH13 truck tractor: a) air intake, b) general view of the air supply system, c) paper filter cartridge

The air supply from the air intake to the filter is provided by a vertical intake duct of rectangular cross-section located outside the rear wall of the cab. Adequate purity of the inlet air to the engine is provided by a baffled air filter. Its filter element is a pleated filter paper cartridge with an active area A_c = 13.72 m^2 shaped into a cylinder. On the outlet line from the air filter there is a sensor for signaling the permissible flow resistance Δp_{fdop}, the value of which is set at Δp_{fdop} = 4.8–5.0 kPa. Completing the intake system is a turbocharger and a charge air cooler, which operates in an "air-to-air" system.

During the tests, commercial diesel fuel was used to power the engine, so before the tests, tests were performed on its basic parameters, which are shown in Table 1. The various parameters were determined during the tests in

a specialized laboratory in accordance with applicable standards.

2.2. Methodology and conditions of engine testing

The experiment was carried out using a dynamometer station, where the engine was loaded with a water brake of the Zöllner PS1-3812/AE type. Measuring instruments, whose technical characteristics are shown in Table 2, were used to measure individual engine operating parameters.

The composition of the exhaust gas was measured using Fourier Transform Infrared Spectroscopy (FTIR) with an Atmos FIR analyzer operating on a 180°C hot sample. the configuration of the instrument used during the tests made it possible to measure several components of the exhaust gas: NO, NO_2, N_2O, HC, CO, CO_2, O_2 and H_2O. The measured values were brought to normal conditions (p_n = = 101325 Pa, T_n = 273.15°C) [66].

The experiment was conducted by varying the engine speed in increments and keeping the engine at full load – the maximum swing of the accelerator pedal. Once the thermal equilibrium conditions of the engine were established, the fuel dosage was adjusted to achieve full engine load. Then, controlling the water brake accordingly, the lowest (n = 1000 rpm) possible speed at which engine operation was still steady was set. After the engine operating conditions stabilized, measurements were taken of the various engine operating parameters. Then the engine load was reduced so as to achieve an increase in speed, and the next higher speed was established (at an interval of 100 rpm), and measurements were taken again. According to the above methodology, engine performance was measured for rotational speeds in the range of 1000–2100 rpm.

During the tests, For each rotational speed in this range, the engine's operating parameters and the parameters of the air flow supplied to the engine, as well as the composition and opacity of the exhaust gas, were measured directly:

- engine speed, n [rpm]
- engine torque, M_o [Nm]
- hourly fuel consumption, G_e [kg/h]
- engine air demand, Q_s [m^3/h]
- air pressures before p_1 and after the air filter p_2 [kPa]
- charge air pressure, p_d [kPa]
- exhaust gas temperature, t_s [°C]
- exhaust gas opacity – light absorption coefficient (absorption), k [m^{-1}]
- concentration of exhaust gas components: HC, NO, NO_2, N_2O, CO, CO_2, O_2, H_2O.

Based on the directly measured values of engine operating parameters, the following parameters were determined indirectly:

- effective engine power, N_e [kW]
- specific fuel consumption, g_e [g/(kWh)]
- mass air demand of the engine $\dot{m}_{rz}$ [kg/h]
- air filter pressure drop Δp_f [kPa]
- specific emissions of exhaust components: HC, NO_x, CO, CO_2, O_2, H_2O
- relative change in: effective engine power, specific air consumption and emissions of exhaust components
- filling factor η_v.

Emissions of the various components of the exhaust gas were determined in accordance with the requirements of [36]. NO_x concentration was determined as the sum of NO + NO_2 + N_2O components. The relative change in emissions of the individual components of the engine's exhaust gas was determined as the ratio of the difference in emissions obtained for the clean "Clean" filter and the filter with reduced airflow, which caused the technical condition of the filter labeled "Dirty," relative to the emissions for the clean "Clean" filter.

During the study, the effect of the technical condition of the air filter (the effect of pressure drop Δ_{pf}) on water vapor emissions was also evaluated. Water vapor is the most important occurring greenhouse gas on Earth. Data from satellites, weather balloons and ground measurements confirm that as the climate warms, the mass of atmospheric water vapor increases. The Sixth IPCC Report states that the total mass of atmospheric water vapor is increasing by 1–2% per decade [67].

In order to eliminate coarse errors that could lead to incorrect conclusions, all tests were repeated twice.

During the tests, the engine's operation was continuously monitored by using the NAVIGATOR TXTs diagnostic interface with IDC 5 TRUCK software. The technical characteristics of the test apparatus used during the tests are given in Table 2.

Table 1. Basic parameters of diesel fuel used to power the engine during the tests

Parameters	Units	Results	Limits	Standard of test method	Device name
Density at 15°C	kg/m^3	828.7	<820; 845>	PN-EN ISO 12185:2002	Densitometer DMA™ 35
Kinematic viscosity at 40°C	mm^2/s	2.84	<2.0; 4.5>	PN-EN ISO 3104:2021-03	Pinkiewicz viscosity meter
Acid number	mg/g KOH	0.06	no requirement	PN-EN ISO 660:2021-03	702 SM Titrino
Cetane number	–	54.5	≥ 51.0	**	IroxDiesel
Cetane index	–	57.5	≥ 46.0	**	
Oxidative stability	min	68.9	no requirement	PN-EN 14112:2021-05	PetroOxy
Flash point	°C	67.5	≥ 55.0	PN-EN ISO 2719:2016-08	Pensky-Martens
Cloud point	°C	–9.2	no requirement	PN-EN ISO 3015:2019-06	ISL CPP 97-2
Cold filter plugging point	°C	–26.7	≤ 0*	PN-EN 116:2015-09	ISL CPP 97-2
Total polyaromatics	% (m/m)	1.73	≤ 8.0	**	IroxDiesel
FAME content	%	5.0	≤ 7.0	**	

* Requirement for summer period gas-oil auto

** The device does not have a standard for the test method; however, there is a correlation of test results performed according to the standard PN-EN ISO 5165:2021-02

Table 2. List of investigation equipment used during investigation

No.	Name of device/measured quantity	Type	Range	Accuracy
1.	Water dynamometer • torque – M_o • rotated speed – n	Zöllner PS1-3812/AE	M_o = 0–7000 Nm n = 0–3000 rpm N_e = 0–1250 kW	± 1 Nm ± 1 rpm ± 1 kW
2.	Fuel weight-meter (diesel) – G_e	AVL 733S Fuel Balance	0–200 kg/h	± 0.005 kg/h
3.	Smoke concentration – extinction coefficient of light radiation – k	AVL Opacimeter 4390	0.001–10.0 m^{-1}	± 0.002 m^{-1}
4.	Exhaust analyser–measuring of toxic elements concentration in exhaust gases • carbon dioxide (CO_2) • carbon monoxide (CO) • nitrogen oxides (NO) • nitrogen diooxide (NO_2) • dinitrogen oxide (N_2O) • oxygen (O_2) • steam (H_2O)	Atmos FIR emissions monitoring FTIR systems	CO_2 (0.01–23)% CO (1.0–11,000) ppm NO (1.0–6000) ppm NO_2 (1.0–300) ppm N_2O (0.5–50) ppm O_2 (0.1–21)% H_2O (0.25–25)%	± 0.1% measured quantity
5.	Thermocouple—measuring of exhaust temperature – t_s	NiCr–NiAl (type K)	–50–1100°C	± 1°C
6.	Mass air consumption – Q_s	SensyMaster FMT430 Thermal Mass Flowmeter	100–6000 m^3/h	± 1.0 m^3/h

During the tests presented in this paper, the influence of two, differing pressure drop, technical states of the air filter: a "Clean" filter element and after a service run "Dirty", on the external characteristics of the Volvo D13C460 EURO V engine was determined. In each case, the same parameters characterizing engine operation were measured.

At an engine speed of n = 1900 rpm, the air filter pressure drop obtained the following values:

- "Clean" condition – air filter with "Clean", brand new, paper insert, Δp_{f0} = 0.580 kPa
- "Dirty" condition – air filter after a service mileage, Δp_{fD} = 2.024 kPa. This condition corresponds to a tractor-trailer mileage of approximately 50,000 km, under long-distance transport conditions.

2.3. Results of inlet system flow tests

The results of engine tests where air filters having different flow resistance values were placed successively in the intake system are presented in the form of characteristics: effective power N_e = f(n), specific fuel consumption g_e = f(n), hourly fuel consumption G_e = f(n), boost pressure p_d = f(n), air flow Q_s = f(n), flow resistance Δp_f = f(n), exhaust gas temperature t_s = f(n), smoke index k = f(n), GAS = f(n) and relative change in emissions of exhaust components (Fig. 5–27).

Figure 5 shows, depending on the speed n of the Volvo engine, the change in the flow resistance of two technical states of the air filter ("Clean", "Dirty") and the effect of the technical states "Clean", "Dirty" on the engine's air demand.

The tests and analysis of the results were performed in the range of rotational speeds that are used during the operation of a vehicle equipped with this type of engine. It was found that an increase in engine speed in the range of n = = 1000–2100 rpm causes an increase in the flow resistance of the air filter, regardless of the degree of contamination of the cartridge. The increase in flow resistance occurs until the engine speed reaches n = 1900 rpm. This is related to the achievement of maximum air demand by the engine and maximum useful power (Fig. 5). The increase in engine speed above n = 1900 rpm causes a decrease in the flow resistance of the air filter, which is due to the decrease in air flow Q_s at this time.

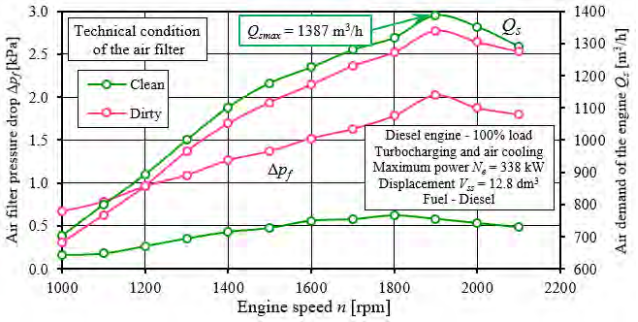

Fig. 5. Change in the flow resistance of two different technical states of the air filter ("Clean", "Dirty") and the change in the air demand of the Volvo D13C460 EURO V engine depending on the speed n

Changing the state of the filter from „Clean" to „Dirty" resulted in a more than threefold increase in the pressure drop of the filter compared to a filter with a „Clean" cartridge. At n = 1900 rpm, the „Dirty" filter reaches a maximum value of 2.024 kPa, when the manufacturer's set permissible pressure drop of 4.8–5.0 kPa is checked at engine speed n = 1900 rpm and engine operating temperature. Exceeding the set value of permissible pressure drop of the filter means the necessity of carrying out servicing consisting in replacing the filter cartridge with a new one – „Clean". Failure to perform this operation does not exclude the filter and the vehicle from further use. Continued operation of the air filter is possible, as the filtration process in the bed continues, characterized by high efficiency (φ_w = = 99.9%), but also by a higher increase in pressure drop. In the air behind the filter, dust grains begin to appear in larger quantities and with increasingly larger sizes, reaching d_{pmax} = 15–20 μm. This phenomenon is caused by the high negative pressure (pressure drop) created behind the filter and the high velocity of the air flow in the spaces between the fibers of the filter bed, resulting in the local detachment of dust grains from the agglomerates formed on the fibers and their migration towards the outlet.

If a certain resistance limit is exceeded, mechanical destruction (rupture) of the filter material of the filter insert may occur, resulting in more and larger dust grains entering the engine cylinders, which will result in accelerated wear of the T-PR-C elements.

During testing using the „Dirty" filter, an acceptable pressure drop value was not achieved. The low (0.604 kPa) pressure drop value of the new „Clean" air filter is the result of the paper's filter area, which guarantees a low air flow velocity through the paper surface, referred to in the literature as the maximum filtration velocity Fmax and calculated from the relationship:

$$\upsilon_{Fmax} = \frac{Q_{smax}}{3600 \cdot A_c} \text{ [m/s]} \quad (1)$$

where: Q_{smax} – the maximum air demand of the engine [m^3/h], A_c – the active area of the filter media [m^2].

For the maximum air demand Q_{smax} = 1387 m^3/h (Fig. 5) and for the filter area A_c = 13.72 m^2, according to relation (1), the filtration velocity in the tested filter assumes the value υ_{Fmax} = 0.0281 m/s, which is 50% less than the permissible value of the filtration velocity υ_{Fmax} = 0.06 m/s, which is assumed during the design work of air filters [44]. The low value of the filtration velocity guarantees a long interval between air filter maintenance – replacements of the paper filter element.

In the case of the engine under test, the air demand Q_s, regardless of the technical condition of the air filter, increases rapidly in value until the engine reaches a speed of n = 1900 rpm, at which it reaches a maximum, and then decreases (Fig. 5). The use of an air filter with higher pressure drop) shifts the characteristics of Q_s = f(n) almost in parallel towards the lower values of the engine's air demand Q_s. At n = 1900 rpm, the drop in Q_s is 3.39%.

Figure 6 shows the variation of the fill factor η_υ = (n) and charge air pressure p_d = (n) in the engine intake manifold for two technical states of the air filter: „Clean", „Dirty". The fill factor was defined by the relation:

$$\eta_\upsilon = \frac{\dot{m}_{rz}}{\dot{m}_t} \quad (2)$$

where: $\dot{m}_{rz}$ – average actual mass flow rate of the air supplied to the engine cylinders at specified operating conditions and for a sufficiently long time interval to eliminate the influence of pressure pulsations in the intake duct, $\dot{m}_t$ – theoretical mass flow rate of the air supplied to the engine cylinders at specified operating conditions.

The actual mass flow rate of the air supplied to the engine cylinders was determined from the measured engine air demand Q_s and the assumed air density ρ_p. The mass theoretical flow rate of the air supplied to the engine cylinders was determined from the relation:

$$\dot{m}_t = Q_{st} \cdot \rho_p \quad (3)$$

where: Q_{st} – the engine's theoretical air requirements, ρ_p – the air density at ambient conditions. The theoretical air requirements Q_{st} were determined from the relationship:

$$Q_{st} = \frac{V_{ss} \cdot n \cdot \eta_\upsilon \cdot k_p \cdot 60}{1000 \cdot \kappa} \text{ [m}^3\text{/h]} \quad (4)$$

where: V_{ss} – engine displacement [dm^3], n – engine speed [rpm], η_υ – filling factor, κ – stroke number factor (2 – for four-stroke engines, 1 – for two-stroke engines), k_p – flushing factor.

Due to the constant angle of coverage – valve co-opening, the flushing coefficient was assumed at a constant level of k_p = 1.

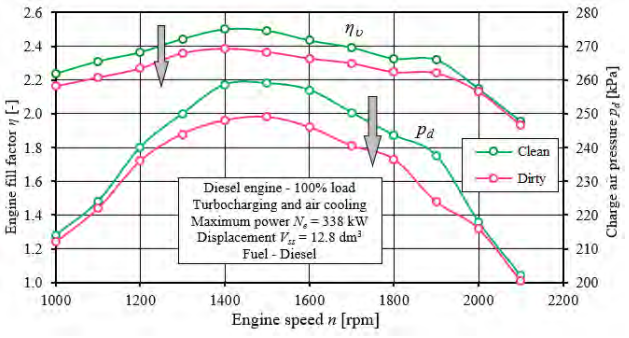

Fig. 6. Change in engine fill factor η_υ and charge air pressure p_d in the intake manifold of the VOVLO DC13C460 engine depending on engine speed n caused by two technical states of the air filter: "Clean", "Dirty"

Independent of the condition of the air filter ("Clean", "Dirty"), the engine boost pressure increases quite sharply in value as the engine speed increases. In the range n = = 1400–1500 rpm, it reaches maximum values (about 260 kPa), after which it steadily decreases. As the engine speed increases, regardless of the condition of the filter, the engine boost pressure increases quite sharply, and in the range n = 1400–1500 rpm it reaches maximum values – up to 260 kPa, after which it systematically decreases. At n = 1600 rpm, the decrease in boost pressure p_d, caused by the increase in air filter flow resistance resulting from the transition from the "Clean" to the "Dirty" state in relation to the value of the resistance of the new "Clean" filter, reaches a value of 4.28%.

The research presented in [68] clearly shows that engine boost pressure has a significant effect on engine performance, the emission of individual exhaust components and the combustion characteristics of the engine regardless of the fuel used – diesel, biofuels. Studies have shown that lowering the boost pressure increases the ignition delay, which has a negative impact on engine performance characteristics. As a consequence, a reduction in boost pressure results in the maximum cylinder pressure and maximum heat release rate moving away from top dead centre (TDC). On the other hand, increasing boost reduces the ignition delay and the heat release phase of the initial combustion phase, thus intensifying the diffusion combustion phase.

Shown in Fig. 6, the changes in the fill factor η_υ of the engine with the increase of the engine speed, indicate that regardless of the technical condition of the filter ("Clean", "Dirty"), the fill factor η_υ of the engine increases and in the range of n = 1400–1500 rpm reaches a maximum value, respectively: η_υ = 2.38 and η_υ = 2.5, after which it steadily decreases to a value of about η_υ = 1.8. As the flow resistance Δp_f increases, the "Dirty" state of the air filter filling characteristics η_υ = (n), in the speed range n = 1000–1900 rpm, is shifted almost parallel towards smaller values.

An increase in the flow resistance of the air filter from the value Δp_{f0} = 0.580 kPa ("Clean" state) to Δp_{fD} = 2.024 kPa ("Dirty" state) results in a decrease in the maximum value of the fill factor from η_υ = 2.5 to η_υ = 2.39, i.e. by about 4.5%.

2.4. Results of tests of effective engine parameters

Figure 7 shows the characteristics of effective power N_e = f(n) and specific fuel consumption g_e = f(n) of the VOVLO DC13C460 engine for the technical states of the air filter ("Clean", "Dirty").

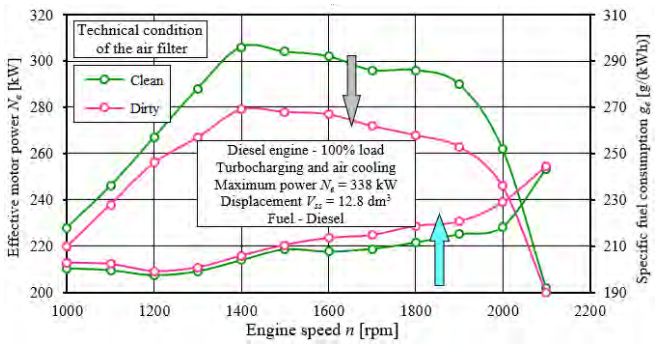

Fig. 7. Variation of effective power N_e and specific fuel consumption g_e of the VOVLO DC13C460 engine as a function of speed n for the technical states of the air filter: "Clean", "Dirty"

The use of a Δp_f air filter with a "Dirty" flow resistance for testing is associated with a displacement of the N_e = f(n) characteristic toward lower engine power values. In the rotational speed range 1400–1900 rpm, the largest relative change in effective power (power drop) was observed, reaching – 10% (Fig. 8).

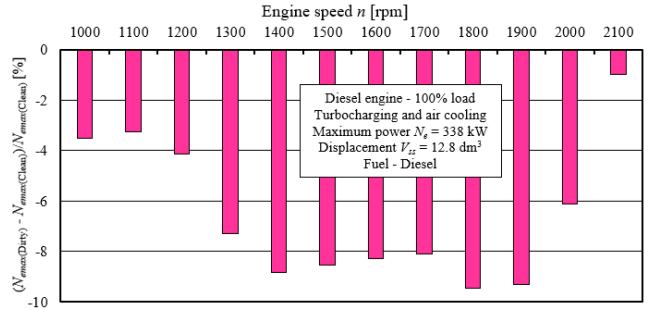

Fig. 8. Relative change in engine power due to change in air filter condition "Clean" – "Dirty"

At a rotational speed of n = 1900 rpm, the reduction in power resulting from the increase in air filter flow resistance takes on values of about 9.4%. This phenomenon occurs with the greatest intensity in the range: n = 1300–1900 rpm, which corresponds to the range of average rpm for the engine under study. This range, is the range of maximum torque for the engine under study, and is used most often when driving on expressways and highways. A reduction in maximum engine power, resulting from increases in flow resistance due to air filter contamination, is a detrimental phenomenon for motor vehicles, especially trucks. A reduction in maximum engine power can cause difficulties in climbing hills and reaching maximum speed in particular gears, especially when moving a loaded vehicle [69].

The increased resistance to air filter flow that results from the contamination of the filter element ("Dirty" condition) is important from the point of view of engine energy efficiency. As a consequence, there is an increase in specific fuel consumption – depending on the speed range and reaches a maximum of about 5% (Fig. 9).

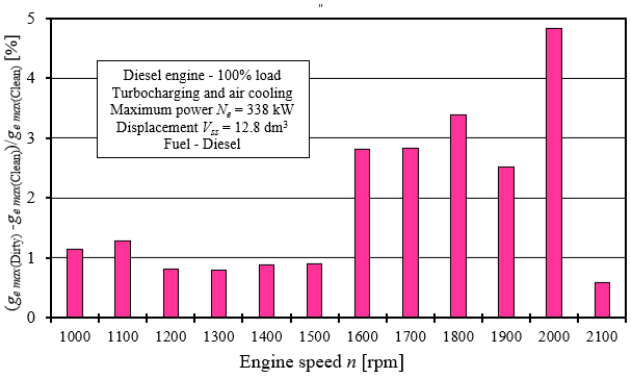

Fig. 9. Relative change in unit ge fuel consumption due to a change in the condition of the air filter "Clean"–"Dirty"

There is also a noticeable reduction in maximum useful power. The change in maximum power is the result of the Engine Control Unit (ECU), which, based on the parameters of the air in the intake system–air pressure (Fig. 6), corrects the current dose of fuel fed to the cylinder. This correction has the task of changing the thermodynamic parameters of the exhaust gas. By changing the thermodynamic parameters of the exhaust gas, an increase in charge air pressure is realized, so as to achieve the required air parameters in the intake manifold. Due to the limitations written in the control algorithm, which result from the desire to ensure the ecological properties of the engine – meeting the relevant Euro standards – it is not possible to achieve the declared maximum engine power in a situation where the flow resistance in the intake system of the engine under study increases

Changes in hourly fuel consumption G_e and exhaust gas temperature t_s as a function of the speed n of the test engine for two different flow resistance ("Clean", "Dirty") air filter states are provided in Fig. 10.

The change in air filter flow resistance from the "Clean" state to the "Dirty" state results in a decrease in hourly fuel consumption G_e, by about 7.9%. The observed phenomenon is the result of a decrease in the mass flow rate of air supplied to the engine Q_s (Fig. 5), and consequently also in the boost pressure (Fig. 6) This is a consequence of increasing flow resistance in the intake system of the vehicle under study. When creating the optimum fuel-air mixture, the fuel-air mass ratio for a given fuel type and engine is important. When too little air mass is supplied to the engine there are problems with optimal fuel-air mixing. When fuel and air are not mixed properly, fuel combustion processes in the engine's combustion chamber occur in an abnormal manner. The negative elect of the lack of complete and total combustion due to improper preparation of the fuel-air mixture is an increase in smoke and increased emissions of

products of incomplete combustion – carbon monoxide and hydrocarbons. To prevent this phenomenon, the fuel dosage control algorithms implemented in the ECU reduce the maximum mass of fuel fed to the cylinder during the engine's operating process. The effect of correcting/changing the fuel dosage is to reduce the maximum engine power and hourly fuel consumption, in proportion to the reduction in air mass.

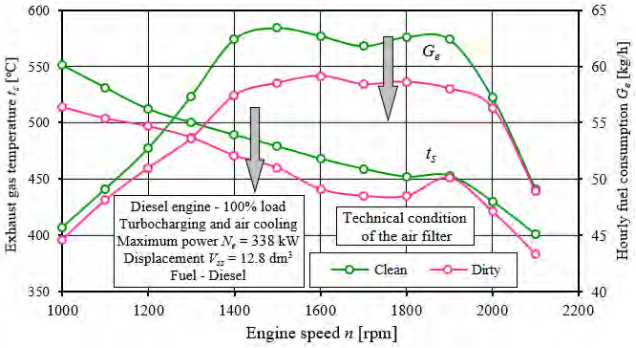

Fig. 10. The effect of technical conditions of the air filter on changes in hourly fuel consumption G_e and exhaust gas temperature t_s at the exit of the turbocharger of the engine under study as a function of engine speed n

As the engine speed increases, the exhaust gas temperature t_s, decreases slowly but steadily (almost linearly) up to a speed of n = 1800 rpm, and then a gentle increase in its value is noticeable, after which it decreases sharply again. The use of an air filter with higher flow resistance Δp_f, ("Dirty"), shifts the characteristics of $t_s = f(n)$ toward lower values of exhaust gas temperature. The results obtained for an engine operating with an air filter with a flow resistance Δp_{fD} = 2.024 kPa (Dirty), show a significant 5% reduction in exhaust gas temperature ts compared to the results obtained for engine operation with a "Clean" filter. For low and medium speeds in the range of n = 1000–1800 rpm, a reduction in exhaust gas temperature t_s of about t_s = 20–30°C was observed, depending on the measurement point. This is the result of a change/reduction in the amount of fuel and air supplied to the cylinder during engine operation.

2.5. Assessment of changes in exhaust emissions

Figure 11 shows the smoke opacity of the exhaust gas as the light radiation extinction coefficient k as a function of engine speed n for two technical states (Clean, Dirty) of the air filters. For low engine speeds n = 1000–1100 rpm, high smoke opacity was observed. The large opacity of the exhaust gas is a result of the low fill factor of the engine, which is due to the low efficiency of the turbocharger at low engine speeds. In addition, low engine speeds have problems with proper charge swirl, which promotes incomplete combustion and high emissions of incomplete combustion products including soot. When increasing the rotational speed, regardless of the condition of the air filter, it has been observed, the opacity decreases. For rotational speeds in the range of n = 1200–1700 rpm, it remains constant, and increases slightly after exceeding 1700 rpm. On the basis of the study, it was concluded that the increase in the air filter's flow resistance has no significant effect on the results of smoke opacity measurements in relation to its permissible value, which is set at 1.5 m^{-1} in the technical conditions of approval for this type of vehicle [70].

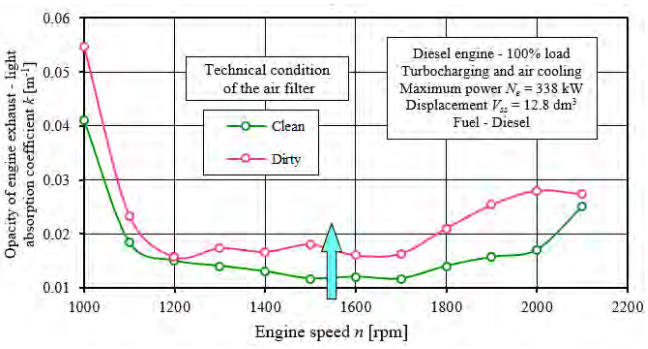

Fig. 11. Exhaust gas opacity of the VOVLO DC13C460 engine – light absorption coefficient k (absorption) as a function of engine speed n for two technical states of the air filter: „Clean" and „Dirty".

Figure 12 shows the results of measuring the concentration of carbon dioxide CO_2 in the exhaust gas of the VOVLO DC13C460 engine. The figure shows the results obtained for two different flow resistance technical states of the air filter: "Clean" and "Dirty".

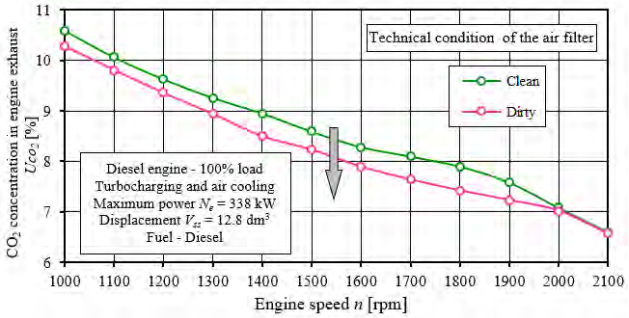

Fig. 12. CO_2 concentration in the exhaust gas of the tested engine caused by a change in the technical condition of the air filter "Clean"–"Dirty"

As the engine speed increases, the concentration of CO_2, decreases in value, until the tested engine reaches its maximum speed. The observed changes are independent of the technical condition of the air filter. Changing the engine speed in the range of n = 1100–2100 rpm results in a significant 10.28% to 6.57% reduction in CO_2 concentration in the exhaust gas, which is the result of an increase in the mass of fresh air entering the cylinders and changes in the mass of fuel delivered to the cylinders, which are due to the maximum fuel dose possible programmed in the engine controller.

The specific CO_2 emissions determined during the tests as a function of speed and the two technical states of the air filter are shown in Fig. 13. Figure 14 illustrates the relative change in specific CO_2 emissions in the engine exhaust for the "Dirty" state, compared to the emissions obtained when the engine was operated with the "Clean" air filter.

Based on the information in Fig. 12–14, it should be noted that the air filter pressure drop is quite important for CO_2 emissions. In the low speed range 1000–1200 rpm, an increase in filter pressure drop results in a decrease in CO_2 emissions. This is due to a reduction in the amount of fuel fed to the engine cylinders by the ECU engine management system, as a result of a reduction in boost pressure.

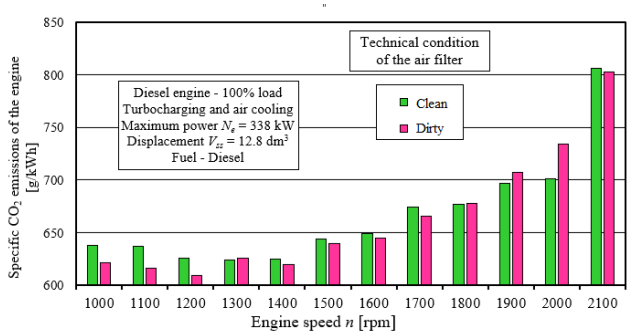

Fig. 13. Unit CO_2 emissions from the engine due to a change in the condition of the air filter "Clean"–"Dirty"

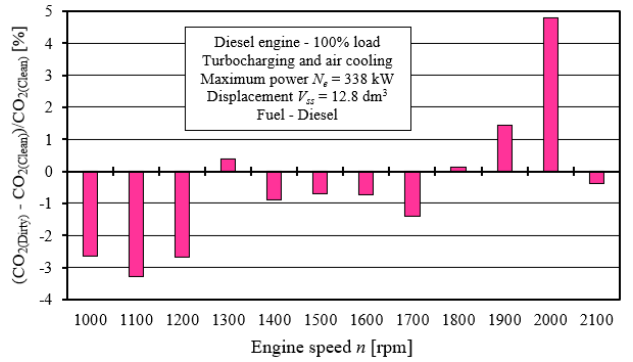

Fig. 14. Relative change in CO_2 emissions from the engine for different speeds due to a change in the condition of the air filter, relative to power with the air filter in „Clean" condition

As the engine speed increases above 1200 rpm, the effect of filter pressure drop on CO_2 emissions is reduced. This is the result of the ECU adjusting the fuel dose to the currently prevailing conditions in the engine air supply system. The relative change in CO_2 emissions does not exceed 4% (Fig. 14). For high engine speeds n = 2000–2100 rpm, a negative effect of the suspended air filter pressure drop on CO_2 emissions can be observed. This phenomenon is the result of increasing air filter pressure drop at the filter baffle of the filter as a consequence of increasing flow velocity in the filter bed. Air filter pressure drop increases as a function of speed in the second power [71]. For speeds above 1600 rpm, a controlled strategy stored in the ECU is designed to ensure adequate boost pressure by interchanging the fuel supply system's operating parameters – dose and fuel injection advance angle. This strategy is designed to provide the amount of exhaust gas necessary to ensure proper turbocharger operating conditions (increasing rpm), resulting in increased charge air pressure. This action, associated with the need to supply a greater mass of fuel to the cylinder while keeping the air mass constant, results in increased CO_2 emissions. It is an unfavorable phenomenon from the point of view of atmospheric pollution; however, in this speed range, the engine does not run very frequently.

When the engine is operated with the "Dirty" filter, there is a significant decrease in CO_2 concentration in the exhaust gas, however, there is not such a significant decrease in CO_2 emissions (Fig. 14), which is due to the simultaneous decrease in the effective power of the engine, which is a component when determining the emissions of the individual gaseous components.

This is to be explained by the fact that an increase in resistance Δp_f results in a decrease in the air flow supplied to the engine Q_s and the boost pressure. The reduction in CO_2 concentration in the exhaust gas is proportional to the change in useful power.

Based on the results in Fig. 12 and 14, it should be concluded that the increase in resistance in the intake system of a modern heavy-duty vehicle CI engine has no significant effect on the CO_2 emissions into the atmosphere.

Figure 15 shows the concentration of carbon monoxide CO in the exhaust gas as a function of rotational speed n for two different pressure drop Δp_f („Clean", „Dirty") technical states of the air filter. As the engine speed increases, the concentration of carbon monoxide CO, irrespective of the technical condition of the air filter – the value of pressure drop Δp_f, decreases its value until the engine reaches its maximum speed of n = 2100 rpm. The greatest changes (intensive decrease in CO concentration) were recorded for rotational speeds in the range of n = 1000–1200 rpm.

As the engine speed increases above 1600 rpm, the effect of pressure drop Δp_f on CO is reduced. This is a result of the engine controller adjusting the fuel delivery to the current conditions in the engine intake system – boost pressure. This problem is described in more detail when analyzing the effect of air filter pressure drop on CO_2 emissions.

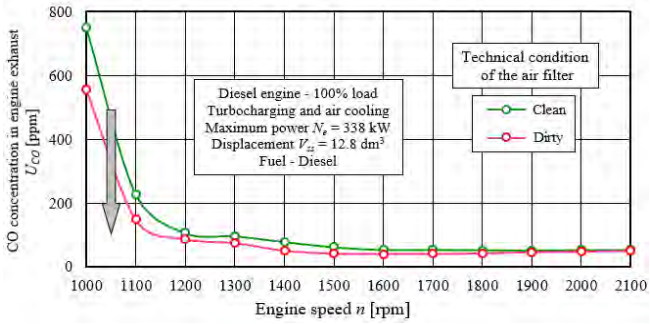

Fig. 15. CO concentration in the exhaust gas of the tested engine caused by a change in the condition of the air filter: "Clean" "Dirty"

Increasing the air filter pressure drop („Dirty") results in a decrease in CO concentration in the exhaust gas; in addition, there is a significant decrease in CO emissions (Fig. 16). This phenomenon is similar in nature to that described for CO_2 emissions.

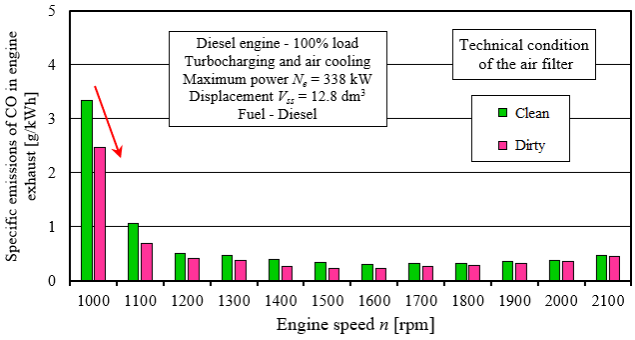

Fig. 16. Unit emission of CO in the engine exhaust due to a change in the condition of the air filter: "Clean"–"Dirty"

The specific CO emissions from the engine exhaust system for each speed caused by the technical states of the air filter p: "Clean", "Dirty" are shown in Fig. 16. The highest CO emissions occur in the 1000–1100 rpm speed range. These changes are not correlated with changes in flow resistance. On the other hand, Fig. 17 shows the determined change in specific CO emissions from the engine caused by a change in the technical state of the air from the "Clean" state to the "Dirty" state, compared to the emissions obtained when the engine was operated with a "Clean" air filter. A significant effect of flow resistance resulting from the change in the technical state of the air filter was found. The "Dirty" condition results in a 15–13% reduction in emissions for low and medium speeds, and about 5% for higher speeds. The nature of the changes is correlated with changes in the fuel flow supplied to the engine and changes in the engine's useful power.

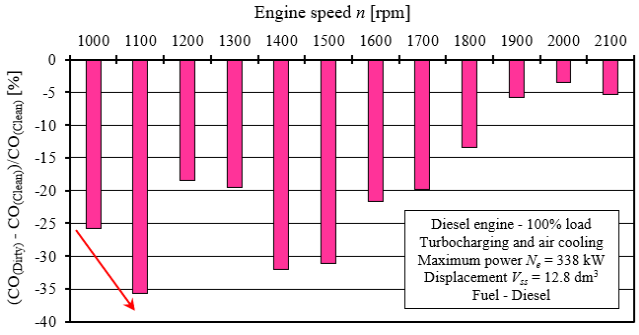

Fig. 17. Relative change in specific CO emissions in the engine exhaust for different speeds due to a change in the condition of the „Dirty" air filter, relative to power with the air filter in „Clean" condition

On the basis of the information in Fig. 15–17, it should be concluded that the condition of the air filter (distinguishable by the value of the pressure drop) is important for carbon monoxide – CO emissions. In the low to medium speed range of 1000–1700 rpm, an increase in the pressure drop of the filter element results in a reduction in CO emissions. This is a result of the ECU reducing the amount of fuel fed to the engine cylinders, as a result of a reduction in boost pressure and the desire of the implemented engine control algorithms to limit the increase in emissions of toxic exhaust components.

In addition, when analyzing the impact of the filter's technical condition (increase in pressure drop Δp_f) on CO emissions, it should also be borne in mind that the measured values in the mid- and high-speed ranges are very small – at the level of several ppm. This is the measuring range of the analyser with a high measurement uncertainty. Therefore, the nature of the changes should be interpreted qualitatively rather than strictly quantitatively.

Figure 18 shows, for two air filters differing in pressure drop („Clean", „Dirty"), the NO_x concentration as the sum of NO, NO_2 and N_2O, and Fig. 19 shows the specific NO_x emission GAS_{NOx}. The relative change in NO_x emissions from the engine for each speed caused by the air filter conditions compared to the emissions obtained when the engine was running with the „Clean" air filter is shown in Fig. 20.

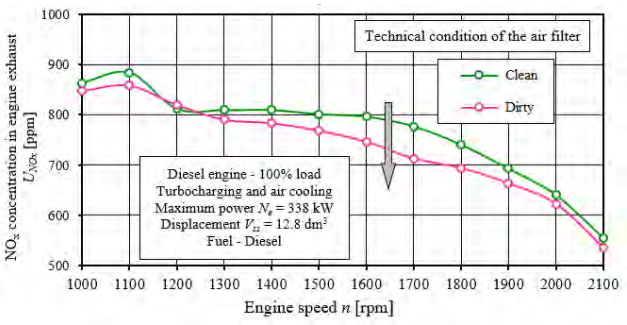

Fig. 18. NO_x concentration in the exhaust gas of the tested engine caused by the change in the technical condition of the "Clean"–"Dirty" air filter

The highest NO_x concentration of 850–890 ppm was obtained for low engine speeds. In this range, the NO_x concentration does not depend on the condition of the filter. The reason for the high NO_x concentration is the low excess air ratio, which promotes an increase in combustion temperature (Fig. 10). High temperature during the combustion process is one of the factors affecting the formation of nitrogen oxides. The small excess air ratio is the result of low boost pressure, (Fig. 6). In addition, in order for the engine to reach the required torque value in the low-speed range, a large amount of fuel is fed into the cylinder relative to the amount of air supplied.

Once the engine exceeds a speed of 1100 rpm, the boost pressure increases. The boost pressure is the result of an increase in the amount of exhaust gas supplied to the turbocharger. This results in an increase in the amount of air relative to the amount of fuel – that is, an increase in the excess air ratio. An increase in the excess air ratio is the same as an increase in the concentration of the amount of oxygen in the fuel-air mixture, resulting in a lower combustion temperature. Reducing the combustion temperature reduces the formation of NO_x and incomplete combustion products such as CO – as described earlier. The increased amount of air allows an increase in the amount of fuel fed, resulting in a sharp increase in the engine's effective power. The rate of increase in effective power is much less than the decrease in NO_x concentration in the exhaust gas. The elect of this process is higher specific emissions of NO_x (Fig. 19). Replacement of the "Clean" air filter with a filter of the "Dirty" state, entails a decrease in the concentration of NO_x in the exhaust gas, however, this is not a significant decrease in NO_x emissions from the point of view of the requirements of EURO standards.

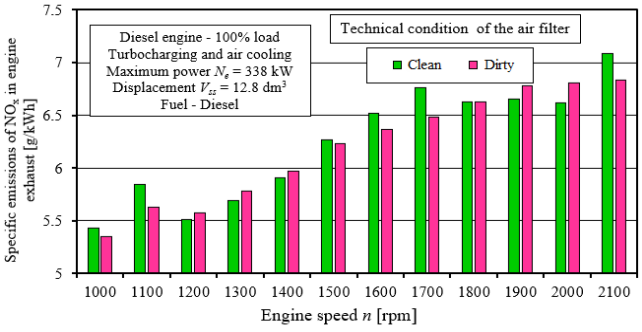

Fig. 19. Unit emission of NO_x in engine exhaust due to change in condition of air filter "Clean"–"Dirty"

Based on the data presented in Fig. 18–20, it was determined that the condition of the air filter, characterized by the flow resistance Δp_f, does not significantly affect NO_x emissions into the atmosphere. The experimentally determined changes in specific NO_x emissions range from –4 to +3%, and depend on the currently prevailing engine operating conditions and the state of the power system. The observed changes do not have a clearly identified character.

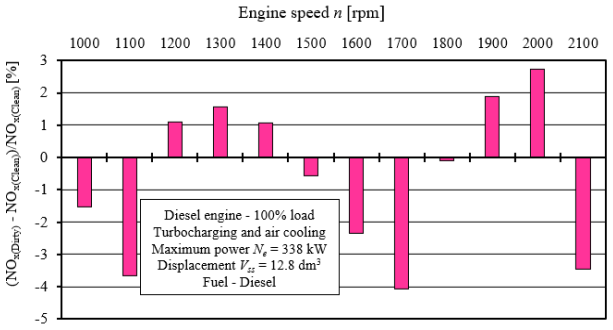

Fig. 20. Relative change in NO_x emissions in engine exhaust due to change in condition of air filter: "Clean"–"Dirty"

In the next stage of the study, the effect of the technical condition of the air filter on the concentration of HC hydrocarbons was determined. The obtained test results are shown in Fig. 21. Due to the measured values of concentrations – at the level of twenty-some ppm, the relative change in emissions was not determined. When evaluating the effect of filter condition on HC emissions, only the nature of the change in HC concentration for the air filters tested was evaluated.

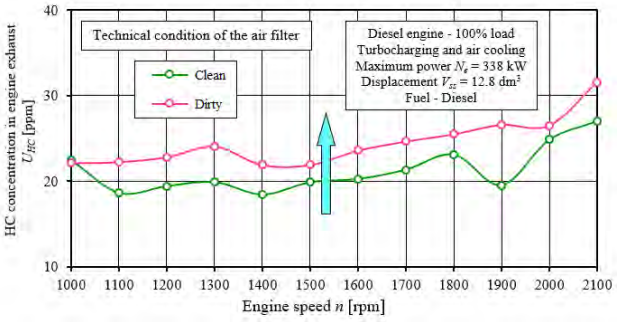

Fig. 21. HC concentration in the engine exhaust caused by a change in the condition of the air filter: "Clean"–"Dirty"

Based on the results, it should be concluded that the state of the air filter, to which a certain value of flow resistance Δp_f corresponds, has no significant effect on HC concentration. After changing the filter from the "Clean" state to the "Dirty" state, an insignificant increase in HC concentration was observed, only by a few ppm. Determined on the basis of the tests, the average HC emissions for an engine with a "Clean" air filter (Δp_{f0} = 0.58 kPa) were 0.0547 g/kWh, and for a filter in the "Dirty" state (Δp_{fD} = 2.024 kPa) were 0.0653 g/kWh, respectively. From the point of view of meeting Euro standards and the environmental characteristics of the engine under study, these values are very small, and have no significant effect on the aforementioned properties.

Figure 22 shows as a function of engine speed n the concentration of oxygen O_2 in the exhaust gas for two technical states of the same air filter.

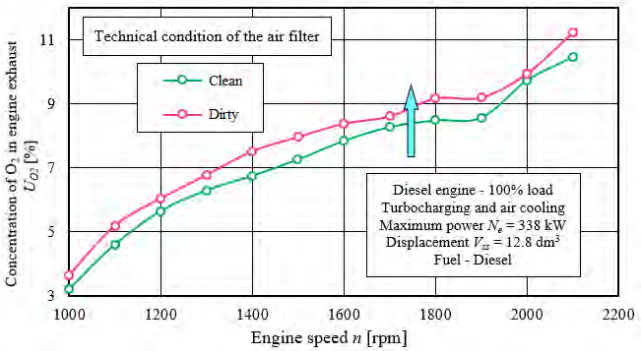

Fig. 22. O_2 concentration in the engine exhaust caused by a change in the condition of the air filter: "Clean"–"Dirty"

Increasing the pressure drop of the air filter („Dirty") results in an increase in exhaust gas oxygen emissions in the range of 7% to 15% depending on engine speed. This is explained by the fact that an increase in air filter pressure drop Δp_f results in a decrease in the air mass delivered to the engine Q_s and the boost pressure (Fig. 6). The lower mass of air supplied to the engine results in a decrease in oxygen concentration, which is a typical phenomenon for this type of process. This is the result of the engine control system reducing the maximum fuel dose delivered to the cylinder in the duty cycle to reduce the effects of the reduction in boost pressure. A reduction in boost pressure results in a reduction in the excess air ratio and leads to an increase in the concentration of particulate and toxic gaseous emissions. To counteract this phenomenon, the ECU causes a reduction in the maximum fuel delivery to the cylinders, which is reflected in a reduction in useful power (Fig. 7) and hourly fuel consumption (Fig. 10) and an increase in exhaust gas oxygen concentration (Fig. 22). The reduction in hourly fuel consumption is due to the engine control strategy, coded in the ECU, which is optimized for reducing emissions of toxic exhaust components. The reduction in fuel delivery is stronger than the reduction in useful power and boost pressure, resulting in an increase in the oxygen concentration in the exhaust gas. This is a positive phenomenon in terms of protecting the engine against an increase in toxic emissions in the event of a decrease in engine cylinder air filling due to an increase in pressure drop Δp_f of the air filter.

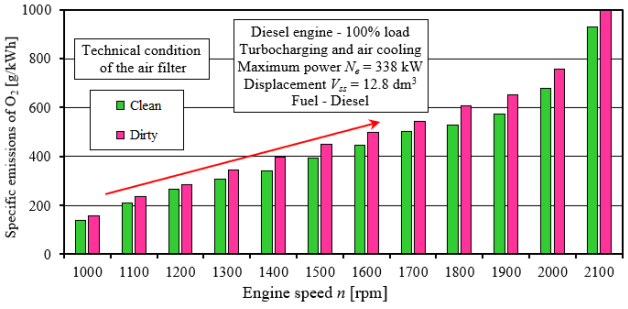

Fig. 23. Unit emission of O_2 in the engine exhaust due to a change in the condition of the air filter: "Clean"–"Dirty"

Based on the results presented in Fig. 22–24, it should be stated that the increase in pressure drop in the intake system of a modern diesel engine of a truck has a significant impact on oxygen concentration and oxygen emission in exhaust gases.

A significant increase in the pressure drop in the intake system causes a reduction in the fuel dose fed to the cylinder, which results in a reduction in power and an increase in oxygen concentration in the exhaust gases. This proves the correct selection of engine control algorithms in the case of increased pressure drop in the intake system.

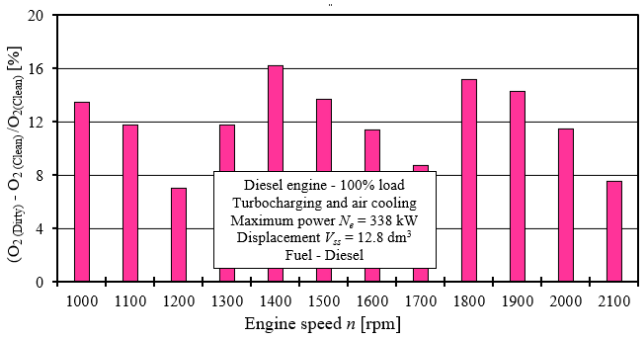

Fig. 24. Relative change in O_2 emission from the engine for particular rotational speeds n caused by a change in the technical condition of the air filter, in relation to the power with the air filter in the „Clean" technical condition

Figure 25 shows the concentration of H_2O water vapor in the exhaust as a function of engine speed n, depending on the condition of the air filter. It is observed that as the engine speed increases, the water vapor concentration decreases its value until the engine reaches its maximum speed. This phenomenon is independent of the technical condition of the air filter. For an engine speed of n = 1000 rpm, the concentration is about 10%, while for an engine speed of n = 2100 rpm, a concentration of 6% was measured. Such a significant reduction in the concentration of H_2O in the exhaust gas is the result of an increase in the mass of clean air supplied to the engine cylinders relative to the mass of fuel.

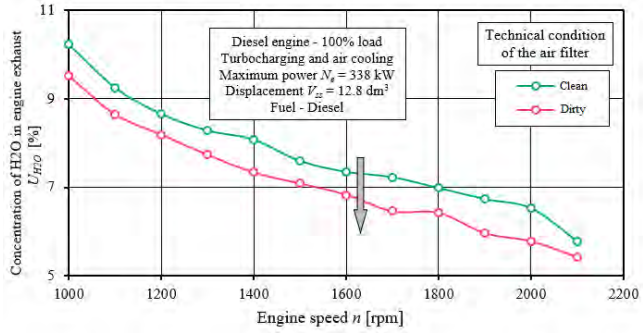

Fig. 25. H_2O concentration in the engine exhaust caused by a change in the condition of the air filter: "Clean"–"Dirty"

Changing the technical condition of the air filter from „Clean" to „Dirty" i.e. an increase in pressure drop in the range of Δp_f = 0.58–2.024 kPa, causes, at the rotational speed of n = 1900 rpm, a decrease in H_2O concentration in the exhaust gas by 11%. The increase in pressure drop in the intake system reduces the amount of fuel supplied to the cylinder, which results in a decrease in CO_2 concentration and a decrease in water vapor concentration.

Increasing (Fig. 26) the air filter flow resistance from the "Clean" state to the "Dirty" state results in a significant reduction in evaporative emissions in the range of 3 to 7%. This phenomenon is associated with an increase in the air flow supplied to the engine Q_s (Fig. 5) and simultaneous changes in air pressure in the supercharging system (Fig. 6). A smaller mass flow of air that is directed into the engine cylinders entails a decrease in the mass of fuel supplied, which produces water vapor during sapping.

Increasing air pressure drop results in a significant reduction in H_2O emissions (Fig. 27). Changing the technical condition of the air filter from „Clean" and „Dirty" causes a decrease in the concentration of H_2O in the exhaust gases by a maximum of 11%.

Changing the pressure drop of the air filter causes a significant emission of water vapor in the range of 3 to 7%. This phenomenon is the result of energy processes taking place in the engine, resulting from changes in the excess air ratio, supercharged pressure, effective power and hourly fuel consumption.

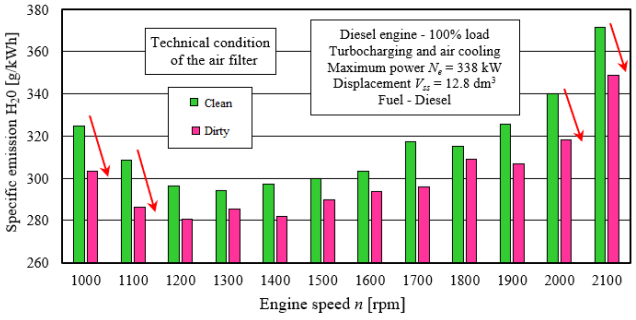

Fig. 26. Unit emission of H_2O in engine exhaust due to change in condition of air filter: "Clean"–"Dirty"

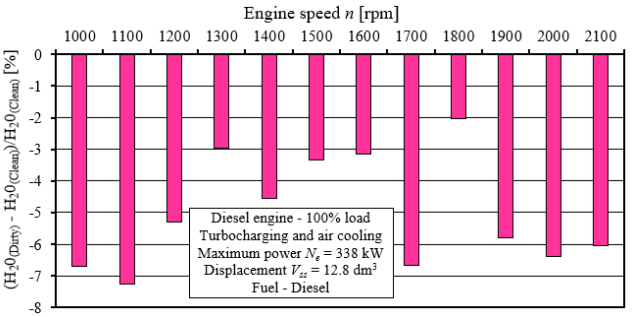

Fig. 27. Relative change in H_2O emissions from the engine for each speed n caused by a change in the condition of the „Dirty" air filter, relative to power with the air filter in „Clean" condition

Figure 28 shows the relative changes in power, useful power, specific fuel consumption and emissions of individual exhaust components for two characteristic speeds of 1400 rpm and 1900 rpm. For the tractor-trailer from which the engine under study was derived, 1400 rpm is the speed at which the engine operates most often when driving in highway conditions – a speed of 86–88 km/h.

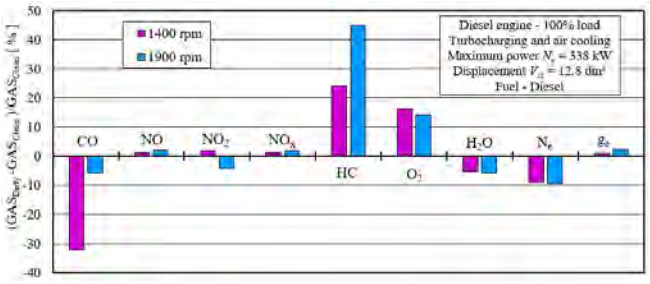

Fig. 28. Relative change in power N_e and specific fuel consumption g_e and emissions from the VOVLO DC13C460 engine for two characteristic speeds n = 1400 rpm and n = 1900 rpm caused by a change in the technical condition of the "Dirty" air filter, relative to power N_e and g_e emissions with the air filter in the "Clean" condition

At this speed, the engine's operation is most efficient – the lowest fuel consumption. The speed of 1900 rpm is the speed of maximum power. This speed is used when accelerating the vehicle with a load, for example: when driving with a semi-trailer, when the total weight of the vehicle approaches the maximum permissible value, which for this type of vehicle is 36 to 40 tons, depending on the version of the transport trailer.

The reduction in carbon monoxide emissions, in the mid-speed range, is the result of a control strategy stored in the ECU, which reduces the amount of fuel fed to the engine's cylinders, because of a reduction in boost pressure and an effort to limit the increase in emissions of toxic exhaust components.

The increase in HC hydrocarbon emissions in the mid- and high-speed ranges is associated with very low HC concentrations (several ppm), which, with the high measurement uncertainty of the analyzer in the range of up to 25 ppm, results in large determined emission changes.

3. Conclusions

The literature available from the recent period lacks the results of studies of modern truck internal combustion engines in the area of the effect of flow resistance in the intake system on changes in emissions of toxic components of exhaust gases and greenhouse gases such as water vapor. The bench tests presented in this paper on the changes in filter flow resistance on the operating conditions of a modern compression-ignition engine used to drive a tractor-trailer, confirm only to some extent, the results of research in the subject literature. This is due to the fact that over the past several years there has been a fundamental change in engine control systems, including air and fuel supply systems. In modern engines, power systems and control of effective engine parameters are based on multi-parameter algorithms, optimized in the direction of minimizing particulate emissions of toxic exhaust components. Providing the required useful power under the given conditions is a subordinate function.

Based on the engine tests obtained, it can be concluded that increasing air filter flow resistance causes the following effects on engine performance and exhaust emissions:

1. An increase in airflow resistance in the intake system of the VOLVO engine by 2 kPa compared to the value obtained for the new "Clean" filter results in a decrease in effective power by 9.31%, which, with respect to a 1 kPa increase in flow resistance, amounts to 4.66% and is a magnitude 10 times greater than that of engines with a mechanically controlled fuel supply system. The observed changes in horsepower are correlated with changes in mass airflow delivered to the engine (3.39%) and boost pressure (4.28%).
2. There are no significant changes in CO_2 concentration and emissions. For low speeds of 1000–1200 rpm, increasing the filter flow resistance results in a slight reduction in CO_2 emissions. When increasing the rotational speed, a reduction in the effect of filter flow resistance on CO_2 emissions was observed, and the relative changes in CO_2 emissions do not exceed 4%.
3. Influences on CO concentrations and emissions. With the increase of engine speed above 1600 rpm, the effect of the effect of flow resistance Δp_f on CO emissions is reduced. When the engine is operated with the air filter in the "Dirty" state, the changes in CO emissions are 10–13% for low and medium speeds and about 5% for higher speeds. The nature of the changes is correlated with changes in hourly fuel consumption and useful engine power.
4. No significant impact on NO_x emissions was observed. The observed changes in NO_x emissions oscillate between –4 and +3%, depending on the current engine operating conditions and the state of the air supply system. The observed changes are not clearly identified.
5. There is no significant effect on HC concentration. The observed changes oscillate around the detection threshold of the exhaust gas analyzer used.
6. Has a significant effect on oxygen emissions. Increasing the flow resistance of the air filter increases the concentration of oxygen in the exhaust gas and increases its emissions by 7% to 15% depending on the engine speed.
7. Has a significant effect on the concentration and emission of water vapor. An increase in resistance in the air intake system entails a significant reduction in H_2O emissions. This phenomenon is positively correlated with an increase in flow resistance. A change in the technical condition of the air filter from "Clean" to "Dirty", causes, a decrease in H_2O concentration in the exhaust gas by a maximum of 11% and a decrease in water vapor emissions in the range of 3 to 7%.

The next stage of the research should be to evaluate the effect of changes in the flow resistance of the air supply system on the traction characteristics of a truck tractor with the tested engine equipped with this type of intake system.

Funding: This work was financed by the Military University of Technology under research project UGB 833/2023.

Nomenclature

CI compression ignition
ECU Electronic Control Unit
SI spark ignition
T-PR-C piston-piston ring-cylinder

Bibliography

[1] Yun J-E. Optimal design of off-road utility terrain vehicle air filter intake. Energies. 2021;14:2269. https://doi.org/10.3390/ en14082269

[2] Mustafa NS, Ngadiman NHA, Abas MA, Noordin MY. Application of box-behnken analysis on the optimisation of air intake system for a naturally aspirated engine. International Journal of Automotive and Mechanical Engineering (IJAME). 2020;17(2):7607-7617. https://doi.org/10.15282/ijame.17.2.2020.21.0602

[3] Szczepankowski A, Szymczak J, Przysowa R. The effect of a dusty environment upon performance and operating parameters of aircraft gas turbine engines. Specialists' Meeting – Impact of Volcanic Ash Clouds on Military Operations NATO AVT-272-RSM-047. Vilnius. 05.2017. https://www.researchgate.net/publication/316877791

[4] Tang R-J, Hu B-F, Zhang M, Lu Z-J. Study on separation characteristics of dust and droplet on air intake pre-filtration systems of CV based on CFD simulation and test. International Conference on Artificial Intelligence and Computing Science (ICAICS 2019). https://doi.org/10.12783/dtcse/icaic2019/29462.

[5] Dahlan AA, Muhammad MF, Abdul Latiff Z, Mohd Perang MR, Abu Bakar SA. Acoustic study of an air intake system of SI engine using 1-dimensional approach. International Journal of Automotive and Mechanical Engineering (IJAME) 2019;16(1):6281-6300. https://journal.ump.edu.my/ijame/article/view/257/298.

[6] Sawant P, Bari S. Effects of variable intake valve timings and valve lift on the performance and fuel efficiency of an internal combustion engine. SAE Technical Paper. 2018. https://doi.org/10.4271/2018-01-0376

[7] Bojdo N, Filippone A. A simple model to assess the role of dust composition and size on deposition in rotorcraft engines. Aerospace. 2019;6(44). https://doi.org/10.3390/aerospace6040044

[8] Smialek JL, Archer FA, Garlick RG. Turbine airfoil degradation in the Persian GulfWar. J Miner Met Mater Soc. 1994;46(12):39-41. https://doi.org/10.1007/BF03222663

[9] Summers CE. The physical characteristics of road and field dust. SAE Technical Paper. 1925. https://doi.org/10.4271/250010

[10] Bojdo N, Filippone A. Effect of desert particulate composition on helicopter engine degradation rate. Proceedings of the 40th European Rotorcraft Forum. Southampton, 2-5.09.2014. https://doi.org/10.13140/2.1.2959.8086

[11] Jaroszczyk T. Air filtration in heavy-duty motor vehicle applications. Proc. Dust Symposium III Vicksburg MS. 15-17.09.1987.

[12] Rienda IC, Alves CA. Road dust resuspension: a review. Atmospheric Research. 2021;261:105740. https://doi.org/10.1016/j.atmosres.2021.105740

[13] Vogel A, Durant AJ, Cassiani M, Clarkson RJ, Slaby M, Diplas S et al. Simulation of volcanic ash ingestion into a large aero engine: particle–fan interactions. ASME J. Turbomach. 2019;141(1):011010. https://doi.org/10.1115/1.4041464

[14] Sawczuk W, Merkisz-Guranowska A, Rilo Cañás A-M, Kołodziejski S. New approach to brake pad wear modelling based on test stand friction-mechanical investigations. Eksploat Niezawodn. 2022;24(3):419-426. http://doi.org/10.17531/ein.2022.3.3

[15] Glišović J, Pešić R, Lukić J, Miloradović D. Airborne wear particles from automotive brake system: environmental and health issues. 1st International Conference on Quality of Life. Kragujevac. 9-10.06.2016. https://www.researchgate.net/publication/308712718

[16] Zimakowska-Laskowska M, Laskowski P. Emission from internal combustion engines and battery electric vehicles: case study for Poland. Atmosphere. 2022;13:401. https://doi.org/10.3390/ atmos13030401

[17] Wagner S, Klöckner P, Reemtsma T. Aging of tire and road wear particles in terrestrial and freshwater environments – a review on processes, testing, analysis and impact. Chemosphere. 2022;288:132467. https://doi.org/10.1016/j.chemosphere.2021.132467

[18] Jaroszczyk T, Pardue BA, Heckel SP. Kallsen KJ. Engine air cleaner filtration performance – theoretical and experimental background of testing. Proceedings of the AFS Fourteenth Annual Technical Conference and Exposition, Tampa. 1.05.2001.

[19] Bojdo N. Rotorcraft engine air particle separation. Doctoral Thesis. Faculty of Engineering and Physical Sciences 2012. https://www.escholar.manchester.ac.uk/uk-ac-man-scw:183545 (accessed on 19.04.2021).

[20] Long J, Tang M, Sun Z, Liang Y, Hu J. Dust loading performance of a novel submicro-fiber composite filter medium for engine. Materials. 2018;11:2038. https://doi.org/10.3390/ma11102038

[21] Siedlecki M, Szymlet N, Fuć P, Kurc B. Analysis of the possibilities of reduction of exhaust emissions from a farm tractor by retrofitting exhaust aftertreatment. Energies. 2022;15:7963. https:// doi.org/10.3390/en15217963

[22] Needelman WM. Madhavan PM. Review of lubricant contamination and diesel engine wear. SAE Technical Paper. 1988. https://doi.org/10.4271/881827

[23] Dziubak T, Dziubak SD. A study on the effect of inlet air pollution on the engine component wear and operation. Energies. 2022;15:1182. https://doi.org/10.3390/en15031182

[24] Wróblewski P, Rogólski R. Experimental Analysis of the Influence of the Application of TiN, TiAlN, CrN and DLC1 coatings on the friction losses in an aviation internal combustion engine intended for the propulsion of ultralight aircraft. Materials. 2021;14:6839. https://doi.org/10.3390/ma14226839

[25] Wróblewski P. Effect of asymmetric elliptical shapes of the sealing ring sliding surface on the main parameters of the oil film. Combustion Engines. 2017;168(1):84-93. https://doi.org/10.19206/CE-2017-114

[26] Wróblewski P. The effect of the distribution of variable characteristics determining the asymmetry of the sealing rings sliding surfaces on the values of friction loss coefficients and other selected parameters of oil film. Combustion Engines. 2017;171(4):107-116. https://doi.org/10.19206/CE-2017-418

[27] Barbolini M, Di Pauli, F, Traina M. Simulation der luftfiltration zur auslegung von filterelementen. MTZ. 2014;75:52-57. https://doi.org/10.1007/s35146-014-0556-5

[28] Schaeffer, JW, Olson LM. Air filtration media for transportation applications. Filtr. Sep. 1998;35(2):124-129. https://doi.org/10.1016/S0015-1882(97)80292-3

[29] Dziubak T. experimental studies of dust suction irregularity from multi-cyclone dust collector of two-stage air filter. Energies. 2021;14(12):3577. https://doi.org/10.3390/en14123577

[30] Muschelknautz U. Design criteria for multicyclones in a limited space. Powder Technol. 2019;357:2-20. https://doi.org/10.1016/j.powtec.2019.08.057

[31] Dziubak T, Dziubak SD. experimental study of filtration materials used in the car air intake. Materials. 2020;13(16):3498. https://doi.org/10.3390/ma13163498
[32] Jaroszczyk T, Petrik S: Donahue, K. Recent development in heavy duty engine air filtration and the role of nanofiber filter media. Journal of KONES Powertrain and Transport. 2009;16(4):207-216. https://kones.eu/ep/2009/vol16/no4/JO%20KONES%202009%20NO.%204%20VOL.%2016%20JAROSZCZYK.pdf
[33] Rieger M, Hettkamp P, Löhl T, Madeira PMP. Efficient engine air filter for tight installation spaces. ATZ Heavy Duty Worldwide. 2019;12(2):56-59. https://doi.org/10.1007/s41321-019-0023-9
[34] Wei S, Qian F, Cheng J, Xiao P, Tang L, Jiang R. Flow field analysis and structure optimization of honeycomb air filter. The Chinese Journal of Process Engineering. 2019;19(2): 271-278. https://www.jproeng.com/CN/10.12034/j.issn.1009-606X.218226
[35] Dziubak T, Boruta G. Experimental and theoretical research on pressure drop changes in a two-stage air filter used in tracked vehicle engine. Separations. 2021;8:71. https://doi.org/10.3390/separations8060071
[36] Poon WS, Liu BY. Dust loading behavior of engine and general purpose air cleaning filters. SAE Technical Paper. 1997. https://doi.org/10.4271/970676
[37] Jaroszczyk T, Fallon SL, Pardue BA. Analysis of engine air cleaner efficiency for different size dust distributions. Fluid-Particle Separation Journal. 2002;14(2):75-88.
[38] Zhang W, Deng S, Wang Y, Lin Z. Modeling the surface filtration pressure drop of PTFE HEPA filter media for low load applications. Building and Environment. 2020;177: 106905. https://doi.org/10.1016/j.buildenv.2020.106905
[39] Barris MA. Total Filtration^{TM}. The influence of filter selection on engine wear. Emissions and performance. SAE Technical Paper. 1995. https://doi.org/10.4271/952557
[40] Bugli N. Automotive engine air cleaners – performance trends. SAE Technical Paper. 2001. https://doi.org/10.4271/2001-01-1356.
[41] Jaroszczyk J, Wake J, Connor MJ. Factors affecting the performance of engine air filters. J Eng Gas Turb Power. 1993;115(4):693-700. https://doi.org/10.1115/1.2906761
[42] Bugli NJ, Green GS. Performance and benefits of zero maintenance air induction systems. SAE Technical Paper. 2005. https://doi.org/10.4271/2005-01-1139
[43] Norman K, Huff S, West B. Effect of intake air filter condition on vehicle fuel economy. U.S. Department of Energy (DOE) Information Bridge. 2009. https://www.fueleconomy.gov/feg/pdfs/air_filter_effects_02_26_2009.pdf
[44] Heywood JB. Internal Combustion Engine Fundamentals. 2nd ed.; McGraw-Hill Education: New York; 2018.
[45] Ziółkowski J, Małachowski J, Oszczypała M, Szkutnik-Rogoż J, Konwerski J. Simulation model for analysis and evaluation of selected measures of the helicopter's readiness. P I Mech Eng G-J Aer. 2022;236(13):2751-2762. https://doi.org/10.1177/09544100211069180
[46] Ziółkowski J, Małachowski J, Oszczypała M, Szkutnik-Rogoż J, Lęgas A. Modelling of the military helicopter operation process in terms of readiness. Defence Sci J. 2021;71:602-611. https://doi.org/10.14429/dsj.71.16422
[47] Zhu Q, Zong Y, Tan YR, Lyu J, Yu W, Yang W et al. Evaluating the effect of n-butanol additive on particulate matter emission in diesel engine. Fuel. 2023;332:126003. https://doi.org/10.1016/j.fuel.2022.126003
[48] Erol D, Yeşilyurt MK., Jaman H, Doğan B. Evaluation of the use of diesel-biodiesel-hexanol fuel blends in diesel engines with exergy analysis and sustainability index. Fuel. 2022;337:126892. https://doi.org/10.1016/j.fuel.2022.126892
[49] Su X, Chen H, Gao N, Ding M, Wang X, Xu H et al. Combustion and emission characteristics of diesel engine fueled with diesel/cyclohexanol blend fuels under different exhaust gas recirculation ratios and injection timings. Fuel. 2023; (32):125986. https://doi.org/10.1016/j.fuel.2022.125986
[50] Andrych-Zalewska M, Merkisz J, Pielecha J. The influence of the heating time of a catalyst-covered glow plug on the exhaust emissions from a diesel engine. Combustion Engines. 2021;184(1):52-56. https://doi.org/10.19206/CE-134738
[51] Yan J, Gao S, Zhao W, Lee TH. Study of combustion and emission characteristics of a diesel engine fueled with diesel, butanol-diesel and hexanol-diesel mixtures under low intake pressure conditions. Energ Convers Manage. 2021; (243):114273. https://doi.org/10.1016/j.enconman.2021.114273
[52] Zhao W, Yan J, Gao S, Lee TH, Li X. The combustion and emission characteristics of a common-rail diesel engine fueled with diesel, propanol, and pentanol blends under low intake pressures. Fuel. 2022;307;121692. https://doi.org/10.1016/j.fuel.2021.121692
[53] Karczewski M, Szczęch L. Influence of the F-34 unified battlefield fuel with bio components on usable parameters of the IC engine. Eksploat Niezawodn. 2016;18(3):358-366. https://doi.org/10.17531/ein.2016.3.6
[54] Dziubak T. Analiza wpływu oporu przepływu filtru powietrza na napełnienie tłokowego silnika spalinowego. Zeszyty Naukowe Politechniki Szczecińskiej. 1992;19(491):33-40.
[55] Dziubak T, Bąkała L. Problems of selecting filter partition in passenger car engine intake air filters. Combustion Engines. 2021;185(2):44-59. https://doi.org/10.19206/CE-139629
[56] Dziubak T, Trawiński G. The experimental research of the air filter flow drag influence on the T359E engine operation parameters. Bulletin of the Military University of Technology. 2001;4(584):135-149. https://biuletynwat.pl/resources/html/newsDetails?id=456
[57] Dziubak T, Trawiński G. The experimental assessment of air supply system modification on inlet air filtration efficiency and military vehicle engine effectiveness improvement. Journal of KONES Powertrain and Transport. 2010;17(3): 79-86. https://kones.eu/ep2010_3.html
[58] Yang A-J, Song Z-J, Yang J-W, Zhao C-J. Effect of air filter on performance of S1110 diesel engine. IOP Conf Ser: Mater Sci Eng. 2019;688(2):022050. https://doi.org/10.1088/1757-899x/688/2/022050
[59] Plotnikov LV, Bernasconi S, Brodov YM. The effects of the intake pipe configuration on gas exchange, and technical and economic indicators of diesel engine with 21/21 dimension. Procedia Engineer. 2017;206:140-145. https://doi.org/10.1016/j.proeng.2017.10.450
[60] Abdullah NR, Shahruddin NS, Mamat AMI. Kasolang S, Zulkifli A, Mamat R. Effects of air intake pressure to the fuel economy and exhaust emissions on a small SI engine. Procedia Engineer. 2013;68:278-284. https://doi.org/10.1016/j.proeng.2013.12.180
[61] Shannak B, Damseh R, Alhusein M. Influence of air intake pipe on engine exhaust emission. Forschung im Ingenieurwesen. 2005;70(2):128-132. https://doi.org/10.1007/s10010-006-0022-8
[62] Thomas J, West B, Huff S. Effect of air filter condition on diesel vehicle fuel economy. SAE Technical Paper. 2013. https://doi.org/10.4271/2013-01-0311

[63] Synák F, Kalašová A, Synák J. Air filter and selected vehicle characteristics. Sustainability. 2020;12(22):9326. https://doi.org/10.3390/ su12229326
[64] Dziubak T, Karczewski M. Experimental study of the effect of air filter pressure drop on internal combustion engine performance. Energies. 2022;15:3285. https://doi.org/10.3390/en15093285
[65] Technical data: FH, FM Silnik D13C460, EU5SCR-M, VOLVO. 2021. https://stpi.it.volvo.com/STPIFiles/Volvo/FactSheet/D13C460,%20EU5SCR-M_Pol_02_1144722.pdf (accessed on 27.03.2022).
[66] PN-ISO 15550:2009; Silniki Spalinowe Tłokowe – Określanie i Metoda Pomiaru Mocy Silnika – Wymagania Ogólne. PKN: Warszawa, Poland, 2009.
[67] AR6 Climate Change 2021: The Physical Science Basis of Climate Change, www.ipcc.ch (accessed on 08.11.2022).
[68] Singh M, Sandhu SS. Effect of boost pressure on combustion, performance and emission characteristics of a multicylinder CRDI engine fueled with argemone biodiesel/diesel blends. Fuel. 2021;300:121001. https://doi.org/10.1016/j.fuel.2021.121001
[69] Karczewski M, Wieczorek M. Assessment of the impact of applying a non-factory dual-fuel (diesel/natural gas) installation on the traction properties and emissions of selected exhaust components of a road semi-trailer truck unit. Energies. 2021;14:8001. https://doi.org/10.3390/en14238001
[70] Rozporządzenie Ministra Infrastruktury z dnia 31 grudnia 2002 r. w Sprawie Warunków Technicznych Pojazdów Oraz Zakresu ich Niezbędnego Wyposażenia (Dz. U. z 2016 r. poz. 2022, z 2017 r. poz. 2338 oraz z 2018 r. poz. 855). https://isap.sejm.gov.pl/isap.nsf/DocDetails.xsp?id=wdu20030320262 (accessed on 08.11.2022).
[71] Karczewski M, Chojnowski J, Szamrej G. A review of low-CO_2 emission fuels for a dual-fuel RCCI engine. Energies. 2021;14:5067. https://doi.org/10.3390/en14165

Tadeusz Dziubak, DSc., DEng. – Faculty of Mechanical Engineering, Military University of Technology, Poland.
e-mail: *tadeusz.dziubak@wat.edu.pl*

Ilona Dziobek, MSc.– Faculty of Mechanical Engineering, Military University of Technology, Poland.
e-mail: *ilona.dziobek@wat.edu.pl*

Mirosław Karczewski, DEng.– Faculty of Mechanical Engineering, Military University of Technology, Poland.
e-mail: *miroslaw.karczewski@wat.edu.pl*

Article citation info:
Gągorowski A. Analysis of the combustion engine exhaust system structure in aspect of shaping acoustic energy. Combustion Engines. 2023;193(2):112-116. https://doi.org/10.19206/CE-162935

Andrzej GĄGOROWSKI

Combustion Engines
Polish Scientific Society of Combustion Engines

Analysis of the combustion engine exhaust system structure in aspect of shaping acoustic energy

ARTICLE INFO

Received: 12 October 2022
Revised: 28 February 2023
Accepted: 2 April 2023
Available online: 16 April 2023

The flow of exhaust gases is the source of many physical processes, including thermal, acoustic, mechanical and chemical phenomena with high dynamics of changes. The study analyzes the impact of the entire structure of the exhaust system on the formation of acoustic energy, determining the transmission loss characteristics of its individual components and the entire system. On the example of a structure based on a proprietary solution of an adjustable reactive muffler, the possibilities of shaping the flow of acoustic waves in the process of designing and selecting exhaust systems for internal combustion engines were determined. The study was carried out with the use of the CFD method and a specialized package for advanced simulations AVL AST.

Key words: *acoustic energy, transmission loss, exhaust system, combustion engine*

1. Introduction

In recent years, in the area of transport, the priority task has become to reduce the emission of pollutants and noise to a minimum, which is related to the operation of a large number of internal combustion(IC) vehicles in the world. Therefore, promoting the so-called Zero-emission vehicles, including electric cars, is common in the world today and many countries present different visions and plans for the development of this type of construction. It seems, however, that the complete replacement of internal combustion vehicles will be difficult to implement and will cause various types of problems. Therefore, the use of various types of solutions in structures currently in operation can be a very valuable way to solve environmental problems, including minimizing noise emissions to the environment. One of the main sources of noise emission in internal combustion vehicles is the engine-exhaust system [1]. Taking into account the subject of reducing acoustic emissions from motor vehicles, the literature most often includes research focused on dedicated devices, namely acoustic mufflers [2, 3]. In this paper, however, a method of testing the impact of the exhaust system design on the shaping of acoustic energy using the CFD (Computer Fluid Dynamics) method, based on a holistic approach, and not only the testing of a selected element, has been proposed. For this purpose, the entire system was analyzed (including all its devices and connections) on the example of a structure based on a proprietary solution of an adjustable reactive muffler, a detailed description of which is presented in the author's previous works [4, 5]. The main objective of the research was to define the possibility of shaping the flow of acoustic waves in the process of designing and selecting exhaust systems of internal combustion engines. The tests were carried out with the use of computer fluid dynamics and the use of the AVL AST advanced simulation package.

2. Review of the construction of combustion engines exhaust systems

With the development of automotive technology and the desire to increase engine efficiency with the simultaneous task of protecting the environment against pollution and noise, the role of the exhaust system has become a priority in the design of modern internal combustion cars. Exhaust system – an often underestimated element of car engine design fulfills a number of functions that are often contradictory and therefore require optimization of the structure and the use of a compromise [6, 7]. It increases the comfort of traveling from the point of view of noise emission, and at the same time allows the engine to work properly and contributes to the reduction of the amount of harmful substances emitted by the car. The most important tasks of the exhaust system include:

- exhaust gas cleaning and reduction of the content of toxic components,
- reduction of acoustic energy generated during exhaust emissions,
- allowing the most efficient operation of the internal combustion engines (ICE), including providing minimum exhaust resistance allowing maximum engine power.

The end result is the discharge of flue gases into the atmosphere. The car exhaust system consists of many parts, starting with the main devices and ending with smaller elements, but no less important from the point of view of the tasks [6–8]. The main devices of the exhaust system are the exhaust manifold, after-treatment device (ATD) such a catalytic converter (CC) and DPF filter for diesel engines [19], single muffler or group of silencing devices, assembly of piping and connecting elements. Among the remaining parts, we can distinguish various elements to reduce vibrations, connection and assembly elements. The most important assembly parts in the exhaust system are hangers, gaskets, o-rings, clamps, bolts, nuts, flexible couplings and rigid couplings. All parts constitute a whole, allowing for proper and safe use of the car by ensuring the desired operational parameters and limiting the negative impact on people and the environment.

When reviewing various car designs, we can notice the variety of shapes and structures of individual devices, as well as differences in their arrangement in the exhaust sys-

tem [6–8]. The catalytic converter as a device for exhaust gas treatment should be installed as close to the engine as possible in order to achieve the operating temperature in a sufficiently short time and thus obtain the effectiveness of chemical processes [9, 18]. However, its actual location (as well as other devices) depends on the space available under the vehicle. The outer shape of the reactor body is most often triangular, oval or round. The ATD unit can also affect the acoustical performance of an exhaust system. From the point of view of the objectives of this paper, the "acoustic effect" closely related to the internal structure of the converter, which is formed by the honeycomb structure, is particularly important. On the other hand, its main goal is to reduce the toxic components contained in the exhaust gas, which is ensured by chemical compounds (catalytically effective materials) and precious metals covering the walls of the pipe structure, which react chemically with exhaust gases [9–11].

The construction material used is also important for the processes taking place inside the converter structure. Due to the material used for construction, we distinguish two types of catalysts: ceramic catalysts (with a ceramic block) and metal catalysts (with a metal block). In the design of the exhaust system, the catalyst must be carefully tuned, because a high level of flow resistance has a significant impact on the engine's operating characteristics [9]. On the other hand, as a result of the flow through narrow, ceramic and numerous channels in the monolith, numerous sources of sound and vibrations can be created [12]. Such a structure causes that the catalytic device also acts as a reactive damper that allows reducing exhaust gas pulsations. The shape and structure of the inlet converter should be designed so that the exhaust gas flows evenly through the monolith. The alternative metal catalyst has a structure made of a thin, crimped metal foil wound and soldered into a high-temperature system. As with a ceramic catalyst, the surface is coated with a catalytically effective material. Due to the thin wall, more channels can be distributed in the same area. This means a certain resistance to the effects of exhaust gases, which is beneficial from the point of view of optimizing the efficiency of the converter at high engine operating parameters [13].

The exhaust system mufflers, as devices dedicated to the reduction of acoustic energy in a specific frequency range, have been described in many references, and their design solutions can be very different [2, 3]. The construction uses two physical principles of shaping acoustic waves, reflection and absorption. That is why silencers can be divided into two main groups according to the above-mentioned principles, i.e. reactive and absorption silencers. Their efficiency is usually satisfactory in a narrow frequency band. Therefore, the third used group consists of reactive-absorption mufflers, which are a combination of the above-described structures – allowing to use the advantages and properties of reducing acoustic energy in a wider frequency band. A more detailed review of various muffler solutions can be found in [14].

As shown by the author's research [15], the geometry of the exhaust system, including individual elements and connection channels, as well as their dimensions and shape, are important for the formation of acoustic processes. Adjusting the geometry of the exhaust system to the chassis structure of a specific motor vehicle model requires the use of both straight and curved connecting segments. Solutions include arcs and bends of various shapes and geometries, including angular and wave elements, as well as arcs and curves with variable deflection angles.

To sum up, by using various structural elements in the exhaust system of an internal combustion engine and specific geometrical parameters, it is possible to shape acoustic energy influencing its flows on the engine-environment path in various ways. In the next chapter, an attempt was made to determine the degree of influence on the formation of acoustic processes for individual devices and for the entire system.

3. Development of models of the exhaust system and its components

They take into account the basic goal described in the introduction to this paper and, based on the theory presented in the previous chapter, a model of the exhaust system was built, containing all the basic elements, and then its parameterization was performed. The specialized AVL AST package was used to achieve the above goals. The model of the exhaust system with a power unit is shown in Fig. 1a. Its main geometric parameters are presented in Table 1.

a)

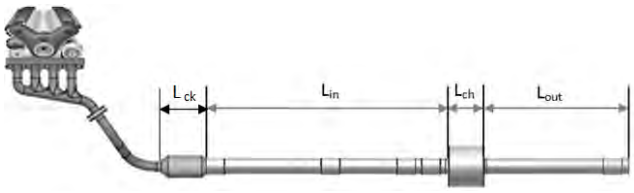

b)

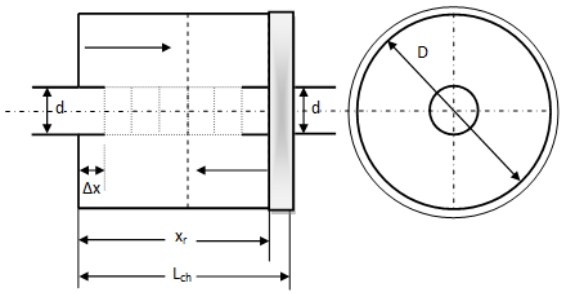

Fig. 1. Exhaust system model a) in combination with the engine b) muffler structure model with an expansion chamber (D) and inlet adjustment with a diameter (d)

The exhaust system model uses a proprietary design of a muffler with a variable structure (Fig. 1b, Table 2). The system belongs to the group of reactive systems and enables the change of the internal structure by gradual (with the assumed step Δx) control of the extended input (x_r) within the scope limited by the length of the main expansion chamber (L_{ch}).

According to the theory of gas dynamics [16], changes in the internal structure of the system cause a variable flow of the gaseous medium (in this case exhaust gases), e.g. by creating a pressure difference at the boundary of certain areas. From the point of view of the analysis of acoustic

energy [16, 17], we deal with changes in the flow resistance and acoustic pressure, as well as the velocity and direction of the flow. As a result, the acoustic energy passing through the system can be reduced or increased by incorporating further acoustic discontinuities with different resistance into the basic system.

Table 1. Geometric parameters of connection segments in the exhaust system model

Parameter and unit	Value
The diameters of the middle, inlet and outlet channels downstream the catalyst [mm]	51
Connection diameters in front of the catalyst [mm]	35.5
The length of the segment in front of the catalyst (inlet part) [mm]	400
The length of the exhaust system – central duct, L_{in} [mm]	1310
The length of the exhaust system – end duct, L_{out} [mm]	450

Table 2. Selected parameters of the muffler with the variable structure

Parameter name and unit	Value
x_r [mm]	$\Delta x \le x_r \le 100$
Δx [mm]	$0 < \Delta x < 100$
d [mm]	51
D [mm]	130
L_{ch} [mm]	110

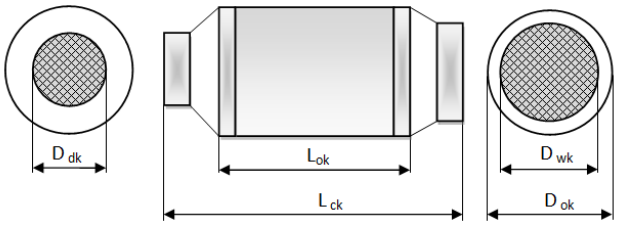

Fig. 2. Model of a catalytic reactor

In the catalyst model, the geometrical parameters of which are shown in Fig. 2, the outer shape of the body (housing) with a circular cross-section was assumed. The monolith placed in it has a "honeycomb" structure with channels visible in Fig. 2 (side views). From the point of view of the objectives of this paper, the "acoustic effect" closely related to the internal structure of the converter, which is created by the system of parallel channels, is particularly important. The kinetic model was developed using the AVL BOOST software. The catalyst parameters used in the construction of the model are presented in Tables 3 and 4. The temperature measured in the center of the monolith was used for the simulation. A monolith model with square-section channels was used. Each channel was digitized in the axial direction using 20 mesh points with a grid aspect ratio of one. Mass transfer through the boundary layer was considered using the Darcy model [17]. The parameters of the monolith sample with the square cell specification used in the simulation tests are described in Table 3.

Table 3. Parameters of the monolith sample (square cell type specification) used in the simulations

Parameter name and unit	Value
Cell density, CPSI [in^2]	400
Wall thickness, δ_{wall} [mm]	0.34
Diameter of monolith sample [mm]	21
Monolith sample length [mm]	20
Catalytic material porosity [%]	0.5

The geometric parameters adopted in the catalytic reactor model are shown in Table 4.

Table 4. Geometric parameters adopted in the catalytic reactor model

Parameter name and unit	Value
Housing diameter, D_{ok} [mm]	60
Housing length, L_{ok} [mm]	160
Monolith length, L_{mk} [mm]	150
Duct diameter, L_{kk} [mm]	1
Inlet diameter, D_{dk} [mm]	35.5
Outlet diameter, D_{wk} [mm]	51
Total length, L_{ck} [mm]	200

As mentioned in the previous chapter, the generation and type of acoustic phenomena are influenced by the geometry of the exhaust system, including the individual connecting elements. Therefore, the research also included an exemplary model of the arc segment between the exhaust manifold and the catalytic converter as an alternative to the straight connection (Fig. 3).

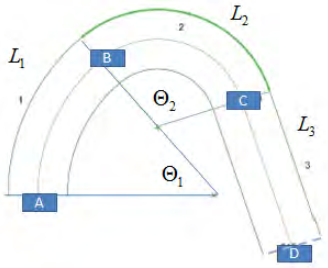

Fig. 3. Model of curvature for a cylindrical segment

In the curvature model, the connecting segment is divided into Li sections of different curvature (L1-AB, L2-BC, L3-CD,). The deflection angle for the ith segment is described in Table 5.

Table 5. Geometric parameters adopted in the curvature model

Parameter and unit	Value
Θ_1 [°]	50
Θ_2 [°]	100

4. Study on the influence of the exhaust system design on the formation of acoustic energy

Using the models described in the previous chapter, tests of the exhaust system were carried out with the use of the computer method of fluid analysis CFD. A 4-stroke internal combustion engine model was adopted as the drive unit. The model of the exhaust gas flow in the engine – exhaust system was built in the AVL AST (Advanced Simulation Tools) software environment, taking into account the AVL BOOST module for the calculation of acoustic flows. At individual stages of the research, various changes were made to the structure of the system in order to analyze the degree of influence of individual devices, as well as the geometry of connection elements on the dynamic flows of acoustic energy through its individual segments.

Table 6 shows the selected reference (initial) parameters and the boundary conditions adopted for the calculations, taking into account the operating cycle of a four-stroke internal combustion engine (SI). At the moment of starting the opening of the exhaust valve, the exhaust gas is "ejected",

and a characteristic phenomenon is the formation of overpressure pulses. These pulses travel along the system. The flow speed depends on the set engine speed. The control of the fuel mixture is determined by the ratio of air to fuel (A/F).

The calculations carried out, taking into account various variants of the exhaust system, allowed to determine, among others values of pressure and velocity of local flows in specific sections of the engine – exhaust system as a function of time, and then assess the attenuation in the assumed frequency domain (0–5000 Hz).

Table 6. Selected reference parameters and boundary conditions

Parameter name and unit	Value
Rotation speed n [rpm]	1200
A/F	14.5
Pressure p [MPa]	0.1013
Temperature T [°C]	20.85

In the work, to analyze the impact of changes in connections and individual devices on the level of transmitted acoustic energy, the indicator determining the transmission loss (TL) in the system was used. Transmission loss was defined as the difference between the sound power levels (W) of the sound determined at the beginning and at the end of a selected section of the exhaust system [15]:

$$TL = 10 \log \frac{W_{in}}{W_{out}} \quad (1)$$

The sound power level in the given section A of the system can be defined as follows:

$$W_i = \int_A \frac{|p^2|}{2\rho c} dA \quad (2)$$

where: p – pressure amplitude in the tested cross-section of the system, ρ – exhaust gas density, c – speed of sound.

Figure 4–6 for the tested frequency range (0–5000 Hz) and for three selected stages of acoustic attenuator input extension adjustment (x_{r1} = 10 mm, x_{r2} = 100 mm, x_{r3} = 40 mm) show examples of the results of the transmission loss level reflecting changes in acoustic energy for the entire exhaust system. The following figures show the waveforms of the transmission loss, respectively for the exhaust system:

– with a regulated muffler, but without a catalytic converter, and with straight-line connections (Fig. 4),
– with a regulated muffler and a catalytic converter and using straight segments (Fig. 5),
– with a regulated muffler and catalytic converter, and with a curved segment in accordance with the adopted deflection model (Fig. 6).

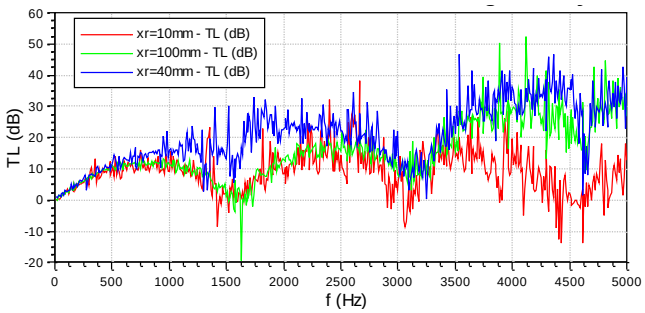

Fig. 4. Comparison of the transmission loss in the system with the regulated muffler without the catalytic converter

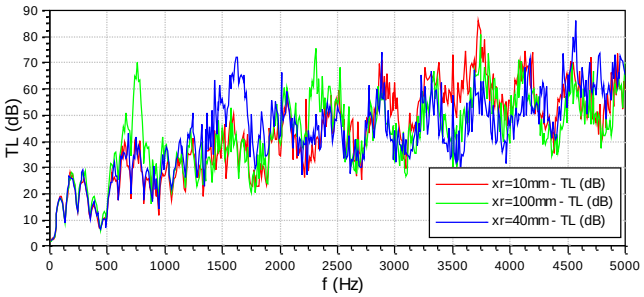

Fig. 5. Comparison of the transmission loss with the use of a straight segment in the system with the muffler and the catalytic converter for the three settings of the input extension (x_r)

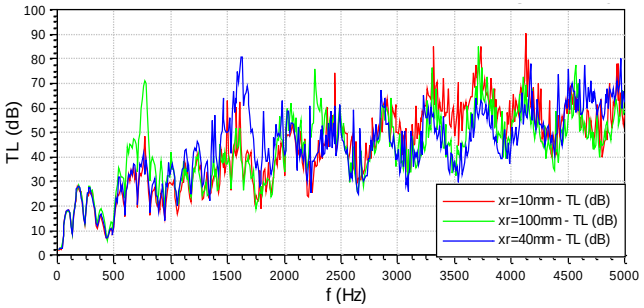

Fig. 6. Comparison of the transmission loss with the use of the arc segment and with the muffler and catalytic converter for the three x_r input extension settings

By analyzing the waveforms of the transmission loss parameter as a function of frequency, it can be concluded that the use of different designs of exhaust systems causes significant changes in terms of acoustic energy attenuation. In the examples of the results shown in Fig. 4–6 for the three design variants, quite significant differences in the TL values can be noticed, taking into account the fact that we are dealing with the decibel scale. The example in Fig. 4, representing the system with the muffler only, shows that even a small change in the internal structure of the system (e.g. changing the x_r input extension from 10 mm to 40 mm) causes quite significant changes in the entire tested frequency range. On the other hand, in the case of introducing into the structure of the exhaust system of the catalytic converter (Fig. 5), we can observe in many areas a strong enhancement of the transmission loss level. It can therefore be concluded that the catalyst has a strong influence on the transfer of acoustic energy in the system, which is consistent with the theory presented in Chapter 2. The use of a curvilinear element (Fig. 6) in the form of an arc connection between the exhaust manifold and the catalyst causes significant changes only in some frequency ranges in relation to the classical system with a straight connecting segment (Fig. 5).

Comparing all the analyzed design cases of the exhaust system, a large variability of the TL level waveforms in all the graphs can be noticed, which is manifested in significant differences in individual frequency areas, both in terms of bandwidth and the value of the transmission loss.

5. Summary

The design of the exhaust system has a considerable influence on car emissions, engine performance and exhaust acoustics. The paper presents the results of research on the

development of acoustic energy in the engine-exhaust system. A method of analyzing the impact of the structure using the CFD method was proposed, based on a holistic approach, not just the study of a selected element. The sample results presented in the article prove the great possibilities of shaping acoustic energy, pointing to its extreme levels when we apply a specific design of the exhaust system. The conducted research has shown that the sources of the formation and shaping of acoustic energy in the process of exhaust gas flow require an analysis of the structure of the entire exhaust system. The obtained results of the attenuation level in individual sections of the system made it possible to compare the waveforms in a wide frequency range and show the high dynamics of changes in the level of acoustic energy.

In the process of analyzing the entire exhaust system, a large possible range of changes in acoustic energy was demonstrated. The obtained results indicate the need for detailed further tests to validate the method taking into account other car constructions. This will confirm the correctness of its use in the process of designing the chassis of a car, taking into account the optimal design of the exhaust system to meet the acoustic requirements (in terms of reducing noise emissions to the environment).

Acknowledgements

The research has been conducted in the international program: "AVL AST University Partnership Program" (AVL, Graz, Austria).

Nomenclature

CFD	computer fluid dynamics	ATD	after-treatment device
IC	internal combustion	DPF	diesel particulate filter
ICE	internal combustion engine	CC	catalytic converter
SI	Spark Ignition	CPSI	cell per square inch
TL	transmission loss	A/F	air fuel

Bibliography

[1] Bender EK, Brammer AJ. Internal combustion engine intake and exhaust system noise. J Acoust Soc Am. 1975;58:1-22. https://doi.org/10.1121/1.380651

[2] Ji Z, Ma Q, Zhang Z. Application of the boundary element method to predicting acoustic performance of expansion chamber mufflers with mean flow. J Sound Vib. 1994;173: 57-71. https://doi.org/10.1006/jsvi.1994.1217

[3] Selamet A, Lee IJ, Huff NT. Acoustic attenuation of hybrid silencers. J Sound Vib. 2003;262(3):509-527. https://doi.org/10.1016/S0022-460X(03)00109-3

[4] Gągorowski A. Badania wybranych struktur tłumików układów wydechowych w środowisku AVL. Prace Naukowe Politechniki Warszawskiej. Transport. 2016;112:101-110.

[5] Gągorowski A. Modeling of adjustable muffler in the exhaust system of an internal combustion engine. Research Methods and Solutions to Current Transport Problems, Advances in Intelligent Systems and Computing. 2020:124-132. https://doi.org/10.1007/978-3-030-27687-4_13

[6] Kesgin U. Study on the design of inlet and exhaust system of a stationary internal combustion engine. Energ Convers Manage. 2005;46(13-14):2258-2287. https://doi.org/10.1016/j.enconman.2004.10.015

[7] Smith PH, Morrison JC. The scientific design of exhaust and intake systems. R. Bentley Cambridge, Mass. 1971.

[8] Winterbone DE, Pearson RJ. Theory of engine manifold design, Wave action methods for IC engines. Professional engineering publishing. 2000.

[9] Sjoblom J, Papadakis K, Creaser D. Use of experimental design in development of a catalyst system. Catal Today. 2005;100(3-4):243-248. https://doi.org/10.1016/j.cattod.2004.09.066

[10] Grzybowiska-Świerkosz B. Elementy katalizy heterogennej. Wydawnictwo Naukowe PWN. 1993.

[11] Perry R, Green D. Perry's chemical engineers handbook, 6th edn. McGraw Hill Book Company. 1984.

[12] Lavrentjev J, Rämmal H, Tiikoja H. The passive acoustic effect of automotive catalytic converters. SAE Technical Paper 2011-24-0219. 2011. https://doi.org/10.4271/2011-24-0219

[13] Koltsakis GC, Konstantinidis PA, Stamatelos AM. Development and application range of mathematical models for 3-way catalysts. Appl Catal B-Environ. 1997;12(2-3):161-191. https://doi.org/10.1016/S0926-3373(96)00073-2

[14] Gągorowski A, Melon A. Selected aspects of modelling mufflers for exhaust systems of vehicles. Journal of KONES. 2013;20(2):97-103.

[15] Gągorowski A. Badanie wybranego połączenia w układzie wylotowym z uwzględnieniem analizy akustycznej. Prace Naukowe Politechniki Warszawskiej. Transport. 2018;121: 57-66.

[16] Rathakrishnan E. Applied gas dynamics. John Wiley and Sons. 2010.

[17] Lage JL. The fundamental theory of flow through permeable media from Darcy to turbulence. Transport Phenomena in Porous Media. 1998:1-30.

[18] Kozioł-Jarosz M, Brzeżański M. The role and tasks of the support mats in the construction of catalytic converters. Combustion Engines. 2017;170(3):96-99. https://doi.org/10.19206/CE-2017-315

[19] Johnson TV, Joshi A. Directions in vehicle efficiency and emissions. Combustion Engines. 2016;166(3):3-8. https://doi.org/10.19206/CE-2016-306

Andrzej Gągorowski, DEng. – Faculty of Transport, Warsaw University of Technology, Poland.
e-mail: *andrzej.gagorowski@pw.edu.pl*

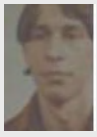

Article citation info:
Regulski P. Assessment of the life cycle of city buses with diesel and electric drive in the operation phase. Combustion Engines. 2023;193(2):117-1212. https://doi.org/10.19206/CE-162108

Paweł REGULSKI

Combustion Engines
Polish Scientific Society of Combustion Engines

Assessment of the life cycle of city buses with diesel and electric drive in the operation phase

ARTICLE INFO

Received: 22 November 2022
Revised: 28 February 2023
Accepted: 11 March 2023
Available online: 16 March 2023

The aim of the article is to analyze the impact of operation on the life cycle assessment of city buses with diesel and electric drive using neural networks based on source data. Two types of diesel buses and two types of electric buses were tested. As a result of the conducted tests, the following optimal values were obtained for buses: operation time, number of inspections, daily refueling time or battery charging time, general efficiency, emissions. The adopted values of the life cycle assessment criteria are optimal for electric and electric city buses. The presented research and analyzes have a significant impact on the processes related to the organization of public transport.

Key words: *life cycle assessment, city buses, neural networks, diesel drive, electric drive*

1. Introduction

The aim of the article is to analyze the impact of operation on the life cycle assessment of city buses with diesel and electric drive using neural networks based on source data. Solaris buses are used in many Polish cities Life Cycle Assessment (LCA) concerns the assessment of potential threats to the environment. The vehicle operation phase will be analyzed. The following evaluation criteria were used:

– material and economic criterion: duration of operation
– number of inspections, daily refueling or battery charging
– time
– energy criterion: overall efficiency
– environmental criterion: emissions of harmful substances.

2. Literature review

The application of the LCA cycle and issues related to buses have been presented in many publications. Publication [13] presents the CO_2 emissions of vehicles with internal combustion and electric drives using LCA. CO_2 emissions during battery production are taken into account. Publication [11] presents two cars, one with a combustion engine and the other with an electric drive. LCA was used for the analysis. Studies have shown that the electricity supplied today in Italy for electric vehicles is, and is likely to be in 2030, mainly generated by fossil fuel power plants. Publication [15] presents a case study and a model for predicting maintenance interventions based on monitoring the condition of engine oil in city buses with internal combustion engines. Publication [21] developed a modeling framework for optimizing electric bus charging schedules that determines both planning and operational decisions while minimizing total annual costs. Comparative analyzes have shown that it is more economical and environmentally friendly to use electric buses than diesel buses. Publication [10] presents a model of longitudinal dynamics for calculating the energy demand for electric buses. The results of the model should serve as the basis for further research into battery sizes, charging strategies and charging infrastructure requirements. Publication [6] presents the results of research on the impact of various forecasted scenarios of modernization of urban bus transport in Krakow on air pollutant emissions. The implementation of the assumed scenarios, consisting in replacing old buses with modern, low- or zero-emission vehicles, will reduce the emission of nitrogen oxides (NO_x) by over 60%, volatile organic compounds (VOC) by over 82%, and carbon monoxide (CO) by nearly 52%, and particulate matter from fuel combustion (PM_{ex}) by over 77% by 2025. Studies also show an increase in N_2O emissions (by almost 43%) as a result of modernization. This phenomenon is characteristic of modern engines. In addition, the introduction of electric buses into the fleet contributes to the gradual reduction of benzo(a)pyrene emissions. Although the replacement of the bus fleet is a long-term and costly process, such actions are necessary for Krakow and the surrounding municipalities to improve air quality in this area, especially due to excessive concentrations of particulate matter and nitrogen oxides. Publication [18] presents research on trolleybuses, diesel hybrids and e-buses, including fuel cell buses. These electric city buses were compared with combustion engine vehicles represented by diesel and CNG (compressed natural gas) buses in terms of energy consumption and costs, greenhouse gas emissions, noise costs and life cycle. The results show that electric buses are a promising means of urban transport. Publication [14] presents an analysis of the life cycle costs of a fleet of electric city buses on various routes of operation. The goal is to determine the charging and battery power requirements, as well as energy consumption and life cycle costs. A special simulation tool has been developed for comprehensive evaluation of electric buses under various operating conditions. The tool allows you to systematically generate and simulate various operating scenarios with the selected bus configuration, charging method and operating route. Publication [17] presents a way to achieve a balance between diesel and electric buses. To achieve this goal, real-world bus network data in Porto, Portugal was studied, and an evolutionary algorithm developed mixed-fleet solutions, with a brief sensitivity

analysis that gave an overview of how to improve performance. Publication [7] presents the impact on the sustainable development of electric buses, noise, energy consumption and costs. In Sweden, the number of electric buses is increasing, contributing to the development of a society free of fossil fuels and reducing emissions. Previous studies of bus systems have shown the need for further study of social costs, total cost of ownership, annualized energy consumption to account for seasonal variations and acceleration noise. Addressing these needs was the aim of this study. Publication [9] developed a mathematical model of urban bus transport to support the implementation of charging infrastructure. The novelty of the model is that it includes infrastructure elements for both static and dynamic charging technologies at the same time. Publication [8] presents a European vision of more environmentally friendly buses. The innovations introduced engines with lower fuel consumption and improved the electric drive. Publication [1] presents technical and economic problems related to the implementation of buses with electric and hydrogen drives. Publication [19] presents an analysis of the total cost of ownership (TCO) of city buses with hybrid and diesel electric drives for selected urban and suburban cycles. The results show that the route and daily trips have a significant impact on the total cost of ownership values. These two factors significantly affect the total cost of the vehicle, regardless of the type of drive. In addition, it was shown that the costs of owning and operating a city bus depend on the type of drive system. The TCO method made it possible to estimate the value of the individual cost of components that make up the purchase of the vehicle and the operating costs. The test results show that electric buses represent the highest TCO values among the analyzed vehicles. Publications [2, 12, 20] present issues related to electric buses. Publication [5] presents a comparative analysis of life cycle emissions of carbon dioxide emitted by electric vehicles using different energy mixes and vehicles with an internal combustion engine. Publication [4] presents an economic analysis of electric vehicles in Poland. Publication [3] presents an analysis of the energy consumption of a hybrid drive system of a passenger car in real road conditions.

The presented publications did not apply the life cycle assessment criteria described in the article for city buses.

3. Research methodology

As part of the life cycle assessment criteria, two types of combustion buses and two types of electric buses were analyzed, taking into account their propulsion sources. The duration of operation was determined on the basis of publication [26]. The inspection of the bus should take place every six months [27]. The time of one-time charging of an electric bus with the use of a pantograph is 20 minutes [23]. The single refueling time of a diesel bus is 10 minutes [24]. Overall efficiency was determined on the basis of publications [22, 25]. Emissions of harmful substances while driving for diesel buses are 1, and for electric buses 0. In Table 1 presents the technical data of the Solaris Urbino 12 bus.

Table 2 presents the technical data of the Solaris Urbino 18 bus. Figure 1 shows the Solaris Urbino 18 bus. Table 3 presents the technical data of the Solaris Urbino 12 Electric bus.

Table 1. Technical data of the Solaris Urbino 12 bus [16, 28]

Type of Solaris Bus	Urbino 12
Years of production	Since 1999
Doors layout	2-2-2 2-2-0 1-2-2 1-2-0
Engines	1) Cummins ISB6.7E6C 250B 2) Cummins ISB6.7E6C 280B 3) Cummins ISB6.7E6C 300B 4) DAF MX-11 210 5) DAF MX-11 240 6) DAF MX-11 271
The power of the engines	1) 189 kW (257 HP) 2) 209 kW (284 HP) 3) 224 kW (304 HP) 4) 210 kW (286 HP) 5) 240 kW (326 HP) 6) 271 kW (368 HP)
Transmission	1) ZF-EcoLife 2) Voith DIWA.6

Table. 2 Technical data of the Solaris Urbino 18 bus [16, 28]

Type of Solaris Bus	Urbino 18
Years of production	Since 1999
Doors layout	2-2-2-0 2-2-2-2 1-2-2-0 1-2-2-2
Engines	1) DAF MX-11 240 2) DAF MX-11 271
The power of the engines	1) 240 kW (326 HP) 2) 271 kW (368 HP)
Transmission	1) ZF-EcoLife 2) Voith DIWA 6

Fig. 1. Solaris Urbino 18 bus

Table. 3 Technical data of the Solaris Urbino 12 Electric bus [28]

Type of Solaris Bus	Urbino 12 Electric
Years of production	Since 2013
Doors layout	2-2-2 2-2-0 1-2-2 1-2-0
Engines	1) asynchronous motor TSA TMF 35-28-4 2) in axis ZF AVE130 350V 3) ZF AVE130 400V option
The power of the engines	1) 160 kW 2) 120 kW 3) 125 kW

Table 4 presents the technical data of the Solaris Urbino 18 Electric bus.

Table 4. Technical data of the Solaris Urbino 18 Electric bus [28]

Type of Solaris Bus	Urbino 18 Electric
Years of production	Since 2014
Doors layout	2-2-2-2 2-2-2-0 1-2-2-2 1-2-2-0
Engines	1) Central asynchronous motor TSA TMF 35-44-4 2) ZF AVE 130 option
The power of the engines	1) 160 kW 2) 2*120 kW 3) *125 kW

Fig. 2 shows the Solaris Urbino 18 Electric bus. Neural networks were used to determine the optimal values of the adopted life cycle assessment criteria.

Fig. 2. Solaris Urbino 18 Electric bus

Table. 5 data summary for optimizing the life cycle assessment of buses

No.	Bus	Duration of operation [years]	Number of reviews	Daily refueling or battery charging time [min]	Overall efficiency [%]	Emissions
1	Solaris Urbino 18	14	28	10	40	1
2		13	26	10	40	1
3		12	24	10	40	1
4		11	22	10	40	1
5		10	20	10	40	1
6		7	14	10	40	1
7		3	6	10	40	1
8	Solaris Urbino 18 Electric	1	2	40	90	0
9	Solaris Urbino 12	13	26	10	40	1
10		11	22	10	40	1
11		10	20	10	40	1
12	Solaris Urbino 12 Electric	0	1	40	90	0

Optimization of the analyzed parameters was carried out using neural networks using the cluster analysis model (Kohonen networks) in the Statistica program.

The following signals are specified:

– quantitative input variables: daily refueling or charging
– time, overall efficiency, emissions
– qualitative input variables: sum of lifetime and number of inspections.

Table 6 shows the prediction sheet. Figure 3 shows the activation histogram. Table 7 presents a list of errors in the cluster analysis model.

Table 6. Prediction sheet

No. – case	Activations
1	0.922341
2	1.071934
3	0.918715
4	0.914997
5	0.911186
6	0.907277
7	0.903268
8	1.269661
9	1.071934
12	1.261194

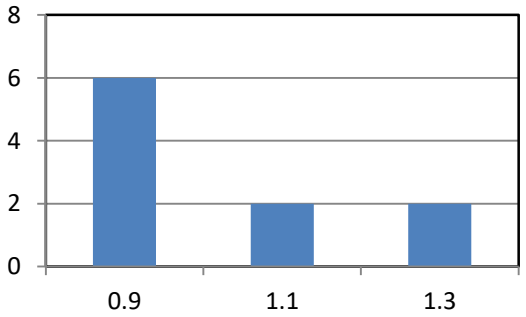

Fig. 3. Activation histogram

Table 7. List of errors in the cluster analysis model

Error (learning)	Error (testing)	Error (validation)
1.071340	0.830259	0.837220

Then, the optimization of the analyzed parameters was carried out using neural networks using a regression model in the Statistica program.

The following signals are specified:

– quantitative input variables: daily refueling or charging,
– time, overall efficiency, emissions,
– qualitative input variables: sum of operation time and number of inspections,
– quantitative output variables: activations of the prediction sheet (Table 6).

Table 8 shows the prediction sheet.

Table 8. Prediction sheet

No. – case	Output
1	1.011498
2	1.010551
3	0.948154
4	0.903268
5	0.903268
6	0.903268
7	0.903268
8	1.273699
9	1.010551
12	1.273699

Figure 4 shows the histogram of the output values.

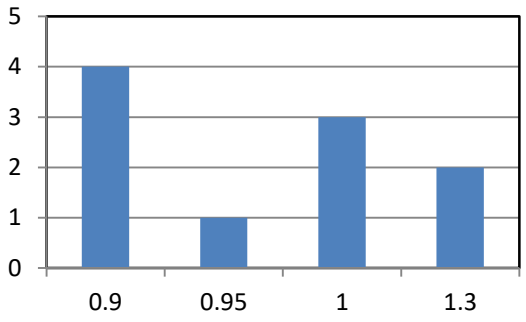

Fig. 4 Histogram of output values

Table 9 shows the list of quality and errors in the regression model.

Table 9. List of quality and errors in the regression model

Quality (training)	Quality (testing)	Quality (validation)	Error (training)	Error (testing)	Error (validation)
0.95645	0	0	0.00083	0.40794	0.40794

4. Research analysis

As a result of using neural networks with a cluster analysis model for buses Solaris Urbino 12 and 18 with diesel drive, the optimal values were for: service life 13 years, number of inspections 26, daily refueling time 10 minutes, overall efficiency 40%, emission 1. for Solaris Urbino 12 Electric buses with electric drive, the optimal values were for: duration of operation 0 (less than one year), number of inspections 1, daily battery charging time 40 min, overall efficiency 90%, emissions 0 and Solaris Urbino 18 Electric with electric drive for: operation duration 1 year, number of inspections 2, daily battery charging time 40 min, general efficiency 90%, emission 0. As a result of using neural networks with a regression model for Solaris Urbino 12 diesel buses, the optimal values were for: operation duration 13 years, number of inspections 26, daily refueling time 10 minutes, overall efficiency 40 %, emissions 1 and Solaris Urbino 18 with diesel drive for: service life 13 and 14 years, number of service intervals 26 and 28, daily refueling time 10 minutes, overall efficiency 40%, emissions 1. For Solaris Urbino 12 Electric buses with drive optimal values were for: operation duration 0 (below one year), number of inspections 1, daily battery charging time 40 min, general efficiency 90%, emission 0 and Solaris Urbino 18 Electric with electric drive for: operation duration 1 year, number of service 2, daily battery charging time 40 min, overall efficiency 90%, emissions 0.

5. Conclusions

On the basis of the conducted tests and analyzes of the life cycle assessment of city buses in the operation phase, taking into account their drive sources, it was shown that the adopted values of the life cycle assessment criteria are optimal for both city buses with diesel and electric drives. Diesel buses have a longer service life and shorter refueling time, but lower overall efficiency and emit harmful substances while driving. Electric buses have a shorter lifespan and longer battery charging times, but they are more efficient overall and do not emit harmful substances while driving. The presented studies and analyzes show that with the current technological development, both diesel and electric buses are used in urban transport. The results of the conducted analyzes have a significant impact on the processes related to the organization of public transport. Further research will be conducted towards the application of other life cycle assessment criteria for various types of urban transport rolling stock.

Nomenclature

CNG compressed natural gas
CO carbon monoxide
CO_2 carbon dioxide
LCA life cycle assessment
NO_x nitrogen oxides
N_2O nitrous oxide
TCO total cost of ownership
VOC volatile organic compounds

Bibliography

[1] Bakker S, Konings R. The transition to zero-emission buses in public transport – The need for institutional innovation. Transport Res D-Tr E. 2018;64:204-215. https://doi.org/10.1016/j.trd.2017.08.023
[2] Basma H, Mansour C, Haddad M, Nemre M, Stabat P. Comprehensive energy modeling methodology for battery electric buses. Energy. 2020;207:118241. https://doi.org/10.1016/j.energy.2020.118241
[3] Bieniek A, Graba M, Mamala J, Prażnowski K, Hennek K. Energy consumption of a passenger car with a hybrid powertrain in real traffic conditions. Combustion Engines. 2022;191(4):15-22. https://doi.org/10.19206/CE-142555
[4] Bienek F, Szczygiel I, Rutczyk B. Economical analysis of electric vehicles in Poland. Combustion Engines. 2023;192(1):55-62. https://doi.org/10.19206/CE-151941
[5] Bogacki M, Bździuch P. Predicting the spatial distribution of emissions from urban buses based on previously measured data and scenarios for their modernization in the future. Case study: Krakow, Poland Atmospheric Environment. 2019;199:1-14. https://doi.org/10.1016/j.atmosenv.2018.11.009
[6] Boren S. Electric buses' sustainability effects, noise, energy use, and costs. Int J Sustain Transp. 2020;14(12):956-971. https://doi.org/10.1080/15568318.2019.1666324
[7] Borkowski A, Zawiślak M. Comparative analysis of the life-cycle emissions of carbon dioxide emitted by battery electric vehicles using various energy mixes and vehicles with ICE. Combustion Engines. 2023;192(1):3-10. https://doi.org/10.19206/CE-147159
[8] Corazza MV, Guida U, Musso A, Tozzi M. A European vision for more environmentally friendly buses. Transport Res D-Tr E. 2016;45:48-63. https://doi.org/10.1016/j.trd.2015.04.001

[9] Csonka B. Optimization of static and dynamic charging infrastructure for electric buses. Energies. 2021;14(12): 3516. https://doi.org/10.3390/en14123516
[10] Gallet M, Massler T, Hamacher T. Estimation of the energy demand of electric buses based on real-world data for large-scale public transport networks. Appl Energ. 2018;230:344-356. https://doi.org/10.1016/j.apenergy.2018.08.086
[11] Girardi P, Gargiulo A, Brambilla PC. A comparative LCA of an electric vehicle and an internal combustion engine vehicle using the appropriate power mix: the Italian case study. Int J Life Cycle Ass. 2015;20:1127-1142. https://doi.org/10.1007/s11367-015-0903-x
[12] Janicka A, Zawiślak M, Głogoza A, Włostowski R. Optimization of the electric bus radiator design in terms of noise emissions and energy consumption by computational fluid dynamics. Combustion Engines. 2022;191(4):41-50. https://doi.org/10.19206/CE-147256
[13] Kawamoto R, Mochizuki H, Moriguchi Y, Nakano T, Motohashi M, Sakai Y et al. Estimation of CO_2 emissions of internal combustion engine vehicle and battery electric vehicle using LCA. Sustainability. 2019;11(9):2690. https://doi.org/10.3390/su11092690
[14] Lajunen A. Lifecycle costs and charging requirements of electric buses with different charging methods. J Clean Prod. 2018;172:56-67. https://doi.org/10.1016/j.jclepro.2017.10.066
[15] Raposo H, Farinha JT, Fonseca I, Ferreria LA. Condition monitoring with prediction based on diesel engine oil analysis: a case study for urban buses. Actuators. 2019;8(1):14. https://doi.org/10.3390/act8010014
[16] Regulski P. The material and economic assessment of the life cycle of city buses in the operational phase. Combustion Engines. 2023;192(1):50-54. https://doi.org/10.19206/CE-151942
[17] Santos D, Kokkinogennis Z, de Sousa JF, Perrotta D, Rossetti RJF. Towards the integration of electric buses in conventional bus fleets. IEEE 19th International Conference on Intelligent Transportation Systems (ITSC). 2016:88-93. https://doi.org/10.1109/ITSC.2016.7795537
[18] Slavik J. Electric buses in urban transport—the situation and development trends. Journal of Traffic and Transportation Engineering. 2014;2(1):45-58.
[19] Szumska EM, Pawełczyk M, Jurecki R. Total cost of ownership analysis and energy efficiency of electric, hybrid and conventional urban buses. Eksploat Niezawodn. 2022; 24(1):7-14. http://doi.org/10.17531/ein.2022.1.2
[20] Verbrugge B, Hasan MM, Rasool H, Geury T, El Baghdadi M, Hegazy O. Smart integration of electric buses in cities: a technological review. Sustainability. 2021;13(21):12189. https://doi.org/10.3390/su132112189
[21] Wang Y, Huang Y, Xu J, Barclay N. Optimal recharging scheduling for urban electric buses: A case study in Davis. Transport Res E-Log. 2017;100:115-132. https://doi.org/10.1016/j.tre.2017.01.001
[22] www.autoexpert.pl/artykuly/o-typach-silnikow-elektrycznych (accessed on 3.10.2022)
[23] ecity.solarisbus.com/baza-wiedzy/ile-trwa-naladowanie-autobusu-elektrycznego (accessed on 1.03.2023)
[24] www.eska.pl/krakow/krakowskie-mpk-zaprezentowalo-autobus-zasilany-ogniwami-wodorowymi-zdjecia-aa-3xss-HCaA-MWNi.html (accessed on 1.03.2023)
[25] www.motofakty.pl/sprawnosc-cieplna-silnika-nie-taka-fizyka-straszna/ar/c4-16275055 (accessed on 3.10.2022)
[26] www.spak.pl (accessed on 1.10.2022)
[27] www.stacjakontrolicel.pl/badanie-techniczne-autobusu (accessed on 3.10.2022)
[28] www.wikipedia.org (accessed on 24.11.2022)

Paweł Regulski, MSc. – graduate Faculty of Mechanical Engineering and Mechatronics, West Pomeranian University of Technology in Szczecin, Poland.
e-mail: *regulski85@gmail.com*

Article citation info:
Chojnowski J. The concept of a mobile automated diagnostic and dynamometer station for heavy trucks. Combustion Engines. 2023;193(2):122-128. https://doi.org/10.19206/CE-163320

Janusz CHOJNOWSKI

Combustion Engines
Polish Scientific Society of Combustion Engines

The concept of a mobile automated diagnostic and dynamometer station for heavy trucks

ARTICLE INFO

Received: 2 March 2023
Revised: 1 April 2023
Accepted: 16 April 2023
Available online: 30 April 2023

Trucks are a key element that performs transport functions in many sectors of human activity. This makes ensuring their proper maintenance and performance critical. One of the solutions to this problem is the concept of a mobile automated testing and testing station. A mobile diagnostic and dynometric station based on a 6-foot container was built at the Military University of Technology in Warsaw. This bench is a self-contained unit that can be transported to various locations and carry out on-site testing and diagnostics of heavy trucks. The station is equipped with a fully open system and software that can accurately measure the performance and efficiency of the truck's engine and driveline and enforce specific automated diagnostic processes analogous to quality control tests during the production process. This information can then be used to make informed maintenance and repair decisions, helping to minimize downtime and increase overall vehicle life. The mobile diagnostic and dynamic station also provides a convenient and cost-effective alternative to traditional off-site testing methods, making it a valuable tool for transport companies and fleet managers.

Key words: *mobile dynamometer, automated tests, trucks, dyno*

1. Introduction

A chassis dynamometer is a device most often used to measure the power and torque of a vehicle engine [19]. The measurement is carried out indirectly by recording the torque on the rollers of the chassis dynamometer. Referring the value of this parameter to the rotational speed of the rollers, and then, via the drive system, to the engine crankshaft drive speed, allows the vehicle power to be calculated (**F**ig. 1). Due to the specificity of their work, trucks generate very high values of torque on the wheels, which is necessary to move heavy loads while maintaining appropriate dynamics and in changing road conditions (e.g. changes in ground elevation or wind speed and direction). Forcing the engine to run under extreme conditions during no-load road tests is impossible or very difficult [16]. Therefore, a reasonable solution is to use a chassis dynamometer, which allows forcing appropriate working conditions of the drive system and maintaining them for a certain period of time.

Fig. 1. View of a truck on a chassis dynamometer [16]

Thus, the work of the vehicle on the dynamometer can perform basic tasks such as [19]:

- measurement of power and torque
- determination of the actual resistance to motion of the vehicle drive system.

However, as additional tasks, we can distinguish the ones that allow to simulate real load conditions that occur on the wheels of the vehicle while driving and the ability to simulate various load conditions and maintain certain conditions for a longer time (constant rotation, constant load) extending the diagnostic capabilities of the tested vehicle. This opens doors to non-standard applications [24].

Small mobile chassis dynamometers and mobile dynamometers loaded from the power take-off shaft, used in the heavy industry and agriculture, have gained popularity on the market mainly among tuning companies that offer modifications and tuning of vehicles [13, 26]. Thanks to the measurements on the dynamometer, it is possible to accurately determine the actual performance of the vehicle before and after making the changes, which allows the tuning to be adjusted to the individual needs of the customer and is extremely helpful in diagnostics. Dynamometers are also used in scientific research where they are used to test new materials, components and drive systems, and to study the impact of various factors on the efficiency and fuel consumption of vehicles, and their mobility allows to achieve vehicle operating conditions as close as possible to those in use In the case of heavy trucks, apart from hub solutions, and one wheeled application, the market of mobile dynamometers is very narrow. This was the motivation to tackle this topic.

2. Characteristics and functionality

2.1. Diagnostic possibilities

Taking into account the diagnostic possibilities, possible applications for the discussed device/dynamometer can be selected, i.e.:

- checking the vehicle before shutting down or putting it into operation (after an accident, damage or repair) [9]

- evaluation of the vehicle's drivetrain wear level (e.g. torque and power analysis) [9]
- tuning (increasing power, modifications to the exhaust gas treatment system, mechanical modifications, eco tuning) [12]
- calibration of non-factory fuel supply systems (LPG, CNG, LNG, hydrogen) [15]
- measurements of emissions of exhaust gas components, fuel consumption (using an exhaust gas analyzer) [19, 20]
- the possibility of using automated procedures for assessing the technical condition of the vehicle using stations and dedicated OBD2 interfaces and tests implemented in them.

2.2. The mobility of the dynamometer

Convenience and Cost-effective are the factors where mobility of the station allows for on-site testing, reducing the need for trucks to be taken off the road and transported to a separate location for operation. The mobile station eliminates the costs associated with transporting the truck to an off-site location for testing, saving time and money. Servicing a large fleet of vehicles directly at the customer's machine park - in the case of modification of the fuel supply system or tuning it's a big advantage [2, 11]:

- Convenience and Cost-effective: The mobility of the station allows for on-site testing, reducing the need for trucks to be taken off the road and transported to a separate location for operation. The mobile station eliminates the costs associated with transporting the truck to an off-site location for testing, saving time and money. Servicing a large fleet of vehicles directly at the customer's machine park – in the case of modification of the fuel supply system or tuning it's a big advantage;
- Increased efficiency: By conducting diagnostics and testing on-site, the time required to diagnose and repair a truck is reduced, leading to increased efficiency and decreased downtime. This is of key importance when operating on the battlefield or, for example, during motorsport competitions;
- Improved accuracy: The advanced sensors and software used in the mobile station provide highly accurate measurements of the truck's performance, helping to identify potential problems before they become major issues;
- Increased accessibility: The ability to bring the station to various locations increases accessibility for fleet managers, allowing them to conduct testing and diagnostics even in remote areas;
- Increased safety: By conducting testing and diagnostics on-site, the risks associated with transporting the truck to an off-site location are reduced, improving the overall safety of the vehicles and the people operating them.

3. Construction of a mobile chassis dynamometer for trucks

3.1. Benchmarking of technological solutions

As part of the research, learning and creative use of the best market models at a given moment, only one company that implemented this idea was found. The company Tylor Dyno, from Milwaukee, USA, was the only one in the world to deal with the subject. The company developed a mobile dynamometer for trucks, in a comprehensive style. Company used an 18-meter semi-trailer, a crane on board and a lot of spectacular automation as shown on Fig. 2 [17].

Fig. 2. Render of the mobile chassis dynamometer solution by Taylor Dyno [19]

The design of the mobile truck dynamometer form Tylor Dyno has a structure built on a semi-trailer, which makes it impossible to use this idea in non-road applications with an emphasis on military use. This solution also takes up a lot of space and requires a truck tractor to change the place of operation each time. Unfortunately, the solution found was far from meeting the needs of the designed device, which prevented deeper inspiration from market solutions.

3.2. Design, construction and testing

The design and construction process of a mobile automated diagnostic and dynamometer station for heavy trucks involved several stages [5, 17].

- Requirements gathering: The assumptions of various types of use (the original need to build a dynamometer was related to the project for mass modifications of trucks with dual-fuel CNG/diesel) and the dedicated possibility of military use in bad or unknows terrain meant that the chassis dynamometer designed at MUT had to be redefined compering to Tylor Dyno solution. Due to this fact, the need to build a dynamometer station with the following design assumptions was put forward:
  - loading/unloading using a hydraulic lift which is an integral part of the transporting vehicle
  - provide the possibility of temporarily setting up a mobile diagnostic and dynamometer station at the customer's site for the duration of the assembly
  - the station is to be able to be folded into a standardized container for transport
- Conceptual design: Based on the requirements, a conceptual design of the station is created. This includes the overall layout of the station, the type of equipment to be used, and the overall functionality of the system as shown on the Fig. 3 below.
- Detailed design: In this stage, the conceptual design was refined into a detailed design. This included the design of the mechanical (as shown on Fig. 4 and 5) , electrical, and software systems that make up the station. All model tests were also performed at this stage which is shown on Fig. 5.

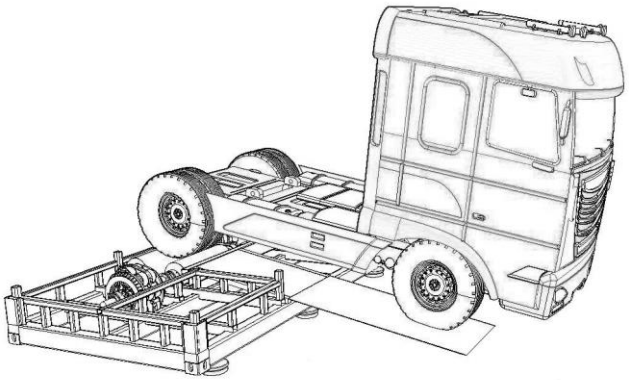

Fig. 3. Concept drawing of a mobile dynamometer for heavy trucks with the vehicle placed

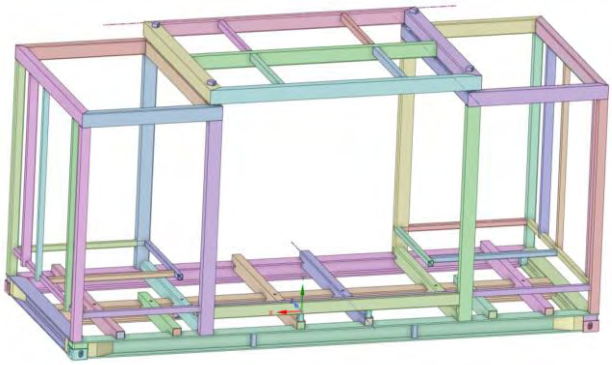

Fig. 4. Technical drawing of the mobile dynamometer support structure

The figure above shows the base of the dynamometer structure, for which a lattice structure with dimensions of a 6-foot sea container was used. In the upper part of the drawing it's notacible a removable part of the roof of the container, enabling diagnosis on the rollers of the dynamometer of higher trucks with bodies.

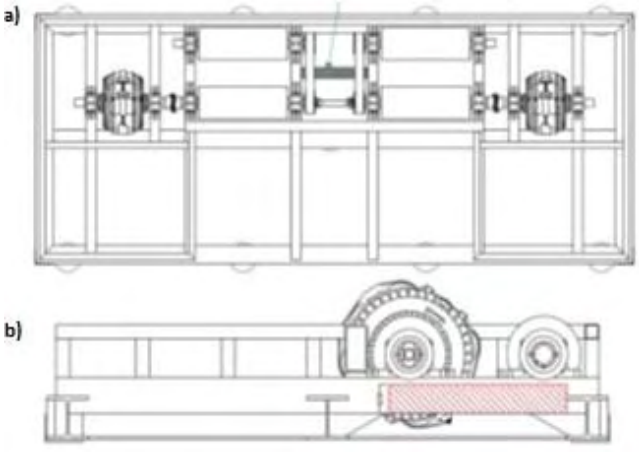

Fig. 5. Technical drawing of the low part of mobile dynamometer with the location of brakes and rollers: a) top view; b) side view

The Figure 5 above shows the low mounting of the roller assembly and eddy current brakes allowed to lower the center of gravity of the machine. The off-center offset of this assembly helped to reduce the angle of attack necessary for the vehicle to climb onto the rollers. This allows vehicles with a small ground clearance to interact with the device and is of great importance, for example, in the context of road tractors or motorsport vehicles. The use of a removable roof and asymmetry in the location of the weight of the device required in-depth research on the stiffness of the load-bearing structure and its loads, which is shown in Fig. 6. This was crucial for maintaining the axiality of the roller-brakes system and the possibility of multiple manipulation (moving) of the device without damage.

Fig. 6. Visualization of the mechanical load model of the mobile dynamometer structure

In Figure 6, there is a tendency to deformation on the axis perpendicular to the axis of the rollers and breaking deformations due to the removable roof. Engineers and designers had to strengthen the base structure and develop a roof structure that would transfer loads in the closed state (only in this state can the station be moved with a crane).

- Manufacturing and assembly: Once the design was finalized, the station has been manufactured and assembled. This included the fabrication of the mechanical components, the assembly of the electrical components, and the integration of the software. The project was implemented by members of a consortium consisting of the following companies: Dyno Revolt, Bart-Bud with the substantive and conceptual support of MUT. The author of this article was the designer and coordinator of this project.
- Testing and commissioning: The completed station has been thoroughly tested to ensure it meets all requirements. Problems that needed to be solved were also identified and a concept for further development of the station was developed (more on this in point 4 of this article). Validation included performance tests, reliability tests and security tests. The figures below show a general view of the station and the dynamometer station being tested before deployment.

During the tests starting operation of the station as shown on Fig. 7c and Fig. 7d, apart from typical things such as the correct operation of the electrical installation, software or correct operation of mechanical systems, they were also checked vibration levels, long-term operation under load and heat distribution were checked, the repeatability of measurements as well as the measurement systems themselves, i.e. strain gauges and rotational speed sensors.

More on this topic the author of this article wrote as part of the work [8].

Fig. 7. General view of the mobile dynamometer station: a) front view with ramps; b) back view; c) view with the truck on the dyno; d) view of the wheels of the vehicle on the dyno

It should be emphasized that this article is a general aid to the recipient. More details on the construction can be obtained by contacting the author of this publication directly.

3.3. The final results

The station has been built on the construction of a 6-foot container and has a fastening system compliant with ISO 1161, i.e. the same as a standard sea container. This allows the dynamometer to be transported using standardized mountings [18]. The roof of the station is removable, which allows for testing vehicles with built-ups. On the Fig. 8 below, a view of the stations while being transported on a truck chassis.

Fig. 8. The diag- dyno station transported on a truck chassis

The dyno structure can be manipulated using the hydraulic crane provided with the vehicles (Fig. 9). The dynamometer can be transported through difficult terrain and set up and armed for operation in several minutes.

One of the goals of the researchers and designers was to leave the dynamometer architecture open in terms of hardware and software, as well as the possibility of designing proprietary operating modes. Therefore, the dynamometer controller has several connectors for digital and analog signals, using USB Bluetooth or PWM controller support. In addition, the software has a fully configurable and compatible CAN protocol. What's more, measurements can be easily corrected according to DIN, EC, ISO, JIS and SAE standards thanks to the built-in weather station

Fig. 9. The diag- dyno. station during unloading using a hydraulic truck crane

In the Table 1 below, some selected parameters of the dynamometer contoured by MUT are highlighted.

Table 1. Selected parameters of the mobile diagnostic and dynamometer station

Parameter	Value/Name/Type
Operating mode	Load, quasi-dynamic
Type of Brakes	2 × Frenelsa FF16 eddy current 3300 Nm
Max/Min track width	5700/1000 mm
Roller diameter, axle pressure system	320 mm, electric winch with tension reading
Dimensions, weight	6058 mm; 2545 mm; 2870 mm; 5574 kg
Transport system	Standardized 6ft container, ISO 1161 lashing system, handling with HDS
V-max on rollers	200 km/h
Modes of operation	Constant torque, constant speed, dynamic, load, ramp, combined
Temperature tolerance (operation) [storage]	–10 to +30 [–40 to +50] °C
Hardware driver	OEM DynoRevolt on Raspberry Pi 4, OBD2 compatible, HDMI connector, 4 × USB 3.0, 4 × HP analog input, 4 × analog input, 3 × low side PWM
Software	OS Debian Linux 5.4.14, OEM dyno software DynoRevolt "Dyno2 RPI 2.17.0" fully configurable, support for CAN, analog, digital PWM, bluetooth, USB and OBD signals, Measurements with corrections according to DIN 70020, EC 95-1, ISO 1585, JIS D1001, SAE J1349

The diagnostic and dynamometer station measures typical dynamometer values such as power, torque and all derivatives resulting from the possibility of programming your own test runs. It is worth noting that the software allows to read up to 166 real values of engine accessories using the vehicle's OBD connector (using a chip, e.g. ELM 327, STN1110). Leaving the system open allows more complex tests to be performed. Table 2 below summarizes selected values can be measured and those that may be

involved in the work of the dynamometer and the implementation of special tests on it.

Table 2. Selected measured, represented and involved in testing values used by discussed station

Parameter	Value/Name/Type
Engine speed [rpm]	Calculated engine speed
RPM acceleration motor speed [rpm/s]	Engine speed delta over time
Road speed [km/h]	Calculated linear "running" speed of the vehicle
Power loss [HP]	total power lost due to speed changes and load changes
Inertia power of the drive system [HP]	Inertia force of the drive system
Power on wheels [HP]	Calculated power at the wheels of the vehicle
Motor moment of inertia [Nm]	Calculated engine moment of inertia
Engine power [HP]	calculated engine power
Motor torque [Nm]	measured and calculated engine torque
Cor. engine power [HP]	corrected engine power
Ambient pressure [hPa], Ambient temperature [°C], Ambient humidity [%]	measured by the dynamometer's built-in weather station system
Cooperation with the vehicle's CAN line	Support for up to 166 actual values of engine accessories using the OBD connector of the vehicle (chip ELM 327, STN1110)

The device in this form has been put into operation, but solutions are being developed at the moment to extend its capabilities by carrying out automated diagnostic tests under load.

4. Automated tests CAN-dynamometer

To explain the possibilities offered by the open architecture of the dynamometer let's use an analogy to the possibilities integrated into the universal electronic external diagnostic system Bosch ESI [tronic] 2.0 KTS Truck [4]. Similar possibilities can also be found in other commercial solutions such as Texa or Delphi diagnostics solution [25]. At ESI [tronic] it's possible to perform many tests that can directly or indirectly tell about the condition of individual components of the engine and drive system. These tests enforce executive functions in the engine controller for the appropriate engine components in order to check their correct functionality [26]. For example, in the software KTS can "provoke" a test regarding:

- examination of the engine using a high-pressure test
- cylinder deactivation test
- compression test
- Adblue dosing test.

Many more are implemented

Let's take an example of a compression test for wallpaper. The current values read from the starter during its operation (without fuel doing which is forced by test algorithm) may indicate discrepancies as to the compression pressure in individual cylinders, this gives us a picture of what can happen to the engine without time-consuming disassembly or classic tests with a manometer.

In a similar way, we can carry out tests under load using the dynamometer's capabilities [10, 14]. The dynamometer can maintain the operating parameters of the drive system in a given state while performing a test defined by us or sewn into its code. What's more, these tests can be blocked into entire test suites. Ultimately, it gives (similar to production control tests) comprehensive, quick knowledge about the actual condition of the vehicle and its drivetrain components. Diagnostics and non-destructive testing play a key role in keeping vehicles operational. They allow you to identify potential technical problems before they become serious problems, which can lead to vehicle failure and danger. Non-destructive testing allows you to detect damage and defects such as cracks, deformation or wear without having to dismantle or destroy vehicle components. Such tests include visual, measurement, ultrasonic, magnetic, penetrant and radiographic tests. In the context of using a dynamometer, testing of wheeled vehicles on them also fits into this definition.

The use of automated CAN-dynamometer tests using advanced technologies such as artificial intelligence, machine learning, data analysis and vision systems translates into more precise and effective diagnostics, which in turn leads to cost reduction or determines the success of a military mission or winning a race. Such investigations can detect potential technical problems and make repairs in time before they become serious safety hazards. In this way, damaged vehicles can also be deployed after repair with great efficiency.

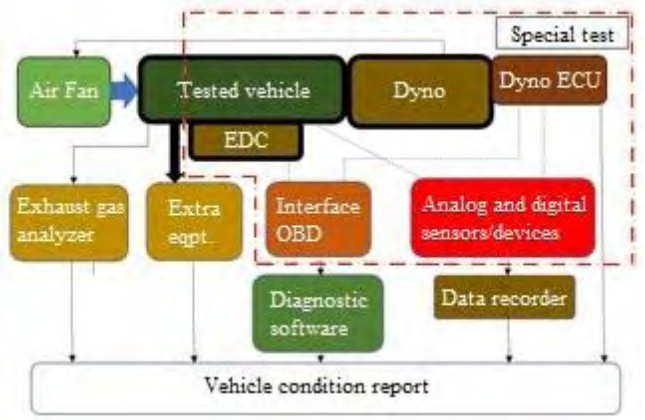

Fig. 11. A block set of elements necessary to perform forced special tests on a mobile chassis dynamometer

The picture above shows the test blocks algorithm. Real-world testing for heavy-duty vehicles may include checking the correct operation under load of components such as:

- the state of wear of individual sets of cylinder-piston rings
- the state of wear of the turbocharger
- the correctness of increasing the boost pressure
- proper operation of the wastegate valve
- correct operation of the engine brake and retarder
- testing the inertia of the drive system
- different tests including exhaust gases
- NVH test and durability can be selected depending on the application.

And much more in pre-programmed dedicated research systems. Tests can be fully automated and end with a ready

report on the status of individual elements. This allows for a quick and automated assessment of vehicle wear or damage, as well as a dynamic assessment of the vehicle's ability to return to service after a breakdown or collision.

5. Discussion

The concept of a mobile automated diagnostic and dynamometer station for heavy trucks built in MUT has great potential for revolutionizing the way in which heavy trucks are tested and calibrated.

One of the limitations of the device is the requirement for an open ECU architecture in order to achieve its full research capabilities. This means that the device and the special tests algorithm may not be suitable for use with all heavy trucks, as some with factory ECU closed setup may not be suitable. However, this limitation is not insurmountable, as open architecture is a typical configuration of vehicles modified in the context of e.g. motorsport [7].

In the case of military cars, the specification of the car delivered to the recipient is a matter of the needs of the army and related tenders [6], in which the exact parameters and functionalities of the vehicle are specified. If the military notices the potential of the dynamometer, adapting the vehicles and getting a new engine controller with an open architecture seems possible [7, 21].

However this device is capable of providing a wide range of special vehicle-dynamometer tests, and can be used for full-scale auto-calibration of external power supply systems, such as LPG or CNG. The use of the mobile automated diagnostic and dynamometer station has the potential to significantly reduce the costs related to modifying vehicles with auxiliary fuel supply. In today's applications, the auto-calibration process is able to adjust the system settings only for low loads at engine idling speed [22]. Full-scale auto-calibration, which is necessary to modify the vehicle with auxiliary power, is a time-consuming process that requires people with appropriate knowledge. However, the use of the station and the algorithms embedded in it may result in a reduction of costs related to modification by several percent.

6. Conclusion

The mobile automated diagnostic and dynamometer station for heavy trucks built in MUT is a highly innovative device that has the potential to revolutionize the way in which heavy trucks are tested and calibrated. Although there are limitations to its use, the device can still be used for a wide range of special vehicle-dynamometer tests and full-scale auto-calibration of external power supply systems. The potential cost savings associated with its use make it an attractive option for those involved in modifying heavy trucks with auxiliary fuel supply [1, 25]. Overall, the device represents a significant step forward in the field of heavy truck testing and calibration.the diagnostic and braking station allows for handling external signals, including data from CAN, and has the ability to program special tests; The above makes it possible to carry out specific automated diagnostic processes analogous to quality control tests during the production process. Research on the topic is ongoing.

Acknowledgements

This work was financed by Military University of Technology under research project UGB 22-833/2023.

Nomenclature

CAN	controller area network
CNG	compressed natural gas
DIN	Deutsches Institut für Normung e.V. (DIN; in English, the German Institute for Standardisation Registered Association)
EC	Directive 95/1/EC of the European Parliament and of the Council
EDC	electronic diesel control
HDS	hydraulic truck mounted crane
ISO	International Organization for Standardization
JIS	Japanese Industrial Standards
LPG	liquified petrolum gas
MUT	Military University of Technology
NVH	noise, vibration, and harshness
OBD	on-board diagnostics
PWM	pulse-width modulation
SAE	Society of Automotive Engineers
UGB	university research grant
USB	universal serial bus

Bibliography

[1] Andrych-Zalewska M, Sitnik L, Sroka Z, Mihaylov V. Fuel with a higher content of bio components in greenhouse effect aspects. Combustion Engines. 2023;192(1):36-42. https://doi.org/10.19206/CE-147741

[2] Animashaun I, Woods G. Design and manufacture of a mobile dynamometer. J Mech Eng Autom. 2018;8:1-7. https://doi.org/10.17265/2159-5275/2018.06.005

[3] Blyth Automotive Solutions. Diagnostic solutions to suit the environment and your budget. Blyth Automotive Solutions. https://blythautomotivesolutions.com/diagnostic-solutions-to-suit-the-environment-and-your-budget/ (accessed on 24. 02.2023)

[4] Bosch Automotive Service Solutions. KTS TRUCK. Bosch Aftermarket . https://www.boschaftermarket.com/gb/en/diagnostics/ecu-diagnosis/ecu-diagnostic-tools/kts-truck (accessed on 21. 02. 2023)

[5] Brown N, Alderson J. Mechanical Engineering Design: Principles and Concepts. 1st ed, 2019.

[6] Brzeżański M, Mężyk P. Heat balance of the military vehicle. Combustion Engines. 2017;170(3):131-134. https://doi.org/10.19206/CE2017-322

[7] Candela T. Automotive wiring and electrical systems. Car-Tech Inc., 2009.

[8] Chojnowski J, Karczewski M. Influence of the working parameters of the chassis dynamometer on the assessment of tuning of dual-fuel systems. Energies. 2022;15(13):4869. https://doi.org/10.3390/en15134869

[9] Chmielewski Z. Reliability states of diesel engine (in Polish). Autobusy: technika, eksploatacja, systemy transportowe. 2016;17(12):872-875.
[10] Di Natale M, Zeng H, Giusto P, Ghosal A. Understanding and using the controller area network communication protocol: theory and practice. Academic Press, 2013.
[11] Dyno Equipment. Portable EMC Chassis Dynamometer. https://www.dynoequip.com/portable-emc-chassis-dynamometer-en/ (accessed on 28.02.2023)
[12] Emsetup. https://www.emsetup.pl/ciezarowe (accessed on 22.02.2023)
[13] Engelmann D, Hüssy A, Comte A, Czerwinski J, Bonsack P. Influences of special driving situations on emissions of passenger cars. Combustion Engines. 2021;184(1):41-51. https://doi.org/10.19206/CE-134828
[14] Federation Internationale de l'Automobile. European Truck Racing Championship. FIA 2019. https://www.fia.com/events/european-truck-racing-championship/season-2019/european-truck-racing-championship (accessed on 25.02.2023)
[15] Gazeo. Kalibracja instalacji LPG z wykorzystaniem hamowni. https://gazeo.pl/biznes/warsztat/Kalibracja-instalacji-LPG-z-wykorzystaniem-hamowni,artykul,6292.html (accessed on 23.02.2023)
[16] Giuliano G, Dessouky M, Dexter S, Fang J, Hu S, Miller M. Heavy-duty trucks: The challenge of getting to zero. Transp Res Part D Transp Environ. 2021;93:102742. https://doi.org/10.1016/j.trd.2021.102742
[17] Hubka V. Principles of Engineering Design. eBook. ISBN: 9781483102030, 2020.
[18] International Organization for Standardization. ISO 1161 Series 1 freight containers – Corner and intermediate fittings – Specifications. https://www.en-standard.eu/iso-1161-series-1-freight-containers-corner-and-intermediate-fittings-specifications/ (accessed on 24.02.2023)
[19] Martyr AJ, Rogers DR. Chassis dynamometers, rolling roads and hub dynamometers (chapter 10). Engine Testing 5 ed. Butterworth-Heinemann; 2021:265-302. https://doi.org/10.1016/B978-0-12-821226-4.00010-3
[20] Merkisz J, Pielecha J, Radzimirski S, et al. Impact of application type of engine in heavy-duty vehicle for CO2, CO emission and fuel consumption (in Polish). WUT Journal of Transportation Engineering. 2013;98:437-445.
[21] Pawlak G. The history of the Scania engines. Combustion Engines. 2010;140(1):40-49. https://doi.org/10.19206/CE-117159
[22] Petro Online. New calibration method for LPG analysis: more convenience, less costs. Petro Online; https://www.petro-online.com/news/analytical-instrumentation/11/trace-elemental-instruments/new-calibration-method-for-lpg-analysis-more-convenience-less-costs/53676 (accessed on 1.03.2023)
[23] Taylor Dynamometer. Portable Chassis Dynamometers. https://www.taylordyno.com/products/chassis-dynamometers/portable/ (accessed on 18.02.2023)
[24] Wiśniowski P, Ślęzak M, Niewczas A. Simulation of road traffic conditions on a chassis dynamometer. Arch Motoryz. 2019;84(2):171-178.
[25] Wijesinghe A, LaFleur C, Meng F, Colvin J, Haut R. Fuel economy and emission characteristics of a high horsepower natural gas/diesel dual-fuel engine in oil & gas operations. Society of Petroleum Engineers. 2018. https://doi.org/10.2118/189590-MS
[26] Ziółkowski A, Fuć P, Lijewski P, Rymaniak Ł, Daszkiewicz P, Kamińska M et al. Analysis of exhaust emission measurements in rural conditions from heavy-duty vehicle. Combustion Engines. 2020;182(3):54-58. https://doi.org/10.19206/CE-2020-309

Janusz Chojnowski, MEng. – Faculty of Mechanical Engineering, Military University of Technology in Warsaw, Poland.
e-mail: *janusz.chojnowski@wat.edu.pl*

Article citation info:
Tarnawski P. The hybrid concept of turboshaft engine working according to Humphrey cycle dedicated to variety power demand – CFD analysis. Combustion Engines. 2023;193(2):129-136. https://doi.org/10.19206/CE-162763

Piotr TARNAWSKI

Combustion Engines
Polish Scientific Society of Combustion Engines

The hybrid concept of turboshaft engine working according to Humphrey cycle dedicated to variety power demand – CFD analysis

ARTICLE INFO

Received: 9 November 2022
Revised: 21 March 2023
Accepted: 28 March 2023
Available online: 18 May 2023

The paper presents a new concept of the turbine engine in the area of pressure gain combustion (PGE). The engine works according to Humphrey's cycle. Minor modification in construction has allowed power generation of 500 kW, 700 kW, 1000 kW, and 1800 kW. The concept successfully resolved the challenges related to the temporary opening and closing of the combustion chamber. The presented valve timing system has ensured effective gas flow and what stands behind it, an effective process of conversion of a high-pressure gas impulse into mechanical energy. Rotating combustion chambers enabled the application of an effective sealing system. The concept characterizes simple construction and potentially low power-to-weight coefficient. The CFD numerical analysis of the presented engine concept showed very promising effective efficiency and low specific fuel consumption.

Key words: *pressure gained combustion, Humphrey cycle, turbine engine, CFD analysis, valve timing system, isochoric combustion, engine energy efficiency, sealing system*

1. Introduction

The internal combustion engine industry is mature, but there is still a need and space for improving the performance of internal combustion engines [1, 2]. A reduction of fuel consumption, while at the same time improving power to weight ratio of the engine for existing on-market engines may be already limited. New opportunities are sought in the PGE (Pressure Gained Combustion) area [3–7].

The piston engine and classical turboshaft engine have different benefits, therefore they have found different applications. Generally, the piston engine has an advantage over the turboshaft engine in effective efficiency, while the turboshaft engine has an advantage over the piston engine in the power-to-mass ratio [7]. The paper presents the concept of a hybrid engine, as it has combined some of elements and benefits of both mentioned engines.

The fundamental assumption of the presented concept of the engine is that it has a temporary closed isochoric combustion chamber that is supplied by external compressed air. The first stage of compression is realized in the turbocharger, using the rest of the kinetic energy behind the turbine, and the second stage of compression is realized in the mechanical compressor. Secondly, a direct injection system is used. Next, the mechanical power is generated in the turbine. The concept of the engine was built to face the performance of turboshaft engines existing on the market.

Mentioned above assumption enabled the realization of the Humphrey cycle, which theoretical thermodynamic cycle has about a 10% advantage over the Bryton-Joule cycle (in compression ratio 20) [8–10]. A realization of the Humphrey cycle required the use of the valve timing system [6]. Its construction was the biggest challenge, as it had to deal with the realization of stages of the engine cycle like filling, isochoric, combustion, and exhaust. It had to ensure effective gas flow for variable thermal parameters (expansion from high to low pressure) and during the idle period [8, 12, 13]. The valve timing system has to deal with partial turbine load. Moreover, the full tightness of the combustion chamber had to be ensured.

The paper presents the concept of a turboshaft hybrid engine for different power applications (500 kW, 700 kW, 1000 kW, and 1800 kW). The concepts differ in the volume of combustion chambers and the number of nozzles. They work at the same engine cycle parameters, using the same diameter of the turbine.

2. 500 kW power hybrid engine concept

2.1. Simulation model of the engine concept

The simulation model of the engine for 500 kW power consists of:

- six rotating combustion chambers (1300 rpm), with a single chamber volume of 0.4 dm3,
- stationary inlet of fresh air and three different de Laval nozzles in a symmetrical arrangement. The nozzles covered 2×68 degrees of turbine circumference,
- turbine with a rotational velocity of 35000 rpm and exhausted port. The turbine width was equal to 7.5 mm (Fig. 1).

Fig. 1. Geometry model and numerical mesh–engine concept of 500 kW power

2.2. Principle of operation of the engine

Rotating combustion chambers fulfilled the role of valve timing of the engine. A single-engine cycle consists of

a filling of the combustion chamber with fresh-compressed air, direct injection of fuel, isochoric combustion, and exhaust. It was realized during 60 degrees rotation of chambers.

A pressure change for individual chambers and individual de Laval nozzles (convergent part) for 120 degrees of rotation of chambers presented is in Fig. 2. The nozzle_1 worked in the pressure range 1.7–5.0 MPa, the nozzle_2 worked in the pressure range 1.5–4.5 MPa, the nozzle_3 worked in the pressure range 1.75–3.5 MPa and the nozzle_4 worked in pressure range 1.75–2.25 MPa (Fig. 2).

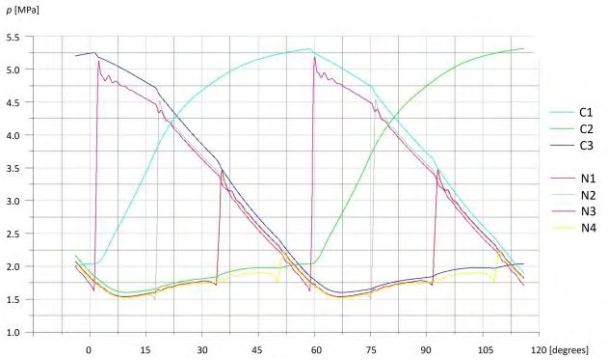

Fig. 2. Pressure change of the gas in chambers (C1, C2, C3) and nozzles (N1, N2, N3, N4) for 120 degrees rotation of chambers (2 engine cycles)

Figure 3 presents a change of oxygen content in individual combustion chambers during its 60 degrees of rotation. In chamber 1 combustion is being realized (C1-COM), in chamber 2 filling is being realized (C2-FIL) and in chamber 3 exhaust takes place (C3-EXH). Figure 4 presents the temperature distribution and Fig. 5 presents the pressure distribution at the same time of the cycle. The thermodynamic parameters pulsated according to different cycle stages. The maximum oxygen content of 18.5% was after the filling, in turn, the minimum oxygen content of 6% was after combustion. The minimum temperature of 920 K was after filling and the maximum temperature of 2320 K was after combustion. The lowest pressure of 1.6 MPa was at the beginning of filling, in turn, the maximum pressure of 5.3 MPa was at the end of combustion.

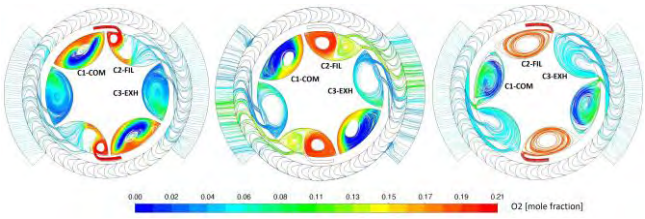

Fig. 3. Change in oxygen content of the gas for 60 degrees of rotation of chambers (1 engine cycle)

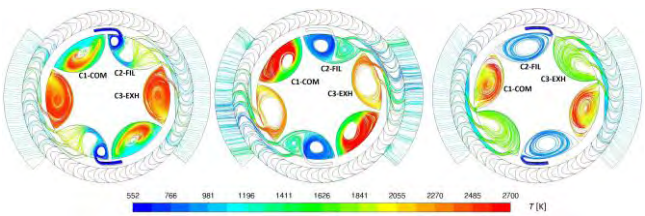

Fig. 4. Change in temperature of the gas for 60 degrees of rotation of chambers (1 engine cycle)

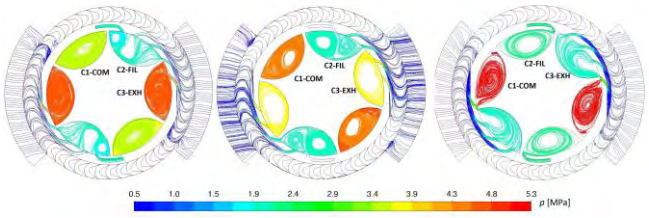

Fig. 5. Change in pressure of the gas for 60 degrees of angle rotation of chambers (1 engine cycle)

The high-pressure gas accelerated in de Laval nozzles reaching max. value of 2.8 Mach (Fig. 6).

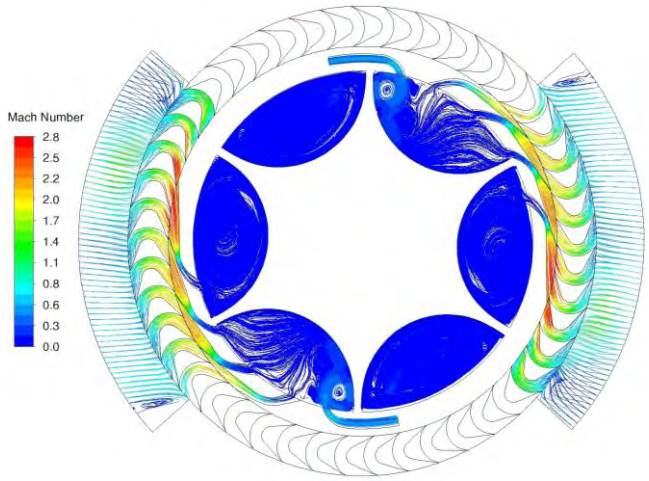

Fig. 6. The Mach number distribution

The kinetic energy of gas was transformed into mechanical energy in the turbine. Pressure distribution around the blades presented is in Fig. 7.

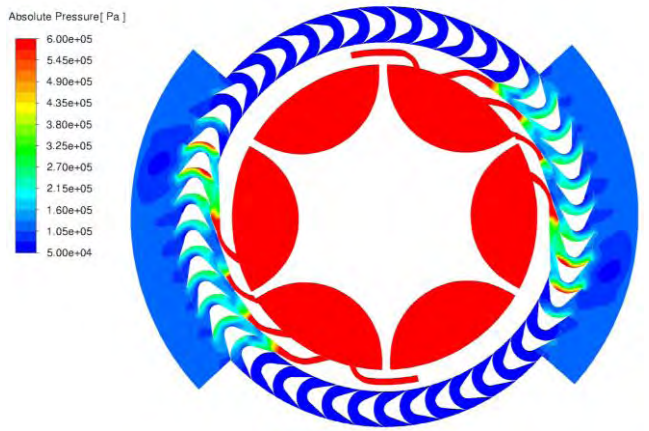

Fig. 7. The pressure distribution around the turbine blades

The torque generated in the turbine was changing from a minimum value of 60 Nm to a maximum value of 120 Nm (Fig. 8). The averaged torque was equal to 94 Nm for the symmetrical half of the engine.

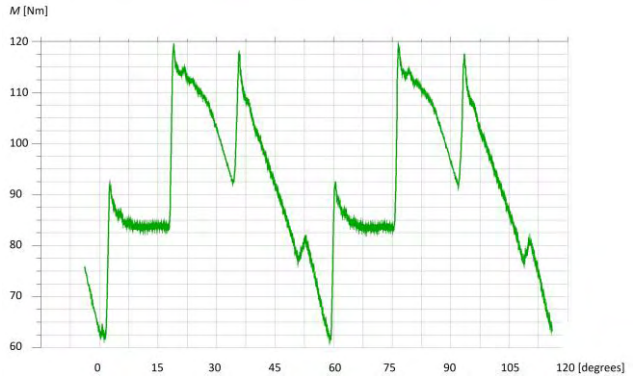

Fig. 8. Torque generated in turbine for 120 degrees rotation of chamber (2 engine cycles)

2.3. Description of the simulation approach

A transient set of Navier-Stokes equations, together with a compressible, semi-ideal, energy equation, species transport, and reaction of combustion were resolved. The thermal properties of gas species (specific heat, thermal conductivity, viscosity) were temperature-dependent. The commercial ANSYS Fluent software was employed in the analysis.

The 3D numerical simulation was performed using mesh consisting of hexahedral elements in the entire domain. The first element in the vicinity of the walls had a size of 0.25 mm. The mesh was created to assure y plus in the range of 30–300 value. The total number of elements differed from case to case between 300–600 thousand. The realizable k-ε with enhanced wall treatment option was chosen to ensure proper resolution of parameters in the boundary layer. The Rotating Mesh Motion was prescribed for rotating combustion chambers and for the turbine. The directly injected Decan was simulated using the Discrete Phase model [13]. A combustion process was simulated using the Eddy Dissipation model [15]. The excess air coefficient $\lambda = 1.6$ was assumed. The walls of the combustion chambers and walls of the nozzle were cooled. The temperature of the walls was set to 1573 K. A perfect tightness of combustion chambers was assumed. More details regarding the simulation description can be found in [15].

2.4. Evaluation of the performance of the engine concept

The 0.00012 kg of decan was injected into a single combustion chamber. The lower heat of combustion for decan was equal to 44240 kJ/kg. The 10.618 kJ of chemical energy of fuel was consumed for a single engine cycle. The kinetic energy of gas behind the turbine covered the energy demand for the turbocharger. An effective work produced by the turbine for one engine cycle (0.00769 s) was equal to 5.036 kJ. It was determined from equation (1). The mechanical efficiency of the turbine was assumed 0.95.

$$L_{eT} = \frac{M_{avg} \cdot n \cdot t_{cycle}}{9549} \eta_m \tag{1}$$

where: L_{eT} [J] – effective turbine work, M_{avg} [Nm] – averaged moment, n [rpm] – rotational velocity, t_{cycle} [s] – cycle time of discharging, $\eta_m = 0.95$ – mechanical efficiency of turbine.

The effective engine work was calculated form equation (2):

$$L_e = L_{eT} - L_{eC\_mech} \tag{2}$$

where: L_e [J] – effective engine work, L_{eC_mech} [J] – effective work demand for mechanical compressor.

Using equation (3) the effective power of the engine reached 462.6 kW.

$$N_e = \frac{L_e}{t_{cycle}} \tag{3}$$

where: $L_e = L_{eT} - L_{eC\_mech}$ [J] – effective engine work.

Using equation (2) the effective power of the engine reached 462.6 kW.

The engine effective efficiency reached 0.335. It was calculated from equation (4).

$$\eta_e = \frac{L_e}{E_{chem}} \tag{4}$$

where: η_e [-] – engine energy efficiency.

The specific fuel consumption was calculated form (5). It amounted to 242.9 g/kWh.

$$g = \frac{m_{C10H22} \cdot 1000 \cdot 3600}{t_{cycle} \cdot N_e} \tag{5}$$

where: g [g/kWh] – specific fuel consumption.

Detailed values of calculated parameters of the presented engine concept presented are in Table 1.

Table 1. Calculation of performance parameters of engine concept for 500 kW power

Parameter description	Calculated value
Chemical energy of fuel	Echem = 0.00012 kg * 2 * 44240 kJ/kg = 10.618 kJ
Effective demand of energy for turbocharger $\eta_{eC} = \eta_{iC} * \eta_T$ = 0.85*0.85*0.97 = 0.7	$L_{eC\_turbospr}$ = 0.769 kJ
Effective demand of work for mechanical compressor $\eta_{eS} = \eta_{iS} * \eta_{mS}$ = 0.85 * 0.97 = 0.83	L_{eC_mech} = 1.478 kJ
Effective work generated by turbine	L_{eT} = [(188 Nm * 35000 rpm * 0.00769 s)/9549] * 0.95 = 5.036 kJ
The kinetic energy of gas behind the turbine	E_{k_T} = 0.769 kJ
Effective work generated by engine for single engine cycle	L_e = 5.036 – 1.478 = 3.558 kJ
Effective engine power	N_e = 3.558/0.00769 s = 462.6 kW
The effective energy efficiency of the engine	η_E = 3.558/10.618 = 0.335
Specific fuel consumption	g = 0.00012 * 2 * 1000 * 3600/ (0.00769 * 462.6) = 242.9 g/kWh

3. 700 kW power hybrid engine concept

3.1. Simulation model of the engine concept

The simulation model of the engine for 700 kW power consists of:

- six rotating combustion chambers at 1500 rpm, with a single chamber volume of 0.5 dm^3,

- stationary inlet of fresh air and three different de Laval nozzles in a symmetrical arrangement. The nozzles covered 2×51 degrees of turbine circumference,
- turbine with a rotational velocity of 35000 rpm and exhausted port. The turbine width was equal to 15 mm (Fig. 9).

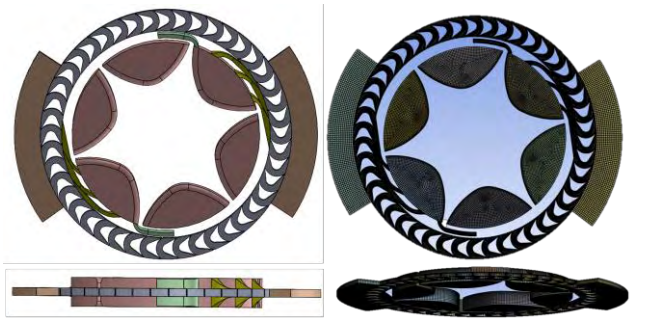

Fig. 9. Geometry model and mesh of the hybrid engine concept – 700 kW power

3.2. Evaluation of the performance of the engine concept

The effective efficiency of the engine was equal to 0.351 whereas specific fuel consumption reached 232.0 g/kWh. A detailed calculation of the performance parameters of the presented engine for 700 kW power presented is in Table 2.

Table 2. Calculation of performance parameters of engine concept for 700 kW power

Parameter description	Calculated value
Chemical energy of fuel	E_{chem} = 0.000148 kg * 2 * 44240 kJ/kg = 13.095 kJ
Effective demand of energy for turbocharger $\eta_{eC} = \eta_{iC} * \eta_T = 0.85 * 0.85 * 0.97 = 0.7$	$L_{eC\_turbospr}$ = 1.134 KJ
Effective demand of work for mechanical compressor $\eta_{eS} = \eta_{iS} * \eta_{mS} = 0.85 * 0.97 = 0.83$	L_{eC_mech} = 1.988 kJ
Effective work generated by turbine	L_{eT} = [(283.4 Nm * 35000 rpm * 0.00667s)/9549] * 0.95 = 6.58 kJ
The kinetic energy of gas behind the turbine	E_{k_T} = 1.134 kJ
Effective work generated by engine for single engine cycle	L_e = 6.58 – 1.988 = 4.593 kJ
Effective engine power	N_e = 4.593/0.00667 s = 688.5 kW
The effective energy efficiency of the engine	η_E = 4.593/13.095 = 0.351
Specific fuel consumption	g = 0.000148 * 2 * 1000 * 3600/ (0.00667 * 688.5) = 232.0 g/kWh

4. 1000 kW power hybrid engine concept

4.1. Simulation model of the engine concept

The simulation model of the engine for 1000 kW power consists of:

- six rotating combustion chambers (1300 rpm), with a single chamber volume of 0.8 dm^3,
- stationary inlet of fresh air and four different de Laval nozzles in a symmetrical arrangement. The nozzles covered 2×68 degrees of turbine circumference,
- turbine with a rotational velocity of 35000 rpm and exhausted port. The turbine width was equal to 15 mm (Fig. 10).

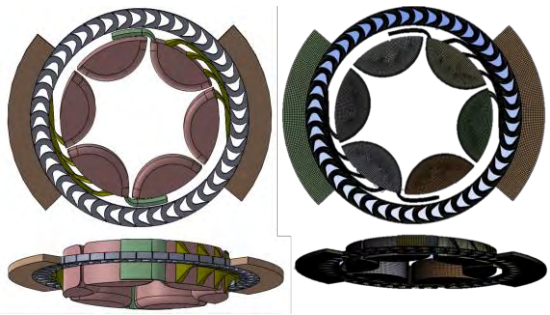

Fig. 10. Geometry model and mesh of the hybrid engine concept – 1000 kW power

4.2. Evaluation of the performance of the engine concept

The effective efficiency of the engine was equal to 0.362 whereas specific fuel consumption reached 224.6 g/kWh. A detailed calculation of the performance parameters of the presented engine for 1000 kW power presented is in Table 3.

Table 3. Calculation of performance parameters of engine concept for 1000 kW power

Parameter description	Calculated value
Chemical energy of fuel	E_{chem} = 0.00024 kg * 2 * 44240 kJ/kg = 21.235 kJ
Effective demand of energy for turbocharger $\eta_{eC} = \eta_{iC} * \eta_T = 0.85 * 0.85 * 0.97 = 0.7$	$L_{eC\_turbospr}$ = 1.704 KJ
Effective demand of work for mechanical compressor $\eta_{eS} = \eta_{iS} * \eta_{mS} = 0.85 * 0.97 = 0.83$	L_{eC_mech} = 2.925 kJ
Effective work generated by turbine	L_{eT} = [(396.0 Nm * 35000 rpm * 0.00769 s)/9549] * 0.95 = 10.618 kJ
The kinetic energy of gas behind the turbine	E_{k_T} = 1.704 kJ
Effective work generated by engine for single engine cycle	L_e = 10.618 – 2.925 = 7.693 kJ
Effective engine power	N_e = 7.693/0.00769 s = 1000.4 kW
The effective energy efficiency of the engine	η_E = 7.693/21.235 = 0.362
Specific fuel consumption	g = 0.00024 * 2 * 1000 * 3600/(0.00769 * 1000.4) = 224.6 g/kWh

5. 1800 kW power hybrid engine concept – variant with 8 chambers in two rows

5.1. Simulation model of the engine concept

The simulation model of the engine for 1800 kW power consists of:

- eight rotating combustion chambers (1700 rpm), arranged in two rows with a single chamber volume of 1.8 dm^3. Such an arrangement enabled supplying the turbine on its entire circumference.
- stationary inlet of fresh air and twelve different de Laval nozzles in a symmetrical arrangement. The nozzles covered 360 degrees of turbine circumference,
- turbine with a rotational velocity of 35000 rpm and exhausted port. The turbine width was equal to 12 mm (Fig. 11).

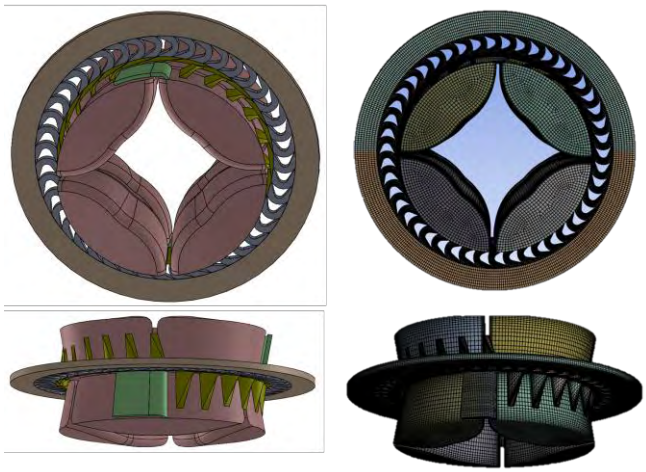

Fig. 11. Geometry model and mesh of the hybrid engine concept with 8 chambers – 1800 kW power

A pressure change for individual chambers and individual de Laval nozzles for 180 degrees of rotation of chambers presented is in Fig. 12.

Fig. 12. Pressure change of the gas in chambers (C1, C2, C3, C4) and nozzles (N1-N12) for 180 degrees rotation of chambers (2 engine cycles)

The torque generated in the turbine was changing from a minimum value of 590 Nm to a maximum value of 760 Nm (Fig. 13). The average torque was equal to 683.5 Nm.

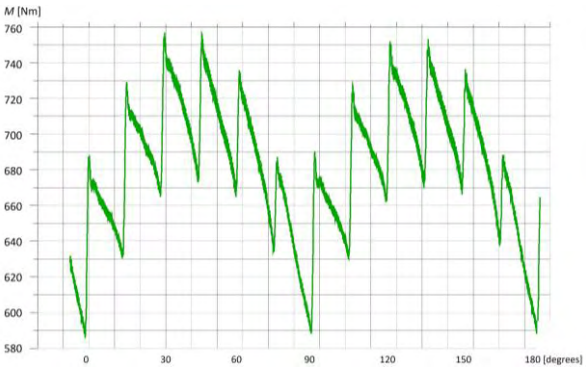

Fig. 13. Torque generated in turbine for 180 degrees rotation of chamber (2 engine cycles)

5.2. Evaluation of the performance of the engine concept

The effective efficiency of the engine was equal to 0.367 whereas specific fuel consumption reached 220.1 g/kWh. A detailed calculation of the performance parameters of the presented engine for 1800 kW power presented is in Table 4.

Table 4. Calculation of performance parameters of engine concept for 1800 kW power

Parameter description	Calculated value
Chemical energy of fuel	E_{chem} = 0.000468 kg * 2 * 44240 kJ/kg = 41.746 kJ
Effective demand of energy for turbocharger $\eta_{eC} = \eta_{iC} * \eta_T = 0.85 * 0.85 * 0.97 = 0.7$	$L_{eC\_turbospr}$ = 2.433 kJ
Effective demand of work for mechanical compressor $\eta_{eS} = \eta_{iS} * \eta_{mS} = 0.85 * 0.97 = 0.83$	L_{eC_mech} = 5.687 kJ
Effective work generated by turbine	L_{eT} = [(683.5 Nm * 35000 rpm * 0.008824 s)/9549] * 0.95 = 21.000 kJ
The kinetic energy of gas behind the turbine	E_{k_T} = 2.433 kJ
Effective work generated by engine for single engine cycle	L_e = 21.000 – 5.687 = 15.313 kJ
Effective engine power	Ne = 15.404/0.008824 s = 1745.8 kW
The effective energy efficiency of the engine	η_E = 15.313/41.746 = 0.367
Specific fuel consumption	g = 0.000468 * 2 * 1000 * 3600/(0.008824 * 1745.8) = 220.1 g/kWh

6. 1800 kW power hybrid engine concept – variant with 6 chambers in two rows

6.1. Simulation model of the engine concept

The simulation model of the engine for 1800 kW power consists of:

- six rotating combustion chambers (1700 rpm), arranged in two rows with a single chamber volume of 2.5 dm^3. The such arrangement enabled supplying the turbine on its entire circumference,
- stationary inlet of fresh air and twelve different de Laval nozzles in a symmetrical arrangement. The nozzles covered 360 degrees of turbine circumference,
- turbine with a rotational velocity of 35000 rpm and exhausted port. The turbine width was equal to 12 mm (Fig. 14).

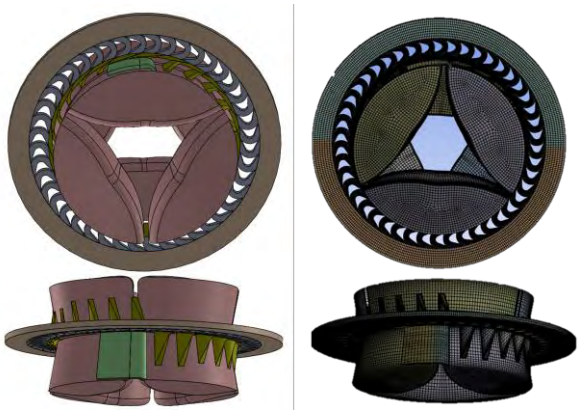

Fig. 14. Geometry model and mesh of the hybrid engine concept with 8 chambers – 1800 kW power

A pressure change for individual chambers and individual de Laval nozzles for 240 degrees of rotation of chambers presented is in (Fig. 15). Figure 16 presents a change of oxygen content in individual combustion chambers during its 60 degrees of rotation.

Fig. 15. Pressure change of the gas in chambers (C1, C2, C3) and nozzles (N1-N12) for 240 degrees rotation of chambers (2 engine cycles)

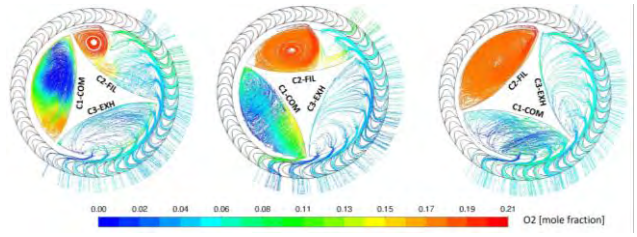

Fig. 16. Change in oxygen content of the gas for 120 degrees of rotation of chambers (1 engine cycle)

Mach distribution and pressure distribution on entire turbine circumference presented is in Fig. 17 and Fig. 18. The torque generated in the turbine was changing from a minimum value of 610 Nm to a maximum value of 750 Nm (Fig. 19). The average torque was equal to 698.0 Nm.

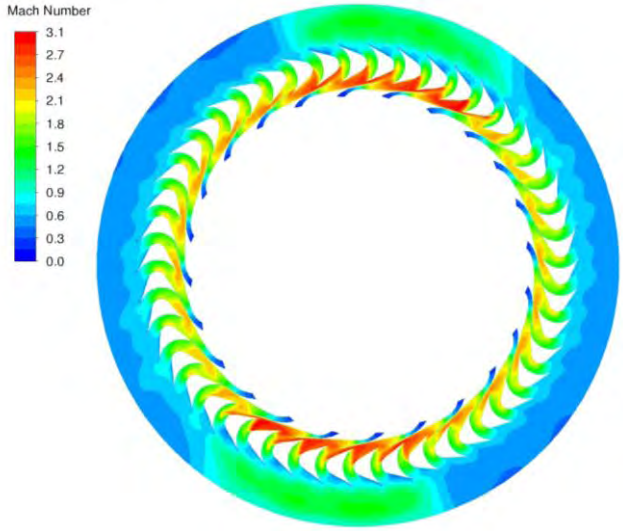

Fig. 17. Mach number distribution in nozzles and turbine

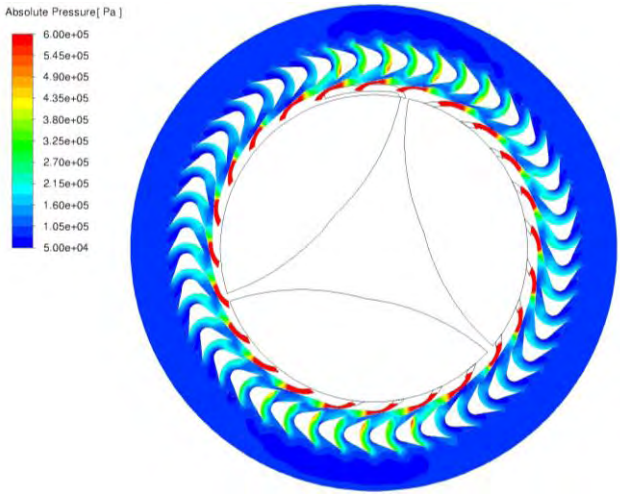

Fig. 18. Pressure distribution in nozzles and turbine

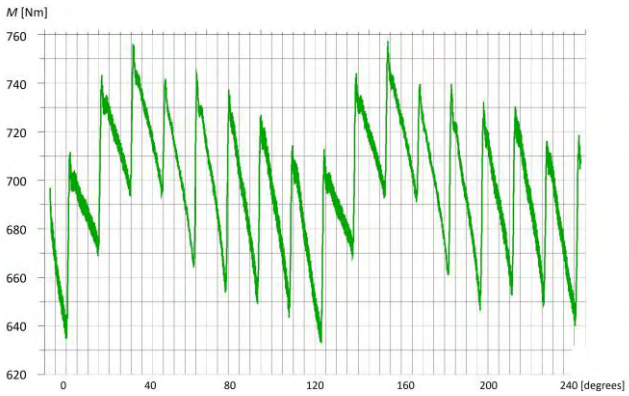

Fig. 19. Torque generated in turbine for 240 degrees rotation of chamber (2 engine cycles)

6.2. Evaluation of the performance of the engine concept

The effective efficiency of the engine was equal to 0.37 whereas specific fuel consumption reached 219.9 g/kWh (Table 5).

Table 5. Calculation of performance parameters of engine concept for 1800 kW power

Parameter description	Calculated value
Chemical energy of fuel	E_{chem} = 0.000638 kg * 2 * 44240 kJ/kg = 56.467 kJ
Effective demand of energy for turbocharger $\eta_{eC} = \eta_{iC} * \eta_T = 0.85 * 0.85 * 0.97 = 0.7$	$L_{eC\_turbospr}$ = 3.285 kJ
Effective demand of work for mechanical compressor $\eta_{eS} = \eta_{iS} * \eta_{mS} = 0.85 * 0.97 = 0.83$	L_{eC_mech} = 7.697 kJ
Effective work generated by turbine	L_{eT} = [(698.0 Nm * 35000 rpm * 0.01177 s)/9549] * 0.95 = 28.594 kJ
The kinetic energy of gas behind the turbine	E_{k_T} = 3.285 kJ
Effective work generated by engine for single engine cycle	L_e = 28.594 – 7.697 = 20.897 kJ
Effective engine power	N_e = 20.897/0.01177 s = 1776.2 kW
The effective energy efficiency of the engine	η_E = 20.897/56.467 = 0.370
Specific fuel consumption	g = 2 * 0.000638 * 1000 * 3600/(0.01177 * 1776.2) = 219.9 g/kWh

7. Conclusions

The paper presents a CFD analysis of the hybrid concept of turboshaft engine. A small modification in construction enabled its application for 500 kW, 700 kW, 1000 kW, and 1800 kW of power.

In all presented variants of the engine, the Humphrey thermodynamic cycle was realized. A temporarily closed combustion chamber assumption forced pulsating character of engine work. The proposed valve timing system reduced losses concerned with pulsating character to a minimum. The valve timing system aimed to come to the continuous power supply as closely as it was possible. A valve timing system ensured effective gas flow despite of idle period that appeared in the engine cycle (during combustion). It ensured continuous expansion in different de Laval nozzles and supplied the turbine on its entire circumference (for the engine concept of 1800 kW power).

A presented hybrid concept of a turboshaft engine is a promising design as it is characterized by the significant effective energy efficiency of 37.0% and low 219.9 g/kWh specific fuel consumption, with a potential small power-to-mass ratio. It has simple construction thus possibly lower production costs, compared to similar engines with isobaric combustion. It has some of the components used in piston engines like fuel injection systems and turbochargers, but there is no need for crankshaft [16]. An effective ceramic sealing system could be applied to the rotating combustion chambers. The segment sealing elements working with ceramic counter-surface can work as self-alignment because of the centrifugal force acting on them. The proposed system of seals ensures full chamber tightness, regardless of thermal conditions and related deformations.

It is worth comparing the results of the simulation to the performance parameters of turboshaft classical engines existing on the market. The hybrid engine concept has higher effective efficiency and lowers specific fuel conception for all presented power units. The highest advantage was for the smallest power (500 kW). The effective efficiency advantage was 33.5% and the percentage reduction of specific fuel consumption was 25.7% (Table 6).

The comparison however should be treated with some caution because of simulation simplification and connected with it margin error. The CFD analysis did not include thermal radiation phenomena. The simulation was done on intermediate mesh with no mesh sensitivity study. For better accuracy also more sophisticated combustion model could be required. Nevertheless, the greatest value of the research is the unique final engine concept that can efficiently realize the Humphrey cycle. It was systematically developed by studying many different constructions that are summarized in [6, 8, 12–14].

Table 6. Performance parameters comparison of turboshaft engines [17] and hybrid engine concept

The hybrid concept of turboshaft engine	Turboshaft engines existing on the market	Percentage advantage in efficiency	Percentage reduction of specific fuel consumption
463 kW η_e = 33.5%, g = 242.9 g/kWh	427 kW PWD207D η_e = 25.1%, g = 327 g/kWh	33.5%	25.7%
689 kW η_e = 35.1%, g = 232 g/kWh	820 kW – PT6C-67C η_e = 27.5%, g = 298 g/kWh	27.6%	22.1%
1000 kW η_e = 36.2%, g = 224.6 g/kWh	958 kW – MTR390 η_e = 29.3%, g = 280 g/kWh	23.5%	19.8%
1719 kW η_e = 36.6%, g = 220.1 g/kWh	1799 kW – RTM322 η_e = 32.1%, g = 255 g/kWh	14.0%	13.7%
1780 kW η_e = 37.0%, g = 219.9 g/kWh	1799 kW – RTM322 η_e = 32.1%, g = 255 g/kWh	15.3%	13.8%

Bibliography

[1] Żmudka Z, Postrzednik S. Improving the effective efficiency of a spark ignition engine through the use of a fully independent valve control system. Combustion Engines. 2021; 187(4):30-35. https://doi.org/10.19206/CE-141541

[2] Friedl H, Fraidl G, Kapus P. Highest efficiency and ultra-low emission – internal combustion engine 4.0. Combustion Engines. 2020;180(1):8-16. https://doi.org/10.19206/CE-2020-102

[3] Brophy C, Roy G. Benefits and challenges of pressure-gain combustion systems for gas turbines. Mech Eng. 2009; 131(3):54-55. https://doi.org/10.1115/1.2009-MAR-8

[4] Walraven F. Operational behavior of a pressure wave machine with constant volume combustion. ABB Technical Report CHCRC 94-10. 1994.

[5] Kurec K, Piechna J, Gumowski K. Investigations on unsteady flow within a stationary passage of a pressure wave exchanger by means of PIV measurements and CFD calculations. Appl Therm Eng. 2017;112(5),610-620. https://doi.org/10.1016/j.applthermaleng.2016.10.142

[6] Tarnawski P. Koncepcja silnika turbinowego o zasilaniu pulsacyjnym. Doctoral dissertation – Warsaw University of Technology 2018.

[7] Kawalec M, Perkowski W, Łukasik B et al. Applications of the continuously rotating detonation to combustion engines at the Łukasiewicz – Institute of Aviation. Combustion Engines. 2022;191(4):51-57. https://doi.org/10.19206/CE-145409

[8] Tarnawski P, Ostapski W. Pulse powered turbine engine concept – numerical analysis of influence of different valve timing concepts on thermodynamic performance. B Pol Aca Sci-Tech. 2018;66(3):373-382. https://doi.org/10.24425/123444

[9] Tarnawski P. Analytical performance evaluation of Humphrey cycle for turbine engine application. Machine Dynamics Research. 2017;41(3):27-37.

[10] Kamiuto K. Comparison of basic gas cycles under the restriction of constant heat addition. Appl Energ. 2006;83(6): 583-593. https://doi.org/10.1016/j.apenergy.2005.05.008

[11] Stathopoulos P. Comprehensive thermodynamic analysis of the Humphrey cycle for gas turbines with pressure gain combustion. Energies. 2018;11(12):3521. https://doi.org/10.3390/en11123521

[12] Tarnawski P, Ostapski W. Pulse powered turbine engine concept implementing rotating valve timing system – numerical CFD analysis. J Aerospace Eng. 2019;32(3). https://doi.org/10.1061/(ASCE)AS.1943-5525.0001001

[13] Tarnawski P, Ostapski W. A concept of a pulse-powered turbine engine with application of self-acting displacement valves-3D numerical analysis. SAE Int J Engines. 2021; 14(3):419-437. https://doi.org/10.4271/03-14-03-0025

[14] Tarnawski P, Ostapski W. Rotating combustion chambers as a key feature of effective timing of turbine engine working according to Humphrey cycle – CFD analysis. B Pol Aca Sci-Tech. 2022;70(5):e143100. https://doi.org/10.24425/bpasts.2022.143100

[15] Theory Guide. ANSYS® Academic Associate CFD, Release 16.2, Help System; ANSYS, Inc.: Canonsburg, PA, 2016.

[16] Tikhonenkov S. An internal combustion engine without a crankshaft. Perspectives. Combustion Engines. 2020; 183(4):39-44. https://doi.org/10.19206/CE-2020-406

[17] Gas Turbine Engines. Aviation week and space technology. http://www.geocities.jp/nomonomo2007/AircraftDatabase/AWdata/AviationWeekPages/GTEnginesAWJan2008.pdf (accessed on 11.11.2022).

Piotr Tarnawski, PhD – Institute of Machine Design Fundamentals, Warsaw University of Technology.
e-mail: *piotr.tarnawski@pw.edu.pl*

FUTURE IS COMING

STAY CALM

and take care of automotive innovations with us

DEPARTMENT OF AUTOMOTIVE ENGINEERING
WROCŁAW UNIVERSITY OF SCIENCE AND TECHNOLOGY

WWW.KIP.PWR.EDU.PL

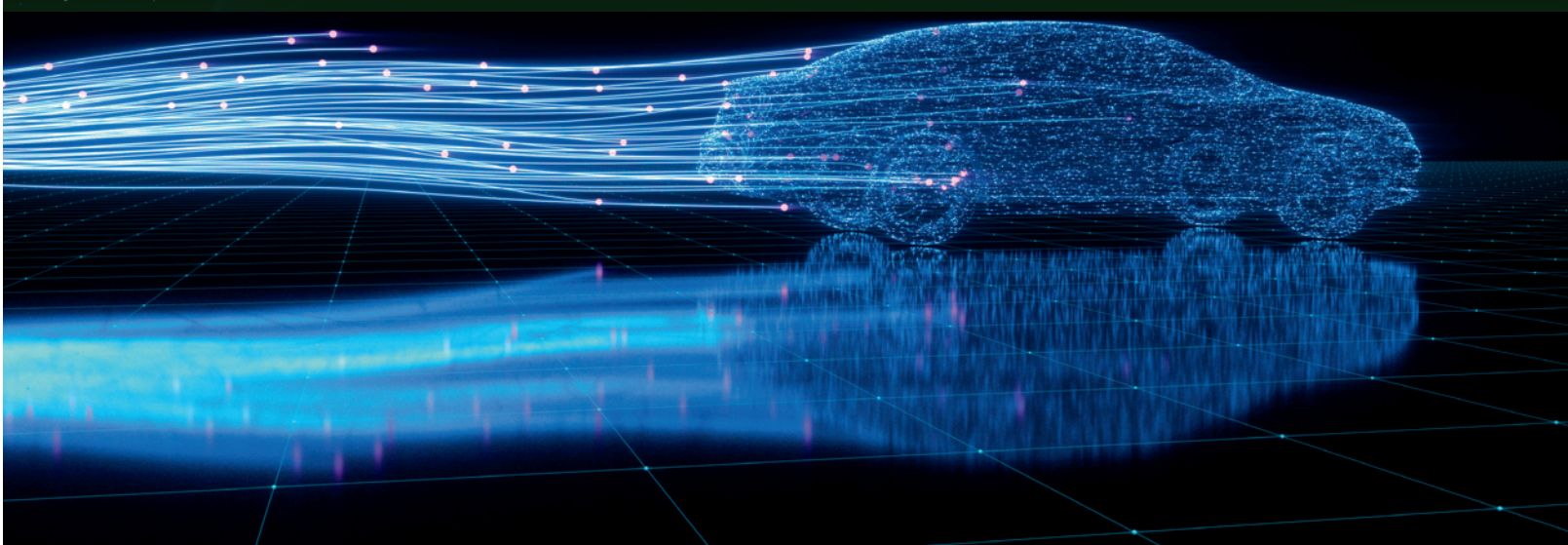

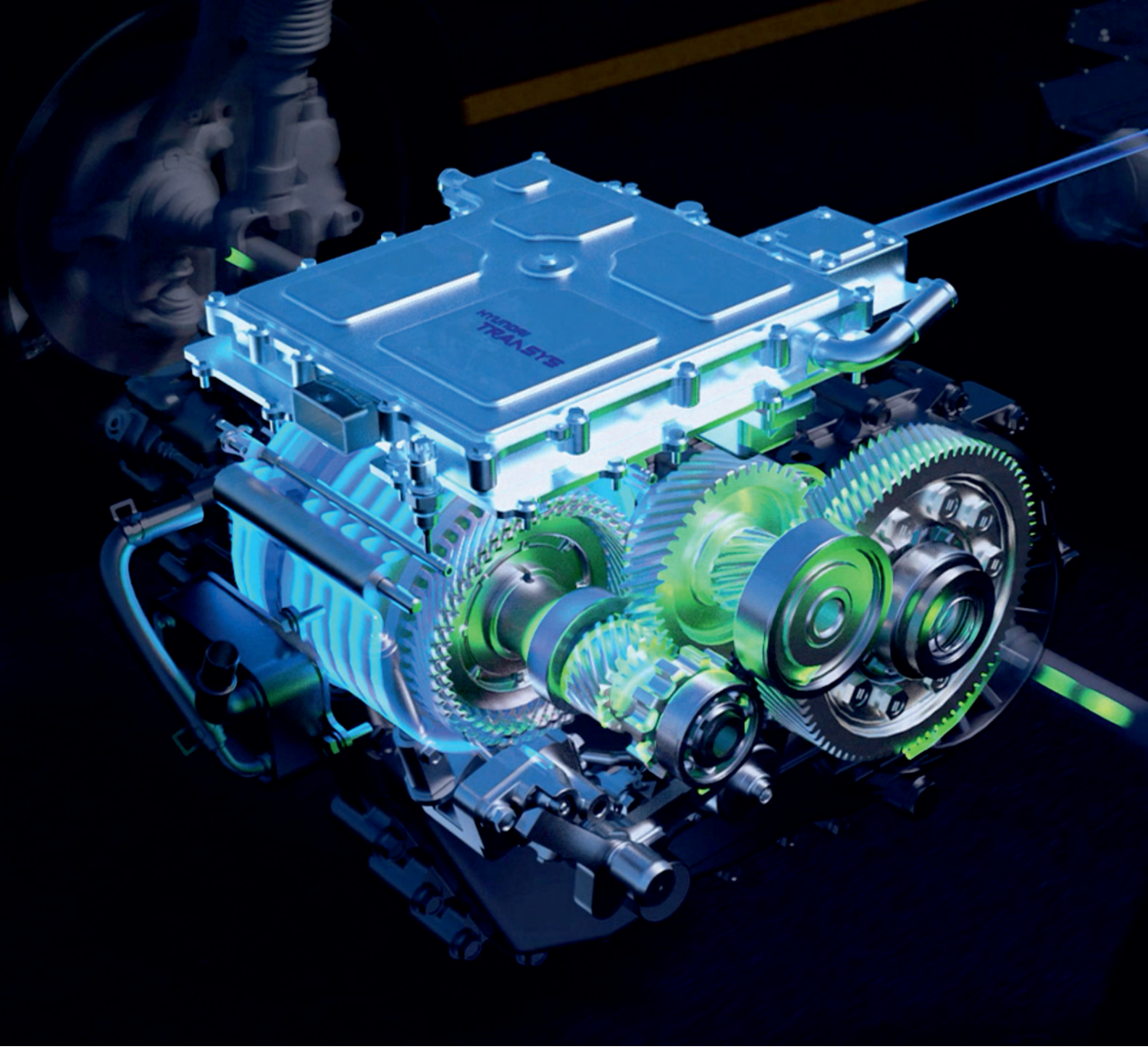

Publisher:

Polish Scientific Society of Combustion Engines

ISSN: 2300-9896
eISSN: 2658-1442

Combustion Engines

Polskie Towarzystwo Naukowe Silników Spalinowych

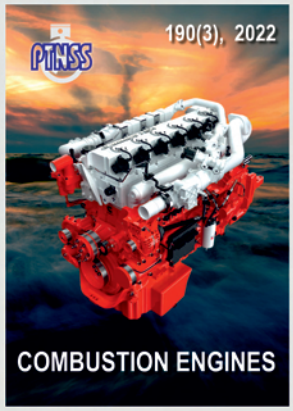

www.combustion-engines.eu